Department of Chemical
and Environmental Engineering

School of Pharmacy

University of Nottingham
UK | CHINA | MALAYSIA

Structure-Guided Design of Artificial Metalloenzymes based on Alcohol Dehydrogenase for Transfer Hydrogenation

Henry Alexander Wright Padley

A thesis submitted to the University of Nottingham for the degree of Doctor of Philosophy

June 2023

BBSRC Doctoral Training Partnerships

Abstract

Artificial metalloenzymes (ArMs) combine the advantages of enzyme and synthetic catalysts to offer novel solutions to the synthesis of high-value fine chemicals. ArMs are assembled by incorporation of an organometallic catalyst into a protein scaffold. This enables the exertion of control over the chemical environment of the catalyst via genetic manipulation of the scaffold, providing one of the key advantages of ArMs over small-molecule catalysts. However, rational genetic optimisation requires an understanding of the interactions between the protein, catalyst, and substrate within the ArM. The incompleteness of such knowledge has been highlighted as a relative gap for exploitation within the wider ArM field. In particular, there is little structural information available on ArMs based on enzymatic scaffolds. These systems offer a promising alternative to highly successful ArMs based on non-enzymatic scaffolds. The naturally evolved architecture of the enzyme can be used to the advantage of ArM catalyst or substrate binding.

Here, we report kinetic and structural insights into ArMs based on an alcohol dehydrogenase (ADH) scaffold for the reduction of nicotinamide cofactors, followed by attempts to expand ArM functionality towards other transfer hydrogenation reactions. The ArM system, which was established and developed by other members of the research group, is based upon covalent anchoring of rhodium piano-stool complexes to *T. brockii* ADH. A section of the previous work began to explore different anchoring locations for the catalyst within the TbADH scaffold, towards optimisation of ArM catalytic performance on different nicotinamide substrates. However, full kinetic characterisation of these ArM variants, and detailed structural information useful for rational optimisation efforts was lacking.

In the present work, rhodium-TbADH ArM variants based on two of the previous covalent anchoring locations (TbADH residue locations 37 and 243), were subject to full kinetic characterisation and docking studies. Location 37 was found to be favourable with regards to ArM affinity for natural $NAD(P)^+$ cofactors, which was estimated using values of the Michaelis constant K_M. This could be explained by reduced obstruction of the entrance to the TbADH nicotinamide cofactor binding pocket. These results prompted the design of a new variant based on anchoring of the catalyst to location 110 which was subject to the same docking and kinetics analyses. As hypothesised, the results indicate further improvement in ArM affinity for the $NAD(P)^+$ substrates. In particular, a greater overlap of the $NADP^+$ binding site with the wildtype TbADH binding site of this cofactor was predicted by docking. This suggests an improved utilisation of the naturally evolved TbADH nicotinamide binding pocket.

The X-ray crystal structure of a residue location 110-modified TbADH ArM co-crystallised with $NADP^+$ also indicates a near-wildtype binding site of the nicotinamide cofactor. While this structure also shows the covalently bound catalyst in an alternative non-catalytic orientation, it appears possible that flexibility of the catalyst in solution allows movement into the catalytically active orientation, which was predicted by docking.

Additionally, the same docking and kinetics studies were completed with the smaller nicotinamide mimic BNA^+. All rhodium-TbADH ArM variants displayed a lower affinity for this mimic in comparison to the natural $NAD(P)^+$ cofactors, predominantly owing to comparatively fewer favourable protein-ligand interactions.

Finally, preliminary experiments were completed to explore the functionality of iridium-TbADH ArMs for nicotinamide and other transfer hydrogenation applications. Very low levels of nicotinamide reduction activity of ArMs modified at residue locations 37 and 110 provide proof of principle for the functionality of these ArMs.

Acknowledgements

Firstly, I would like to express my huge gratification for all of the supervision, wisdom, and knowledge, as well as the general support and guidance that Dr Anca Pordea has provided over the years of my project as my primary supervisor. She was always on hand with detailed and decisive advice or feedback with regards to all aspects of the work, be it technical experimental detail or broader project perspectives. Next, I would like to thank and acknowledge my second supervisors Dr Ingrid Dreveny and Dr Christof M. Jäger for providing essential knowledge, guidance, and advice with regards to the crystallographic and computational aspects of the project respectively. They have both been instrumental in the outcomes of this project. Thirdly, I would like to thank Dr Simone Morra, not only for his enduring provision of level-headed and pragmatic input in response my experimental challenges, but also for always being on hand to help with practical lab-based issues. Thank you also, to my colleagues in the Pordea group. In particular, Mattias, Floriane and Maria who provided advice and support in the early stages of my lab work, and who's published theses contain links with this project. Also, I will be ever grateful to all members of the wider Sustainable Process Technologies group. The entertaining and obscure lunchtime debates, the laughs, and the genuine comradery could not have been better. Finally, I would like to thank my immediate and wider family, and friends outside of the group, for being there for me throughout this project. You, along with the group members, have all kept my spirits up and supported me in your own ways throughout my years in Nottingham.

Contents

Figures

Tables

Abbreviations

ATH	Asymmetric transfer hydrogenation
ADH	Alcohol dehydrogenase
ArM	Artificial metalloenzyme
BNA(H)	1-benzylnicotinamide
Bpy	Bipyridine
EDTA	Ethylenediaminetetraacetic acid
ee	Enantiomeric excess
EPR	Electron paramagnetic resonance
ES	Michaelis complex
ESI-TOF MS	Electrospray ionisation time of flight mass spectrometry
Fc	Calculated structure factors
Fo	Observed structure factors
ICP MS	Inductively coupled plasma mass spectrometry
IPTG	Isopropyl β-D-1-thiogalactopyranoside
K_a	Association equilibrium constant
K_d	Dissociation equilibrium constant
K_M	Michaelis constant
K_s	Dissociation equilibrium constant of the Michaelis complex
NAD(H)	Nicotinamide adenine dinucleotide
NADP(H)	Nicotinamide adenine dinucleotide phosphate
NMR	Nuclear magnetic resonance spectroscopy
MM	Molecular mechanical
OD_{600}	Optical density at 600 nm
QM	Quantum mechanical
RMSD	Route mean square deviation
SDS-PAGE	sodium dodecyl sulfate–polyacrylamide gel electrophoresis
SPAAC	Strain promoted azide–alkyne cycloaddition
TOF	Turnover frequency
TON	Total turnover number
Tris	Tris(hydroxymethyl)aminomethane
uAA	Unnatural amino acid
U/mg	Enzyme specific activity (μM/min/mg)
V_{max}	Theoretical maximal enzyme rate at full saturation with subsrtate

1 Introduction

1.1 Artificial metalloenzyme assembly, applications, and opportunities

1.1.1 Overview

Artificial metalloenzymes (ArMs) are assembled by incorporating a synthetic metal complex or catalyst (terms used interchangeably) into a protein scaffold (Figure **1.1**).[1] As hybrid catalysts, ArMs combine advantageous features of synthetic and biological catalysts, unlocking novel alternatives for fine chemicals synthesis.[2] ArMs offer the possibility to expand the biocatalytic toolbox, having been shown to catalyse non-natural reaction chemistries.[3-5] Meanwhile, they also present opportunities to enhance the capabilities of synthetic catalysts. Such studies have demonstrated improvement of reaction selectivities[3, 6] and rates owing to unique features of ArMs. For example, stabilisation of the catalyst[7, 8] or imparting enantioselectivity on its activity[9, 10] as a result of protein scaffold encapsulation.

In the context of transition metal chemistry, the primary coordination sphere comprises the ligands coordinated to the metal centre of a catalytic complex. It follows that in an ArM, the amino acid residues in the vicinity of the metal complex, but not directly coordinated to the metal, constitute the secondary coordination sphere.[3] As part of this sphere, they can form important interactions with the substrate or with the catalyst, as exemplified by natural metalloenzymes.[11-13] Therefore, the protein scaffold is a key determinant in catalytic reactivity and selectivity. Arguably the most attractive advantage of ArMs over their synthetic counterparts is the opportunity for genetic optimisation of catalytic performance or features, via mutation of the protein scaffold.[4, 14]

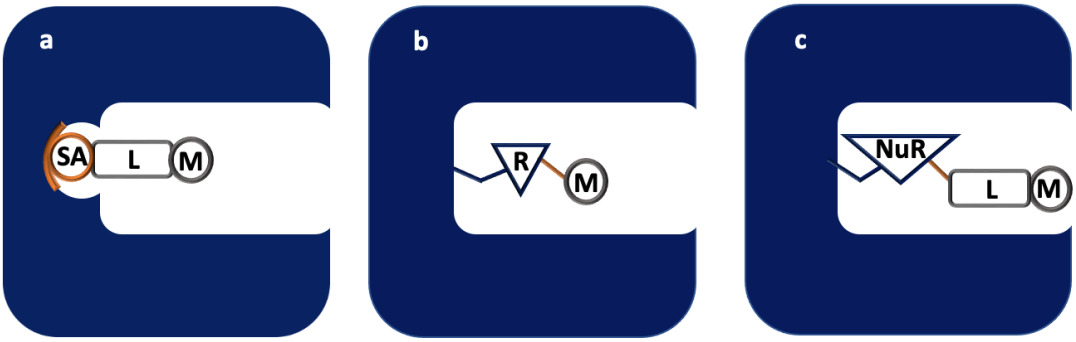

Figure 1.1: Summary of artificial metalloenzyme assembly methods

a = *supramolecular*, **b** = *direct metal binding*, **c** = *covalent*. **SA** = supramolecular anchor, **L** = ligand of the catalyst complex, **M** = metal centre of the catalyst complex, **R** = scaffold residue which binds to the metal or metal complex, **NuR** = nucleophilic scaffold residue.

R can be a native residue (*metal substitution* and *direct metal binding to native fortuitous site*) or introduced by genetic mutation (*direct metal binding to non-native site*). In the case of covalent anchoring, **L** contains an electrophilic handle which reacts with **NuR**. Adapted from[3, 4]

The first decision towards achieving any of the aforementioned ArM benefits is the selection of protein scaffold and catalyst components, and a suitable assembly strategy. There are three[3] or four[4] protein scaffold-catalyst anchoring strategies, depending on how they are categorised. These are supramolecular, direct metal binding (can be sub-divided) and covalent binding (Figure **1.1**). Each strategy has specific benefits and drawbacks, and they have been applied to a range of catalysis applications.

1.1.2 ArM assembly via supramolecular binding

The non-covalent or supramolecular approach to metal complex anchoring utilises an intrinsic affinity of a protein site for a complex ligand (Figure **1.1a**). This is arguably the most versatile and practical way to assemble ArMs. In most cases, the approach lends itself to non-catalytic protein scaffolds with large open binding pockets, the most successful and extensively reported of which is streptavidin.[3]

1.1.2.1 Streptavidin scaffolds for supramolecular ArM assembly

ArMs based on the strept(avidin)-biotin system exploit the naturally high affinity between biotin and its binding site on either *Streptomyces* streptavidin or eukaryotic avidin.[15] These ArMs possess several advantages which are common to non-catalytic scaffolds used for supramolecular assembly. Naturally high affinity (K_a ~ $1x10^{12}$ M^{-1}) between the complex and the scaffold at a single site[16] enables ArM assembly *in vivo*.

This feature is crucial to the practicality of ArM directed evolution.[17] Other desirable features are heat and pH tolerance,[4] ease of protein purification, and the structures available from which rational mutations can be inferred.[18]

Inspired by seminal work,[19] streptavidin and avidin were used as hosts for transition metal complexes for the hydrogenation of activated double bonds,[7] and the transfer hydrogenation of ketones.[20] In the latter study, the solvent served as the hydride donor, regenerating the various d^6-piano-stool complexes catalysing hydride transfer to the substrate (Figure **1.2**). Such complexes based on rhodium, iridium and ruthenium are some of the most effective catalysts known for transfer hydrogenation (Section **1.2**).[4] The metal occupies the centre, with the aromatic ring as the seat of the stool and the various possible ligands as the legs.[21] A library of complex ligands with subtle variations in structure were synthesised. These were combined with several streptavidin variants, followed by screening to determine which combination achieved the highest enantioselectivity.[7] In another study,[20] a similar chemical optimisation step was used involving several catalyst complex and substrate isoforms. These were combined with a more extensive genetic mutant library, generated by site saturation mutagenesis at S112 (Figure **1.2**). This method involves substitution of the single target amino acid residue for any of the other 19 naturally occurring residues.[22]

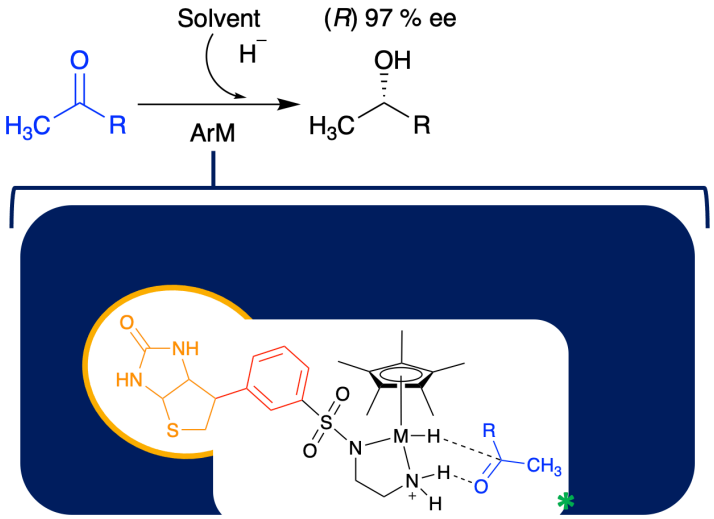

Figure 1.2: (Biotin)catalyst-streptavidin ArM for ketone reduction

Metal and ligand moieties of the complex (black) were varied in a chemical optimisation step. Shown as an example ligand is pentamethylcyclopentadienyl (Cp*). The green star represents site saturation mutagenesis at S112 in a genetic optimisation step. Substrate and product are shown in blue and black respectively. Biotin and its binding site in the streptavidin scaffold are shown in orange. Shown in red is the complex spacer group which can also be chemically optimised.[7] ee = enantiomeric excess. Adapted from[20]

In a more recent streptavidin example, a piano-stool rhodium complex was incorporated into the scaffold for the asymmetric synthesis of δ-lactams, thereby demonstrating non-natural reaction chemistry.[23] Also achieved with streptavidin-based ArMs is the phenomenon of scaffold acceleration. This can be defined as an increase in reaction rate as a direct result of incorporation of the catalyst into the protein scaffold.[4, 24] For example, via rhodium catalyst incorporation into streptavidin the rates of rhodium catalysed hydrogenation[7] and asymmetric C-H activation[8] were increased. The term is not to be confused with scaffold protection which usually refers to ArM-incorporation of metal catalysts to protect against catalyst poisoning by cellular components such as thiol groups, or against mutual inactivation of the enzyme and catalyst (explained and discussed further in Sections *1.2.5.2* and ***1.3.5***).[3, 25] Other notable new to nature chemistries achieved with (biotin)catalyst-streptavidin ArMs include olefin metathesis[26] and allylic alkylation.[27]

1.1.2.2 Other scaffolds for supramolecular ArM assembly

There are several alternative scaffold proteins used in supramolecular anchoring reviewed elsewhere.[3, 4] One that has received a lot of interest recently is the multidrug resistance regulator of *Lactococcus lactis* (LmrR). This has been used for many reactions, such as the enantioselective copper (II) catalysed Friedel-Crafts alkylation of indoles.[24] The copper (II) phenanthroline complex interacts by pi-stacking with two central tryptophan residues within the hydrophobic binding pocket (Figure **1.3**).[28] This pocket is a common feature of scaffolds used in supramolecular assembly. The space available enables a range of different complex-substrate combinations, making for good reaction scope.[3] However, this can also lead to increased conformational freedom of the complex, potentially reducing the product selectivity achieved.

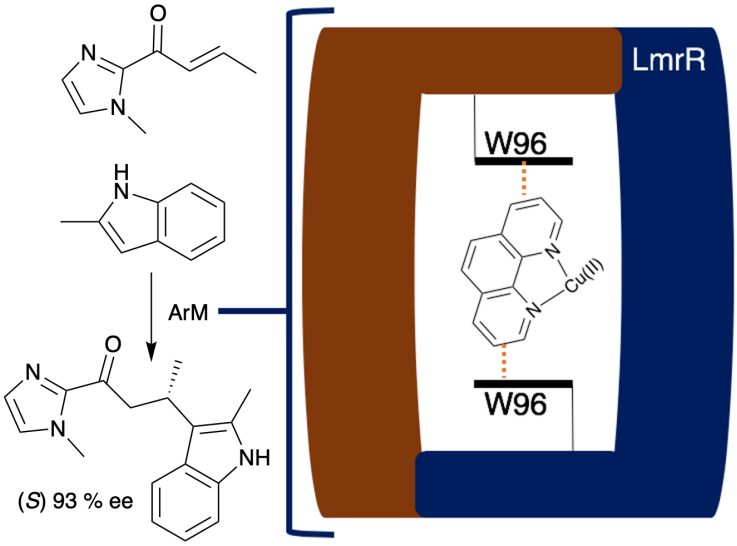

Figure 1.3: Cu(II)-LmrR ArM for Friedel-Crafts alkylation of indoles
Highlighted are the tryptophan residues from each of the LmrR subunits which sandwich the complex phenanthroline ligand with pi-stacking interactions (orange). ee = enantiomeric excess. Reproduced from[24, 28]

1.1.3 ArM assembly via direct metal binding

Another broad category of metal complex anchoring for ArM assembly is direct metal interaction with the scaffold (Figure **1.1b**). This category can be subdivided into: native metal substitution; exploitation of a fortuitous metal binding site; engineering a metal binding site into the scaffold protein.[3] Elsewhere,[4] the latter two sub-categories have been grouped as “dative metal anchoring”, while regarding “metal substitution” as a separate category.

1.1.3.1 Metal substitution

Metal substitution requires a genetic,[29] or more commonly, chemical preparation step to remove the native metal or metal complex, followed by coordination of the non-native metal or metal complex for ArM assembly.

Early examples include the repurposing of carbonic anhydrases for alternative catalytic activities such as enantioselective epoxidation,[30] alkene hydrogenation[31] and hydroformylation.[32] Dialysis of a carbonic anhydrase (CA) against a zinc chelator was used to remove the natural metal from the enzyme, followed by dialysis with the rhodium complex to be incorporated, yielding a rhodium-CA ArM.[32] More recently, Cp*Ir complexes with sulfonamide ligands were incorporated into a CA scaffold for

whole-cell *in vivo* transfer hydrogenation in *E. coli*.[33] The CA-based ArM was compartmentalised to the periplasm via expression with an N-terminal fused outer membrane protein signal peptide. Such studies demonstrate the compatibility of ArMs within a whole-cell environment.[4]

One of the most important scaffolds for metal substitution-assembled ArMs is myoglobin. The natural iron-porphyrin complex has been shown to catalyse addition and insertion of carbenes and nitrenes to C-H bonds to form C-C and C-N products. However, the haem complex cannot handle less reactive substrates such as unactivated alkenes. An ArM approach offered a solution to this by its replacement with artificial transition metal-porphyrin alternatives.[34] A myoglobin homologue with its haem substituted for an iridium complex catalysed C-H functionalisation of challenging substrates, such as aliphatic olefins (Figure **1.4**).

In another example, similar replacement of myoglobin haem yielded native oxygenation activity enhancement and several new catalytic activities.[35] Removal of the native cofactor was achieved by acidic treatment followed by reconstitution with the new cofactor at neutral pH. Though simple, this method relies on stability of the native and apo-enzyme under acidic conditions. Such haem substitution examples demonstrate the concept of taking the native catalytic activity of an enzyme and enhancing[35] or expanding[34] its substrate scope by incorporation of a non-natural complex. This exploitation of a naturally evolved enzyme architecture is a key advantage of using enzyme scaffolds. However, regarding these examples, metal complex catalysts with porphyrin-like structures (which are suitable for this assembly method) are limited in terms of potential reaction scope.

Also worthy of note is that metal substitution assembled ArMs appear to have higher stabilities in general than dative or supramolecular alternatives, with the exception of strept(avidin).[4] The frequent use of a naturally evolved metal binding site might be an aid to this. However, this also means that the range of scaffolds available for metal substitution is more limited.

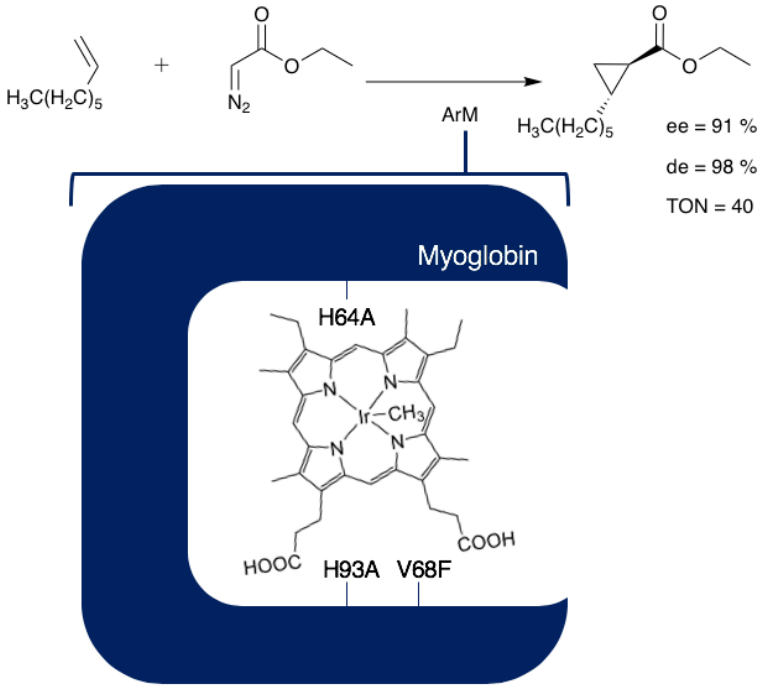

Figure 1.4: Iridium(porphyrin)-myoglobin reconstituted ArM for olefin carbene addition *Physeter macrocephalus* myoglobin was expressed under low-Fe growth conditions for purification in apo-form, with mutations at H93 (the proximal ligand in natural haem coordination). The mutants were reconstituted with iridium(porphyrin) complexes such as the one shown, to achieve various reaction chemistries. Several rounds of directed evolution found a H93A, H64A, V68F scaffold mutant to provide the best ArM catalytic performance in carbene addition to aliphatic olefins. ee = enantiomeric excess, de = diastereomeric excess, TON = turnover number. Adapted from[34]

1.1.3.2 Direct metal binding to native fortuitous sites

Arguably the most intrinsically simple approach to ArM assembly from scaffolds which do not bind metals naturally; one or more native residues coordinate the metal or interact with the metal complex directly (Figure **1.1b**). The approach has seen variable success with albumin,[36] apoferritin,[37] lysozyme [38] and streptavidin.[39] The latter study incorporated a vanadyl ion into the biotin binding pocket of streptavidin, relying on hydrogen bonding between the complex and native residues. Enantioselective oxidation of prochiral sulfides was achieved.

More recently, dimeric piano-stool ruthenium, rhodium and iridium complexes were incorporated into the non-metal binding lactoglobulin and lysozyme scaffolds for the enantioselective transfer hydrogenation of ketones in aqueous medium.[40]

1.1.3.3 Direct metal binding to non-native site

If no suitable natural metal binding site is available, a new one can be introduced genetically, followed by direct or dative metal anchoring to this residue (Figure **1.1b**). While lower stability is often observed in comparison to metal substitution and covalent anchoring approaches,[4] this approach expands the range of scaffolds available for direct metal binding. Furthermore, greater control over the catalyst binding site has been achieved by the incorporation of unnatural amino acids (uAAs) into a scaffold using various blank codon technologies.[41] Many of the >200 uAAs available have higher affinities for various metals than natural amino acids. The technology enables ArM assembly and catalytic activity screening *in vivo*, thus enabling ArM directed evolution. In one example the uAA (2,2'-bipyridine-5yl)alanine was incorporated at various locations in the LmrR hydrophobic binding pocket. An LmrR residue location 89-modified ArM variant showed good performance in enantioselective Friedel-Crafts alkylation of indoles. The ArM was then evolved towards the enantioselective hydration of enones, also showing good catalytic performance.[24]

1.1.4 ArM assembly via covalent binding

This method of ArM assembly involves a chemical reaction for covalent bioconjugation of a complex ligand to a scaffold residue (Figure **1.1c**).[4] In addition to the metal centre, complexes anchored in this way must possess a reactive ligand functional group for bioconjugation.[3] Despite some practical challenges, this assembly method enables greater flexibility and control over the metal complex binding site. As for supramolecular assembly, the protein scaffolds selected often possess a large hydrophobic binding pocket.[3]

A common covalent assembly approach is the alkylation of cysteine thiols via nucleophilic substitution.[3, 42] The target reactive cysteine residue should be unique within the scaffold to avoid non-desirable modification of other residue locations. Ligands containing electrophilic alkyl halides, acyl halides and maleimides (Figure **1.5**, entries **1**, **2**, and **3** respectively) are the most popular choices for these complexes. A significant practical drawback is reaction promiscuity. In a cellular environment, there are many other groups present with will react with free thiols for example, leading to non-specific binding and potentially a low assembled ArM yield. Therefore, unless uAAs are incorporated (Figure **1.5**, entry **4**),[43] the covalent binding approach is generally not applicable to ArM directed evolution efforts, which require assembly *in vivo*.

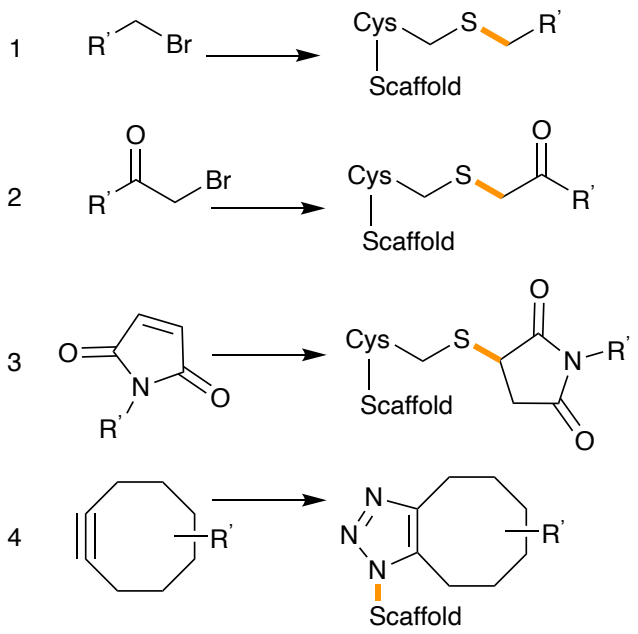

Figure 1.5: Examples of ArM covalent assembly reactions

Entries 1-3: Commonly used cysteine nucleophilic substitutions as defined in Section ***1.1.4*** above. Entry 4: SPAAC 'click chemistry'. Showing from left to right: Entry number; ligand moiety which facilitates the linkage; assembled ArM. R' indicates all metal complex constituents not shown. Scaffold-complex link highlighted in orange. Adapted from[3, 43]

1.1.4.1 Key examples of covalent ArM assembly

In an early example of the this method, C117 of adipocyte lipid binding protein was alkylated with iodoacetamido-1,10-phenanthroline (Figure **1.5**, entry **2**). Subsequent metalation with copper (II) completed the catalytic complex. The resulting ArM catalysed enantioselective ester and amide hydrolysis.[44] An enantioselectivity of 86 % was achieved, but no scaffold acceleration was observed in comparison to use of the free catalyst.

Papain offers a similar large hydrophobic pocket which contains a native cysteine at residue location 25. This residue was alkylated with the electrophilic moiety (Figure **1.5**, entry **2**) of a bidentate phosphorus based ligand.[45] The resulting papain bound ligand conjugate was then metalated with an rhodium complex. This ArM served as an acid hydrogenation catalyst with 100 % conversion but no enantioselectivity. The same residue of papain was alkylated with phenanthroline or bipyridine Cp*Rh complexes for the ketone transfer hydrogenation, with formate as the hydride donor.[46] Rates were found to be affected by choice of ligand, an example of chemical optimisation. Enantioselectivity was low at 7-10 %.

For further control over the complex bioconjugation site, cysteines for alkylation can be introduced genetically. This was achieved using the LmrR scaffold for a copper (II) catalysed asymmetric Diels-Alder reaction.[47] Cysteines were introduced at either residue location 89 or 19 within the hydrophobic binding pocket, followed by alkylation with the electrophilic bromoacetamide moieties (Fig. **1.5**, entry **2**) of phenanthroline or bipyridine ligand-bearing copper (II) complexes. Enantioselectivity was 97 % when using the phenanthroline ligand complex at location 89 (Figure **1.6**). Furthermore, scaffold acceleration was achieved.

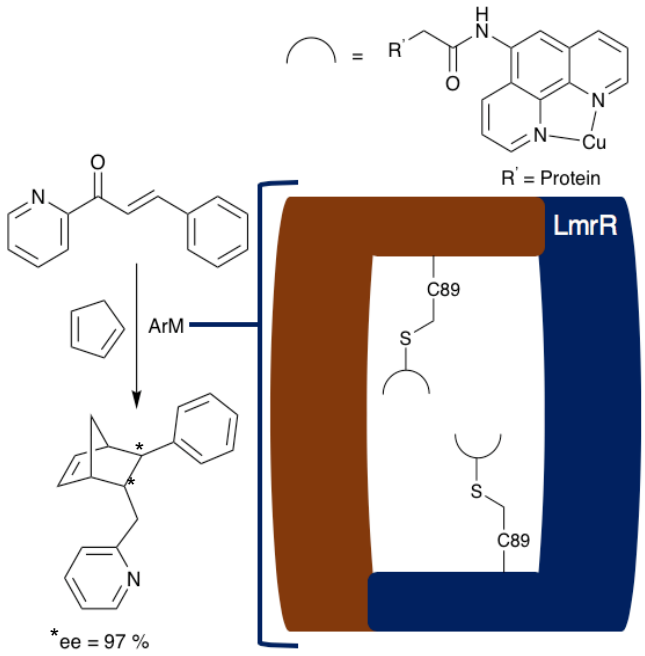

Figure 1.6: Copper (II)-LmrR ArM for a Diels-Alder reaction
Catalysing the reaction of azachalcone with cyclopentadiene. Reproduced from[47]

As an alternative to non-catalytic scaffolds such as streptavidin and multidrug resistant regulators (MDRs), ArMs can also be assembled by incorporating the metallocofactor into an enzyme sacffold.[34, 35, 48] The key advantage of such systems is the opportunity to take advantage of a naturally evolved protein architecture, to the benefit of ArM catalytic performance. There are fewer examples of covalently assembled ArMs which utilise this method of assembly.

1.1.4.2 Outlook on covalent ArM assembly

Aside from the use of uAA incorporation,[41] more commonly used covalent assembly approaches such as cysteine alkylation necessitate protein purification prior to

assembly or catalytic activity tests, limiting applicability to ArM directed evolution. Furthermore, reactive residues at non-desirable sites must be removed to prevent catalyst binding at these sites.[29] However, for the purposes of structure informed ArM design, the covalent approach shows a lot of promise. This is exemplified by the approaches to address low enantioselectivities[46] or rates of catalysis,[44] highlighted as a recurring issue with covalently assembled ArMs.[3] Efforts have been made to increase understanding of how the metal complex interacts with proximal (secondary coordination sphere) protein scaffold residues. This has led to both high enantioselectivity, and significant scaffold acceleration.[24, 47] Gaining such insight is made easier by precise control over the complex binding site, an intrinsic feature of covalent assembly. In other words, the site of complex binding can be altered with relative ease in comparison to other assembly methods. Structural and computational insights[46, 47] enable both fine tuning of complex positioning (within the limits of scaffold structural integrity), and a deeper understanding of scaffold, catalyst, and substrate interactions. This may prove especially relevant for improving performance in systems where the ArM substrate binds to a naturally evolved pocket of the enzyme scaffold.[29]

1.1.5 Conclusions

From the selection of primary literature discussed and from several in-depth reviews of the field, the potential value of ArM systems to the field of biocatalysis is clear. Studies from across the full range of ArM assembly approaches (Figure **1.1**) exemplify the advantageous features of these hybrid catalysts in comparison to enzyme and small-molecule catalyst alternatives, whether the outcome is improving product selectivity, scaffold acceleration, non-natural reaction chemistry, or a combination of these features. All assembly methods have intrinsic benefits and drawbacks in terms of practicality, potential reaction and substrate scope, control and flexibility over catalyst binding site, and the strategies available for genetic optimisation. Based on these features, it is clear that some methods are more naturally suited to specific types of development and optimisation than others. In particular, covalent assembly methods enable considerable flexibility in the selection of the catalyst binding site (via protein mutagenesis to introduce the reactive residue). Therefore, the approach provides a strong platform for this form of rational genetic optimisation of ArMs which is presented as a significant gap in the field. Moreover, in comparison to other approaches, there are fewer covalently assembled ArM examples based on enzyme scaffolds. These systems take advantage of naturally evolved substrate binding sites. These relative gaps within the existing literature present an opportunity for expansion.

In particular, towards a greater understanding of how the protein scaffold, metal complex and ArM substrate interact with each other, as discussed with examples from the literature in Section **1.3**. In consideration of the range applications to which such ArMs can be applied, the selective reduction of ketone, imine and nicotinamide substrates via transfer hydrogenation are of particular industrial relevance.

1.2 Transfer hydrogenation of ketones, imines, and nicotinamides

1.2.1 Overview

Chiral alcohols and amines are key building blocks in pharmaceuticals, agrochemicals, food additives and cosmetics.[49, 50] For example, it is estimated that 40 to 45 % of all pharmaceuticals and other bioactive fine-chemicals contain chiral amine fragments, largely secondary and tertiary in structure.[51] Owing to the resulting industrial applicability of enantioselective ketone and imine reduction, organometallic catalysts for these reactions make up an expansive field.

Advantageous enzymatic alternatives to these catalysts such as alcohol dehydrogenases and imine reductases have been extensively studied.[52, 53] However, use of such enzymes is accompanied by the issue of regenerating expensive redox cofactors such as NAD(P)H, and the acceptance of nicotinamide cofactor mimics by such enzymes is challenging.[54]

1.2.2 Key organometallic catalysts for transfer hydrogenation

Early examples of asymmetric ketone and imine reduction used molecular hydrogen as the hydride source rather than transfer from a donor molecule,[55, 56] and these methods have seen more recent developments.[57-60] However, obvious practical issues are associated with the use of H_2 gas. Other efforts to afford chiral alcohols and imines have focused on transfer hydrogenation (TH). This can be broadly defined as the addition of hydrogen to a molecule from any non-H_2 source. Small-molecule TH catalysts make up an expansive field, comprised of organocatalysts, nanoparticles and organometallic catalysts (transition metal complexes), the homogeneous category of the latter making up the majority in 2015.[61] In these examples, the hydride donor for the reduction of C=O and C=N bonds can also serve as the solvent, or be mixed with the water in aqueous systems.[62, 63] Catalysts possessing chiral ligands are capable of asymmetric transfer hydrogenation (ATH). Indeed, interactions between the reactant and ligand are important in determining the enantioselectivity achieved.[64-66]

The enantioselectivities displayed by asymmetric hydrogenation with molecular H_2 were not achieved by ATH until the 1990s.[62] In 1996, Noyori-class Ru(II)-diphosphine complexes such as **1**[67] were used for ketone reduction with propan-2-ol as the hydride donor, achieving low reversibility and 97 % ee.[67, 68] This was shortly followed by the ATH of cyclic imines using Ru(II) piano-stool complexes such as **2**[69], achieving similar % ee values (Figure **1.7**).

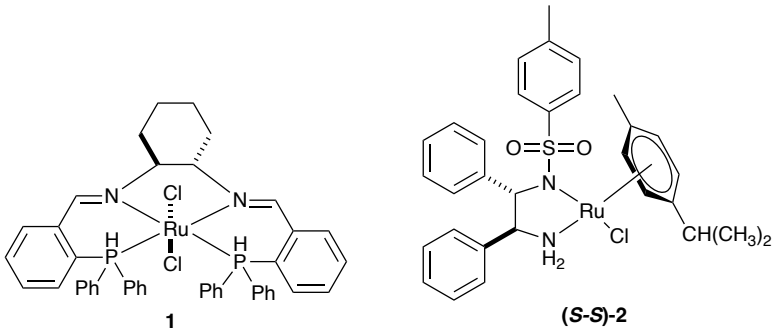

Figure 1.7: Pioneering examples of transfer hydrogenation catalysts

Early examples of transition metal complexes for the asymmetric reduction of ketones and imines.

Ruthenium complexes bearing *p*-cymene[70, 71] and the ubiquitous *trans*-1-diphenylethane-1,2-diamine (DPEN)[72] ligands have been used in aqueous prochiral ketone reduction, achieving ee values of >90 %. In more recent examples, a ruthenium(*p*-cymene) complex with polymeric chitosan ligands demonstrated high enantioselectivities for heterocyclic ketone reduction.[73] Ruthenium (II) catalysts containing N-functionalised TsDPEN ligands (sulfonamide-based monotosylated derivative of DPEN) were used for the ATH of acetophenone derivatives to form alcohol products of up to 99 % ee.[74] Extensive work has gone into developing similar piano-stool catalysts for ATH on a range of ketones, mainly using aqueous-compatible transition metal complexes including those based on rhodium and iridium.[75-77]

Several plausible mechanisms have been proposed for transfer hydrogenation of ketones using such transition metal complexes. A widely accepted variation does not involve direct metal-substrate coordination intermediates but instead proceeds via transition states. This mechanism is depicted in Figure **1.8**, for the reduction of an example aromatic ketone using the piano-stool chiral ruthenium (II) complex **2** in Figure **1.7**.[78]

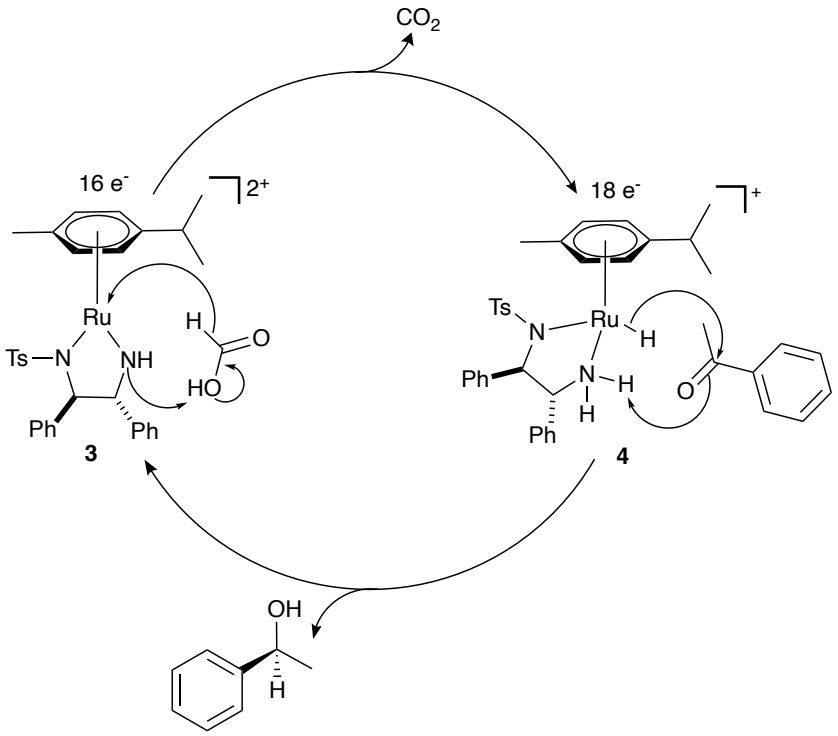

Figure 1.8: Simplified ketone transfer hydrogenation mechanism

Catalytic cycle for the reduction of acetophenone to 1-phenylethanol using example catalyst [Ru(*p*-cymene)(TsDPEN)Cl] **2 (**Figure **1.7**), with formate as the hydride donor. The 18 e^- complex **2** is first base-activated by loss of Cl^- to form the 16 e^- catalytically active complex **3**. Hydride ion donation from formate leads to the elimination of CO_2 and formation of the 18 e^- complex **4** (the proton required for this step can be derived from formate as shown here, or from the solvent). From this complex, a hydride ion and proton are transferred to the substrate to form the alcohol product and reform the 16 e^- complex **3**. The enantiomer configuration of the product is determined by that of the catalyst.[78] Adapted from[65, 78]

The use of formate rather than propan-2-ol as the hydride donor provides the advantage of inherent irreversibility of hydride donation owing to the elimination of CO_2.[78, 79] Furthermore, the formate is compatible with less or non-toxic aqueous systems,[80] which are relevant to the reduction of ketones and imines by water soluble catalysts such as ArMs. The advantages of aqueous TH include the reduced use of organic solvents, simpler product separation, and improved atom economy.[72]

The ATH reduction of imines to chiral amines catalysed by chiral catalysts is proposed to occur via a similar mechanism to that depicted in Figure **1.8**.[81, 82] Many of the conversions reported have been performed under aqueous conditions with formate as the hydride donor, and neutral pH found to be optimum for catalytic rates.[83, 84] The TsDPEN ligand constituent of complex **2** (Figure **1.7**) and derivatives are likely the most widely used for imine ATH.[85, 86]

In addition to the ruthenium complexes shown in Figure **1.7**, iridium (III) complexes bearing sulfonamide and phenanthroline ligands such as **6**[87] **7**[88, 89] and **8**[9] (Figure **1.9**), have been highly successful in the ATH of imines.

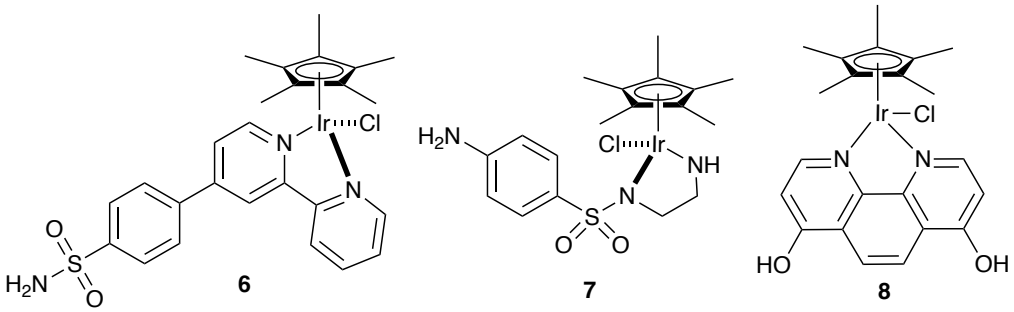

Figure 1.9: Example Cp*Ir catalysts for ATH of imines

A similar iridium (III) piano-stool complex was used for the reduction of eight different aromatic imines.[66] The initial ee value was 90 %, although in this case, the product mixture became racemic over time owing to different kinetic orders of reaction for the two product enantiomers. Specifically, to form the *S*-amine product, the rate limiting step was hydride transfer from the complex to the imine substrate, making the rate of *S*-amine formation first order with respect to imine concentration. Whereas to form the *R*-amine product, the rate limiting step was complex-product dissociation, making the formation of this enantiomer zero order with respect to imine concentration. Therefore, as imine substrate concentration decreased over time, less enantioselectivity towards the *S*-amine product was observed. The difference in rate limiting steps was presumed to be owing to subtle differences in intermolecular interactions between the iridium complex and each product enantiomer. Using the (*S*-*S*) rather than the (*R*-*R*) TsDPEN ligand in the iridium complex produced the opposite result. The loss of enantioselectivity over the course of the reaction in this study highlights a potential challenge in the use of such complexes for asymmetric conversions.

In summary, organometallic catalysts for the ATH of ketones and imines to make valuable chiral amines and alcohols make up a highly expansive field. High yields and enantioselectivities have been achieved under aqueous conditions. However, these catalysts still lack key advantages displayed by enzymes. For example, these biocatalysts can achieve formidable rate enhancements under mild conditions. They are non-toxic natural molecules which often display better chemo- regio- and stereo-selectivities than homogeneous catalysts.[90-92]

1.2.3 Alcohol dehydrogenases for transfer hydrogenation

Considering the catalytic efficiency and sustainability advantages of enzymes, continued expansion of use for industrially relevant reactions is not surprising. Whole-cell catalysis approaches are still being developed in the field of industrially relevant enzymatic reduction.[93, 94] However, the pharmaceutical industry has largely moved towards isolated enzyme[95, 96] or cell-extract approaches which increasingly involve multi-catalyst cascades.[53] This shift arguably brings analytical-scale (including academic) work with purified enzymes closer to industrial application. The focus of these biocatalytic systems is high value chiral intermediates for the pharmaceutical and fine chemical industries.[92]

Alcohol dehydrogenases (ADHs) have been described as the biocatalyst of choice for ketone reduction.[53, 91] These enzymes rely on NAD(P)H as the hydride donor.

Alcohol dehydrogenases (ADHs, Enzyme Class 1.1.1),[97] are a major class of NAD(P)H-dependent enzymes within the oxidoreductase family, which constitutes the largest proportion of enzymatic activity on the BRENDA (BRaunshweig ENzyme DAtabase). A system of categorisation for ADHs based on sequence motifs, protein and substrate chain length, and mechanistic features has been established.[98] This places them into short, medium, and long chain sub-families. The catalytic activity of medium chain ADHs is zinc-dependent (Figure **1.10**).[52] This sub-family includes some of the most extensively characterised homologues with regards to structure and mechanism.[99-103] Alcohol dehydrogenase from *Thermoanaerobacter brockii* (TbADH) is medium chain ADH.[104] Features of high thermostability and solvent tolerance make it particularly suitable for biocatalytic applications and protein engineering efforts.

1.2.3.1 Catalytic mechanism of TbADH

In the holoenzyme resting state, the zinc (II) ion is coordinated by residues C37, H59, D150 and E60, all of which are important for catalytic activity.[105] The putative mechanism of alcohol oxidation which involves two pentacoordinated zinc intermediates (transient complexes) is described in Figure **1.10**.[100, 103]

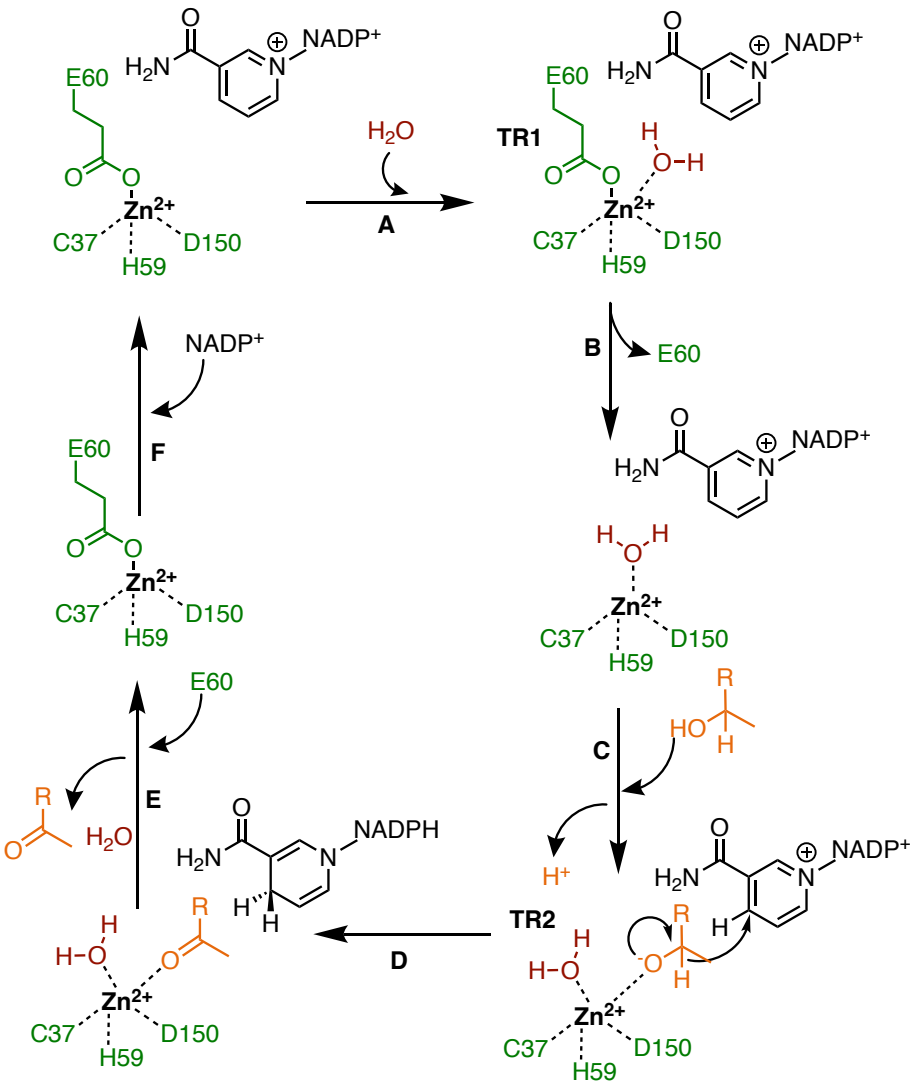

Figure 1.10: TbADH mechanism of secondary alcohol oxidation

In step **A**, addition of water to the tetracoordinated zinc (II) in the holo-enzyme forms the first pentacoordinated transient complex (**TR1**). Residue E60 dissociates in step **B**, followed by coordination with the alcohol substrate in step **C** to form **TR2**. In step **D**, hydride transfer occurs from the zinc-stabilised alcohol substrate to the nicotinamide C4 of $NADP^+$. Dissociation of water and re-ligation of E60 in step **E** to form the original tetracoordinated zinc ion, followed by binding of a new $NADP^+$ cofactor in step **F** to complete the cycle. Adapted from[101, 103]

The reverse of this mechanism occurs in the production of chiral alcohols from ketones, accompanied by the oxidation of NADPH (nicotinamide adenine dinucleotide phosphate), as shown for *Thermoanaerobacter brockii* ADH (TbADH) in Figure **1.11**. Hydride transfer to the substrate from NADPH forms the zinc-stabilised alcoholate (alkoxide) intermediate, followed by protonation to form the alcohol product. Complete enantioselectivity is achieved via orientation of the substrate, resulting in attack from the hydride on either the Re-face or the Si-face to furnish the (*S*)- or (*R*)-alcohol repectively.[92, 106]

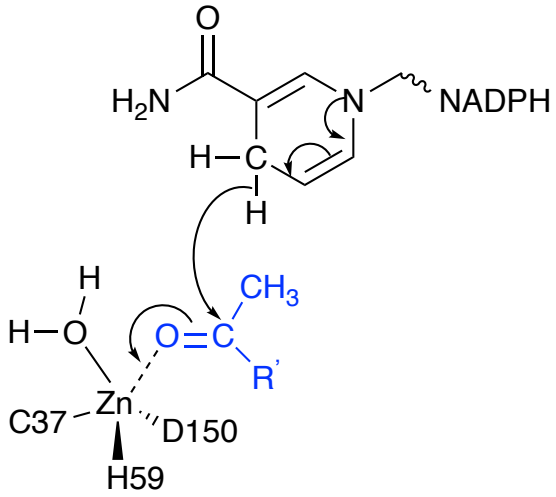

Figure 1.11: Inferred ketone reduction step of TbADH reduction mechanism
Corresponding to transient complex 2 in Figure **1.10**, hydride transfer from the NADPH nicotinamide C4 to the ketone substrate (blue). Adapted from[101, 103]

1.2.3.2 Structure of TbADH

The first high-resolution crystal structures of TbADH were solved in the mid to late 90s, followed by a range of variants which have gradually joined the PDB (Protein Data Bank) since then.[107-109] TbADH is a homotetramer with one NADPH binding site per subunit (Figure **1.12**), each has a nucleotide (nicotinamide cofactor) binding domain containing residues 157-292, and a catalytic domain of residues 1-149 and 297-352.[108] These domains form distinguishable substrate and nicotinamide cofactor binding pockets.

A deep cleft between the two domains forms the hydrophobic substrate channel, which is lined with residues I49, L107, W110, Y267, L294, and C283, M285 from the adjacent subunit[108] leading into what be referred to as the substrate binding pocket. Given that adjacent subunit residues contribute to this pocket, it is assumed that the monomeric unit is not catalytically active. The TbADH literature to date indicates that the reaction mechanism (Figure **1.10**) does not involve subunit cooperativity.[103, 110] The hydrophobicity of the substrate pocket residues likely contributes to the organic solvent tolerance of TbADH. The catalytic zinc (II) ion sits at the end of this channel and is permanently coordinated by C37, H59 and D150. Meanwhile, the latter two residues, along with I86, W110 and L294, form van der Waals interactions with the 2-butanol substrate (Figure **1.13**).[108]

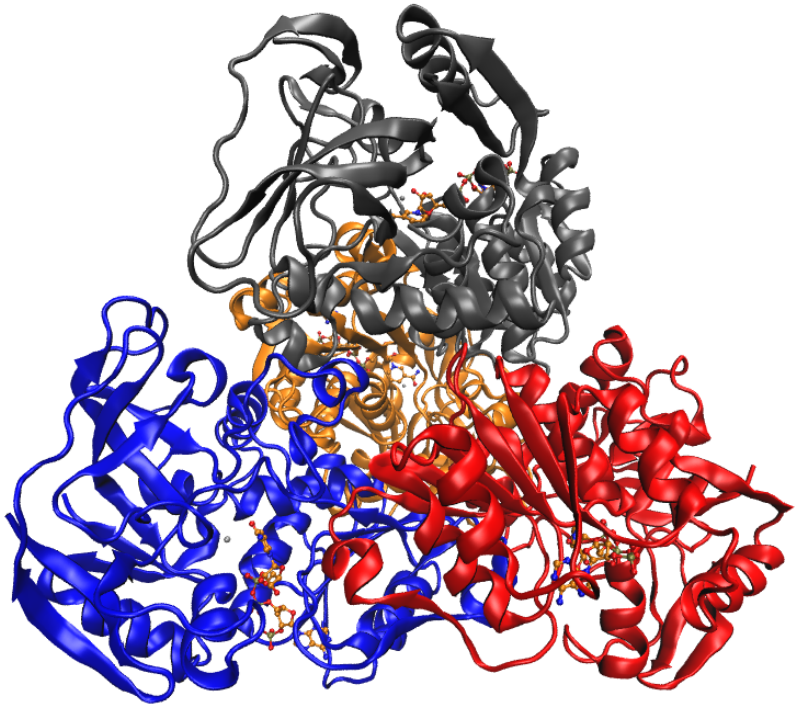

Figure 1.12: TbADH quaternary structure

Crystal structure of wildtype holo-TbADH coloured by subunit with $NADP^+$ in orange and the catalytic zinc (II) in silver. Generated using PDB 1YKF[107] in VMD (Visual Molecular Dynamics).[111]

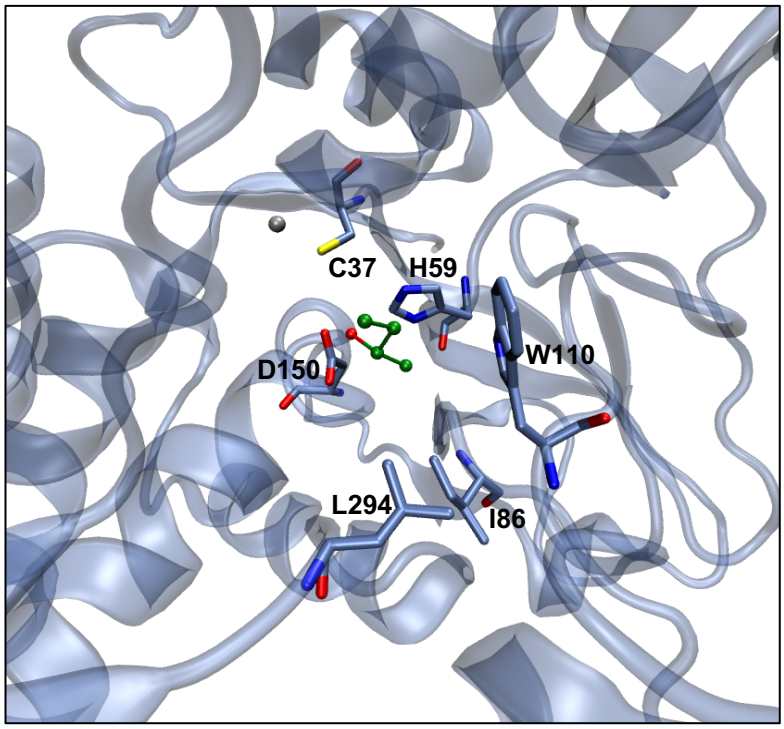

Figure 1.13: WT TbADH 2-butanol substrate binding site

Wildtype TbADH with residues of the substrate binding pocket (ice-blue) and *in-crystallo* 2-butanol (green) shown by atom type and the catalytic zinc (II) (silver). Generated using PDB 1BXZ[108] in VMD.[111]

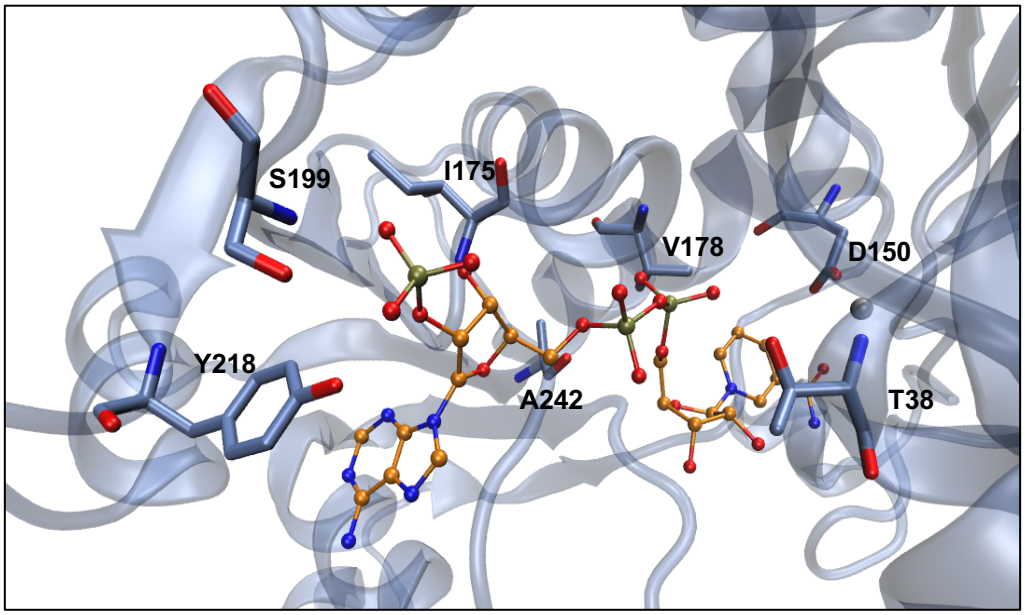

Figure 1.14: WT TbADH nicotinamide cofactor pocket residues

Wildtype holo-TbADH residues of the nicotinamide pocket (ice blue) and *in-crystallo* NADPH (orange) shown by atom type, and the catalytic zinc (II) (silver). Generated using PDB 1YKF[107] in VMD.[111]

Figure **1.14** illustrates a selection of the residues which line the NADPH binding pocket of TbADH. The nicotinamide C4 position of the NADPH nicotinamide ring is 4 Å away from the catalytic zinc ion in structure 1YKF.[107] G198, S199, R200 and Y218 determine preference for NADPH over NADH.[107] Y218 forms hydrogen bonds with the 2'-phosphate oxygens of NADPH, and pi-stacking interactions with the adenine moiety. Substitution of these four specificity residues via site saturation mutagenesis achieved the reversal of cofactor preference from $NADP^+$ to NAD^+ for the reduction of isopropanol.[112] It was suggested that the steric bulk introduced by mutations G198S and S199K would prevent $NADP^+$ from binding.

Enzymatic methods for imine reduction are beyond the scope of this thesis. However, it is worth noting that imine reductases (E.C. 1.5.1)[52] (IREDs) catalyse NAD(P)H-dependent prochiral imine reduction to produce chiral amines.[113] In contrast to previously known IREDs such as dihydrofolate and dihydroreticuline reductases which display narrow substrate scope, new examples which have rapidly emerged within the last decade are highly relevant to industrial application.[113] These efforts have included the characterisation of a growing library of stereo-complementary IREDs,[92] as well as the implementation and genetic engineering of these biocatalysts in industrial settings.[53]

1.2.4 Methods for nicotinamide cofactor recycling

Along with 50 % of all oxidoreductases, ADHs and IREDs utilise redox cofactors NAD(P)H for hydride addition to the substrate.[52, 113] Owing to the expense of these cofactors,[114] a cheaper co-substrate is used as the sacrificial hydride donor for reduction of the evolved $NAD(P)^+$, to regenerate NAD(P)H. This cofactor "recycling" step poses a significant challenge in the use of enzymes for ketone and imine reduction. Widely used sacrificial hydride donors include isopropanol, glucose-6-phosphate and formate, the latter being advantageously irreversible as discussed in Section ***1.2.2***.[67] A second catalyst must be added for the regeneration step, creating a "one-pot" recycling system. In catalyst selection, consideration factors include the following: Catalytic performance based on total turnover number (TON) and turnover frequency (TOF); regioselectivity for the nicotinamide C4 position to avoid loss of the cofactor by formation of inactive radicals and side products such as 1,6-NAD(P)H; by-product generation; ease of separation; catalyst inactivation.[115] TON is defined as the total number of catalytic turnovers or molecules of substrate converted to product over the entire duration of the reaction, while TOF is the defined as the TON per time unit such as per second (s^{-1}) or per hour (h^{-1}).

1.2.4.1 Second enzyme method

The use of a second enzyme to regenerate NAD(P)H (Figure **1.15a**)[116] is by far the most ubiquitous and is the current method of choice for industry, often with the enzyme immobilised.[95, 115] This is also clear from the filing of several patents.[117] Alcohol,[118] formate,[114] glucose, lactate and glutamate dehydrogenases[91, 115] can catalyse enantioselective hydride transfer from the respective donors to $NAD(P)^+$. Until recently, enzymatic cofactor regeneration offered rates which were orders of magnitude higher than chemical approaches.[115, 119] However, this has changed with new piano-stool catalysts[116] compatible with aqueous conditions which display impressive rates of up to 7825 h^{-1}, approaching the ~8400 h^{-1} achieved using formate dehydrogenase.[120] Furthermore, the fact that the two enzyme approach suffers from moderate enzyme stability, is restrictive in attempts to use cofactor mimics (Section ***1.2.6***),[121, 122] and is limited with respect to choice of hydride source.[119]

1.2.4.2 Electrochemical methods

Electrochemical approaches involve direct electron movement from the cathode straight to $NAD(P)^+$, or indirectly[123] from the cathode via a redox active mediator such as a rhodium piano-stool catalyst complex (Figure **1.15b**).[117] The direct method comes with the drawback of inactive side product and radical formation.[115] Though this issue is addressed by the indirect method, there are limited mediator-electrode combinations which offer high turnover frequencies.[115] Electrochemical systems can be described as heterogenous because they involve a second state in addition to aqueous. Other examples are the use of H_2 gas rather than an organic solvent as the hydride source,[124, 125] an immobilised second enzyme,[123, 126] and solid photocatalysis. These approaches have been reviewed recently and praised for their intrinsic simplicity; often not requiring an organic hydride donor, lacking the formation of by-products such as CO_2, or being 100 % atom efficient.[125] However, practical issues associated with using H_2 gas for example, and lower TOFs reported[126] in comparison to homogeneous approaches must be considered.

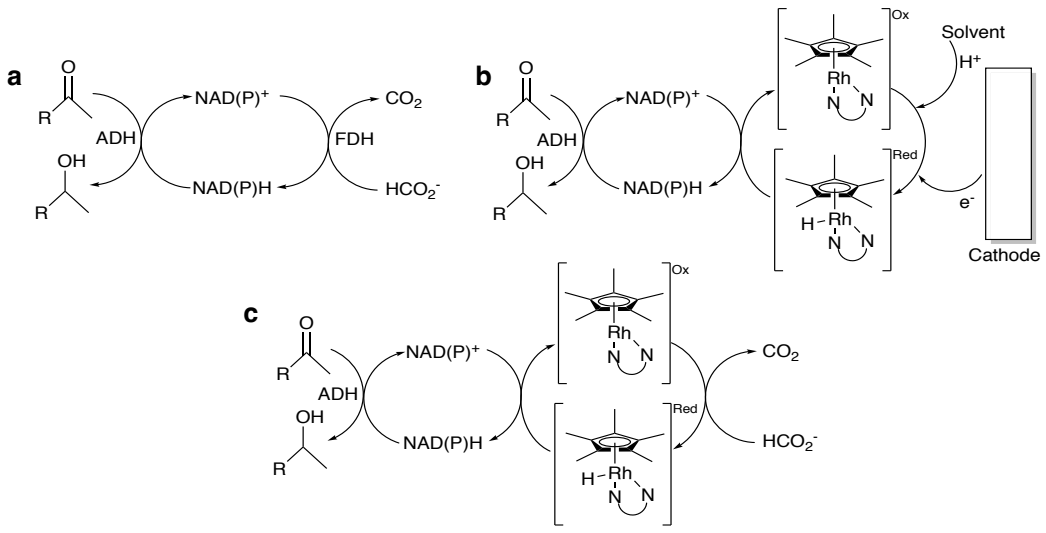

Figure 1.15: Approaches to NAD(P)H cofactor regeneration

a shows the use of a second enzyme (alcohol dehydrogenase and formate dehydrogenase are shown as example substrate and cofactor reductases respectively), **b** indirect electrochemical and **c** homogeneous catalytic approaches to cofactor regeneration.

1.2.5 Homogeneous catalytic method of nicotinamide cofactor recycling

The third and arguably most versatile approach to recycling nicotinamide cofactors is homogeneous catalytic, utilising an aqueous chemical catalyst and sacrificial hydride donor. As for the indirect electrochemical method, transition metal catalysts are used as mediators of electron transfer to the substrate (Figure **1.15c**). However, the solid-state cathode (as the primary source of electrons) is replaced by a hydride donor, such as those used in the two-enzyme approach.[117]

Although further from industrial use[115] these systems have the advantage of reduced complexity and improved organic solvent tolerance in comparison to the two-enzyme method, and potentially higher overall cascade efficiencies in comparison to two-enzyme and heterogenous approaches respectively.

For reductases which can accept cheaper nicotinamide cofactor mimics (Section ***1.2.6***),[127] a further advantage in comparison to the second enzyme approach is the ability of organometallic complexes to reduce these mimics.

Meanwhile, the main challenges associated with the homogeneous method are catalyst inactivating interactions and enzyme–catalyst mutual inactivation (Section *1.2.5.2*).

1.2.5.1 Mechanism of nicotinamide cofactor transfer hydrogenation

The most ubiquitous examples of homogeneous nicotinamide recycling catalysts for aqueous conditions are N^N rhodium piano-stool complexes.[128] In a pioneering study, $[Cp^*Rh(bpy)H_2O]^{2+}$ (bpy = bipyridine) **9** (Figure **1.17**) was coupled with TbADH and formate in a butanone reduction system, achieving enantioselective butanol production.[129] The complex catalysed the regiospecific reduction of NAD^+ at the nicotinamide C4 position, without the production of 1,2- or 1,6-regioisomers. It was later shown using the 1-benzylnicotinaimde (BNA^+) mimic that the origin of this regioselectivity is in the ability of the complex to coordinate the amide of the nicotinamide (Figure **1.16C**).[130] This also applies to the selectivity of similar Cp* rhodium, iridium and ruthenium complexes containing 1,10-phenanthroline and derivatives **10**, **11** in place of bipyridine,[83] and to Cp*Ir complex catalysts **12**, **13** with various chelating ligands, all using formate as the hydride donor (Figure **1.17**).[116, 131] A recent study solved the X-ray crystal structure of the rhodium-hydride intermediate (Figure **1.16B**) of a bis-carbene Cp*Rh complex providing support for the involvement of this species in the increasingly accepted general mechanism.[132]

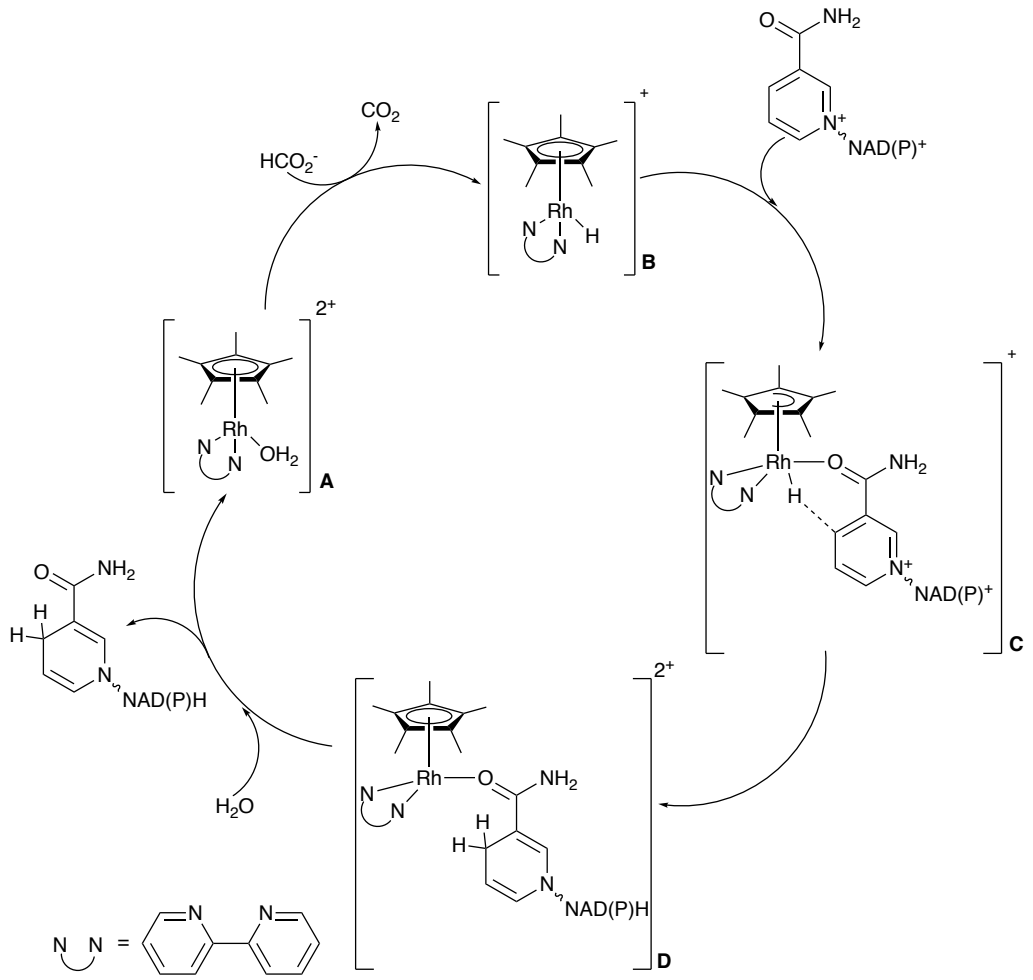

Figure 1.16: Putative rhodium catalyst NAD(P)H regeneration mechanism

Catalytic cycle for the reduction of NAD(P)+ to NAD(P)H using [Cp*Rh(bipyridine)(H)], with formate as the hydride donor. The water ligand in the pre-catalytic complex **A** is replaced by a hydride ion donated from formate, to form the catalytic complex **B**. Cp* ring slippage enables coordination with the $NAD(P)^+$ substrate nicotinamide amide moiety to form transition state complex **C**. Hydride transfer to $NAD(P)^+$ at C4 and reversion of the Cp* coordination state forms complex **D**. Elimination of the NAD(P)H product and coordination to water from the solvent reforms complex **A**. Adapted from[130]

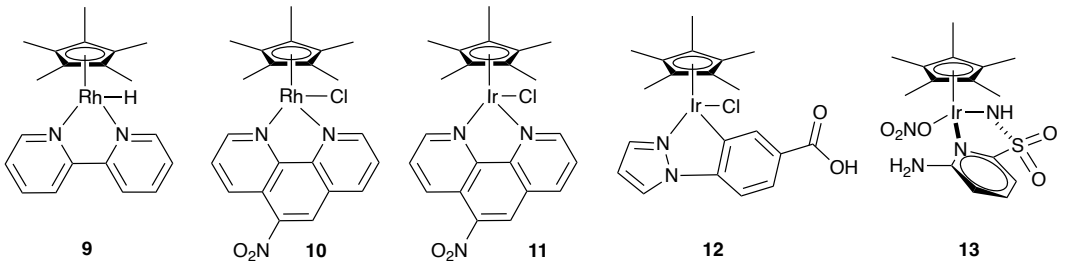

Figure 1.17: Example piano-stool metal complexes for NADH reduction

Catalytic performance is strongly influenced by the electronic properties of coordinating ligands. Direct comparisons of TOF values between complexes are complicated by the use of different conditions and catalyst loadings (Table **1.1**). However, in general, Cp*Rh phenanthroline and bipyridine complexes are on the order of hundreds of turnovers per hour, while similar or higher rates have been achieved recently using Cp*Ir complexes with various ligands.[116]

Table 1.1: TOF values for catalysts 9[120, 130] 10,11[83] 12[116] 13[131]

Catalyst	[Catalyst] μM	[NAD^+] mM	[$HCOO^-$] mM	pH, T °C	TOF h^{-1}
9	25	0.25	500	7.5, 50	~300
10	80	8	350	7.0, 38	150
11	80	8	350	7.0, 38	58
12	80	8	350	7.4, 37	126
13	10	0.77	400	6.6, 40	2321

1.2.5.2 Enzyme-catalyst mutual inactivation

The choice of reaction buffer for homogeneous nicotinamide recycling systems is important, especially when using formate as the hydride donor. Exchange of metal coordinating ligands such as NH_3, Tris or OH^- was found to be rate limiting in NADH regeneration.[120] When the catalyst is mixed with the ketone or imine reductase of the cascade system, similar interactions can occur between the metal and coordinating residue side chains, causing catalyst inactivation. Meanwhile, the complex can also inactivate the enzyme, acting as an unfolding catalyst. These effects are dually termed mutual inactivation, and were investigated using $[Cp^*Rh(bpy)(H_2O)]^{2+}$ and alcohol dehydrogenase from *Thermus sp.* ATN1.[133] It was found that incubation of the catalyst at pH 7.0 with histidine, methionine, tryptophan and cysteine caused significant reduction in catalyst $NADP^+$ reduction activity. This effect was increased by raising incubation temperature from 25 to 40 °C. In the same study, the catalyst-induced protein unfolding mechanism was deduced to occur via a two-step process. Binding of the catalyst to external hydrophilic residues results in a partially unfolded inactive enzyme, in equilibrium with the fully folded active state. This is followed by binding of more catalyst molecules (catalyst concentration dependent), which shifts the equilibrium towards the unfolded state by stabilising this form of the protein. The resulting surface exposure of hydrophobic residues usually residing internally causes denaturation. Mutual inactivation of enzyme and complex is arguably the most significant challenge associated with the homogenous approach to nicotinamide

cofactor recycling. Inactivation of both the complex and the enzyme has been observed in several studies.[122, 133, 134] Suggested solutions have included: derivatisation of peripheral enzyme groups with polymer containing epoxide, preventing complex interaction; removal of nucleophilic residues by mutation; physical separation of the enzyme and complex; the use of buffers containing S- or N- ligands which coordinate the metal complex to provide mutual protection. The latter has been described as having the least negative impact on catalytic performance, and the most widely applicable to different enzymes.[133] However, based on the above discussion of rate limitation due to ligand exchange, this is not a viable solution in homogeneous recycling systems.[120] Examples of where ArMs can be utilised to address the challenges of enzyme-catalyst mutual inactivation are discussed in Sections ***1.3.4*** and ***1.3.5***.

1.2.6 Nicotinamide cofactor mimics

In addition to the expensive natural redox cofactors NAD(P)H, cheaper synthetic nicotinamide mimics such as **N1** (BNA^+) in Figure **1.18** offer a promising alternative for use in enzymatic redox cascades. These small synthetic cofactors are usually devoid of the ribose, pyrophosphate and adenine moieties found in NAD(P)H, and have been applied in both second enzyme and homogeneous catalytic systems.

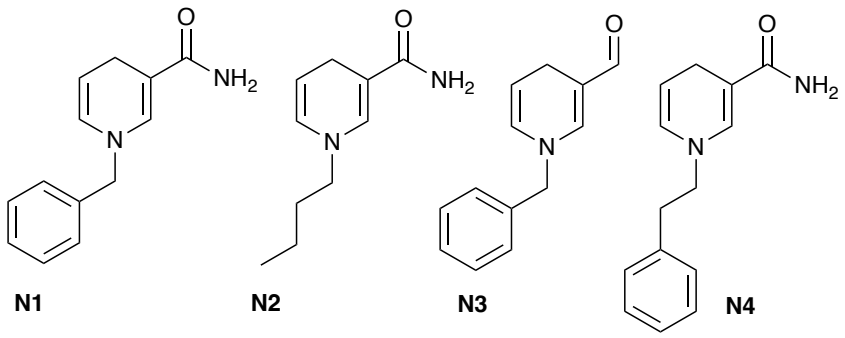

Figure 1.18: Nicotinamide cofactor mimics tested in various reductases
N1-3 were used shown to be recycled by a rhodium catalyst for use in flavin-dependent ene reductases.[135] Recycling of **N4** was by a GDH for use by an enoate reductase.[136] **N1** has also been tested for use with various ADH's.[54, 137]

The use of nicotinamide mimics to replace NAD(P)H is most established in flavin dependent reductases. For example, a selection of ene reductases from the old yellow enzyme family were shown to accept the mimics such as **N1-3** for the asymmetric reduction of pro-chiral alkenes. Some of these enzymes displayed greater rates of reduction with use of mimics as the sacrificial hydride donors (k_{app} values of up to 26

s^{-1}) than with NAD(P)H. $[Cp^*Rh(bpy)H_2O]^{2+}$ was then incorporated as the nicotinamide mimic recycling catalyst using formate as the hydride donor, with more modest conversion of pro-chiral alkene substrates reported.[135] In a second-enzyme approach example, another flavin dependent enzyme was used to recycle mimics, again for use by an ene reductase for the reduction of pro-chiral alkenes.[138]

Meanwhile, cascade systems for the reduction of pro-chiral imines or ketone substrates are less established. For example, the topic of whether wildtype horse liver alcohol dehydrogenase (HLADH) can accept mimics such as **N1** for ketone reduction is still contentious.[54, 137]

However, concerning the interaction of nicotinamide mimics with other reductase enzymes which are not flavin-dependent, several studies report successful two-enzyme cascade reactions.[136, 139] For example, a glucose dehydrogenase (GDH) from *Sulfolobus solfataricus* was shown to recycle mimic **N4** for use by an enoate reductase. This GDH homologue was then engineered to achieve a 10-fold improvement in mimic reduction activity in comparison to the wildtype enzyme. Clearly, mimics such as those in Figure **1.17** can bind to and be recycled by enzymes which contain a nicotinamide cofactor binding pocket such as GDH. This provides promise for engineering of alcohol dehydrogenases and imine reductases (which also possess such pockets) for the use of nicotinamide mimics[140] as redox cofactors in ketone and imine reduction cascades.

1.2.7 Conclusions

The use of organometallic small molecule catalysts such for asymmetric imine and ketone reduction makes up an expansive field. However, NAD(P)H redox cofactor dependent enzymatic alternatives such as ADH's and IRED's can achieve higher rates and selectivities, as well as offering potential for genetic optimisation. The expense of NAD(P)H means that recycling of the cofactors is necessary if such enzymatic ketone and imine reduction systems are to be industrially viable. While second enzyme and electrochemical approaches are currently more industrially applicable, homogeneous catalytic recycling arguably offers the greatest versatility and scope for optimisation. Along with the merits of homogeneous catalytic NAD(P)H regeneration using piano-stool transition metal catalysts comes the challenge of enzyme-catalyst mutual inactivation. Cheaper nicotinamide cofactor mimics are available as alternatives to the

larger natural cofactors. However, acceptance of these mimics by reductases with defined NAD(P)H binding pockets such as ADHs is challenging.

1.3 Rational design of artificial metalloenzymes for transfer hydrogenation

1.3.1 Overview

The ability to genetically manipulate and optimise ArMs presents a key advantage over small molecule catalysts.[4] Approaches follow the same principles as those in the wider field of enzyme engineering. The goal is to enhance or improve features such as substrate scope, product selectivity and turnover rate,[141] often using crystallographic and computational methodologies.

Several recent reviews[4, 5] have highlighted the need for more ArM structural characterisation efforts. Specifically, to gain a better understanding of ArM-complex interactions and ArM-substrate interactions. The latter in particular has been largely unexplored,[4] and ArM crystal structures to date remain few in number.[33, 87, 142-145]

In the context of ketone, imine and nicotinamide transfer hydrogenation approaches discussed in Section **1.2**, ArMs designed for these reductions offer a good platform for rational design. ArMs have been shown to exert control over enantioselectivity in the reduction of imines to chiral amines, and can provide novel solutions to the challenges of nicotinamide cofactor generation discussed in Section ***1.2.5***. There are of course a wide range of other catalytic activities for which ArMs have been rationally optimised, such as hydrogenation, C-H activation, Diels-Alder reactions,[4] as well as carbene and nitrene transfer reactions.[146] Although partially covered in Section **1.1**, these studies are beyond the scope of this thesis.

1.3.2 Enzyme engineering

Enzyme engineering methodologies use genetic mutations to enhance or improve catalytic features such as substrate scope and substrate turnover rate or k_{cat}.[141]

Directed evolution can be considered a “random” approach and has revolutionised the entire field of biocatalysis.[147] It requires a method for gene diversification to enable exploration of the sequence space. This is followed by high throughput selecting or screening for advantageous mutations based on a genotype-phenotype linkage. Iterative rounds of this process enable the evolution of a specific activity or a desirable characteristic.[17, 148]

On the other hand, the textbook rational design approach to enzyme engineering involves site-directed mutagenesis to substitute one or more residues at a specific location, towards a specific activity or desirable characteristic. These mutations are informed by structural insight, based on the central dogma of protein structure-function relationship, and predictions on substrate or cofactor binding.[149, 150] Structures can be obtained via biophysical techniques such as X-ray crystallography, NMR and increasingly, owing to recent technology advances, single particle cryo-electron microscopy (cryo-EM).[151, 152] The latter continues to achieve increasingly impressive resolutions, enabling the visualisation of atomic positioning essential for understanding of structure and function. A practical advantage over crystallography is the need for much less material, given that optimisation of crystallisation conditions is usually required.[153] Despite these advances in cryo-EM, X-ray crystallography continues to be the most common method, particularly within the realms of ArM rational design. One alcohol dehydrogenase rational mutagenesis example which relied on homology models based on the crystal structure of Geobacillus thermoglucosidasius ADH achieved an increase in selectivity for butanol production over ethanol.[154] In comparison to ethanol, butanol has a higher air-to-fuel ratio, higher energy density, and lower hygroscopicity which are attractive features in the context of renewable biofuels.

Rational mutations can also be informed by computational techniques which fall under molecular mechanics (MM) or force fields, and quantum mechanical (QM) simulations.[155] Search algorithms are often used in combination with MM methods. These can be stochastic Monte Carlo searches such as RosettaDesign[156] or deterministic molecular dynamic simulations.[157] Molecular docking is an MM method widely applied to structure-based drug discovery.[158] It can be used to model interactions between macromolecules such as enzymes, and small molecules such as substrates or cofactors. Probable binding modes of the ligand and receptor respectively are predicted based on software-encoded chemical logic. Commonly used platforms include Schrodinger Glide,[46, 159] DOCK6, AutoDock[160] and GOLD.[161] In the context of enzyme engineering, this enables the inexpensive filtering of mutations, reducing experimental time and fund expenditure while retaining candidate library size. Computational insights can also supplement experimental data. A recent ADH *in silico* engineering example achieved an increase in substrate promiscuity.[162] Most MM-based docking algorithms allow flexibility of the ligand, but restrict flexibility of the protein to just a few residues. By reducing the size of the geometric space to explore, less computational power is required for the simulations. However, this means that

normal MM methods cannot predict fine electronic effects, limiting their ability to simulate mechanistic details.[163] QM methods predict such details with greater accuracy but are limited in their application to problems with large geometric spaces to be explored, owing to the computational power required. A hybrid QM/MM approach has seen successes in natural enzyme engineering.[164]

The use of these genetic engineering tools is not exclusive to natural enzymes. Both directed evolution and rational engineering are also crucial for the optimisation of ArMs.

1.3.3 Design of ArMs for ketone and imine reduction

There are numerous other examples of the incorporation of achiral piano-stool catalyst complexes into protein scaffolds to control enantioselectivity of imine and ketone reduction. These include the sulfonamide containing iridium catalysts mentioned in Section ***1.2.2***.[9, 87, 88] When used free in solution, some of these catalysts are incapable of this feature entirely, or only with specific substrates.[165, 166] The ArMs can then be genetically optimised to control or improve this selectivity as well as catalytic rates. The former can be likened to natural enzyme engineering approaches to invert enantioselectivity.[167]

The incorporation of a ruthenium piano-stool complex into streptavidin imparted enantioselectivity in the reduction of challenging ketone substrates.[166] Based on the crystal structure, two residues thought to interact with the complex were selected for site saturation mutagenesis. After initial activity tests, hit variants were purified and tested further. Mutants with higher enantioselectivity that the original ArM were identified. This study and its forerunner (involving chemo-genetic optimisation),[20] are early examples of a directed evolution-rational engineering hybrid approach to ArM optimisation. In a more recent example,[46] low enantioselectivities of 7-10 % were observed in ketone reduction by a papain scaffold ArM. These values could be explained by running QM simulations to predict the effect of complex conformational freedom on this catalytic performance factor.

Mechanistic insight into imine transfer hydrogenation catalysed by a streptavidin scaffold Cp*Ir(biotin)-streptavidin ArM was gained using QM/MM docking simulations and crystallography.[89] The streptavidin S112A Cp*Ir ArM variant displayed 96 % ee

for the (*R*)-salsolidine product, while the S112K Cp*Ir variant displayed 78 % ee for the (*S*)-product. Crystallisation of the latter ArM suggested a potential preference for an absolute configuration of (*R*) around the iridium ion, dictated by the presence of a lysine at residue location 112. Docking of the racemic Cp*Ir complex provided support for this hypothesis, indicating preference of the S112K and S112A ArM variants for (*R*)-Ir and (*S*)-Ir configurations respectively. This would explain enantio-preference for the (*S*) and (*R*)-products respectively.

Further examples of using computational and structural approaches to genetic optimisation in concert include an ArM assembled imine ATH based on human carbonic anhydrase II (hCAII). Cp*Ir complexes were datively anchored to the hCAII via interaction of sulfonamide bearing ligands with the native zinc (II) of the scaffold.[87] The ArM was subject to a computational screen using Rosetta Design.[145] Mutations resulted in an increase in both protein backbone stability and affinity for the iridium complex. Crystallisation of one of the ArM variants was then able to confirm some of the computational predictions. For example, methionine residues introduced at residue locations 140 and 197 form hydrophobic interactions with metallocofactor (Figure **1.19**). The most successful ArM variant included a further six mutations from wild-type hCAII, resulting in a 4-fold increase in imine reduction activity and a 20 % increase in enantioselectivity for the production of (*S*)-salsolidine (ee 92 % (*S*), TOF = 59 h^{-1}).

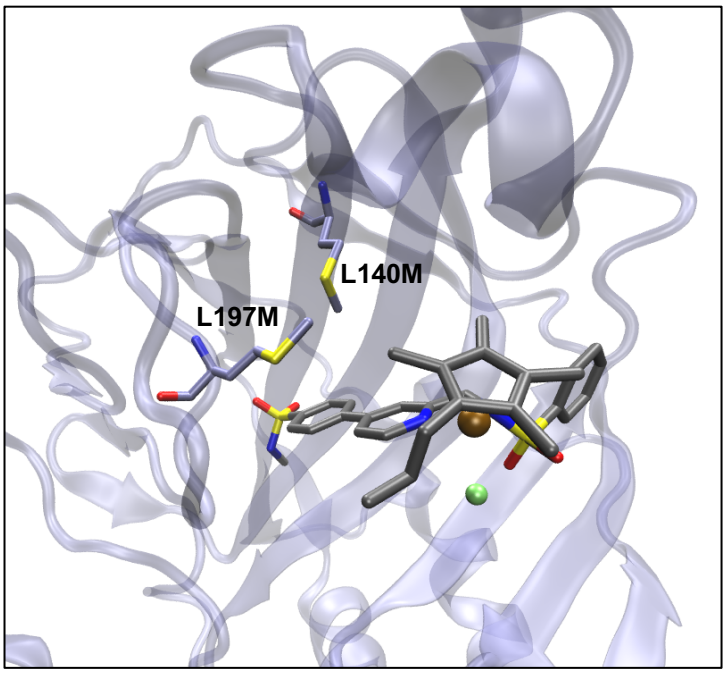

Figure 1.19: X-ray crystal structure of Cp*Ir hCAII-based ArM

The two mutations shown in ice blue were introduced to increase the affinity of hCAII for the iridium catalyst complex which is shown in grey with iridium (III) centre in bronze and coordinating Cl^- in light green. Reproduced from PDB 5BRU.[145]

In a more recent hCAII example, the problem of catalyst flexibility (potentially leading to reduced product selectivity) was addressed via dual anchoring to the ArM scaffold. A covalent bond was introduced between the datively zinc-anchored Cp*Ir complex and the scaffold. This second linkage was shown to stabilise the orientation of the scaffold. Increased enantioselectivity in imine reduction was achieved by directed evolution of the ArM variant.[168]

The examples selected above demonstrate the successful and extensive use of crystallography and computational approaches to gain insight into ArM structure and function, in order to achieve rational optimisation of ketone and imine reduction.[4, 5] Other more recent studies have achieved similarly impressive results using other protein scaffolds.[169, 170] However, there are few examples of such studies in which the ArM scaffold possesses a binding pocket which is naturally evolved towards the desirable ArM catalysed reaction.

1.3.4 Design of ArMs for nicotinamide cofactor recycling

As redox cofactor recycling catalysts in cascade systems for the reduction of both ketones and imines, ArMs can serve as advantageous alternatives to enzymes and small molecule catalysts. In addition to enabling catalyst genetic optimisation, ArMs can also address the enzyme-catalyst mutual inactivation challenge associated with homogeneous catalytic recycling of nicotinamide cofactors (Section ***1.2.5***).

Papain was used as a scaffold for the covalent binding of ruthenium piano-stool complexes.[171] Using formate as the hydride donor, this ArM catalysed the regioselective reduction of NAD^+ to NADH. The next step would have been to couple this NADH regenerating ArM with an enzyme which consumes this cofactor naturally. Such an NADH recycling system was achieved using a streptavidin-based ArM.[172] For assembly, a biotinylated iridium piano-stool complex was incorporated into the scaffold. The ArM was combined with an NADH dependent monooxygenase to achieve regeneration of the cofactor for the desired hydroxylase activity by the latter enzyme. Although regeneration in the absence of streptavidin was observed, rapid complex-monooxygenase mutual inactivation occurred. Therefore, the streptavidin provided a "shielding environment" for both enzyme and catalyst. Moreover, a similar streptavidin-based ArM was also used for this cofactor regeneration function but with cheaper NAD(P)H mimics.[173, 174]

These examples provide scope for genetic optimisation to improve the performance of ArMs for nicotinamide cofactor recycling. A promising protein scaffold for such efforts is alcohol dehydrogenase.

1.3.5 Design of ArMs based on alcohol dehydrogenase

Alcohol hydrogenases such as TbADH (Section ***1.2.3***) possess both a hydrophobic substrate binding pocket and nicotinamide cofactor pocket (Figure **1.20**). These structural features, in addition to practically useful organic solvent and thermal tolerance,[104, 175] make this enzyme an ideal candidate scaffold for ArMs which require binding to nicotinamide cofactors for catalytic function. In principle, the substrate pocket provides space for anchoring of the metal catalyst, while the nicotinamide pocket is naturally evolved to bind $NADP^+$ as the ArM substrate with high affinity. Such ArM designs have received less attention than highly versatile and successful

alternatives based on non-enzymatic scaffolds such as streptavidin[176] and the multidrug resistance regulator LmrR.[177]

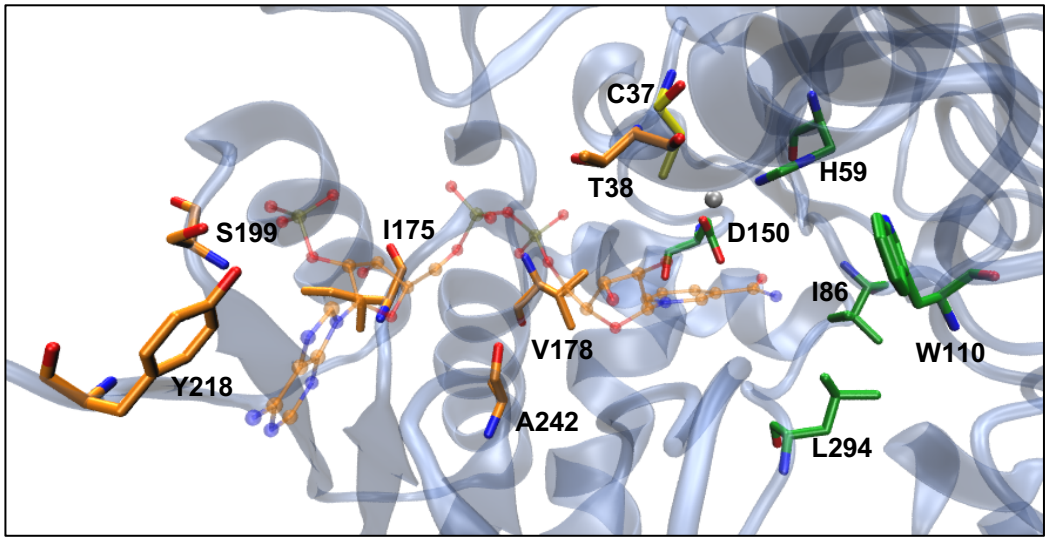

Figure 1.20: Nicotinamide and substrate binding pockets of WT TbADH

Wildtype holo-TbADH (ice blue) with *in crystallo* NADPH (transparent orange) and the catalytic zinc (II) (silver). Residues of the nicotinamide binding pocket (orange) and the substrate binding pocket (green) are highlighted (as in Figures **1.13** and **1.14** respectively). Cysteine 37 which was covalently modified* with metal catalysts in ArM assembly[29] is shown in yellow. Generated from PDB 1YKF[107] using VMD.[111]

*Note that the term "modified" is used throughout this thesis to refer to the residue location of the scaffold TbADH mutant to which the metal complex catalyst was covalently anchored, while the term "unmodified" refers to the apo-TbADH scaffold mutant, devoid of the native zinc (II) ion which is present in wildtype TbADH.

Building on the ArM systems for nicotinamide cofactor regeneration discussed in the previous Section ***1.3.4***,[172, 173] the Pordea group designed an NADPH-recycling ArM to work in concert with wildtype TbADH for chiral alcohol production.[29] For ArM assembly, rhodium piano-stool catalysts were covalently anchored to the native cysteine residue at location 37 of TbADH. All other cysteines had been mutated to prevent non-specific anchoring. The ArM and wildtype TbADH fulfil the roles of NADPH regeneration catalyst and ketone reduction catalyst respectively (Figure **1.21**). In our system, an 18-20 % improvement in efficiency of model ketone reduction was observed in comparison to using the rhodium catalyst free in solution. Both the TbADH incorporated catalyst and the wildtype enzyme were shown to be protected from mutual inactivation. For example, 33-42 % residual rhodium catalyst $NADP^+$ reduction activity was observed following incubation with wildtype TbADH, while 80 % residual wildtype TbADH butanone reduction activity was observed following incubation with

rhodium catalyst (further detail provided in Section *3.2.1.3*).[29] The scaffold protection effect (Section *1.1.2.1*), achieved by metal catalyst encapsulation within a protein environment is an important concept in the wider ArM field.[9, 25, 172]

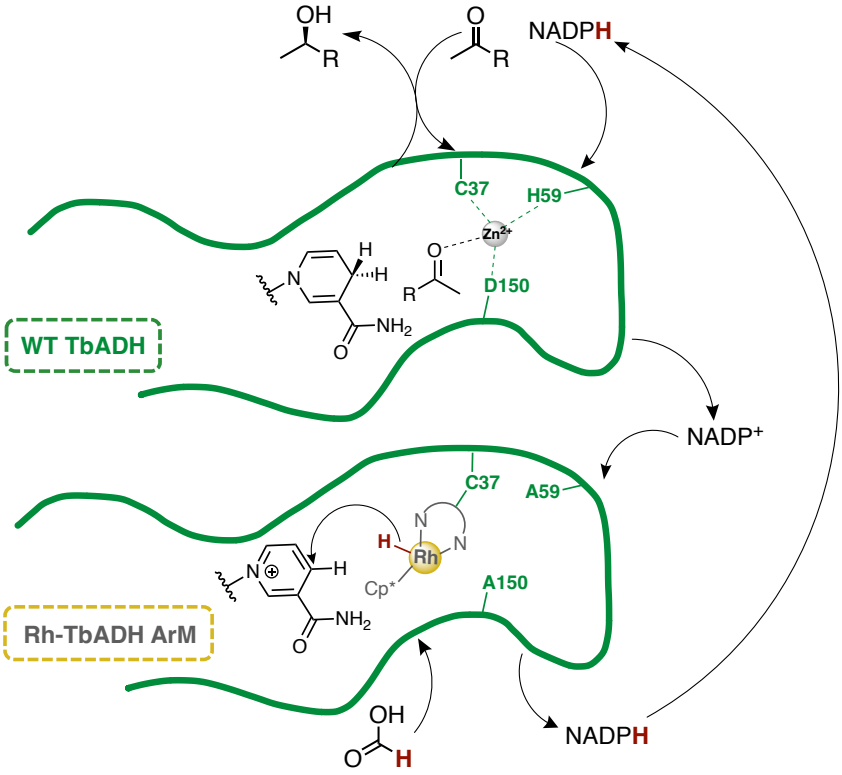

Figure 1.21: Biocatalyst-artificial metalloenzyme cascade based on alcohol dehydrogenase

A one-pot ketone reduction system using an ArM-mediated approach to NADPH recycling, with formate as the hydride donor. Protein components are shown in green and the rhodium catalyst in red. Adapted from[29]

This novel TbADH-based ArM solution to nicotinamide recycling presents an opportunity for rational genetic optimisation of nicotinamide reduction performance. The ability to engineer catalytic activity in this way is arguably the most attractive feature of ArMs over their synthetic counterparts.[5] With regards to genetic optimisation in the context of covalently assembled ArMs, several studies have highlighted the importance of catalyst anchoring position or binding site.[161, 178, 179] The availability of TbADH crystal structures makes this scaffold a logical choice for rational engineering efforts.[107]

Concerning substrate scope, the ability of ArMs to recycle not only the natural nicotinamide cofactors NAD(P)H, but also cheaper nicotinamide mimics has been shown.[136, 139] Furthermore, there is also scope for the anchoring of other piano-stool

catalysts to TbADH to generate ArMs for redox applications such as asymmetric imine reduction. In this case, the nicotinamide compound would serve as the redox cofactor for hydride transfer to imine substrate, retaining the use of the naturally evolved binding pocket. The examples discussed in Section ***1.3.3*** demonstrate the potential to improve enantioselectivity of imine reduction via genetic manipulation of the ArM active site.

1.3.6 Conclusions

ArMs offer promising alternatives to small molecule organometallic and enzymatic approaches to ketone, imine, and nicotinamide cofactor transfer hydrogenation. The examples highlighted directly exploit some of the key features of ArMs which give these hybrid catalysts a unique advantages, particularly over small molecule catalysts. Namely, exertion of tight control over enantioselectivity via genetic manipulation, and the concept of shielding to prevent mutual inactivation between catalyst and enzyme components of cascade systems. Within the context of ArM rational engineering, the need to improve understanding of protein scaffold, catalyst and substrate interactions has been highlighted by major reviews of the field. ADHs as scaffolds for covalently assembled ArMs to be applied to transfer hydrogenation reactions serve as a promising platform for such efforts. The naturally evolved nicotinamide binding pocket can accommodate NAD(P)H or indeed smaller cofactor mimics as either the substrate for nicotinamide recycling systems, or the cofactor for imine reduction systems.

1.4 Project Aim and Objectives

1.4.1 Overall aim

Artificial metalloenzymes can provide advantageous solutions to the challenges of industrially relevant transfer hydrogenation reactions. For example, improving the efficiency of nicotinamide cofactor regeneration, or controlling the enantioselectivity of imine reduction. A range of examples have demonstrated the successful optimisation these catalytic features via genetic manipulation of the protein environment. From review of the literature to date however, the need for a greater understanding of ArM protein scaffold, metal catalyst, and substrate interactions is clear. Such insight would enable more effective ArM rational deign. In particular, there are fewer examples in which the protein scaffold possesses a naturally evolved binding pocket for either the substrate or redox cofactor. Furthermore, examples of direct measurement and optimisation of ArM-substrate affinity are rare. Therefore, the aim of this project is to achieve structural understanding of scaffold, metal catalyst, and substrate interactions within TbADH-based ArMs. Specifically, the covalent anchoring of piano-stool transition metal complex catalysts for ArM assembly, and the binding nicotinamide cofactors for transfer hydrogenation reactions.

1.4.2 Objectives

1a: TbADH-based ArMs containing rhodium piano-stool catalysts have been designed and investigated previously for the purpose nicotinamide cofactor reduction. The residue location 243-modified variant displays promising results with regards to the efficiency of covalent assembly, and reduction activity on both $NAD(P)^+$ and small nicotinamide mimics. However, a structural understanding of ArM-nicotinamide binding behaviour is lacking. To address this, full kinetic characterisation of this ArM variant is completed, followed by docking studies. The objective is to understand how different nicotinamide cofactors interact with this ArM variant (Section **3.2**).

1b: Residue location 243 may not be the optimal site for catalyst anchoring with regards to ArM affinity for nicotinamide cofactors. Therefore, two other locations are investigated via kinetics and docking studies. Whilst the location 37-modified variant has been characterised previously for ketone reduction cascades, full kinetic characterisation and is yet to be completed. Secondly, a new variant is identified subjected to the same analyses. The objective is to explore the effect of catalyst positioning on ArM nicotinamide reduction, in order to improve catalytic efficiency via

increased ArM-nicotinamide affinity (Section **3.3**). If achieved, this along with objective **1a** will add to the range of studies in the literature which have demonstrated rational genetic optimisation of ArMs.

2a: Atomic resolution crystal structures of TbADH-based ArMs are yet to be obtained. Therefore, two promising genetic variants are selected for co-crystallisation with $NADP^+$. The rhodium catalyst in these ArMs is substituted for the equivalent iridium catalyst (bearing the same ligands), to maximising the chances of successful crystallisation via homogeneity of ArM samples. The objective is to gain structural understanding the interactions between the TbADH-based ArMs and nicotinamide cofactors (Section **4.2**). If achieved, this would serve to build upon insight gained from **1a** and **1b**, as well as adding to the limited pool of enzyme-scaffold based ArM structures.

2b: The catalytic potential of iridium-TbADH based ArMs is intriguing because iridium is capable of catalysing reactions which could benefit from the NADPH-specific pocket of TbADH. Specifically, there is potential for asymmetric reduction of imines using a nicotinamide cofactor as the hydride donor. As an initial step towards such work, the objective here is to investigate the functionality of these ArMs for various reduction activities, all using NAD(H) as either the substrate or redox cofactor (Section **4.3**). If achieved, this would enable progression towards control over enantioselectivity via ArM structure-informed rational optimisation.

2 Materials and Methods

The present chapter provides an introduction and justification for selection (where applicable) of each methodology, followed by the experimental detail. All reagents were sourced from Merck (Sigma Aldrich) unless stated otherwise.

2.1 Docking

Computational docking enables the prediction of interactions between protein receptors and small molecule ligands using the principles of molecular mechanics (MM). MM force fields such as OPLS3[180] can be used to define both covalent and non-covalent (supramolecular) bonding between the atoms in the system. Docking approaches can be categorised into rigid, semi-flexible and flexible classes. The former keeps both the protein and ligand rigid, considering only translational and rotational degrees of freedom. The semi-flexible approach considers internal degrees of freedom within the ligand only while in the flexible approach, both the ligand and receptor are flexible. While enabling more flexibility improves the accuracy of output ligand pose and affinity predictions, the computational cost is much higher, especially when the protein is made flexible. Empirical scoring functions have been developed to provide estimates of binding affinity.[181] These include ChemScore, ID-Score and GlideScore (Schrodinger).

All docking was completed in Schrodinger Maestro using Glide.[182] This is a hierarchical procedure starting with the generation of a grid which represents the receptor shape and properties. In the first step, a set of low-energy ligand conformational isomers are generated for docking to the receptor. Next, screening of ligand poses is completed, involving an exhaustive search of possible ligand positions within a defined grid. The ligand is then minimised in the receptor grid using a force field, followed by a final selection of ligand poses based on optimising torsional bond angles.[182] In the docking presented, the ligand was kept flexible while the receptor was kept rigid.

2.1.1 Protein preparation

All protein preparation was completed in Schrodinger Maestro.[182] The crystal structure of wildtype holo-TbADH with the NADPH bound[107] (PDB: 1YKF) was imported. Protein preparation using the in-built wizard was performed prior to all ligand docking steps. Specifically, missing hydrogens were added, and any originals removed, bond orders were assigned, waters beyond 5 Å of het groups (defined as atoms which do not belong to proteogenic residues), or with fewer than 3 hydrogen bonds to non-waters

were removed. Both of these steps resulted in no water in the binding site. Heteroatom charge states were generated using Epik in aqueous solution at pH 7.0 ± 2.0. Refinement steps involving optimisation of the H-bond network and the restrained minimisation of steric clashes were run as default within the protein preparation wizard. This involved use of the OPLS3 force field to geometrically optimise the structure. Following this first round of preparation, NADPH and the catalytic zinc ion were removed. Mutations were introduced (Table **2.1**). The same protein preparation steps were then run again in case of necessary optimisations as a result of these changes.

Table 2.1: TbADH mutants

Mutant name	Template	Mutations
5M-C37	Wildtype	C203S, C283A, C295A, H59A, D150A
6M	5M	C37A
7M-C243	6M	G243C
7M-C110	6M	W110C

Mutant nomenclature: The '5M', '6M' and '7M' prefixes denote the number of point mutations made, while the 'C37', 'C243' and 'C110' suffixes denote the single cysteine residue present in each respective mutant. In the case of 5M-C37, the single cysteine is native to TbADH, whereas in 7M-C243 and 7M-C110, cysteines were introduced at residue locations 243 and 110 respectively.

2.1.2 Ligand preparation

The rhodium catalyst Cp*Rh(Br**L1**)Cl used in covalent docking was built in Maestro, while $NADP^+$ as the ligand for supramolecular docking was obtained from the wildtype holo-TbADH crystal structure.[107] Preparation of ligands for both covalent and supramolecular docking was performed using the in-built tool in Maestro (Schrodinger), with the OPLS3 force field.[180] For the Cp*Rh(Br**L1**)Cl ligand, special considerations had to be made, owing to the presence of the rhodium ion. Force fields have not yet been fully developed to handle non-standard transition metal coordination geometries and bonding. Therefore, in accordance with current Schrodinger guidelines and elsewhere in the literature,[159] zero-order bonds were created from the metal to the cyclopentadienyl, phenanthroline and hydride ligands. Generation of all possible protonation and ionisation state combinations was performed using Epik in aqueous solution at pH 7.0 ± 2.0. Chiral centres were determined from the 3D structure and those of NADPH were checked prior to supramolecular docking. Finally, structures

were then minimised using the “minimise selected atoms” function within the Maestro workspace.

2.1.3 Covalent docking

The Cp*Rh(Br**L1**)Cl complex was covalently docked to TbADH mutants using the Glide SP procedure in Maestro. Docking to the 7M-C243 mutant was completed in collaboration with Dr F. L. Martins. The docking site was defined by a single reactive cysteine residue at the centre of the grid, and grid size was set to the default <= 20.0 Å. Reaction type was selected as nucleophilic substitution, resulting in recognition of the bromoacetamide and thiol groups of the docked ligands and receptor respectively. Core and constraints parameters were left as default. In docking settings, pose prediction was set to thorough, with refinement parameters left as default, the number of output poses per ligand reaction site set to 5, and the maximum number of top scoring ligands to report set to 1000.

2.1.4 Supramolecular docking

$NADP^+$ and BNA^+ were docked to the above ArM covalent docking poses. Docking to the residue location 243-modified variant was completed in collaboration with Dr F. L. Martins. The centre of the receptor grid was defined by a centroid of selected residues Y218, N245, H42, V178, M151, A295 and N266, forming a suitable ~10 Å radius around the position of $NADP^+$ in the wildtype crystal structure (PDB 1YKF).[107] No restraints or rotatable groups were introduced to the grid. Parameters for van der Waals radii scaling of non-polar atoms were left as default (1.0) in both the receptor grid and the docked ligands. Ligand docking was first run using Glide SP under default settings. The top three poses from the standard precision procedure where then subject to Glide XP (extra precision) docking. The number of output poses to be displayed per ligand was set to 5, and post-docking minimisation performed. From each docking simulation, the top three Glide XP output poses with the highest-ranking (lowest energy or best) glide scores were selected for qualitative analysis of ligand positioning.

2.2 Molecular biology

2.2.1 E. coli strains and cloning

Competent Escherichia *coli* NEB5a and BL21(DE3) (New England Biolabs) were used for plasmid extraction and protein expression respectively. The former, a derivative of K-12 DH5α, is well-suited to high-efficiency cloning owing to features such as: the absence of endonuclease I; low levels of homologous recombination aiding plasmid stability during storage; primed for efficient transformation of unmethylated DNA owing to disruption of the endonuclease EcoK1.[183] Bl21(DE3), one of the most popular strains for protein expression, carries the T7 RNA polymerase gene under the control of the *lac*UV5 promoter.[184] In comparison to other *E.coli* polymerases, T7 is more active and terminates transcription less frequently.[185]

The N-terminally strep-tagged (Section ***2.3.4***) wildtype *T. brockii* ADH gene in expression vector pET-21a was available in our laboratory. The gene had been inserted between restriction sites NdeI and XhoI in the multiple cloning site, enabling expression under the control of the upstream T7 promoter. pET-21a confers ampicillin resistance, enabling the use of carbenicillin for selection of colonies following transformation of cells. The TbADH 5M-C37 mutant (Table **2.1**) had been prepared previously by Dr S. Morra,[29] followed by the 6M, and 7M-C243 mutants by Dr M. Basle[186] using site directed mutagenesis (mutant nomenclature is explained in Table **2.1**). The sequences of these plasmid constructs were re-confirmed using Sanger sequencing (Source BioScience).

2.2.2 Site directed mutagenesis

Site directed mutagenesis enables the introduction of a single point mutation to the plasmid using mutagenic primers, followed by PCR to amplify the DNA for subsequent transformation into cloning or expression host cells.[187] Plasmid constructs containing the 5M-C37 and 7M-C243 mutant genes had been prepared previously by Dr S. Morra[29] and Dr M. Basle[186] respectively. The TbADH 6M mutant construct was used as a template for the creation of the 7M-C110 construct. Plasmid DNA concentration was determined using the A260 nm absorbance peak on a BioDrop instrument (Biochrom). Primers were generated using the online Agilent QuickChange Primer Design tool, and made to order by Integrated DNA Technologies (Table **2.2**).

Table 2.2: Primers used to obtain the 7M-C110 plasmid construct

Mutation	Template	Primers	Mutant name
W110C	6M	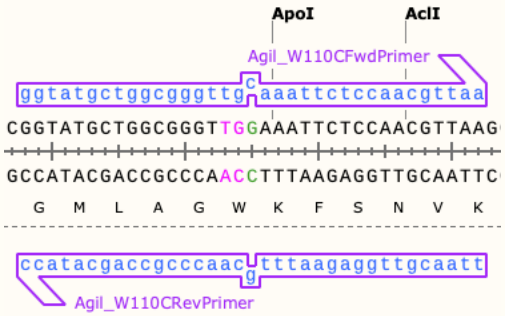	7M-C110

The new construct was generated in a 20 µL PCR reaction using nuclease-free water. 0.5 µL of the template DNA (~100 ng/µL stock), 1 µL of each primer (10 µM stocks), 0.4 µL dNTPs (10 mM stock) and 12.5 µL of Q5 polymerase (New England Biolabs) were mixed in a standard PCR tube. Thermal cycles were completed using an Eppendorf Mastercycler nexus, with annealing and extension parameters determined by the size of the 6.607 kb construct:

- 1 cycle of initial denaturation:
    - 98 °C for 30 s
- 25 cycles of denature, anneal, extend:
    - 98 °C for 10 s, *64 °C for 20 s, 72 °C for 20 s per kb
- Final extension
    - 72 °C for 120 s

*Annealing temperature provided by the online Agilent QuickChange tool

The PCR product was incubated with 1.5 µL FastDigest Dpn1 (Thermo Scientific) in nuclease free water for 2.5 h at 37 °C to digest the methylated template DNA. The plasmid was transformed into *E. coli* NEB5α by heat shock, followed by growth on carbenicillin selection plates. Several colonies were picked for plasmid extraction using a MiniPrep kit (Merck), followed by sequencing at (Source BioScience) to confirm the success of the mutagenesis procedure.

2.3 Protein expression and purification

2.3.1 Protein expression

TbADH variants were expressed in *E. coli* BL21(DE3) (New England Biolabs) using LB Broth Miller (Thermo Scientific) with induction by IPTG. 2 L conical flasks containing 0.5 L of LB were supplemented with carbenicillin to 100 mg/mL prior to inoculation with 2.5 mL of primary overnight culture. Following incubation at 37 °C with shaking (200 RPM) until an OD_{600} of 0.8 had been reached, cells were induced with IPTG to 1 mM. The wildtype culture was also supplemented with $ZnCl_2$ to 1 mM. Cultures were then incubated for an induction period of ~20 hrs at 30 °C with shaking (200 RPM). Cells were harvested by centrifugation at 4000 RPM at 4 °C for 10 minutes (Avanti J-26 XP, Beckman Coulter). Pellets were stored at -20 °C.

2.3.2 Cell disruption

Cell pellets were re-suspended in 10 mL of buffer A (Table **2.3**) at 4 °C and supplemented with protease inhibitor cocktail to reduce digestion of desirable protein, benzonase nuclease to hydrolyse nucleic acids resulting in reduced viscosity and improved protein yield, and lysozyme to assist with bacterial cell lysis.[188] The suspension was stirred on ice until homogenous followed by sonication to lyse the cells for 10 seconds every 30 seconds for 5 minutes. Cell debris were removed by centrifugation at 25,000 RPM (Avanti J-26 XP, Beckman Coulter) at 4 °C for 15 minutes.

2.3.3 Heat treatment purification

The high thermostability of TbADH enables this unique step of the purification procedure. By denaturing and removing the majority of native host proteins prior to the second affinity column step, final purity is improved.[189] The supernatant was incubated at 60 °C for 15 minutes followed by incubation on ice for 10 minutes. This was followed by centrifugation at 14000 RPM for 10 minutes to remove aggregated protein.

2.3.4 Strep-tag affinity chromatography purification step by FPLC

In the second purification step, the load fraction isolated above was applied to a StrepTrap™ HP 5 mL column (GE Healthcare) after equilibration with 5-10 column volumes of buffer A (Table **2.1**). The column contains Strep-Tactin (modified

streptavidin) which has a high affinity for the 8-amino acid sequence of the N-terminal strep tag.[190] Although larger than the 6-His tag used in immobilised nickel-affinity purification, the greater specificity results in higher final purity.[191] The protein was eluted in 2.5 mL fractions by the addition of buffer B. The constituent d-Desthiobiotin has a higher affinity for the strep tag than Strep-Tactin, competing the desirable protein from the column.[190] Elution fractions displaying a strong A_{280} nm peak, were analysed by SDS-PAGE. d-Desthiobiotin was removed from these pooled fractions by using a 10000 MWCO Viva-Spin 6 column (Sartorius), for exchange into buffer C. The protein was stored at -80 °C.

Table 2.3: Buffers used for protein purification

Buffer	Composition
A Loading	100 mM Tris HCl, 150 mM NaCl
B Elution	100 mM Tris HCl, 150 mM NaCl, 2.5 mM d-Desthiobiotin
C Storage	100 mM Tris HCl

2.4 Protein quantification

2.4.1 SDS-PAGE

Sodium dodecyl sulfate polyacrylamide gel electrophoresis (SDS-PAGE) is the simplest and most effective analytical method to determine the purity of a protein sample. Exposure to the SDS at high temperatures denatures the protein, while also imparting a uniform negative charge via binding of the detergent molecules. The subsequent electrophoresis step involves migration of the protein through a porous polyacrylamide gel matrix, leading to separation of the constituent proteins based on molecular mass.[192] All protein fractions isolated from the above purification procedure (Section ***2.3.3-4***) were subject to this analysis.

Sample buffer (60 mM Tris pH 6.8, 2.5 % v/v SDS, 0.002 % v/v bromophenol blue, 10 % v/v glycerol, 0.6 % v/v beta mercaptoethanol) with 20 % v/v protein sample, was incubated at 95 °C for 5 minutes. Samples were then loaded onto a 10 % polyacrylamide pre-cast gel (Bio-Rad) submerged in SDS running buffer (14.4 g/L glycine, 3 g/L Tris base, 1 g/L SDS), along with Precision Plus Protein Dual Colour Standard (Bio-Rad). Gel electrophoresis was run at a 200 V for 35 minutes followed by staining with InstantBlue (Abcam).

2.4.2 Bradford assay

The most popular method for estimating the concentration of a pure protein sample is by measurement of absorbance at 280 nm. This absorbance value and the molar extinction coefficient (specific to the protein of interest) are used to calculate the concentration via the Beer-Lambert law.[193] In the present work however, this method was considered unsuitable owing to absorbance spectra of the transition metal complexes to be anchored to TbADH. In particular, the [Cp*Rh(Br**L1**)Cl]Cl complex (Section **2.5**) displayed a broad absorbance peak at 280 nm. As absorbance in this region would have made it challenging to determine the concentration of assembled ArM (Section ***2.6.1***), protein concentration was instead estimated using Bradford assay. A set of bovine serum albumin (BSA) standards were prepared via serial dilution in a range of 0.125 to 2 mg/mL, in addition to several dilutions of protein sample. Assays were performed in a 96-well plate in triplicate by mixing 300 µL of Bradford reagent (Bio-Rad) with 10 µL of either TbADH sample, BSA standard, or sample buffer (control). Samples, standards and controls were incubated in the dark at room temperature for 30 minutes prior to measurement of absorbance at 595 nm using a FLUOstar OPTIMA plate reader (BMG Labtech). Measurements from the BSA standards were used to generate a standard curve from which protein sample concentrations were estimated.

2.5 Chemical synthesis

^{1}H NMR spectra were acquired at 298 K using a Bruker AV400 instrument. ESI-MS analysis was completed in water using a Bruker microTOF 61 instrument.

*2-bromo-N-(1,10-phenanthrolin-5-yl)acetamide (**L1**)*

The compound was synthesised according to a previously established protocol.[29] Under nitrogen, bromoacetyl bromide (131 µL, 1.5 mmol) was added to phenanthroline-5-amine powder (195 mg, 1 mmol) suspended in anhydrous $CHCl_3$ (30 mL). This mixture was heated under reflux overnight. The resulting product suspension was filtered and dried (crude yield = 372 mg, 0.937 mmol, 94 %). Product Mr = 397.

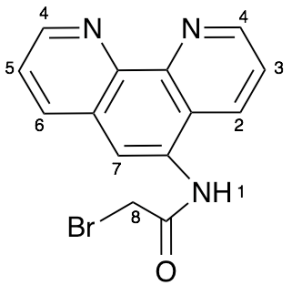

^{1}H NMR (400 MHz, DMSO) δ 10.93 (s, 1H, H^1), 9.34 (dd, *J* = 4.6, 1.4 Hz, 1H, H^3), 9.23 (dd, *J* = 5.1, 1.5 Hz, 1H, H^5), 9.17 (dd, *J* = 8.3, 1.5 Hz, 1H, H^6), 9.08 (dd, *J* = 8.5, 1.5 Hz, 1H, H^2), 8.59 (s, 1H, H^7), 8.24 (dd, *J* = 8.4, 4.9 Hz, 2H, H^4), 4.37 (s, 2H, H^8).

ESI-MS$^+$ calculated for $C_{14}H_{10}BrN_3O$ = 316.16, found $C_{14}H_{11}BrN_3O$ = 318.0086 ($M+H^+$). Also found $C_{14}H_{10}BrN_3ONa$ = 337.9899 ($M+Na^+$) (Appendix **4**)

*[Cp*Rh(Br**L1**)Cl]Cl*

The synthesis was completed according to a previously established protocol.[29] Under nitrogen, pentamethylcyclopentadienyl rhodium(III) chloride dimer (50 mg, 0.081 mmol, 1 eq.) was suspended in methanol (2 mL). To this was added a second fine suspension of 2-bromo-*N*-(1,10-phenanthrolin-5-yl)acetamide hydrobromide (56 mg, 0.161 mmol, 2 eq.), also in methanol (1 mL). Triethylamine (25 mg, 0.243 mmol 3 eq.) was added with stirring and the suspension immediately turned into a yellow/orange clear solution. Addition of cold diethyl ether resulted in product precipitation. After 20 minutes on ice, the precipitant was filtered and dried to a bright yellow powder. Product Mr = 589.

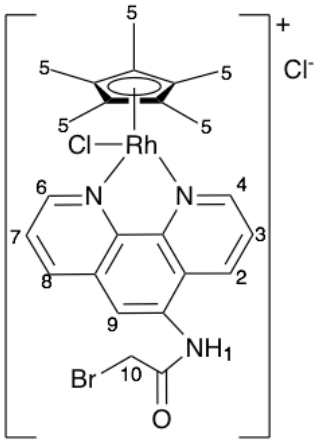

^{1}H NMR (400 MHz, $CDCl_3$) δ 11.84 (s, 1H, H^1), 9.98 (d, *J* = 8.5 Hz, 1H, H^4), 9.09 (d, *J* = 5.2 Hz, 1H, H^2), 8.99 (d, *J* = 5.0 Hz, 1H, H^6), 8.76 (s, 1H, H^9), 8.54 (d, *J* = 8.2 Hz, 1H, H^8), 8.15 (dd, *J* = 8.5, 5.2 Hz, 1H, H^3), 7.95 (dd, *J* = 8.2, 5.1 Hz, 1H, H^7), 5.32 (s, 1H), 4.97 – 4.83 (m, 3H, H^9), 3.51 (d, *J* = 5.2 Hz, 1H, MeOH), 1.85 (s, 13H, H^5), 1.59 (s, 55H, H2O), 1.28 (s, 5H).

ESI-MS$^+$ calculated for $C_{24}H_{25}BrClN_3ORh$ = 588.74, found $C_{24}H_{25}BrClN_3ORh$ = 589.9902 (M^+) (Appendix **5**)

*[Cp*Ir(Br**L1**)Cl]Cl*

The synthesis was achieved by adaptation of the protocol used to synthesise *Cp*Rh(Br**L1**)Cl]Cl*. It was found that increased incubation times and the additional dissolution and drying step improve the purity of the final product. Under nitrogen, pentamethylcyclopentadienyl iridium(III) chloride dimer (95 mg, 0.120 mmol, 1 eq.) and 2-bromo-*N*-(1,10-phenanthrolin-5-yl)acetamide hydrobromide (95.5 mg, 0.234 mmol, 1.95 eq.) were suspended in methanol (3 mL). Triethylamine (25 mg, 0.243 mmol 3 eq.) was added with stirring and the suspension immediately turned into a yellow/orange clear solution. The solution was stirred for 1 hour at room temperature to reaction completion. Addition of cold diethyl ether followed by incubation at -20 °C for 15 minutes resulted in product precipitation. The precipitant was filtered and dried under vacuum to a obtain a bright yellow powder (Yield = 13 %). Remaining precipitant was dissolved through the filter with dichloromethane before solvent evaporation and drying to obtain an orange powder (Yield = 28 %). The latter sample was determined to be of higher purity (H^1 NMR, ESI-MS) and was selected for further experiments.

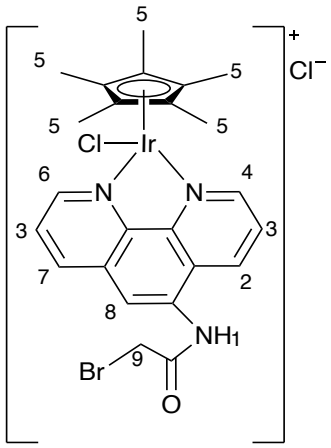

H^1 NMR ^{1}H NMR (400 MHz, MeOD) δ 9.41 (dd, *J* = 6.8, 5.5 Hz, 1H, H^4), 9.37 – 9.29 (m, 1H, H^6), 8.95 (t, *J* = 8.9 Hz, 1H, H^2), 8.83 (t, *J* = 8.7 Hz, 1H, H^7), 8.54 (s, 1H, H^8), 8.19 (dtd, *J* = 28.0, 8.0, 5.4 Hz, 2H, H^3), 5.51 (s, 1H, DCM), 4.50 (s, 2H, H^9), 3.22 (q, *J* = 7.3 Hz, 4H, TEA-HCl), 1.83 (d, *J* = 11.4 Hz, 15H, H^5), 1.49 (t, *J* = 7.3 Hz, 7H, TEA-HCl)

ESI-MS Mr calculated for $C_{24}H_{25}Br_1Cl_1N_3O_1Ir_1$ = 678.05, Mr found = 678.04 (Appendix **6**)

*[Cp*Ir(Br**L2**)Cl]Cl*

The synthesis was completed according to a previously described protocol.[194] Under nitrogen, pentamethylcyclopentadienyl iridium(III) chloride dimer (100 mg, 0.125 mmol, 1 eq.) and 4,7-dihydroxy-1,10-phenanthroline (62.5 mg, 0.295 mmol, 2.36 eq.) were suspended in 5 mL DMF and stirred for 12 hours at 80 °C. Following cooling of the mixture to room temperature, a pale-yellow precipitant was filtered off and dissolved in ethanol. The volume of solution was reduced under vacuum. Addition of cold diethyl ether resulted in a pale-yellow precipitant which was filtered and dried under vacuum.

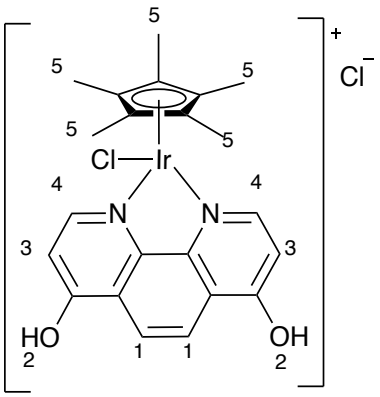

^{1}H NMR (400 MHz, DMSO) δ 8.94 (d, *J* = 6.2 Hz, 2H, H^4), 8.20 (s, 2H, H^1), 7.49 (d, *J* = 6.0 Hz, 2H, H^3), 1.69 (s, 14H, H^5).

ESI-MS Mr calculated for C_{22} H_{24} Cl_1 Ir_1 N_2 O_1 = 574.10, Mr found = 538.65 (C_{22} H_{24} Ir_1 N_2 O_1) (Appendix **7**)

*[Cp*Ir(Br**L4**)Cl]Cl*

Synthesis was completed according to the procedure used for *[Cp*Ir(Br**L1**)Cl]Cl*, replacing ligand **L1** with 1,10 phenanthroline.[194]

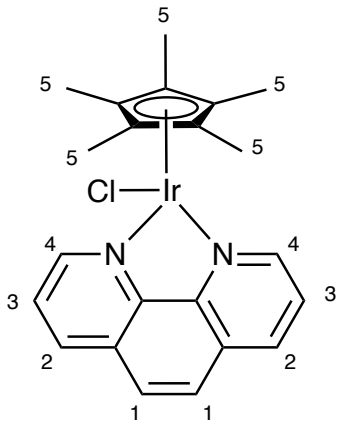

^{1}H NMR (400 MHz, DMSO) δ 9.41 (dd, *J* = 5.3, 1.2 Hz, 2H, H^4), 8.99 (dd, *J* = 8.2, 1.2 Hz, 2H, H^2), 8.38 (s, 2H, H^1), 8.23 (dd, *J* = 8.2, 5.3 Hz, 2H, H^3), 1.74 (s, 15H, H^5).
ESI-MS Mr calculated for C_{22} H_{22} Cl_1 Ir_1 N_2 Cl_2 = 542, Mr found = 543 (Appendix **8**)

*([Cp*Ir(**L4**)H_2O]$(PF_6)_2$*

The synthesis was completed according to a previously described protocol.[195] Under nitrogen, a solution of pentamethylcyclopentadienyl iridium(III) chloride dimer (100 mg, 0.125 mmol) was stirred with 4 mol equivalent of $AgNO_3$ in MeOH (5 mL) and water (10 mL) at room temperature for 24 h. Following the removal of $AgCl_2$ precipitant by filtration, 1 mol equivalent of 1,10 phenanthroline was added and the mixture was stirred at room temperature for 12 h. 10 mol equivalents of NH_4PF_6 was added to form a yellow precipitant which was washed in diethyl ether following filtration, then recrystallised from hot MeOH.

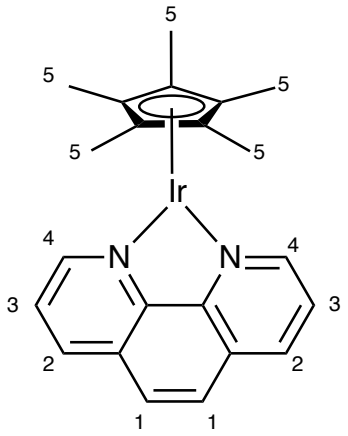

^{1}H NMR (400 MHz, DMSO) δ 9.47 (dd, *J* = 5.4, 1.2 Hz, 2H, H^{4}), 9.14 (dd, *J* = 8.3, 1.2 Hz, 2H, H^{2}), 8.46 (s, 2H, H^{1}), 8.35 (td, *J* = 7.8, 4.7 Hz, 2H, H^{3}), 7.09 (s, 4H), 2.08 (s, 2H), 1.72 (s, 15H, H^{5}).

ESI-MS Mr calculated for C_{22} H_{22} Cl_{1} Ir_{1} N_{2} = 506.65, Mr found = 507, 254 (2+ ion) (Appendix **10**)

2.6 ArM assembly and characterisation

2.6.1 Bioconjugation of metal catalysts to TbADH

Covalent ArM assembly (bioconjugation) via thiol alkylation comes with the necessity of introducing a reactive cysteine residue, in addition to removing all native cysteines to prevent multiple catalyst conjugation (covalent binding) sites.[3] Despite this practical drawback, the method enables precise control over the exact anchoring location of the metal catalyst, as discussed in Section ***1.4.4***. Such control was needed here for the purposes of understanding the effect of catalyst positioning within the TbADH scaffold on ArM catalysed nicotinamide reduction.

Covalent bioconjugation was performed broadly according to procedures established previously by Dr S. Morra, with some minor adaptations.[29] In the case of rhodium catalysts, a 4-fold molar excess of the complex was mixed with the protein. In the case of iridium catalysts, a 6-fold molar excess of the complex was used. All bioconjugation experiments were performed in 100 mM Tris HCl pH 7.0. Samples were mixed by gentle inversion, then incubated at 30 °C for 1 hour with inversion every 15 minutes. The purpose increasing the incubation temperature was to increase the percentage of TbADH successfully conjugated with metal catalyst. Excess metal complex was removed by PD-10 desalting column (GE Healthcare), followed by concentration of

samples with a 10,000 MWCO Vivaspin 6 column (Sartorius). Bioconjugate samples were stored at -80 °C.

2.6.2 Ellman's assay

The Ellman's assay is a chromogenic method for the determining the concentration of unmodified (free) reduced cysteine thiol groups within a protein sample. The assay was selected as an initial estimate of bioconjugation completeness as (in contrast to mass spectrometry) it can be performed immediately following the procedure with minimal time a specialist instrument requirements. $DTNB^{2-}$ (Ellman's reagent) reacts with reduced sulfhydryl to form TNB^{2-} (λ_{max} = 412 nm).[196] Therefore, by measuring absorbance at this wavelength, the molar extinction coefficient of TNB^{2-} can be used to determine its concentration. Based on a known quantity of thiol groups (cysteine residues) per protein monomer, this concentration value can be used to estimate the percentage of cysteines which are unmodified in the protein sample.
Free thiol availability of 5M-TbADH samples was measured via Ellman's assay before and after each bioconjugation experiment, providing a quantitative estimate bioconjugation efficiency.

$$\%\ Free\ thiol\ availability = \frac{[T]}{([E]\ \times\ n)}\ \times\ 100$$

$$[\mathrm{T}] = \text{thiol concentration } (\mu\mathrm{M}),\ [\mathrm{E}] = \text{subunit concentration } (\mu\mathrm{M}),\ \mathrm{n} = \text{number of thiol groups per subunit}$$

According to manufacturer (Thermo Scientific) suggested ratios, in each assay, 176 µL of reaction buffer (100 mM sodium phosphate pH 8.0, 1 mM EDTA) were mixed with 4 µL of Ellman's reagent (4 mg/mL) and 20 µL of sample, or 20 µL of sample buffer in control reactions. UV-compatible plastic 0.5 mL cuvettes were used. Following 20 minutes of incubation at room temperature, A412 nm was measured using a UV-spectrophotometer (SHIMADZU UV-2600) in spectrum mode. Control readings were subtracted from sample readings, and thiol concentration was calculated using the using the Beer-Lambert law (ε_{412} = 14150 M^{-1} cm^{-1} = 0.01415 μM^{-1} cm^{-1})[197] after correction by the dilution factor.

$$[T] = \frac{A}{\varepsilon l}$$

$$[T] = \text{thiol concentration } (\mu M),\ A = \text{absorbance units},\ \varepsilon = \text{extinction coefficient } (\mu M^{-1}\ cm^{-1}),\ l = \text{light pathlength } (cm)$$

2.6.3 ICP MS

Inductively coupled plasma mass spectrometry is a highly sensitive analytical technique which enables accurate quantification of trace elements within a biological sample. These features make the method suitable for analysing the metal content in an ArM sample, as a measure of the proportion of protein modified with metal catalyst. Free catalyst or ArM rhodium or iridium containing samples were diluted to 150 ppb of metal content in 10 % nitric acid prepared using Mili-Q water. The samples were then incubated in a 95 °C water bath for 30 minutes, followed by cooling to room temperature before centrifugation at 4000 RPM for 15 minutes. The resulting supernatant was diluted 5-fold in Mili-Q water to give a final metal content of 30 ppb in 2 % nitric acid for analysis using a Thermo Scientific iCAP-Q instrument.

2.6.4 ESI-TOF MS

Whole-protein denaturing electrospray ionisation time-of-flight (ESI-TOF) mass spectrometry is an analytical technique which can be used to quantify the precise molecular masses of protein species in sample. The method involves fragmentation of the protein into cations which then travel through a mass analyser for detection, with the TOF corresponding to the mass-to-charge (m/z) ratio of the ion. This provides a spectrum of charged states for each species of a given molecular mass in solution. Software is then used to deconvolute this series of peaks to obtain the masses of species present, with the approximate proportions of each species observable based on corresponding peak intensities. The method is defined as a top-down proteomics approach, as unlike bottom-up alternatives, no endoproteinase digestion is required prior to analysis.[198] The method was selected because it enables the identification of both unmodified native protein, and protein modified with metal complexes (ArM), based on the difference in mass between these species.[199]

The procedure was completed using a Bruker IMPACT II instrument. Protein samples were prepared by exchange into pure water using a PD-10 desalting column (GE Healthcare). The samples were then concentrated to between 2 and 5 mg/mL using a 10000 MWCO Viva-Spin 6 column (Sartorius) and mixed with an equal volume of acetonitrile (0.1 % formic acid), followed by centrifugation in a benchtop microfuge (Eppendorf) at max RPM prior to injection of the supernatant into the instrument.

2.7 Kinetic assays

2.7.1 UV-Visible spectroscopy for reduction of nicotinamides

Absorbance at 340 nm by nicotinamide cofactors enables monitoring of reduction or oxidation by measuring change in absorbance at this wavelength as a function of time, as performed previously by other members of the Pordea group, and other research groups.[200] This method was selected as a simple and effective means to monitor both free metal catalyst and ArM rates of nicotinamide reduction.

Reduction of $NAD(P)^+$ (Apollo Scientific) to NAD(P)H or BNA^+ (synthesised by Dr M. Basle)[186] to BNAH by [Cp*Rh(Br**L1**)Cl]Cl, [Cp*Ir(Br**L1**)Cl]Cl and corresponding ArMs was measured by change in absorbance at 340 nm,[201] using a UV-visible spectrophotometer (SHIMADZU UV-2600) in kinetics mode in quartz cuvettes with a pathlength of 1 cm. The sample rates were then corrected for background activity by measuring change in absorbance prior to addition of the catalyst. ΔA_{340} was monitored for 180 seconds for free catalysts and 900 seconds for ArMs. The Beer-Lambert law was used to calculate change in NADPH concentration with the extinction coefficient for NADPH (ε_{340} = 6220 M^{-1} cm^{-1} = 0.00622 μM^{-1} cm^{-1}).[202] These values were multiplied by rhodium catalyst Mr to obtain TOF h^{-1} values. Experiments were performed in triplicate with free catalysts and in doublet with ArMs, and the standard errors of mean TOF h^{-1} values were calculated.

Conditions were as follows: $NADP^+$ (0.15 mM); sodium formate (500 mM); rhodium catalyst (ArMs 12.5 μM, free catalyst 25 μM); sodium phosphate buffer (100 mM pH 7.0); 50 °C. The total reaction volume was 1 mL for free-catalyst assays, or 0.2 mL for ArM assays.

2.7.2 UV-Visible spectroscopy for oxidation of 2-butanol by wild-type TbADH

The $NADP^+$ dependent oxidation of 2-butanol by purified wildtype TbADH was monitored using the production of NADPH (ΔA_{340}/min) as a reporter. The equipment used and enzyme specific activity calculations (U/mg) were completed as for Section ***2.7.1***, with samples run in triplicate.

Conditions were as follows: 2-butanol (150 mM) $NADP^+$ (0.5 mM); wildtype TbADH (25 nM); Tris HCl buffer (pH 8.0, 100 mM); 40 °C. Total reaction volume 1 mL.

2.7.3 UV-Visible spectroscopy for oxidation of NAD(P)H by iridium catalysts

Oxidation of NAD(P)H to $NAD(P)^+$ by [Cp*Ir(Br**L1**)Cl]Cl and iridium-TbADH ArMs was monitored by change in absorbance at 340 nm. Socks of NAD(P)H (Apollo Scientific) and catalyst were prepared in sodium phosphate buffer (100 mM, pH 7.0). The equipment used and TOF h^{-1} calculations were completed as for Section ***2.7.1***, with samples run in triplicate.
Reaction conditions were as follows: NAD(P)H (0.15 mM); catalyst (0.15 mM); sodium phosphate buffer (100 mM, pH 7.0); room temperature; reaction volume 1 mL.

2.7.4 HPLC for reduction of imines by iridium catalysts

The reduction of 6,7-dimethoxy-1-methyltetrahydroisoquinoline (imine **1**) by [Cp*Ir(**L2**)Cl]Cl using NADH as the hydride donor was measured by normal phase HPLC. Socks of imine **1** (Enamine), NADH (Apollo Scientific) and [Cp*Ir(**L2**)Cl]Cl catalyst were prepared in sodium phosphate buffer (100 mM, pH 7.0). [Cp*Ir(**L2**)Cl]Cl was first solubilised in DMSO. Reaction conditions in airtight plastic vials were as follows: NADH (15 mM); imine **1** (15 mM); catalyst (0.3 mM); sodium phosphate buffer (100 mM, pH 7.0); room temperature; reaction volume 0.25 mL. Reactions were stopped after 21 hours by the addition of 10 M NaOH (27.5 µL), followed by extraction into ethyl acetate (400 µL). The organic extract was dried over $NaSO_4$ before analysis using a ChiralPak OD column on 1260 Infinity series HPLC (Agilent Technologies) equipped with a UV detector (5 µL injection volume; mobile phase of Hexane (0.1 % diethylamine) / isopropanol in 95 / 5 ratio; 30 °C; with flow rate of 1 mL/min). A control reaction with no catalyst was run, extracted, and analysed using the same method. A standard of the amine product (10 mM) was prepared from powder stock by dissolution in ethyl acetate and analysed using the same method.

2.7.5 Reduction of quinones by iridium catalysts

2.7.5.1 Solvent-suppressed ^1H NMR

The reduction of menadione by iridium catalysts was monitored by ^1H NMR under aqueous conditions at 298K. The water peak was suppressed using pre saturation. The solvent mixture was 90 % sodium phosphate buffer (100 mM, pH 7.2) / 10 % deuterated methanol-*d4* to enable locking onto the deuterium signal. The analysis was performed at several timepoints over 36 hours.

For preparation of reaction samples, NADH (2 mM); catalyst (1 or 0.1 mM); menadione (1 or 20 mM) were mixed in a standard NMR tube to a total volume of 1 mL and incubated at room temperature.

2.7.5.2 EPR

Electron paramagnetic resonance spectra were recorded on a Bruker EMX continuous wave X band instrument at room temperature. Samples were loaded into 1.0 mm diameter quartz tubes. Typical EPR settings were modulation frequency 100 KHz, modulation amplitude 2 G, microwave power 0.63 or 1.2 mW, 8 or 16 scans, with sweep times of 20 to 40 seconds.
For preparation of reaction samples, NADH (2 mM); catalyst (1 or 0.1 mM); menadione (1 or 20 mM) were mixed in a standard NMR tube to a total volume of 1 mL and incubated at room temperature.

2.7.6 Calculation of TOF values

Turnover frequency or TOF values for both ArM and free in solution catalysts were calculated via the following steps:

$$\Delta A\ min^{-1}/E = \Delta A\ min^{-1}\ \mu L^{-1}$$

$$\Delta A\ min^{-1}\ \mu L^{-1}\ x\ [E] = \Delta A\ min^{-1}\ mg^{-1}$$

$$\Delta A\ min^{-1}\ mg^{-1}/\ \varepsilon = \Delta c\ \mu M/min/mg$$

$$(\Delta c\ \mu M/min/mg/1000)\ x\ V = \Delta c\ \mu mol/min/mg = U/mg$$

$$U/mg\ x\ Mr = TOF$$

Where:

E = amount of enzyme stock added to assay (μL)

$[E]$ = enzyme stock concentration ($mg\ \mu L^{-1}$)

ε = extinction coefficient ($\mu M^{-1}\ cm^{-1}$)

V = reaction volume (mL)

Mr = mass of catalyst or mass of enzyme catalytic subunit

2.7.7 Michaelis-Menten characterisation of rhodium-TbADH ArMs

By measuring reaction rate at different substrate concentrations, the Michaelis-Menten equation can be used to obtain important information about the kinetics of a biochemical reaction. In particular, while the Michaelis constant K_M is usually defined as the concentration of substrate required to achieve half of the maximal rate at saturating substrate concentration (V_{max}), it can also be used to estimate enzyme-substrate affinity.[203] When combined with computational and structural methodologies, these kinetic insights can serve as a useful tool for investigating enzyme-substrate or ArM-substrate binding.

The standard Michaelis-Menten equation from which kinetic parameter values can be extracted assumes the following basic enzyme catalysed reaction model:[106]

$$E + S \underset{k_{-1}}{\overset{k_1}{\rightleftharpoons}} ES \xrightarrow{k_2} E + P$$

Where:
E = enzyme
S = substrate
ES = enzyme-substrate complex or Michaelis complex
P = product
k = rate constants of the enzyme-substrate association, dissociation, and forward reaction

Following the initial transient phase of the reaction involving mixing of the enzyme and substrate, it is assumed that the concentration of the ES remains approximately constant for the duration of the reaction. This is the so-called steady state assumption, and was considered valid in the case of the system investigated in this thesis, in which an artificial metalloenzyme (E) was mixed with substrate (S).
Under the steady state assumption, the following kinetic parameter values are derived:

$$K_M = \frac{k_{-1} + k_2}{k_1}$$

$$V_{max} = k_2[E]_T$$

Where:
K_M = Michaelis constant

V_{max} = maximal velocity of reaction

$[E]_T$ = total enzyme concentration

Using non-linear regression, these parameters can be extracted from the Michaelis-Menten equation which describes the rectangular hyperbola obtained when initial rate values v_0 are measured at a series of substrate concentrations [S], and plotted against [S]:

$$v_0 = \frac{V_{max}[S]}{K_M + [S]}$$

Where:

v_0 = initial rate of reaction

$[S]$ = substrate concentration

By mathematical rearrangement, K_M can also be expressed as:

$$K_M = \frac{k_{-1}}{k_1} + \frac{k_2}{k_1}$$

Meanwhile, the dissociation constant K_S which describes enzyme-substrate affinity is calculated as:

$$K_S = \frac{k_{-1}}{k_1}$$

Where:

K_S = dissociation constant of the Michaelis complex

Therefore, assuming that the value of k_2/k_1 is small compared with k_{-1}/k_1, K_M is an estimate of substrate affinity. In other words, K_M is effectively equal to K_S, owing to negligible k_2.[106]

The conditions and method used for Michaelis-Menten assays were as described in Section ***2.7.1*** for measuring ArM TOF h^{-1} values. The nicotinamide substrates $NAD(P)^+$ were added to final concentrations of 0.05, 0.1, 0.15, 0.42, 1.2 and 2.0 mM. The BNA^+ mimic was added to final concentrations of 0.15, 0.42, 1.2, 2.0 and 4.0 mM. Values of K_M and TOF_{max} were calculated by non-linear regression in Prism 9 (GraphPad) using the Michaelis-Menten model under *Enzyme kinetics – Velocity as a function of*

substrate, with default parameters. Adjusted R squared values were calculated under the diagnostics tab.

2.8 Crystallographic methods

Protein X-ray crystallography can provide atomic resolution structural information about the detailed nature of interactions with small molecule cofactors and substrates. From research groups across the ArM field, there have been many highly successful examples of high-resolution crystal structures, some of which are discussed in Section ***1.3.3***. In the case of our system, the there are several crystal structures of various TbADH variants already available within the literature, providing a good starting point for solving the first high-resolution structure of an ArM based on this scaffold.

2.8.1 Crystallisation

Crystal trials of all protein and ArM variants were completed using the sitting drop vapour diffusion, via pipetting of the protein and commercial screening buffer solutions into 96 well MRC crystallisation trays (SWISSCI, Molecular Dimensions). 75 µL aliquots of screening buffers were pipetted into each buffer well using a multi-channel pipette from three commercial screens (Molecular Dimensions): JCSG-plus HT-96 (MD1-40-ECO); PACT premier HT-96 (MD1-36-ECO); Structure Screen 1+2 HT-96 (MD1-30). Protein samples were first exchanged into 25 mM Tris HCl, 150 mM NaCl, pH 7.5 using a PD-10 desalting column (GE Healthcare), concentrated using 10000 MWCO Viva-Spin 6 columns (Sartorius), and diluted to 5 or 10 mg/ml following Bradford assay. 0.4 µL drops of both screening buffer and protein were pipetted into the trays next to the buffer wells using a Mosquito liquid handling robot (TTP Labtech), and sealed for incubation at 20 °C.

For screening optimisation of ArM variant $[Cp^*Ir(5M\text{-}C37\mathbf{L1})Cl]^{2+}$ (Appendix **2)**, 1 uL drops of both screening buffer and protein were pipetted into 24 well crystallisation trays (Hampton Research) next to 400 uL of optimised JCSG-plus Eco Screen buffer conditions B4 and B5, prior to sealing and incubation at 20 °C.

Crystal drops were examined at regular intervals using a light microscope (Nikon). After 5-10 days, crystals were selected for cryoprotection using 100 % glycerol or ethylene glycol, and snap freezing in liquid nitrogen for transport to Diamond Light Source synchrotron.

2.8.2 X-ray data collection and processing

All X-ray diffraction data from Diamond Light Source was collected either remotely by Dr Ingrid Dreveny on beamline i03 or using automated collection on beamline i04 at 100 K. The automated data reduction suite Xia2 with either dials or 3dii was used to determine the space group, unit cell dimensions and resolution limit, as well as for indexing, integrating, and scaling of reflections. MTZ files were downloaded from the ISPyB server for structure determination.

2.8.3 Structure determination

The structures of all protein and ArM variants were solved by molecular replacement using Phaser-MR (full-featured)[204] within the Phenix[205] software suite, following Matthews Cell Content Analysis in the CCP4 suite.[206] The structure of holo-wildtype TbADH (PDB: 1YKF) was used as the input ensemble following removal of water $NADP^+$ and zinc, and mutation of residues to 5M-C37 (Table **2.1**). Phenix AutoBuild[207] and stepped-refine in Coot[208] were used for initial modelling. Multiple rounds of refinement using Refmac5[209] in the CCP4i2 suite,[210] and manual model building using real space refine and other features in Coot, were used to improve R_{work}/R_{free} values. The $NADP^+$ ligand was imported to Coot from the standard CIF dictionary. Phenix eLBOW[211] was used to generate a CIF file of the iridium complex ligand[205] which had prepared previously in Schrodinger Maestro and converted to PDB format. Phenix ReadySet was used to prepare the ligand and protein model for further refinement in CCP4i2 Refmac5. MolProbity was used to validate models from refinement. Create a map from map coefficients in Phenix was used convert omit maps into CCP4 format for figure generation using Schrodinger Maestro.

3 Characterisation of rhodium-TbADH artificial metalloenzymes for nicotinamide reduction

3.1 Introduction

In our original ArM cascade system[29] (pioneered by Dr S. Morra) the metal catalyst was anchored (Figure **3.1**) at residue location 37, towards the interior of the TbADH substrate binding pocket (Section ***1.3.5***). Further developments of this ArM by Dr M. Basle explored alternative catalyst binding sites, reduction of a nicotinamide mimic cofactors or substrates (terms used interchangeably) and use of different ligands within the metal complex (Figure **3.2**). The objectives were to improve both bioconjugation efficiency and nicotinamide reduction performance, as well as to explore ArM nicotinamide substrate scope.[186] Based on a computational screening procedure, it was reasoned that repositioning of the catalyst to more solvent exposed locations might allow better access of nicotinamide cofactors to the catalyst. Of the ArM variants assembled using catalyst [Cp*Rh(Br**L1**)Cl]Cl (Figure **3.3a**), similar rates of $NAD(P)^+$ reduction activity were observed regardless of catalyst anchoring position. However, [Cp*Rh(7M-C243**L1**)Cl]$^{2+}$, with the catalyst covalently bound at cysteine 243 was identified as the most promising variant with regards to bioconjugation efficiency. ESI-MS results indicate a single species, and only a small proportion of 7M-C243 protein left unmodified by [Cp*Rh(Br**L1**)Cl]Cl in solution (Figure **3.3b**). This may be at least partially explained by the greater reactivity of the acyl bromide group of ligand Br**L1** in comparison to alkyl bromide group of the other ligands used for TbADH modification via nucleophilic substitution (Figures **3.1-2**). Furthermore, [Cp*Rh(7M-C243**L1**)Cl]$^{2+}$ was the only ArM variant which displayed activity on the nicotinamide mimic 1-benzylnicitnaimde (BNA^+).[186]

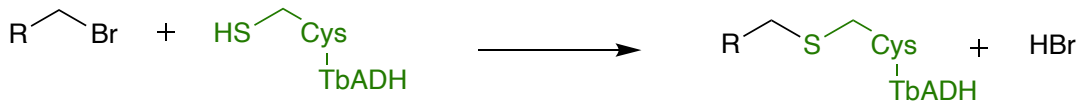

Figure 3.1: General rection scheme for TbADH covalent ArM assembly

Nucleophilic substitution occurs between a cysteine thiol group of TbADH and the alkyl bromide or acyl bromide group of the complex ligand (R = transition metal piano-stool complex shown in Figures **3.2-3**).

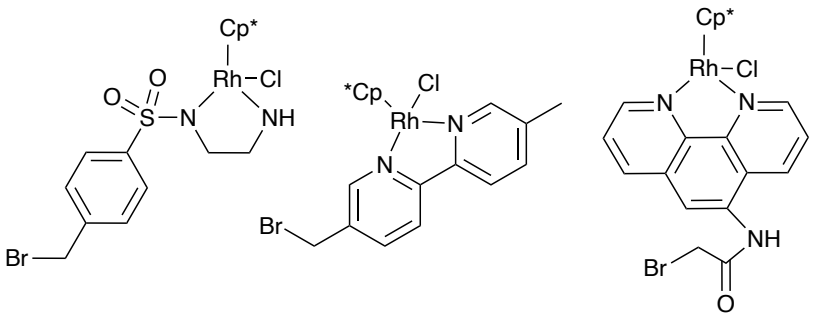

Figure 3.2: Cp*Rh catalysts used in previous work by the Pordea group
Catalysts were incorporated into TbADH for nicotinamide reduction.[29]

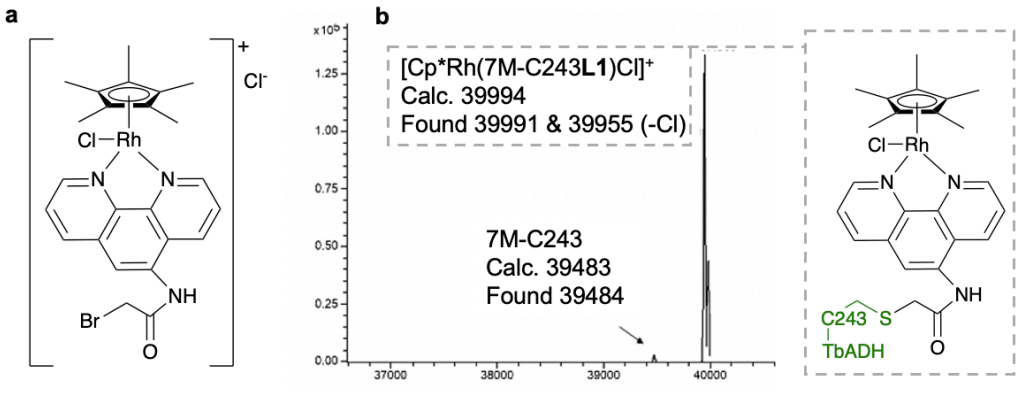

Figure 3.3: ArM variant [Cp*Rh(7M-C243L1)Cl]$^{2+}$
a) Catalyst [Cp*Rh(Br**L1**)Cl]Cl **b**) ESI-TOF MS charge deconvoluted spectrum of ArM variant [Cp*Rh(7M-C243**L1**)Cl]$^{2+}$ acquired by Dr M. Basle. Adapted from[212]

The present work further develops the investigation of alternative rhodium-TbADH ArM catalyst binding sites, and the nicotinamide substrate scope of these genetic variants. In line with the overall aim of this project, the angle of focus for addressing objectives 1a and 1b (Section **1.4**) is to better understand protein scaffold, catalyst, and substrate interactions in ArM catalysis. Specifically, how different nicotinamide cofactors bind to different genetic variants. Therefore, full kinetic characterisation via variation of nicotinamide substrate concentration was performed on ArM variants to obtain estimate affinity values for each combination. These experiments included the natural cofactors NAD(P)$^+$ and the mimic BNA$^+$. The ArM variants were also subject to docking analysis with NADP$^+$ and BNA$^+$.

Encouraged by promising bioconjugation and kinetics results shown previously for [Cp*Rh(7M-C243**L1**)Cl]$^{2+}$ (Figure **3.3**),[186] this variant was selected for initial docking and kinetics studies to elucidate the binding behaviour of different nicotinamide substrates. Based on these results, two other variants with the catalysts covalently conjugated to TbADH residue locations 37 and 110 were selected and subjected to the same docking and experimental analyses. The former was studied previously by the Pordea group[29, 186] but not yet subject to full kinetic characterisation. The rationale behind the selection of these variants is explained in Section ***3.3.1***. It was hypothesised that these changes may improve ArM nicotinamide reduction efficiency via increased affinity for these substrates. Furthermore, docking and kinetics studies would provide valuable information regarding the interactions between ArM scaffold and substrate components.

3.2 Kinetics and docking studies using rhodium-TbADH ArM modified at residue location 243

Focusing on the objective of better understanding nicotinamide substrate scope and binding to TbADH-based ArMs a suitable variant was selected. [Cp*Rh(7M-C243**L1**)Cl]$^{2+}$ was shown previously to be the most promising with regards to bioconjugation efficiency, and reduction activity on BNA^{+} in addition to the natural NAD(P)$^{+}$ cofactors.[186] This ArM was reproduced and characterised for subsequent kinetics studies with different nicotinamide substrates.

*3.2.1 Assembly and analysis of ArM variant [Cp*Rh(7M-C243L1)Cl]$^{2+}$*

3.2.1.1 Preparation of protein and catalyst ArM components

TbADH mutant 7M-C243 (Table **2.1**) was prepared according to a previously optimised two-step purification procedure.[29] 7M-C243 contains a single cysteine residue for covalent bioconjugation with the bromoacetamide-bearing Br**L1** (Figure **3.5**). The plasmid containing the mutated TbADH gene was previously prepared by Dr Basle and was available in our laboratory.[186, 212] Following overexpression in *E. coli* and cell disruption by sonication, a heat treatment step was used to separate TbADH from the bulk of cellular proteins. Affinity column chromatography was then used to for purification. The A280 nm absorbance elution profile obtained from FPLC and qualitative determination of protein presence according to Bradford reagent were used in the selection of elution fractions. SDS-PAGE was used to monitor each stage of the purification procedure (Figure **3.4**). Intense bands with a molecular weight of around 40 kDa were observed in the pellet, load and elution fractions indicating successful overexpression and purification of 7M-243 TbADH, with a purified protein yield of approximately 33 mg/L of reaction medium. The pooled elution fractions were considered of sufficient purity for subsequent experiments.

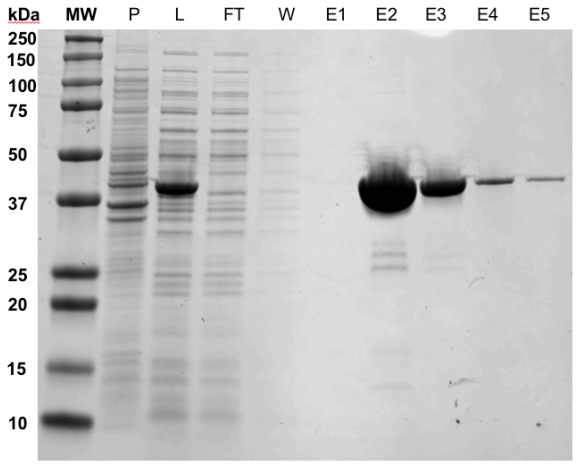

Figure 3.4: SDS-PAGE analysis of 7M-C243 TbADH purification by affinity chromatography
Bands corresponding to strep-tagged TbADH are prominent in elution fractions 2 to 5 which were pooled and concentrated for subsequent analysis. Lanes were loaded with the following samples: MW = molecular weight ladder; P = cell lysate; L = soluble constituents loaded onto the affinity column (following heat treatment step); FT = affinity column flow-through fraction; W = Wash of the column with non-elution buffer; E1-5 = FPLC elution fractions.

Ligand Br**L1** was synthesised according to the same procedures used in previous studies[29, 47] (Figure **3.5**). Bromoacetyl bromide reacted immediately with phenanthroline-5-amine without the addition of any co-solvents. ^{1}H NMR and positive ESI-MS analyses confirmed successful production of Br**L1**, bearing a reactive bromoacetamide group at the 5-position of the phenanthroline ring. The presence of chloroform indicated by the former after extensive drying was considered negligible and the purity of the final compound was calculated by ^{1}H NMR and factored into solution calculations (Appendix **4**). The sample was considered of high enough purity for subsequent formation of the rhodium catalyst.

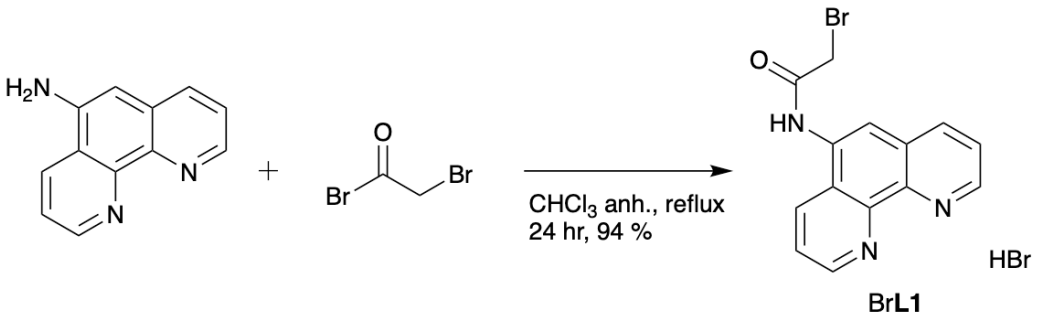

Figure 3.5: Synthesis of 2-bromo-N-(1,10-phenanthrolin-5-yl)acetamide hydrobromide

The rhodium catalyst [Cp*Rh(Br**L1**)Cl]Cl was prepared by metalation of ligand Br**L1** (Figure **3.6**) according to the procedure used in previous studies.[29, 186] The addition of triethyl amine to a suspension of the two starting materials deprotonates the nitrogen atoms of ligand Br**L1**, making them available for reaction with the $[Cp^*RhCl_2]_2$ dimer. The product was precipitated by addition of cold diethyl ether. This was followed by the removal of unreacted triethyl amine and other solvents by filtration and drying. Product presence was confirmed by ^1H NMR and positive ESI-MS (Appendix **5**). Minor contamination from triethyl amine salts and dichloromethane which could not be removed by drying were used to calculate product purity which was factored into solution calculations. The sample was considered of high enough purity for subsequent experiments.

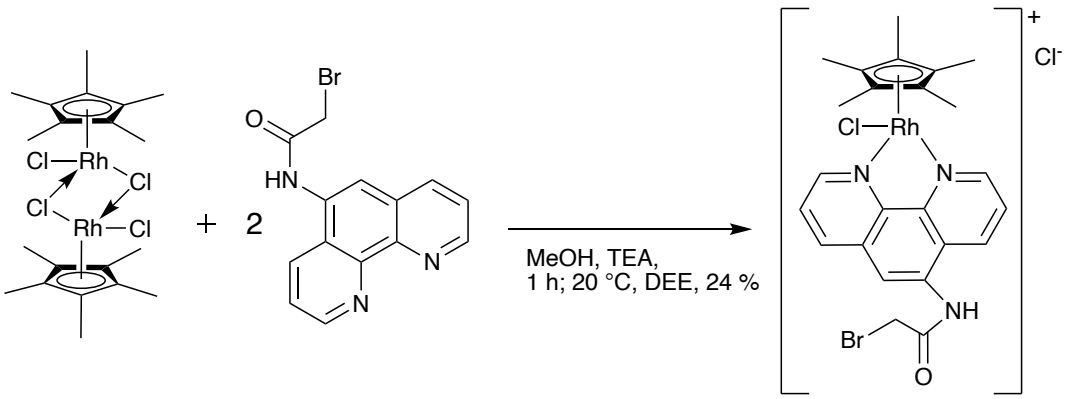

Figure 3.6: Preparation of Cp*Rh(2-bromo-N-(1,10-phenanthrolin-5-yl)acetamide)chloride

3.2.1.2 Assembly, Ellman's assay and ICP-MS analysis

Following confirmation of [Cp*Rh(Br**L1**)Cl]Cl catalytic activity (Section ***3.2.2***), ArM assembly was performed by covalent conjugation of the brominated catalyst to the cysteine residue of 7M-C243 TbADH based on procedures established previously by Dr S. Morra.[29] The proportion of free thiol groups in the 7M-C243 TbADH sample available for bioconjugation to [Cp*Rh(Br**L1**)Cl]Cl was estimated via Ellman's assay. The free thiol availability was calculated to be 57 %, based on Bradford assay estimated protein concentration (Figure **3.7**). This is similar to the 51 % availability reported by Dr M. Basle for this mutant.[186]

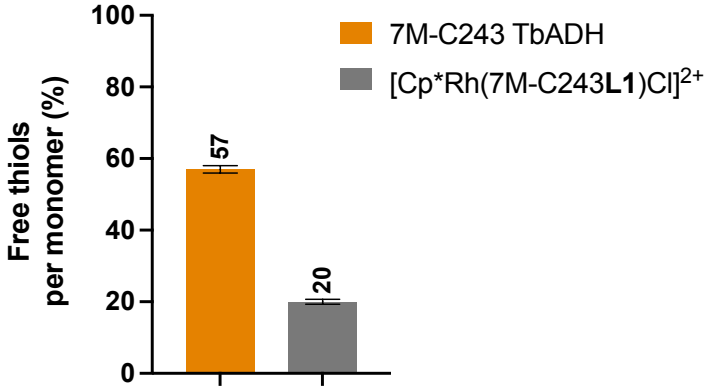

Figure 3.7: Free thiol availability of [Cp*Rh(7M-C243L1)Cl]$^{2+}$

Ellman's assay to determine the availability of free thiols in the 7M-C243 sample before (orange) and after (grey) bioconjugation with catalyst [Cp*Rh(Br**L1**)Cl]Cl.

Covalent bioconjugation was completed by incubation of 7M-C243 with four molar equivalents of the [Cp*Rh(Br**L1**)Cl]Cl catalyst. Preliminary experiments to assess the suitability of bioconjugation conditions utilising [Cp*Rh(Br**L1**)Cl]Cl and the 5M-C37 TbADH mutant (Table **2.1**) had shown a significant proportion of unmodified protein remaining after the procedure. Therefore, small alterations from the original TbADH bioconjugation protocol[29] were made, with the aim of increasing desirable interactions between ArM components. Incubation temperature was increased from ambient to 30 °C with frequent sample inversion. These conditions were considered a compromise, as higher temperatures or continuous shaking may have increased undesirable non-specific coordination of rhodium to non-cysteine residues.[213, 214] Following incubation, the excess catalyst was removed via size exclusion chromatography.

Comparison between an Ellman's assay of the assembled [Cp*Rh(7M-C243**L1**)Cl]$^{2+}$ ArM with that of the unmodified 7M-C243 mutant indicated a 74 % reduction in the available free thiol groups. Therefore, by this measure in combination with Bradford assay-estimated protein concentration, 42 % of the total protein molecules in solution were successfully modified with rhodium catalyst (Figure **3.7**). In contrast, the rhodium content of the sample based on ICP-MS analysis was calculated to be 76 %, suggesting that this percentage of total protein was modified. These data from both Ellman's and ICP-MS are broadly consistent with previous samples of [Cp*Rh(7M-C243**L1**)Cl]$^{2+}$.[186] The discrepancy between these two analyses with regards to the percentage of total cysteines modified may be explained by a combination of Ellman's assay duration, and partial accessibility of the DTNB reagent to thiol groups. These two factors are interlinked, as the reagent takes longer to reach and interact with cysteines which are buried within protein pockets, in comparison to surface cysteines.

This hypothesis is supported by literature on measuring cysteine accessibility using DTNB, describing partially accessible cysteines as showing a slow creep in A412 nm absorbance increase over time.[215] Accordingly, basic tests were completed here, to determine whether increasing Ellman's assay duration both before and after the bioconjugation procedure increased A412 nm absorbance. No visual increase in peak-height was apparent by leaving the assay at room-temperature for an extra 40 minutes (1-hour total assay duration). Unfortunately, further quantitative measurements and increases to assay duration or temperature were not completed to investigate this issue further. Overall, the percentage rhodium content according to ICP-MS was considered the most accurate determinant of bioconjugation completeness. This value was used to determine the concentration of catalytically active ArM in solution in all subsequent kinetic analyses in this thesis. The possible effects of the presence of unmodified TbADH in ArM samples on kinetic assays is discussed at the end of Section ***3.2.2***.

3.2.1.3 Assessment of ArM catalyst shielding functionality

TbADH-based ArMs have been shown to protect the metal catalyst from inactivation by a cascade partner enzyme and vice versa, increasing overall cascade efficiency (Section ***1.3.5***).[29, 133] To assess the functionality of [Cp*Rh(7M-C243**L1**)Cl]$^{2+}$ in the context of this shielding effect, a stability test was performed. Wildtype TbADH was incubated with the ArM at 50 °C for 24 hours. The butan-2-ol oxidation activity of TbADH was measured following this incubation and determined to be 70 % relative to the no ArM control sample (Figure **3.8**). In previous work by Dr S. Morra,[29] activity was determined to be 20 % after incubation with the free catalyst [Cp*Rh(Br**L1**)Cl]Cl, whilst 80 % activity remained after incubation with ArM variant [Cp*Rh(5M-C37**L1**)Cl]$^{2+}$ under the same conditions. Taken together, these results indicate that by incorporation of the metal complex, ArM [Cp*Rh(7M-C243**L1**)Cl]$^{2+}$ offers protection of wildtype TbADH against metal catalyst-induced inactivation (discussed in Section *1.2.5.2*), albeit to a slightly lesser extent than that displayed by [Cp*Rh(5M-C37**L1**)Cl]$^{2+}$. This may be explained by the catalyst being conjugated to a more solvent exposed location than in the latter variant. However, the minor percentage difference suggests that the catalyst binding site does not have a significant impact on the shielding functionality of TbADH-based ArMs. The [Cp*Rh(7M-C243**L1**)Cl]$^{2+}$ sample was taken forward for characterisation of nicotinamide reduction activity.

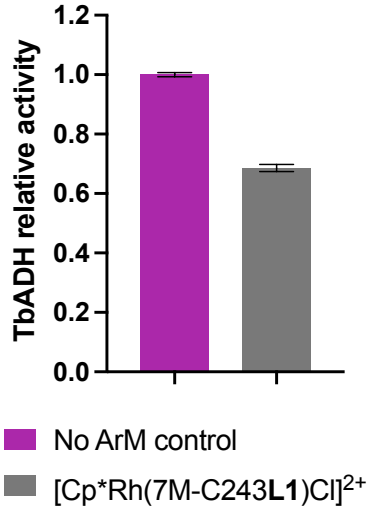

Figure 3.8: Effect of the presence of ArM variant [Cp*Rh(7M-C243L1)Cl]$^{2+}$ on wildtype TbADH butanol-2-ol oxidation activity

Wildtype TbADH (1 μM) was incubated with (grey) and without (purple) the ArM (5 μM) at 50 °C for 24 hours in sodium phosphate buffer (100 mM, pH 7.0). Subsequent butan-2-ol oxidation activity was measured by mixing this substrate (150 mM) with $NADP^+$ (0.5 mM) and the incubated wildtype TbADH sample (25 nM). The rate of oxidation in the presence of ArM variant [Cp*Rh(7M-C243**L1**)Cl]$^{2+}$ is shown relative to that in the no ArM control (29.04 ± 0.19 U/mg). Error bars show the standard error of mean (n = 3).

*3.2.2 Kinetics of nicotinamide reduction by ArM variant [Cp*Rh(7M-C243L1)Cl]$^{2+}$*

To confirm suitability for use in ArM assembly, and to provide a benchmark for the measurement of ArM catalytic activity, $NADP^+$ reduction activity of the [Cp*Rh(Br**L1**)Cl]Cl catalyst was measured (Table **3.1**). Formate serves as the hydride donor (electron source) for the reduction of $NADP^+$ to NADPH. The UV-visible spectrum of the NADPH product allows reaction rate to be monitored via increasing absorbance at 340 nm.[202]

Table 3.1: Reduction of nicotinamides by [Cp*Rh(BrL1)Cl]Cl

Nicotinamide substrate	TOF (h^{-1})
$NADP^+$	255 ± 7.2
NAD^+	250.3 ± 4.5
BNA^+	59.0 ± 1.9

Sodium formate (500 mM) sodium phosphate buffer (100 mM, pH 7.0) was equilibrated to 50 °C in a quartz cuvette. The nicotinamide substrate was added (0.42 mM) followed by referencing of the instrument to zero absorbance, and measurement of baseline absorbance change. The catalyst [Cp*Rh(Br**L1**)Cl]Cl (25 μM) was then added, and the reaction was monitored at 340 nm for 120 seconds. The standard errors of mean are shown (n = 3). The extinction coefficients were 6220 M^{-1} cm^{-1} and 4800 M^{-1} cm^{-1} for $NAD(P)^+$ and BNA^+ respectively at 340 nm. The method used for TOF value calculation throughout this thesis is described in Section ***2.7.6***.

Focusing on the objective of investigating rhodium-TbADH ArM substrate scope, and towards the wider aim of understanding ArM component interactions, kinetic characterisation of [Cp*Rh(7M-C243**L1**)Cl]$^{2+}$ was completed with three different nicotinamide substrates. The Michaelis-Menten characterisation enabled estimation of ArM affinity for $NAD(P)^+$ and BNA^+ via the Michaelis constant K_M. It should be noted that using K_M as an estimate of affinity requires the assumption described in Section ***2.7.7***. While there are other methods of affinity measurement such as determination of K_d,[135] the selected method avoids the requirements for pre-steady state kinetics and stopped-flow equipment, as discussed in Chapter **5**.

The conditions for monitoring nicotinamide reduction were identical to those used for the corresponding free catalyst. As observed with variant [Cp*Rh(5M-C37**L1**)Cl]$^{2+}$ in previous work by the group,[29] rates were lower in comparison to the free catalyst owing to reduced accessibility of substrates to the TbADH conjugation site of the catalyst. It

was found that mirroring the free catalyst, the ArM displayed similar rates of reduction activity on the natural cofactors $NADP^+$ and NAD^+, and lower activity on BNA^+ (Table **3.2**).

Table 3.2: Reduction of nicotinamides by $[Cp^*Rh(7M\text{-}C243L1)Cl]^{2+}$

Nicotinamide substrate	TOF (h^{-1})
$NADP^+$	70.2 ± 1.9
NAD^+	71.1 ± 0.2
BNA^+	27.0 ± 4.3

The procedure was performed as described for the free catalyst (Table **3.1**). ArM variant $[Cp^*Rh(7M\text{-}C243\mathbf{L1})Cl]^{2+}$ (12.5 μM) was mixed with nicotinamide substrate (0.42 mM) in sodium formate (500 mM) sodium phosphate buffer (100 mM, pH 7.0), 50 °C. The reaction was monitored at 340 nm for 900 seconds. The standard errors of mean are shown (n = 3). The extinction coefficients were 6220 M^{-1} cm^{-1} and 4800 M^{-1} cm^{-1} for $NAD(P)^+$ and BNA^+ respectively at 340 nm.

Probing further into ArM kinetic characteristics, $NAD(P)^+$ and BNA^+ were tested at a range of concentrations at saturating formate concentration.[201] It is important to note that the formate hydride donor was added in considerable excess in all experiments, enabling analysis of $NAD(P)^+$ and BNA^+ kinetics independent of formate concentration. While this justified the use of the simple Michaelis-Menten model described in Section ***2.7.7***, a two-substrate model may have been more suitable, as discussed in Chapter **5**.

We observed enzyme-like Michaelis-Menten behaviour in the reduction of both the natural cofactors (Figure **3.9a**,**b**) The value of K_M^{NADP+} calculated by non-linear regression in GraphPad Prism was 52 μM (Figure **3.9d**) which was 7.5-fold higher than the reported K_M^{NADP+} value (7 μM) of wildtype TbADH.[216] Adjusted R^2 values are reported in Appendix **1**. It should be noted that the wildtype TbADH K_M^{NADP+} value is derived from measurement of zinc-dependent hydride transfer between the nicotinamide and an alcoholate species (Section *1.2.3.1*), while the value for the ArM is derived from hydride transfer from the rhodium catalyst to the nicotinamide. Therefore, the direct comparison of these K_M values assumes similarity between these enzyme-substrate combinations. The apparent lower affinity of $NADP^+$ for TbADH after covalent modification of residue location 243 indicates potential blockage of the natural nicotinamide binding pocket by the metal complex, and a possible alternative binding site.

$[Cp^*Rh(7M\text{-}C243\mathbf{L1})Cl]^{2+}$ was also found to reduce BNA^+. Interestingly, in contrast to the natural cofactors, the shape of the rate Vs [S] curve for the BNA^+ substrate (Figure

3.9c) was different to that for the NAD(P)$^+$. While still fitting the Michaelis-Menten kinetic model, the precision and accuracy of K_M^{BNA+} calculation was lower than for the natural nicotinamide substrates. The SEM values were higher, and adjusted R^2 values lower (Appendix **1**). This suggests a less specific binding site for this mimic. To gain further insight into these kinetic observations, docking studies were performed (Section ***3.2.3***).

Concerning the presence of unmodified protein identified by the above analyses, the question of whether and how this might impact on the kinetic parameter values obtained from subsequent ArM nicotinamide reduction assays was considered. Under the assumption that the unmodified protein is catalytically inactive for nicotinamide reduction, its presence would have no effect on the Michaelis constant K_M (defined in Section ***2.7.7***), as the same concentration of substrate would be required to achieve half of the maximal rate. The value of V_{max} would also remain unaffected, as the amount of catalytically active ArM (catalyst-modified TbADH) in solution would not have changed. V_{max} remaining unaffected would rely on the assumption that unmodified protein was not factored into the calculation of ArM concentration for the purposes of kinetic assays. This was the main reasoning behind using ICP-MS derived rhodium content of samples as a measure of ArM concentration.

The question of whether NAD(P)$^+$ occupancy of the unmodified TbADH nicotinamide pocket would have an effect on kinetic parameter values was also considered. This phenomenon would cause the concentration of nicotinamide substrate in solution to be lower than intended for the respective assay, with some of it occupying unmodified protein rather than ArM active site pockets. This could have reduced the accuracy of individual rate values measured. However, assuming that approximately the same amount of unmodified protein was present in each assay completed, this effect would be proportional between assays of varying substrate concentration, making it unlikely to have a significant impact on K_M. Regarding V_{max}, the effect would also be minimal, assuming that the highest substrate concentration tested was far enough in excess of the saturating substrate concentration; in other words, were all ArM active sites already occupied at lower concentrations of substrate. Therefore, the effect of marginally reducing the substrate concentration would not significantly alter the measured V_{max} value.

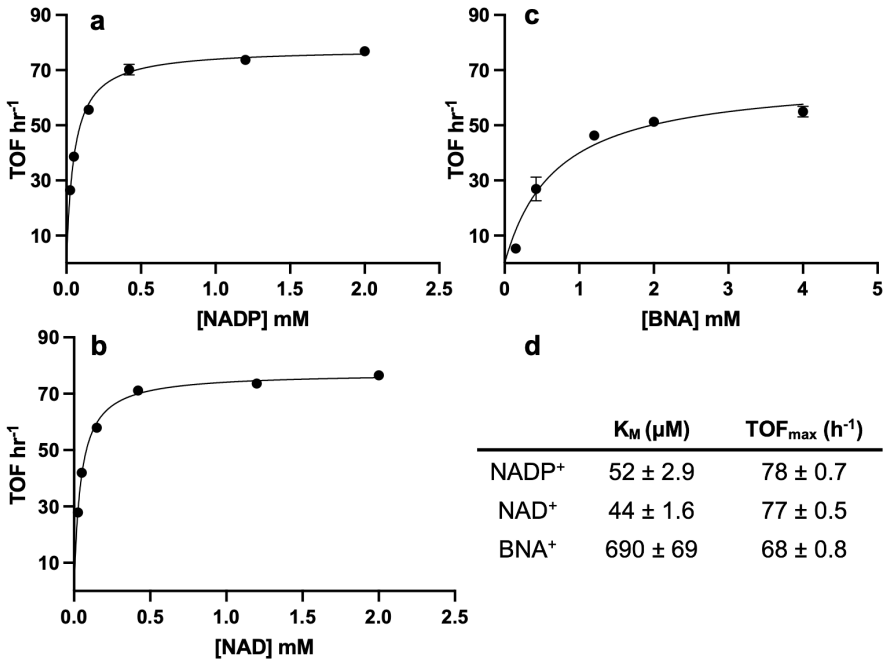

Figure 3.9: Kinetic characterisation of [Cp*Rh(7M-C243L1)Cl]$^{2+}$ nicotinamide reduction
A range of **a**) NADP$^+$, **b**) NAD$^+$ and **c**) BNA$^+$ concentrations were tested under the conditions described in Table **3.2**. Error bars show the standard error of mean (n = 2). **d**) Kinetic parameter values for reduction of the natural NAD(P)$^+$ cofactors were calculated using non-linear regression in GraphPad Prism 9.0.

*3.2.3 Docking studies on ArM variant [Cp*Rh(7M-C243L1)Cl]$^{2+}$*

Seeking to better explain experimentally observed differences in the kinetic behaviour of [Cp*Rh(7M-C243**L1**)Cl]$^{2+}$ in the reduction of different nicotinamide cofactors, computational docking using Schrodinger Glide[217] in Maestro was performed. Preliminary work involved covalent docking of the metal-free bidentate phenanthroline ligand to various single-cysteine TbADH mutants (including 5M-C37 and 7M-C243) which were subject to protein preparation in Maestro. In each case, the single reactive cysteine residue was used to define the centre of the covalent docking grid. A suitable receptor grid for docking of NADP$^+$ was then selected according to residues of the natural nicotinamide binding pocket. This was followed by supramolecular docking of NADP$^+$ to the resulting modified mutants. For both covalent and supramolecular docking steps, the ligands were docked flexibly while the receptor was kept rigid. This work gave insight into the interactions of both the phenanthroline ligand and NADPH with these mutants, prompting the development of this docking methodology to include the metal portion of the catalyst as applied here.

Docking experiments for the present subsection were performed in collaboration with Dr F. L. Martins who executed the initial docking. Experimental design and data

analysis was completed by the author. Metal complex [Cp*Rh(Br**L1**)Cl]Cl was covalently docked to the 7M-243C TbADH mutant, followed by supramolecular docking of $NADP^+$ and the BNA^+ mimic to the resulting ArM $[Cp^*Rh(7M\text{-}C243\mathbf{L1})Cl]^{2+}$. $NADP^+$ was selected for this study as the cofactor with the highest affinity for the unmodified wildtype TbADH nicotinamide binding pocket, to probe the kinetic differences to BNA^+ identified in the previous section.

The lack of direct validation of the molecular modelling algorithms and methodologies used in the present section and Section ***3.3.1*** should be noted. Experimentally derived X-ray crystallographic or cryo-EM structures of the ArM species examined were not available for comparison with docking poses. This must be taken into account in assessing the level of confidence with which conclusions can be drawn. However, the docking results serve to tentatively indicate possible locations and positions of the catalyst and nicotinamides within the ArM variants.

The results from covalent docking suggested that the C243-bound metal complex is oriented towards the protein surface and potentially blocking the entrance to the nicotinamide binding pocket. Indeed, subsequent supramolecular docking of $NADP^+$ suggests a protein surface binding site (Figure **3.10**), away from the putative position of $NADP^+$ in wildtype TbADH.[107]

The distance between the rhodium centre and the nicotinamide C4 in the $NADP^+$ docking pose with the highest-ranked (lowest energy or best) glide XP score is 5.8 Å (Figure **3.10a**). This distance is greater than the 4 Å between zinc (II) and the nicotinamide C4 of $NADP^+$ in wildtype holo-TbADH, where the metal stabilises the alcoholate species during hydride transfer to the C4 (mechanism shown in Section *1.2.3.1*). The difference in atomic radii between rhodium and zinc (II) should also be noted at 1.34 and 0.74 Å respectively,[218] as this effectively increases marginally, the difference between these distances, were the measurement to be made to the centre of the rhodium ion. However, some degree of flexibility to enable interaction for hydride transfer from the rhodium (III) to the C4 is likely in the ArM, especially considering that the $[Cp^*Rh(7M\text{-}C243\mathbf{L1})Cl]^{2+}$ receptor was kept rigid during supramolecular docking of nicotinamides. Therefore, it may be reasonable to conclude that $NADP^+$ is reduced within ArM $[Cp^*Rh(7M\text{-}C243\mathbf{L1})Cl]^{2+}$ (Figure **3.9**) at this approximate binding site.

It would be logical to assume that binding of the cofactor at this reduction site is with lower affinity than to the naturally evolved nicotinamide binding pocket. This statement is supported by: a) using tools in Maestro, fewer $NADP^+$-ArM interactions were identified in comparison to the wildtype-bound $NADP^+$ (Table **3.3**) and b) the greater value of K_M^{NADP+} displayed by this ArM, from which a lower affinity for $NADP^+$ relative

to wildtype TbADH was estimated (Figure **3.9d**). Clearly, for the purposes of $NADP^+$ reduction, it appears that the ArM would benefit from repositioning of the metal catalyst to a site where the rhodium atom could interact with the nicotinamide bound at its natural internal site.

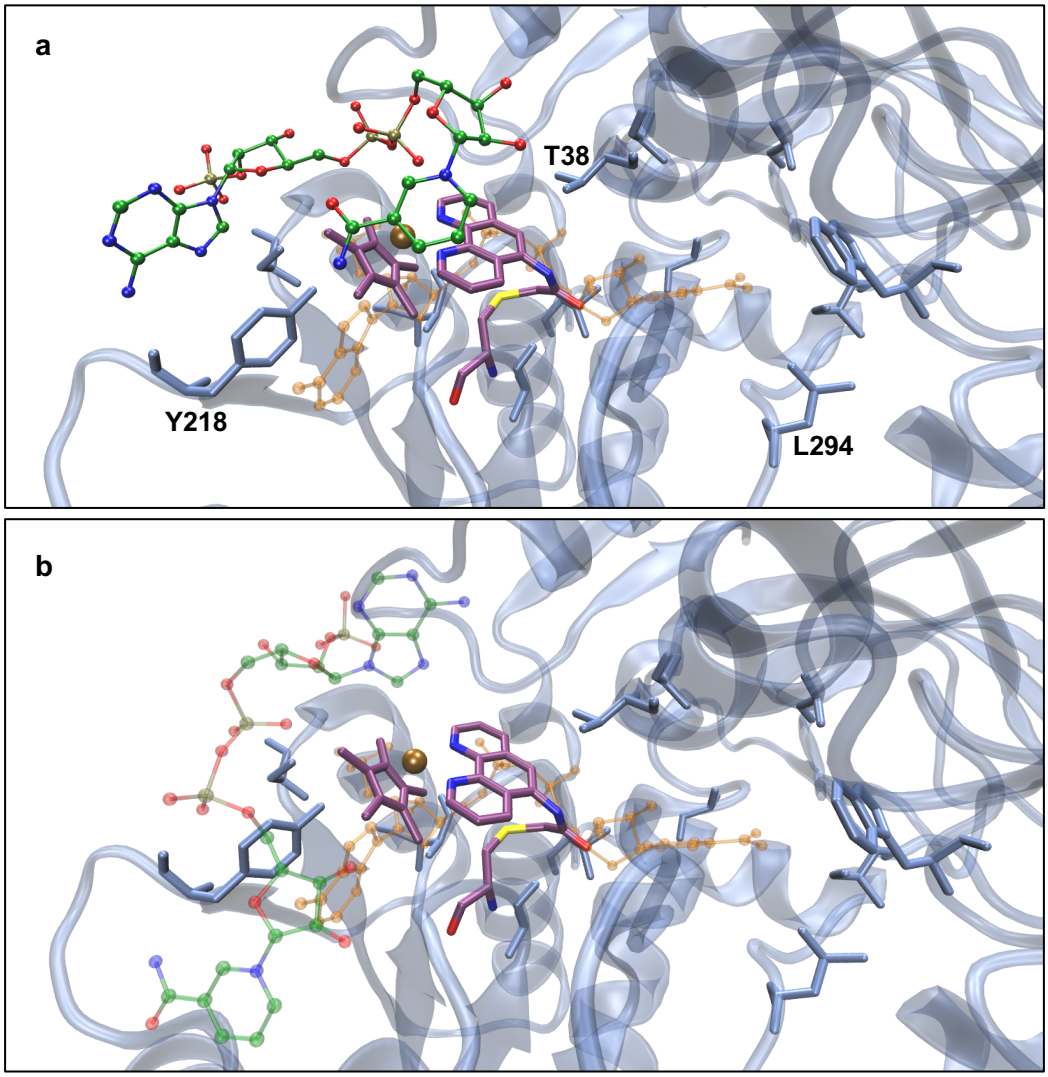

Figure 3.10 Docking of $NADP^+$ to $[Cp^*Rh(7M\text{-}C243L1)Cl]^{2+}$

Covalent docking of [Cp*Rh(Br**L1**)Cl]Cl (purple) to C243 of 7M-C243 TbADH, followed by supramolecular docking of $NADP^+$ showing the first (panel **a**) and second (panel **b**) highest-ranked poses in green by atom type. Residues of the nicotinamide and substrate binding pockets are coloured here by chain (ice blue), with Y218, T38 and L294 highlighted in **a** for reference of orientation. Overlayed in transparent orange is *in-crystallo* $NADP^+$ from wildtype TbADH (PDB: 1YKF).[107]

Table 3.3: Docking interactions, scores, and distances for [Cp*Rh(7M-C243L1)Cl]$^{2+}$

Variant	Hydrogen bonds	Salt bridges	Pi-stacking interactions	glide XP score	Distance (Å)
Wildtype-NADP$^+$	10	3	1	-11.0	-
243-NADP$^+$	4	2	0	-6.1	5.8
243-BNA$^+$	2	0	2	-5.8	8.0

The first column shows residue location in the TbADH mutant modified in covalent docking to produce the corresponding ArMs to which NADP$^+$ and BNA$^+$ were docked. Residue location 243 was modified in covalent docking to produce ArM [Cp*Rh(7M-C243**L1**)Cl]$^{2+}$ to which NADP$^+$ and BNA$^+$ were docked. Interactions were identified using Structure Analysis tools in Maestro. Distance measurements are from the bound catalyst Rh centre to the nicotinamide C4.

In contrast to NADP$^+$, the smaller BNA$^+$ mimic displayed binding both inside and outside of the natural nicotinamide pocket according to the docking results (Figure **3.11**), these poses ranking second and first highest respectively. The docking score was also better than that obtained with NADP$^+$, corroborating the apparent lower affinity observed with BNA$^+$ according to kinetic characterisation of the ArM (Figure **3.9d**). The distance between the rhodium centre and the nicotinamide C4 is 8.0 Å in the highest-ranked BNA$^+$ pose (Table **3.3**). It is possible that the mimic binds at the same site but in a different orientation which would reduce these distances, but likely at the expense of favourable interactions. As mentioned above for NADP$^+$, some degree of receptor flexibility (especially of the covalently bound catalyst) which is not accounted for by this docking procedure is expected. Therefore, it is possible that BNA$^+$ reacts at this external binding site.

While all three nicotinamide cofactors display some degree of flexibility in binding to this ArM, BNA$^+$ likely forms fewer favourable substrate-protein interactions owing to its size. This was supported by the prediction of such nicotinamide-ArM interactions in Maestro for both BNA$^+$ and NADP$^+$ (Table **3.3**). In further contrast to NADP$^+$, the direct effect of rhodium catalyst positioning on the binding and reduction of BNA$^+$ is less clear owing to the size of this cofactor. However, as suggested for NADP$^+$, the efficiency of reduction would likely be greater were the reaction to take place at an alternative site for which BNA$^+$ had a higher affinity, subject to reasonable proximity between the nicotinamide C4 and rhodium centre.

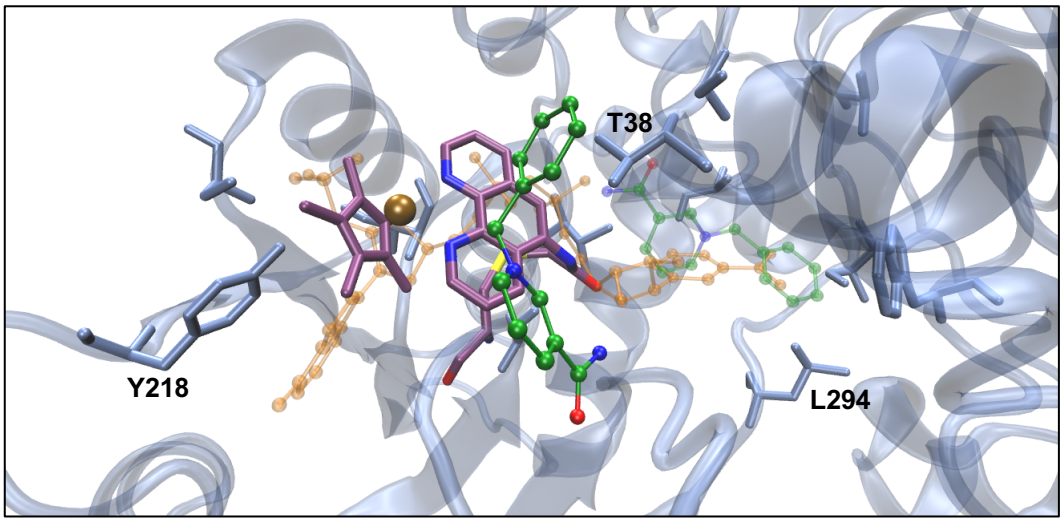

Figure 3.11: Docking of BNA$^+$ to [Cp*Rh(7M-C243L1)Cl]$^{2+}$

Covalent docking of [Cp*Rh(Br**L1**)Cl]Cl (purple) to C243 of TbADH, followed by supramolecular docking of BNA$^+$, showing the first and second highest-ranked poses in green and transparent green respectively. Overlayed in transparent orange is *in-crystallo* NADP$^+$ from wildtype TbADH (PDB: 1YKF).[107] Pocket residues are shown as for Figure **3.10**.

3.2.4 Conclusions

Based on promising results from ArM assembly analyses, [Cp*Rh(7M-C243**L1**)Cl]$^{2+}$ was selected for kinetic characterisation of nicotinamide reduction activity and docking studies. The objective was to improve understanding of ArM-nicotinamide interactions and substrate scope, towards genetic optimisation of TbADH-based ArMs. Wildtype TbADH stability tests involving incubation with [Cp*Rh(7M-C243**L1**)Cl]$^{2+}$ suggest that as reported for other variants, the ArM is effective at preventing enzyme-catalyst mutual inactivation.

It is clear that [Cp*Rh(7M-C243**L1**)Cl]$^{2+}$ can bind and reduce both the natural nicotinamide cofactors NAD(P)$^+$, and the mimic BNA$^+$. Taken together, docking and kinetics studies suggest an enzyme-substrate like interaction between the ArM and the natural nicotinamide NADP$^+$. However, binding is at external sites, away from the natural NADP$^+$ binding site within the TbADH interdomain pocket, as indicated by $K_M^{NAD(P)+}$ values, and predicted by the docking results. Based on the orientation of the residue location 243-bound catalyst in covalent dock outputs, this may be owing to obstruction of the entrance to the TbADH interdomain pocket.

Meanwhile, the smaller BNA$^+$ mimic also displays enzyme-like kinetic characteristics, but with a much lower affinity than the natural cofactors, and with binding possibly occurring both inside and outside of the nicotinamide pocket, according to docking predictions.

3.3 Kinetics and docking studies using rhodium-TbADH ArMs modified at residue locations 37 and 110

Kinetics and docking studies on the ArM variant [Cp*Rh(7M-C243**L1**)Cl]$^{2+}$ gave useful insight into the effect of nicotinamide substrate size on rhodium-TbADH ArM kinetic characteristics, and affinity for these substrates. Based on the conclusion that the efficiency of natural nicotinamide cofactor reduction would likely benefit from movement of the catalyst [Cp*Rh(Br**L1**)Cl]Cl binding site, focus was shifted to alternative genetic variants. It was envisaged that docking and kinetics studies on these variants for comparison with [Cp*Rh(7M-C243**L1**)Cl]$^{2+}$ would provide further understanding the effect of catalyst positioning on ArM performance, and in particular, on substrate affinity. This work builds upon insight towards structural and mechanistic understanding of TbADH-based ArMs.

It was reasoned that movement of the catalyst binding site further away from the entrance to the nicotinamide pocket would improve affinity for NAD(P)$^+$ substrates. An example of such an ArM variant already tested for the purposes of nicotinamide recycling in chiral alcohol production cascades is [Cp*Rh(5M-C37**L1**)Cl]$^{2+}$. TbADH mutant 5M-C37 serves as the scaffold (Table **2.1**). This variant was shown previously to work in concert with wildtype TbADH for a chiral alcohol production cascade,[29] but docking studies and full kinetic characterisation in nicotinamide reduction were yet to be completed. In contrast to residue location 243, and as discussed in Section *1.2.3.2* and shown below in Figure **3.12**, location 37 is within the wildtype TbADH natural substrate binding pocket. Therefore, [Cp*Rh(5M-C37**L1**)Cl]$^{2+}$ was considered a logical starting point for efforts to increase the space available for internal binding of NAD(P)$^+$ substrates.

Other possible TbADH residue locations were also considered for catalyst covalent binding. The aim was to position the catalyst at a location which would allow binding of NAD(P)$^+$ with affinity closer still to that for wildtype TbADH,[107] thus enabling optimal interaction between the nicotinamide C4 and the hydride donating rhodium centre. In wildtype TbADH, residue 110 is located deep within the natural substrate binding pocket and further away than location 37 from the entrance to the nicotinamide pocket (Figure **3.12**). Work by other groups (discussed further in Chapter **5**) found that mutation of TbADH W110 does not affect correct protein folding or native ketone reduction activity.[219] Considering the putative position of NADP$^+$ in wildtype TbADH, the nicotinamide moiety sits in relative proximity to W110 while still allowing space for the extra steric bulk of the rhodium catalyst. Furthermore, owing to the size of the

tryptophan indole ring, substitution of this residue for a large cysteine-conjugated catalyst presents less change of the combined (substrate and nicotinamide) pocket size in comparison to substitution of a smaller residue. In summary, it was hypothesised that covalent conjugation of a catalyst at location 110 may allow relatively unencumbered binding of $NAD(P)^+$, followed by optimal catalyst-substrate interaction. TbADH mutant 7M-C110 serves as the scaffold for ArM variant $[Cp^*Rh(7M\text{-}C110\mathbf{L1})Cl]^{2+}$.

Regarding the BNA^+ nicotinamide mimic, it is more difficult to optimise affinity of binding owing within the TbADH nicotinamide pocket which is naturally evolved to bind the much larger $NADP^+$. However, it was envisaged that other binding sites for the mimic with higher affinity than the two best poses from docking to $[Cp^*Rh(7M\text{-}C243\mathbf{L1})Cl]^{2+}$ may be identified. Therefore, BNA^+ was also taken forward for experiments with the alternative variants.

Based on the above rationale, the same docking procedure and parameters used in the previous section was applied to rhodium-TbADH ArM variants modified at residue locations 37 and 110. This was followed by kinetics to validate predictions made from docking. The objective was to explain the effect of catalyst positioning on ArM-nicotinamide cofactor affinity and reduction activity, via understanding of scaffold interactions with these substrates.

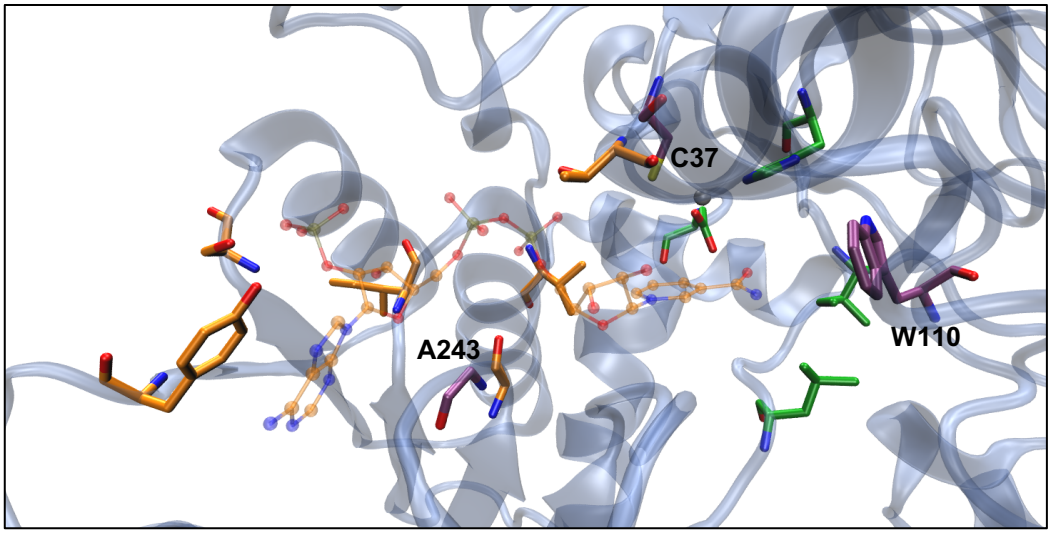

Figure 3.12: WT TbADH residue locations selected for modification in ArM assembly
Wildtype holo-TbADH (ice blue) with *in crystallo* NADPH (transparent orange) and the catalytic zinc (II) (silver). Also highlighted are residues of the nicotinamide binding pocket (orange) and the substrate binding pocket (green) (Section *1.2.3.2*). Residue locations modified with metal catalysts for ArM assembly in this thesis are shown in purple. Location 110 was identified as a promising new catalyst binding site. Generated from PDB 1YKF[107] using VMD.[111]

3.3.1 Docking studies

*3.3.1.1 [Cp*Rh(5M-C37**L1**)Cl]$^{2+}$*

Covalent docking of catalyst [Cp*Rh(Br**L1**)Cl]Cl to C37 of TbADH mutant 5M-C37 is shown in Figure **3.13**. In a similar fashion to docking at location 243, the results suggest that the catalyst could be oriented towards the entrance of the nicotinamide pocket. Therefore, it appears that the middle portion of this pocket is occupied by the catalyst in ArM variant [Cp*Rh(5M-C37**L1**)Cl]$^{2+}$.

Subsequent supramolecular docking of NADP$^+$ suggests binding in a folded conformation at the pocket entrance. Both the adenine and nicotinamide terminal moieties of the docked cofactor are located outside of the natural nicotinamide pocket, according to the docking results (Figure **3.13**).[107] Despite this, the adenine-proximal ribose moiety of the docked cofactor overlaps with the adenine of wildtype TbADH-bound NADP$^+$. The pyrophosphate moiety forms hydrogen bonds with nicotinamide pocket residues such as I175. Therefore, this binding site could be considered more "internal" with respect to the nicotinamide pocket in comparison to the [Cp*Rh(7M-C243**L1**)Cl]$^{2+}$ apparent binding sites. The latter suggest no overlap of ArM-bound NADP$^+$ with the wildtype location of this cofactor in either of the highest-ranked dock poses (Figure **3.10**). Furthermore, the highest-ranked pose obtained from docking of NADP$^+$ to [Cp*Rh(5M-C37**L1**)Cl]$^{2+}$ has a better score than that obtained from docking to the location 243-modified variant (Tables **3.3** and **3.4**). Therefore, as hypothesised, these docking results suggest that the affinity of NADP$^+$ for ArM [Cp*Rh(5M-C37**L1**)Cl]$^{2+}$ may be greater than for the location 243-modified variant. However, the predicted distance between the nicotinamide C4 and the rhodium centre is greater than in [Cp*Rh(7M-C243**L1**)Cl]$^{2+}$ by 1.1 Å (Table **3.4**), which could translate that NADP$^+$ reduction rates values could be marginally lower. Furthermore, it is apparent that the hydride transfer would not be able to occur in the exact orientation observed in Figure **3.13**, with the C4 sitting above the plane of the Cp* ring. Whilst some flexibility of the nicotinamide substrate is assumed, this would also have diminishing effect on catalytic rate.

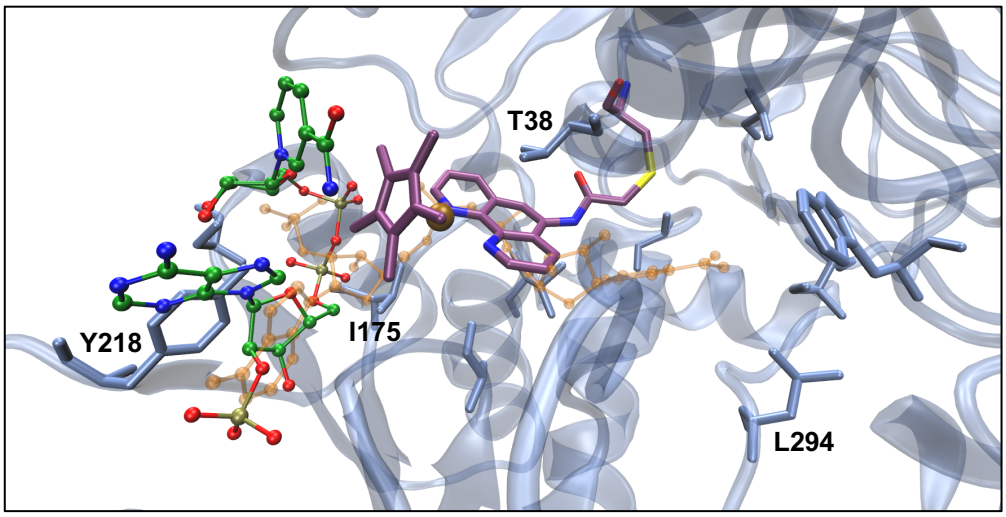

Figure 3.13: Docking of NADP$^+$ to [Cp*Rh(5M-C37L1)Cl]$^{2+}$

Covalent docking of [Cp*Rh(Br**L1**)Cl]Cl (purple) to C37 of 5M-C37 TbADH, followed by supramolecular docking of NADP$^+$ (green) showing the highest-ranked pose. Residues of the nicotinamide and substrate binding pockets coloured here by chain (ice blue), with Y218, T38 and L294 highlighted for reference of orientation. I175 which interacts with the docked NADP$^+$ pyrophosphate. Overlayed in transparent orange is *in-crystallo* NADP$^+$ from wildtype TbADH (PDB: 1YKF).[107]

BNA$^+$ was also docked to the same [Cp*Rh(5M-C37**L1**)Cl]$^{2+}$ receptor (Figure **3.14**). These results suggest that the mimic binding site may overlap with the adenine moiety of wildtype TbADH-bound NADP$^+$. Since this adenine has been shown in the literature to form pi-stacking interactions with Y218,[107] it is plausible that pi-stacking occurs between the BNA$^+$ benzyl and the same residue in the ArM. It is possible that allowing flexibility of Y218 during docking of BNA$^+$ would result in the identification of this interaction using tools in Maestro (Table **3.4**). It should also be noted that the highest-ranked score obtained from docking of BNA$^+$ to [Cp*Rh(5M-C37**L1**)Cl]$^{2+}$ is worse than that obtained from docking of the mimic to the 243-modified variant (Tables **3.3** and **3.4**), suggesting a lower affinity.

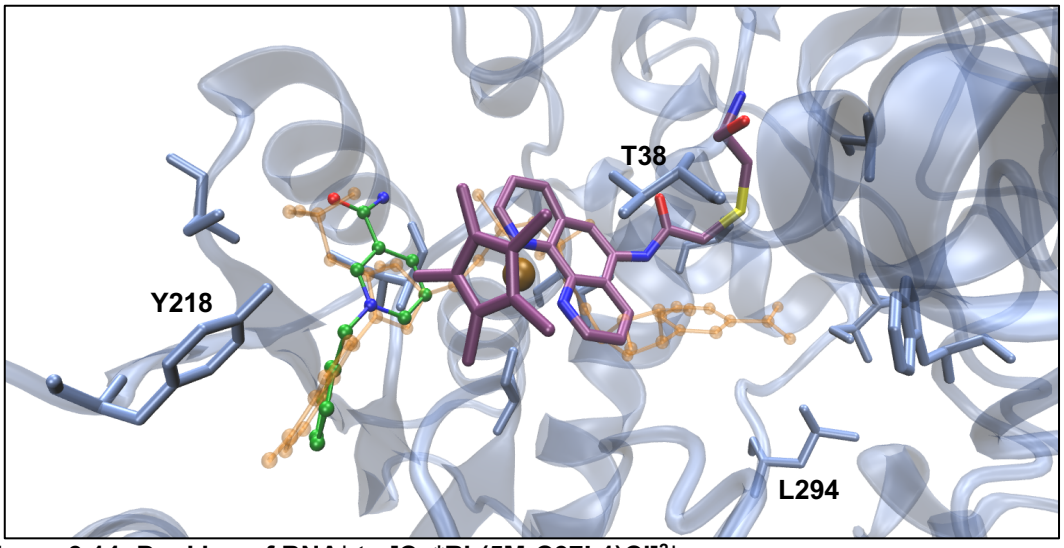

Figure 3.14: Docking of BNA$^+$ to [Cp*Rh(5M-C37L1)Cl]$^{2+}$

Covalent docking of [Cp*Rh(Br**L1**)Cl]Cl (purple) to C37 of 5M-C37 TbADH, followed by supramolecular docking of BNA$^+$, with the highest-ranked pose shown (green). Overlayed in transparent orange is *in-crystallo* NADP$^+$ from wildtype TbADH (PDB: 1YKF).[107]

Table 3.4: Docking interactions, scores, and distances for [Cp*Rh(5M-C37L1)Cl]$^{2+}$ and [Cp*Rh(7M-C110L1)Cl]$^{2+}$

ArM-cofactor	Hydrogen bonds	Salt bridges	Pi-stacking interactions	glide XP score	Distance (Å)
37-NADP$^+$	5	1	0	-11.0	6.9
37-BNA$^+$	2	0	0	-4.5	5.5
110-NADP$^+$	5	3	0	-8.8	7.6
110-BNA$^+$	2	0	1	-8.8	11.6
***110-NADP$^+$**	5	4	0	-7.0	14.22

The first column shows residue location in the TbADH mutant modified in covalent docking to produce the corresponding ArMs to which NADP$^+$ and BNA$^+$ were docked. *110 is an alternative covalent docking pose of [Cp*Rh(7M-C110**L1**)Cl]$^{2+}$ in which the catalyst is oriented in an "outward" conformation (Figure **3.17**). Interactions were identified using Structure Analysis tools in Maestro. Distance measurements are from the bound catalyst Rh centre to the nicotinamide C4.

*3.3.1.2 [Cp*Rh(7M-C110**L1**)Cl]$^{2+}$*

Covalent docking of [Cp*Rh(Br**L1**)Cl]Cl to C110 of TbADH mutant 7M-C110 is shown in Figure **3.15**. Residue location 110 resides on the periphery of the wildtype TbADH substrate pocket. In the highest-ranking covalent dock pose, the catalyst is oriented from the anchoring 110 location into the substrate pocket, and towards where the native zinc (II) would be in wildtype TbADH.

Subsequent supramolecular docking of NADP$^+$ to [Cp*Rh(7M-C110**L1**)Cl]$^{2+}$ suggests a more linear conformation in comparison to the other ArMs variants, and importantly, more of the cofactor is bound within the natural nicotinamide pocket. Indeed, catalyst binding at location 110 appears to provide the most space for “internal” binding the large nicotinamide substrate. The nicotinamide moiety, and proximal ribose and phosphates overlap with the middle-portion of the wildtype TbADH-bound NADP$^+$ (Figure **3.15**). This leaves the adenine and proximal ribose further out from the natural pocket. However, two salt bridges and a hydrogen bond were identified according to the docking pose between the ribose phosphate and K342, which would provide some stability to this end of NADP$^+$. In total, 5 hydrogen bonds and 3 salt bridges were identified between the cofactor and the ArM scaffold (Table **3.4**). Finally, while the highest-ranked NADP$^+$ pose is slightly worse that that obtained from docking to the location 37-modified variant, both scores are more favourable than for the location 243 variant (Tables **3.3** and **3.4**). Overall, these docking results provide tentative support for the hypothesis NADP$^+$ binds to [Cp*Rh(7M-C110**L1**)Cl]$^{2+}$ with higher affinity than to the location 243-modified variant. The fact that the positioning of NADP$^+$ in the location 110-modified variant predicted by docking is closer to the putative position in wildtype TbADH[107] may also suggest higher affinity. However, the predicted greater distance between the nicotinamide C4 and the rhodium centre of 7.6 Å would likely reduce rates of NADP$^+$ reduction at this site.

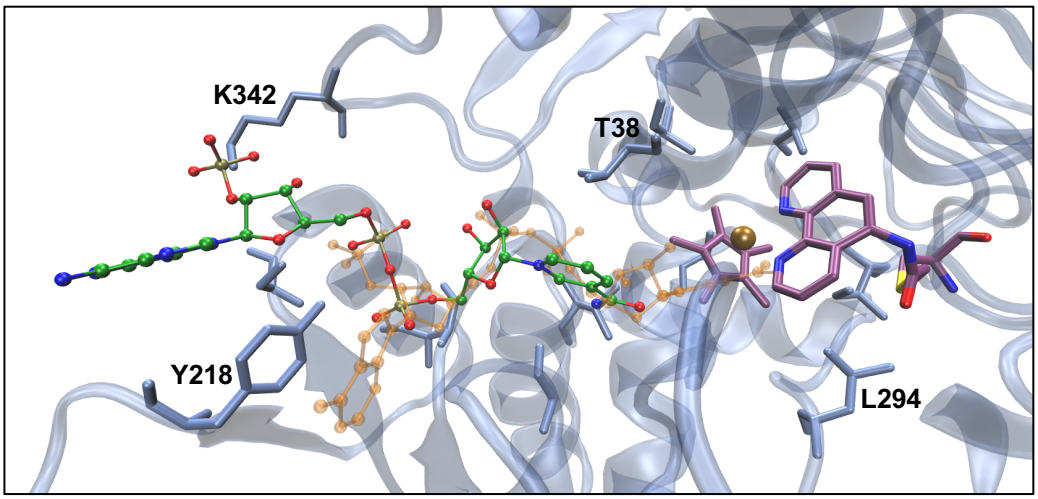

Figure 3.15: Docking of $NADP^+$ to $[Cp^*Rh(7M\text{-}C110L1)Cl]^{2+}$

Covalent docking of [Cp*Rh(Br**L1**)Cl]Cl (purple) to C110 of 7M-C110 TbADH, followed by supramolecular docking of $NADP^+$, showing the highest-ranked pose. K342 interacts with the docked $NADP^+$ ribose phosphate. Overlayed in transparent orange is *in-crystallo* $NADP^+$ from wildtype TbADH (PDB: 1YKF).[107]

BNA^+ was also docked to $[Cp^*Rh(7M\text{-}C110\mathbf{L1})Cl]^{2+}$ (Figure **3.16**). The predicted binding site can be likened to that of BNA^+ in the location 243-modified ArM as it is also external to the nicotinamide binding pocket. A Maestro-identified edge-to-face pi-stacking interaction may be possible between H42 and the nicotinamide ring, along with 2 hydrogen bonds between the nicotinamide and backbone amides of G244 and G269. The highest-ranked score obtained from docking of BNA^+ to $[Cp^*Rh(7M\text{-}C110\mathbf{L1})Cl]^{2+}$ is the best of the three ArM variants (Tables **3.3** and **3.4**). Based on these results, binding of BNA^+ at this site may be with higher affinity than to either of the other two variants. However, in the context of BNA^+ reduction catalysis, the predicted nicotinamide C4 location is too far away from the rhodium centre for hydride transfer in this pose (Table **3.4**). It is possible that the mimic could bind in the opposite orientation, resulting in a reduced Rh-C4 distance while allowing pi-stacking between H42 and the benzyl group of the mimic. Although this would be at the expense of the predicted glycine hydrogen bonds, similar interactions could be formed with the backbone amide of T38.

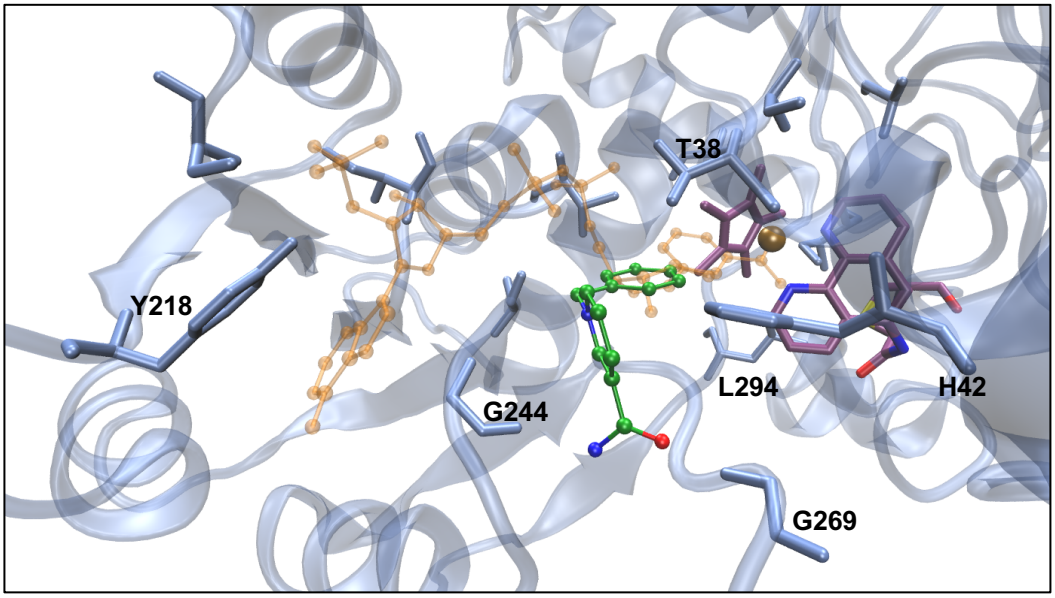

Figure 3.16: Docking of BNA^+ to $[Cp^*Rh(7M\text{-}C110L1)Cl]^{2+}$

Covalent docking of [Cp*Rh(Br**L1**)Cl]Cl (purple) to C110 of 7M-C110 TbADH, followed by supramolecular docking of BNA^+ (green). H42, G244 and G269 interact with docked BNA^+. Overlayed in transparent orange is *in-crystallo* $NADP^+$ from wildtype TbADH (PDB: 1YKF).[107]

It is also worth noting that an alternative lower-scoring covalent docking pose was identified for this ArM variant (Figure **3.17**). This pose positions the catalyst out from the nicotinamide and substrate binding pockets. Subsequent docking of $NADP^+$ to $[Cp^*Rh^{Out}(7M\text{-}C110\mathbf{L1})Cl]^{2+}$ places the nicotinamide deeper into the natural nicotinamide pocket than wildtype-bound $NADP^+$.[107] The nicotinamide moiety is suggested to reside in the substrate binding pocket, with the C4 atom 6.8 Å from the catalyst-bound C110 sulfur atom. The resulting nicotinamide C4 to rhodium distance of 14.22 Å would render this conformation inactive for $NADP^+$ reduction. However, this orientation of the catalyst may not be favoured under reaction conditions.

In summary, Figure **3.17** suggests the possibility of an alternative catalytically inactive ArM conformation. However, the docking results in Figures **3.15-16** predict binding of nicotinamide substrates at sites active for reduction, potentially with higher affinity than for the other two ArM variants tested. Based this prospect of improved ArM catalytic efficiency in natural and mimic nicotinamide reduction, $[Cp^*Rh(7M\text{-}C110\mathbf{L1})Cl]^{2+}$ was assembled experimentally for kinetic characterisation (Section ***3.3.3***).

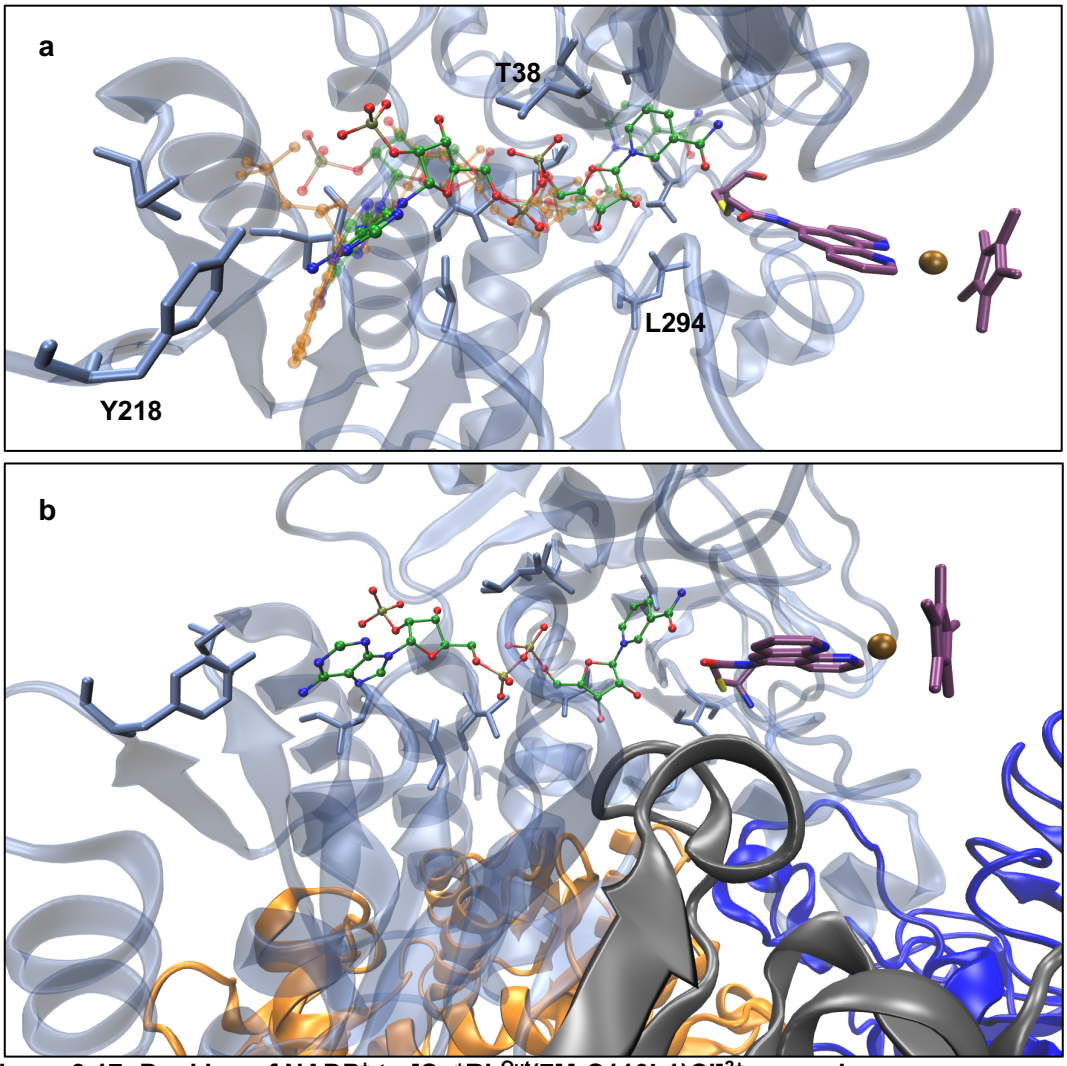

Figure 3.17: Docking of $NADP^+$ to $[Cp^*Rh^{Out}(7M\text{-}C110L1)Cl]^{2+}$ secondary pose

Alternative covalent docking pose of [Cp*Rh(Br**L1**)Cl]Cl (purple) to C110 of 7M-C110 TbADH, followed by supramolecular docking of $NADP^+$. Panel **a** shows the first and second highest-ranked $NADP^+$ poses in green and transparent green respectively. Overlayed in transparent orange is *in-crystallo* $NADP^+$ from wildtype TbADH (PDB: 1YKF).[107] Panel **b** shows the other three subunits of TbADH coloured by chain.

*3.3.2 Assembly and analysis of [Cp*Rh(5M-C37L1)Cl]$^{2+}$ and [Cp*Rh(7M-C110L1)Cl]$^{2+}$*

3.3.2.1 Preparation of protein and catalyst ArM components

The plasmid containing the mutated 5M-C37 TbADH gene (Table **2.1**) was prepared previously by Dr S. Morra and was available in our laboratory.[29] SDS-PAGE analysis confirmed successful overexpression and purification of the mutant (Figure **3.18**). The pooled elution fractions were considered of sufficient purity for subsequent experiments.

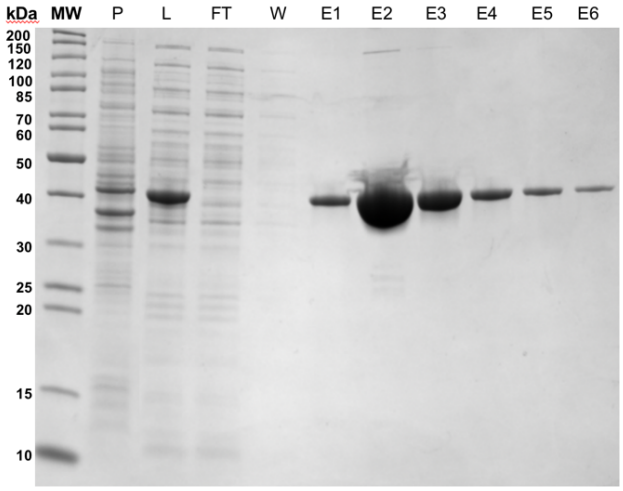

Figure 3.18: SDS-PAGE analysis of 5M-C37 TbADH purification by affinity chromatography

Bands corresponding to strep-tagged TbADH are prominent in elution fractions 1 to 4 which were pooled and concentrated for subsequent analysis. Lanes were loaded with the following samples: MW = molecular weight ladder; P = cell lysate; L = soluble constituents loaded onto the affinity column (following heat treatment step); FT = affinity column flow-through fraction; W = Wash of the column with non-elution buffer; E1-6 = FPLC elution fractions.

Meanwhile, site directed mutagenesis was used to generate the TbADH 7M-C110 mutant. The cysteine-devoid 6M mutant plasmid (prepared previously by Dr M. Basle) was used as a template for the W110C point mutation (Table **2.1**). Success of the mutagenesis procedure was confirmed by sequencing.

Expression and purification of 7M-110C TbADH was performed as for previous two mutants (Section **3.2**). SDS-PAGE analysis confirmed successful overexpression and purification of the mutant, showing intense bands with a molecular weight of around 40 kDa in the pellet, load, and elution fractions (Figure **3.19**). The presence of a similar

band in the flow-through fraction suggests minor over-loading of the column, owing to the volume of expression media used. The pooled elution fractions were considered of sufficient purity for subsequent experiments.

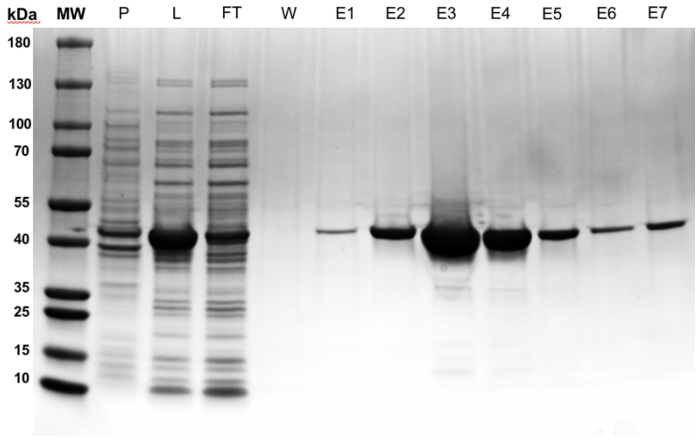

Figure 3.19: SDS-PAGE analysis of 7M-110C TbADH purification by affinity chromatography

Bands corresponding to strep-tagged TbADH are prominent in elution fractions 2 to 7 which were pooled and concentrated for subsequent analysis. Lanes were loaded with the following samples: MW = molecular weight ladder; P = cell lysate; L = soluble constituents loaded onto the affinity column (following heat treatment step); FT = affinity column flow-through fraction; W = Wash of the column with non-elution buffer; E1-7 = FPLC elution fractions.

3.3.2.2 Assembly, Ellman's assay and ICP-MS analysis of ArMs

Based on an Ellman's assay, thiol availability of unmodified 5M-C37 was determined to be 64 %, similar to the value of ~70 % previously reported for this mutant.[29] Comparison between an Ellman's assay of the assembled [Cp*Rh(5M-C37**L1**)Cl]$^{2+}$ ArM with that of the unmodified 5M-C37 indicated a 61 % reduction in the available free thiol groups. Therefore, by this measure in combination with Bradford assay-estimated protein concentration, 39 % of the total protein molecules were successfully modified with rhodium catalyst (Figure **3.20**). In contrast, the rhodium content of the sample based on ICP-MS analysis was calculated to be 89 %, suggesting that this percentage of total protein was modified. These results are consistent with those obtained previously for this variant.[29]

The thiol availability of the 7M-C110 TbADH sample was determined to be 45 %. Comparison between an Ellman's assay of the assembled [Cp*Rh(7M-C110**L1**)Cl]$^{2+}$ ArM with that of the unmodified 7M-C110 protein indicated a 60 % reduction in the available free thiol groups. Therefore, by this measure in combination with Bradford

assay-estimated protein concentration, 27 % of the total protein molecules in solution were successfully modified with rhodium catalyst (Figure **3.20**). In contrast, the rhodium content of the sample based on ICP-MS analysis was calculated to be 100 %. Owing to possible insufficient assay duration and partial accessibility of the DTNB reagent to thiol groups (Section *3.2.1.2*), ICP-MS was taken as the most reliable measure of the concentration of ArM in solution.

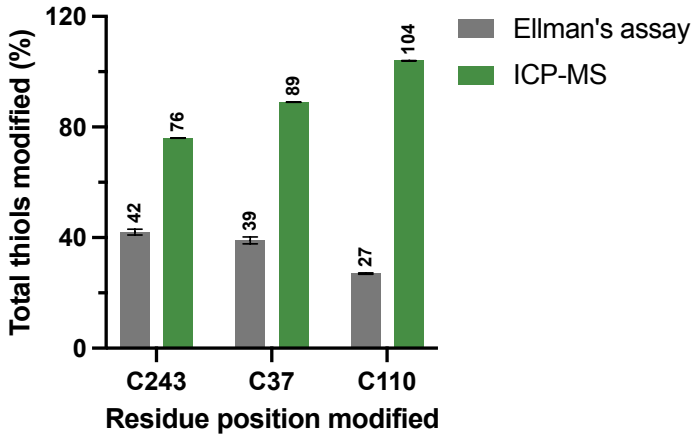

Figure 3.20: Summary of Ellman's and ICP-MS data for all rhodium ArM variants
Summary of data from Ellman's and ICP-MS analysis of TbADH samples before and after bioconjugation with [Cp*Rh(Br**L1**)Cl]Cl. The x-axis shows the single cysteine residue location in the TbADH mutant modified to produce the corresponding ArMs. The y-axis total % thiol modification values were calculated based on Bradford assay-estimated protein concentration. For the Ellman's assay, these values may have been affected by the assay duration required for the DTNB reagent to reach and interact with poorly accessible cysteines within the TbADH nicotinamide pocket.

Overall, there is reasonable consistency of values from these analyses for the two reproduced variants in comparison to previous work.[29, 186] The greater rhodium content observed with the new [Cp*Rh(7M-C110**L1**)Cl]$^{2+}$ variant may be explained by marginally improved bioconjugation efficiency as a result of catalyst relocation. In further analysis of ArM assembly success, ESI-TOF MS analysis was performed.

3.3.2.3 ESI-TOF MS analysis of ArMs

To confirm the presence of the desirable ArM and any contaminants based on the masses of species in solution, whole-protein denaturing ESI-TOF MS analysis was performed on both variants.

The spectra obtained were first deconvoluted automatically via a tool within the Bruker Compass software (Figure **3.21**). Regarding the reproduced variant [Cp*Rh(5M-C37**L1**)Cl]$^{2+}$, the most prominent species **A** was of mass corresponding to the desirable ArM with a single covalently bound rhodium catalyst, identified with 100 % relative intensity. Sample heterogeneity was evident, with secondary peaks present of masses corresponding to double-labelled species **E** with and **B** without a Cl atom, the unmodified protein scaffold 5M-C37 **C**, and the desirable ArM lacking a Cl atom **D** at relative intensities of 26, 46, 45 and 37 % respectively. The double-labelled species **B** has been observed in samples of [Cp*Rh(5M-C37**L1**)Cl]$^{2+}$ previously[29] and possesses an extra non-specifically bound rhodium catalyst. It is known that rhodium can coordinate residues such as histidine.[213, 214] Previous work by Dr S. Morra with rhodium-TbADH ArMs showed that this is a more likely explanation for this species than covalent modification of residues other than cysteine.[29] The presence of unmodified 5M-C37 supports the observation of <100 % rhodium content according to ICP-MS (Figure **3.20**). The Cl atom missing from **D** is most likely that which coordinates the rhodium atom. This species has also been observed previously[29] and can likely be considered catalytically active based on the putative mechanism of hydride transfer.[130]

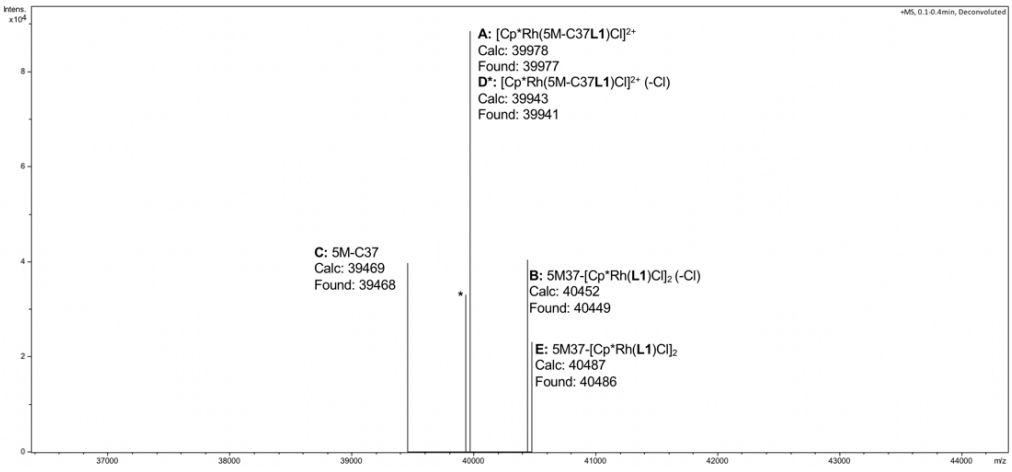

Figure 3.21: ESI-TOF MS auto-deconvoluted spectrum of [Cp*Rh(5M-C37L1)Cl]$^{2+}$
Signals were identified with mass corresponding to the desirable species **A** and **D** (lacking one Cl atom), double-conjugated species **B** (lacking one Cl atom) and **E**, and unmodified protein **C**. Bioconjugation conditions: Tris HCl buffer (100 mM, pH 7.0), 4:1 molar ratio of [Cp*Rh(Br**L1**)Cl]Cl to 5M-C37, 1 hour incubation at 30 °C with frequent sample inversion.

For further confirmation of the species present in this sample, the raw spectrum was manually deconvoluted via tools within the Bruker Compass software (Figure **3.22**).

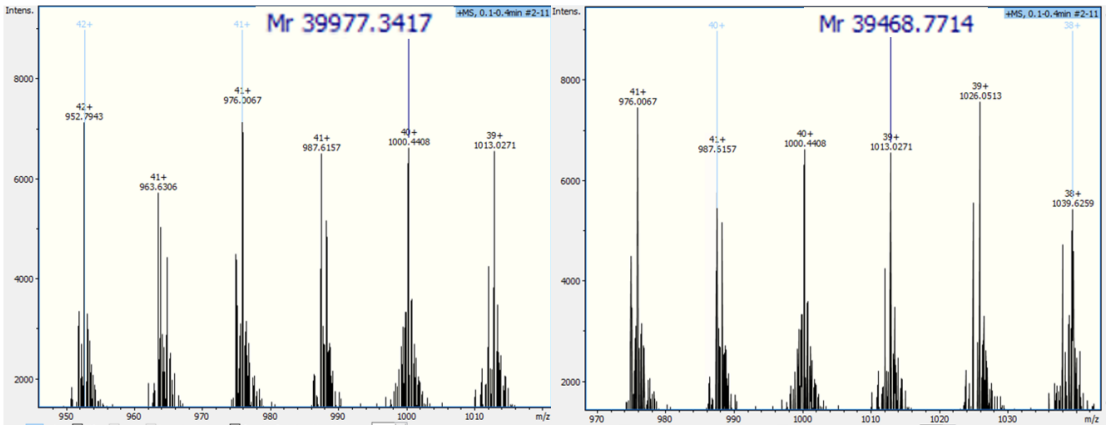

Figure 3.22: ESI-TOF MS manual-deconvoluted spectrum of [Cp*Rh(5M-C37L1)Cl]$^{2+}$
Signals were identified with mass corresponding to the desirable species **A** (left), and the unmodified 5M-C37 species **C** (right). This sample was taken forward for subsequent experiments.

The desirable ArM [Cp*Rh(5M-C37**L1**)Cl]$^{2+}$ **A** and the unmodified 5M-C37 **C** were identified. These results indicate that most of the rhodium in this sample was located at the desired residue location 37, and in combination with the presence of **C**, justifies the use of ICP-MS to determine the concentration of ArM in solution. The fact that the double-conjugated species **B** and **E** could not be identified by manual deconvolution suggests that these signals could be an artifact of the automated method.

The significant background noise adjacent to the major peaks identified in Figure **3.22** was noted, and prevented use of the spectrum baseline subtraction and smoothing features in Bruker Compass. To investigate this issue, a different (separately prepared) sample of [Cp*Rh(5M-C37**L1**)Cl]$^{2+}$ which (along with many others) had given an apparently much cleaner spectrum previously (Figure **3.23**) was run through the instrument again. Similar levels of noise were observed in the resulting spectrum. Therefore, it was concluded that this apparent contamination was derived from the instrument rather than from the ArM sample shown in Figure **3.22**. The identification of mass values in this alternative sample via manual deconvolution (Figure **3.23**) further supports the existence of species **A** and **C**.

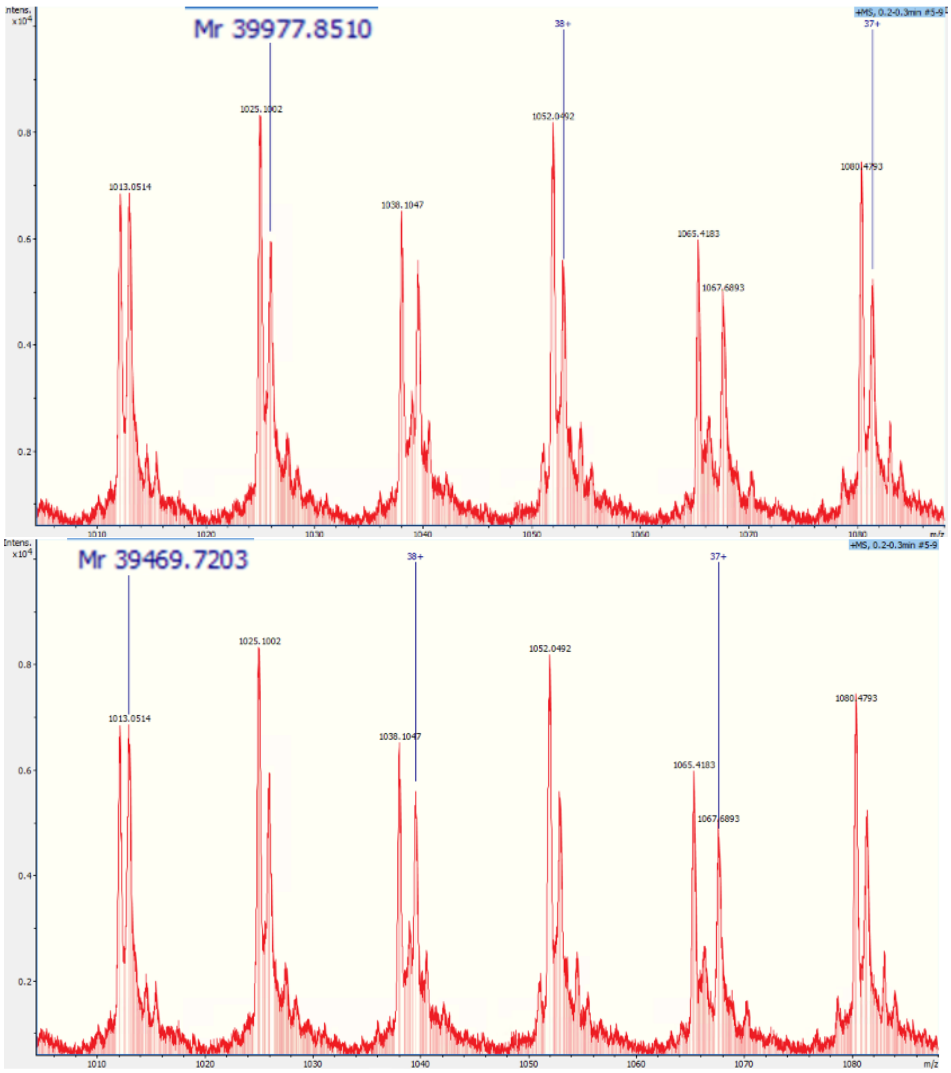

Figure 3.23: Manual-deconvoluted alternative sample of [Cp*Rh(5M-C37L1)Cl]$^{2+}$
Signals were identified with mass corresponding to the desirable species **A** (top), and the unmodified 5M-C37 species **C** (bottom).

Taken together, Ellman's assay, ICP-MS and ESI-TOF MS analyses indicate successful assembly of [Cp*Rh(5M-C37**L1**)Cl]$^{2+}$, albeit with a level of solution heterogeneity similar to that observed in previous studies.[29, 186] The sample was considered suitable to take forward for full kinetic characterisation.

Next, automated deconvolution was performed on the new [Cp*Rh(7M-C110**L1**)Cl]$^{2+}$ variant (Figure **3.24**). The most prominent species identified was of mass corresponding to the desirable single-conjugated species lacking a Cl atom **A**, with the desirable ArM at 82 % relative intensity **B**. The third and fourth most prominent species, at 52 and 34 % relative intensity respectively, were of masses corresponding to a double-labelled species **C** with and **D** without a Cl atom as observed in the 5M-

C37 modified sample. Indeed, any non-specific coordination of rhodium to non-cysteine residues should not change significantly between the two TbADH mutants.

Manual deconvolution of the 7M-C110 modified sample confirmed the presence of species **A** and **B** (Figure **3.25**). The lower intensity peaks marked with asterisks could not be reliably assigned mass values, possibly owing to the instrument contamination issue discussed above. These peaks may correspond to the either double-labelled or unmodified protein. In the case of the latter, species **C** and **D** could be artifacts of the automated deconvolution method. It should be noted that the presence of such double-labelled species could have an impact on the rates of nicotinamide reduction measured, assuming catalytic activity of the non-specifically bound catalyst. However, these species could not be reliably identified via the manual deconvolution process in any of the multiple samples analysed on separate occasions. Therefore, the decision was made to take these ArM variants forward for kinetic analysis.

In contrast to the location 37-modified samples, unmodified protein was not identified by either of the deconvolution methods. In agreement with ICP-MS analysis (Figure **3.20**), this suggests an improvement to the proportion of 7M110 modified in comparison to 5M-C37, and therefore, a slight improvement of bioconjugation efficiency as a result of catalyst relocation.

Overall, the [Cp*Rh(7M-C110**L1**)Cl]$^{2+}$ sample was considered similar in quality to the to the location 37-modified sample, and suitable for assessment of catalytic activity.

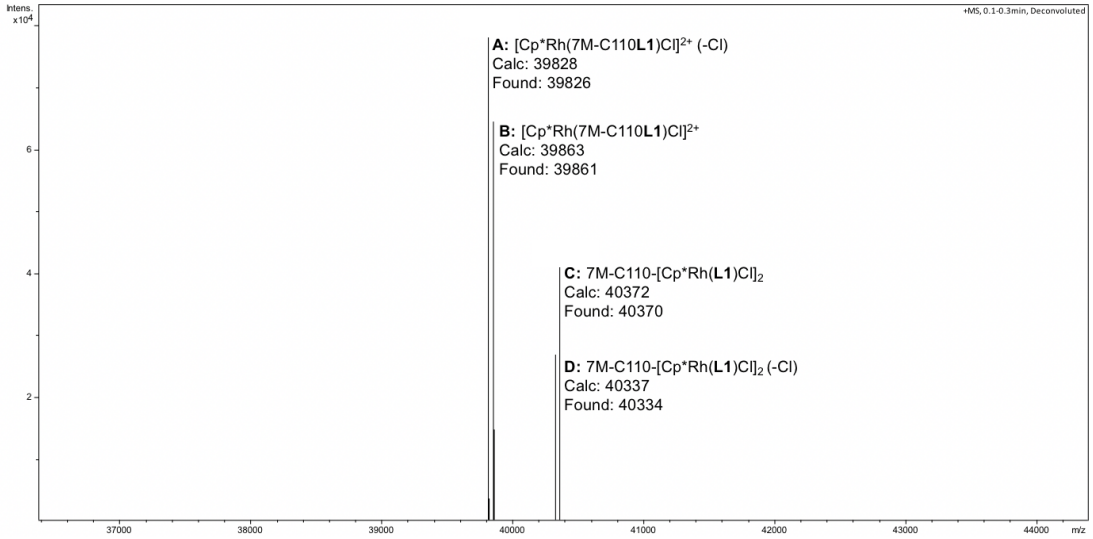

Figure 3.24: ESI-TOF MS auto-deconvoluted spectrum of [Cp*Rh(7M-C110L1)Cl]$^{2+}$

Signals were identified with mass corresponding to the desirable species **A** (lacking one Cl atom) and **B**, and double-conjugated species **C** and **D** (lacking one Cl atom). Bioconjugation conditions: Tris HCl buffer (100 mM, pH 7.0), 4:1 molar ratio of [Cp*Rh(Br**L1**)Cl]Cl to 7M-C110, 1 hour incubation at 30 °C with frequent sample inversion.

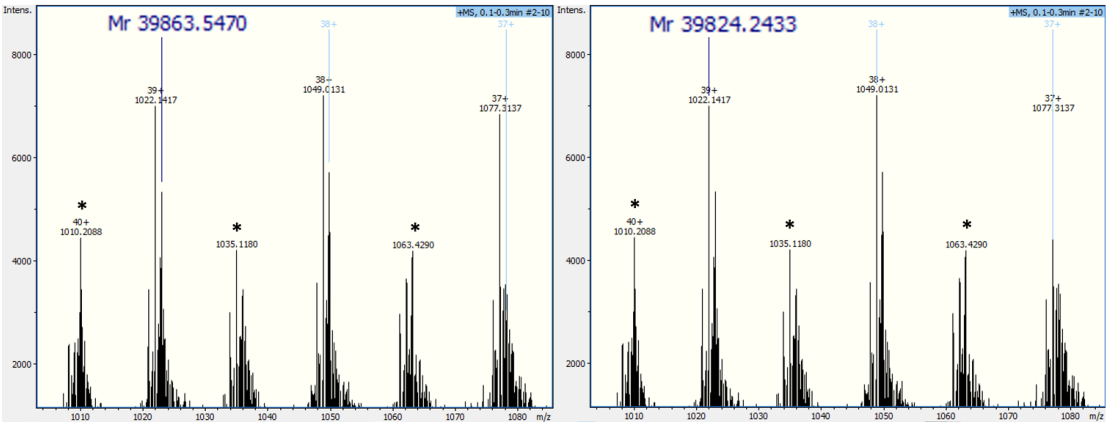

Figure 3.25: ESI-TOF MS manual-deconvoluted spectrum of $[Cp^*Rh(7M\text{-}C110L1)Cl]^{2+}$

Signals were identified with masses corresponding to the desirable species **A** (left), and the desirable species lacking a Cl atom **B** (right). The species marked with an asterisk may corresponds to either unmodified 7M-C110, or the double-labelled species as identified by the automated method.

3.3.3 Kinetics of nicotinamide reduction

To further understand the effect of catalyst positioning on rhodium-TbADH ArM nicotinamide substrate binding and scope, kinetic characterisation of variants modified at residue locations 37 and 110 was completed. Based on structural insights gained from docking, it was expected that nicotinamide affinity for these variants would be higher than for [Cp*Rh(7M-C243**L1**)Cl]$^{2+}$.

*3.3.3.1 [Cp*Rh(5M-C37**L1**)Cl]$^{2+}$*

Michaelis-Menten characterisation of [Cp*Rh(5M-C37**L1**)Cl]$^{2+}$ was completed with both the hydrophobic nicotinamide mimic BNA$^+$, and the two natural nicotinamide substrates NAD(P)$^+$ (Figure **3.26**). The ArM displayed enzyme-like kinetic behaviour in the reduction of the NAD(P)$^+$. The value of K_M^{NADP+} calculated by non-linear regression in GraphPad Prism was 36 μM (Figure **3.26d**).

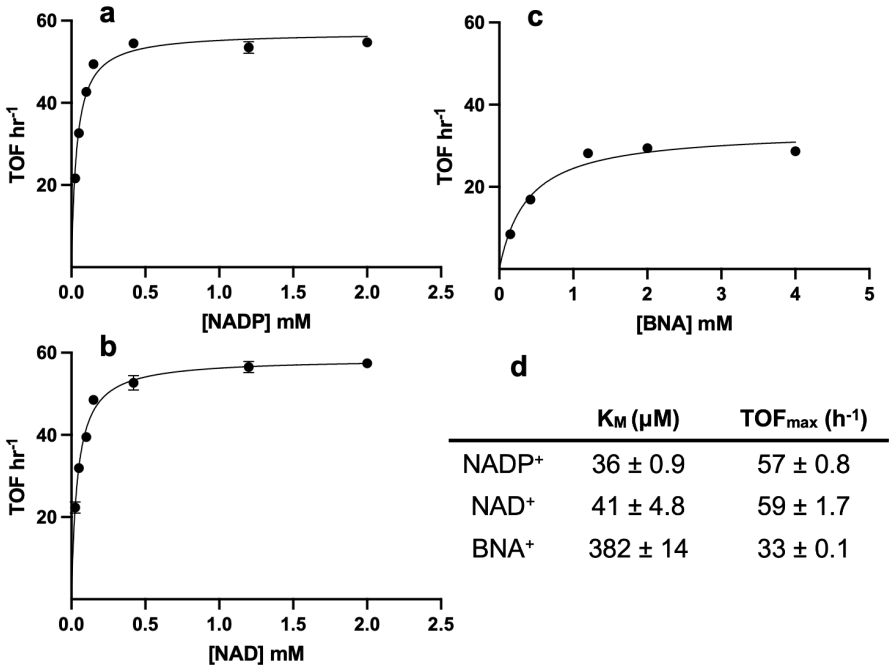

Figure 3.26: Kinetic characterisation of [Cp*Rh(5M-C37L1)Cl]$^{2+}$ nicotinamide reduction
A range of a) NADP$^+$, b) NAD$^+$ and c) BNA$^+$ concentrations were tested under the conditions described in Table **3.2**. Error bars show the standard error of mean (n = 2).

Based on the docking-predicted proximity between the nicotinamide C4 and the rhodium centre of the catalyst, it was assumed that this K_M value serves as an estimate of $NADP^+$ affinity for this reactive binding site. Therefore, the observed 1.4-fold reduction of K_M^{NADP+} in comparison to the location 243-modified variant suggests greater $NADP^+$ affinity of [Cp*Rh(5M-C37**L1**)Cl]$^{2+}$. This supports the theory that alteration of the catalyst binding site away from the entrance to the nicotinamide binding pocket increases ArM affinity for $NADP^+$. The improved affinity may be explained to an extent by docking-suggested partial overlap of $NADP^+$ with the wildtype TbADH nicotinamide binding site.[220] The fact that the highest-ranked $NADP^+$ docking score is better for the location 37-modified (Tables **3.3** and **3.4**) may add further support to the notion of higher affinity.
In further contrast to [Cp*Rh(7M-C243**L1**)Cl]$^{2+}$, a lower TOF_{max}^{NADP+} was calculated for this variant. It should also be noted that an optimised ICP-MS procedure was used to calculate the solution concentration of ArM for both the 37 and 110-modified variants. Therefore, an apparently lower rhodium content of the 243-modified sample may have biased rate values calculated. However, the reduction in TOF_{max} may also be partially explained by the increased C4-Rh distance and the potentially unfavourable relative positions of these moieties, which were predicted by docking.

The value of K_M^{NAD+} was 1.1-fold higher than K_M^{NADP+}. Docking of NAD^+ to [Cp*Rh(5M-C37**L1**)Cl]$^{2+}$ was completed in the interest of identifying differences in binding site interactions between the two natural cofactors, particularly the $NADP^+$ ribose phosphate. However, the binding sites overlapped, and no extra interactions could be identified (not shown). It is possible that the higher-than-expected K_M^{NAD+} value is the result of greater standard error of mean for this variant (Figure **3.26d**).

The approximate value of K_M^{BNA+} for [Cp*Rh(5M-C37**L1**)Cl]$^{2+}$ was 382 μM (Figure **3.26d**). As for the 243-modified variant, the SEM values were higher, and adjusted R^2 values lower in comparison to the natural cofactors (Appendix **1**). The apparent 1.8-fold reduction in K_M^{BNA+} achieved by moving the catalyst from residue location 243 to 37 does not corroborate with the fact that the highest-ranked docking score for the former was 1.3-fold better. Therefore, considering both the adjusted R^2 and SEM values from kinetic measurements (Appendix **1**) alongside the lack of docking model validation, the difference in BNA^+ affinity for these two ArM variants remains unclear.

*3.3.3.2 [Cp*Rh(7M-C110**L1**)Cl]$^{2+}$*

Based on the rationale for the selection of location 110 for ArM assembly (Figure **3.12**) and on subsequent docking results, it was hypothesised that K_M values displayed by [Cp*Rh(7M-C110**L1**)Cl]$^{2+}$ may be the lowest of the three variants. Figure **3.27** shows these results.

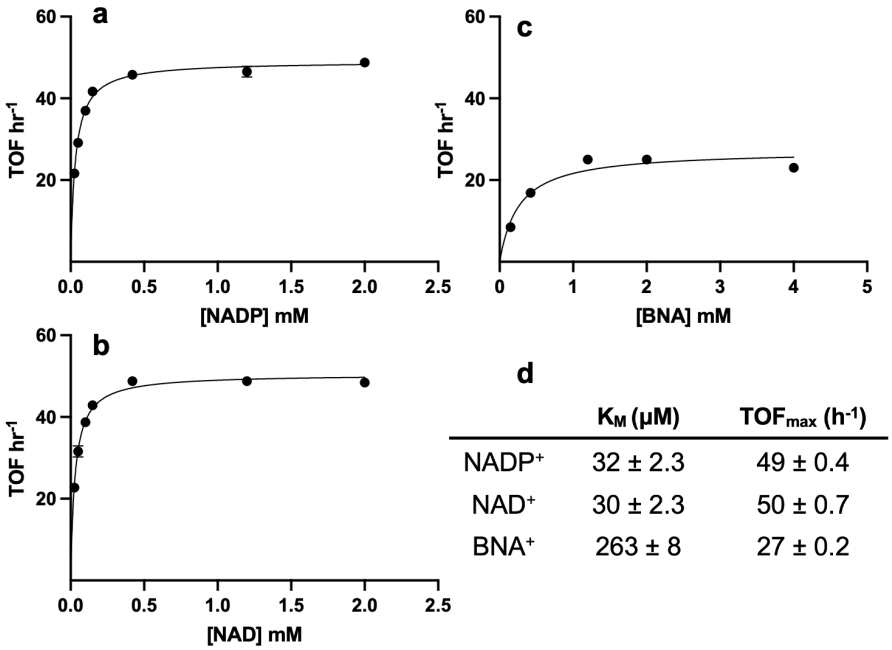

Figure 3.27: Kinetic characterisation of [Cp*Rh(7M-C110L1)Cl]$^{2+}$ nicotinamide reduction
Panels as for Figure **3.25**.

Figure **3.28** shows the K_M values for all ArM-NAD(P)$^+$ substrate combinations tested. These results indicate a general trend of increasing affinity for the natural NAD(P)$^+$ substrates by altering the rhodium catalyst binding site in the following order of residue location: 243 < 37 < 110.

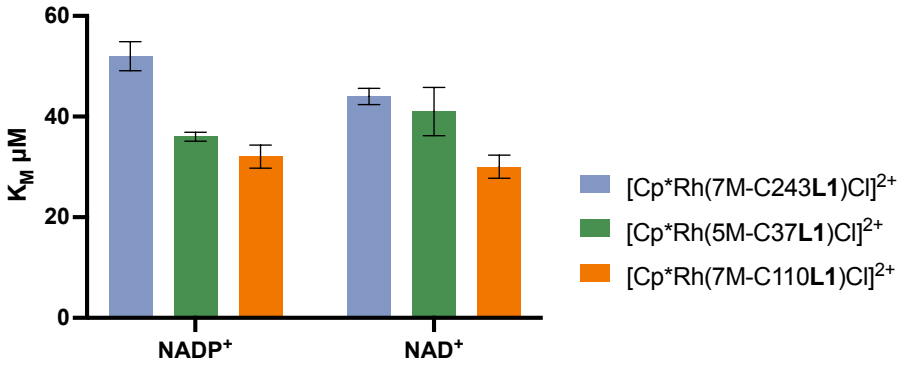

Figure 3.28: K_M values for reduction of NAD(P)$^+$ cofactors by rhodium-TbADH ArMs
K_M and TOF_{max} values for reduction of the natural NAD(P)$^+$ cofactors were calculated using non-linear regression in GraphPad Prism 9.0. Standard errors of mean values are shown (n = 2)

The K_M values of [Cp*Rh(7M-C110**L1**)Cl]$^{2+}$ for NADP$^+$ and NAD$^+$ were 1.1 and 1.4-fold lower respectively than those for [Cp*Rh(5M-C37**L1**)Cl]$^{2+}$, and 1.6 and 1.5-fold lower than those for [Cp*Rh(7M-C243**L1**)Cl]$^{2+}$. This makes the K_M^{NADP+} measured for this new ArM variant only 4.6-fold higher than that reported for wildtype TbADH[216] which is a notable improvement from the 7.6-fold difference measured for residue location 243-modified variant (Section ***3.2.2***). Therefore, as hypothesised, the location 110-modified variant is superior with respect to catalytic efficiency according to this measure of NAD(P)$^+$ substrate affinity. This is mostly supported by NADP$^+$ docking results which suggest the greatest overlap of the three ArM variants tested with the naturally evolved binding site of this cofactor in wildtype TbADH.[107] Furthermore, more Maestro-identified substrate-ArM interactions were identified for [Cp*Rh(7M-C110**L1**)Cl]$^{2+}$, and the highest-ranked poses obtained for the location 37 and 110-modified variants scored better than that for location 243 (Tables **3.3** and **3.4**). It should be noted that the best docking score was obtained for [Cp*Rh(5M-C37**L1**)Cl]$^{2+}$, meaning that the kinetics and docking are not fully in agreement. However, the results in combination indicate that NADP$^+$ affinity is similar for the location 37 and 110-modified variants, which are both higher than for [Cp*Rh(7M-C243**L1**)Cl]$^{2+}$. The lower TOF_{max} value observed by moving the catalyst to location 110 may be explained by the increased C4-Rh distance predicted by docking (Table **3.4**).

As for NADP$^+$, the value of K_M^{BNA+} for [Cp*Rh(7M-C110**L1**)Cl]$^{2+}$ was also the lowest of the ArM variants. While the docking-predicted nicotinamide C4-Rh distance appeared too great for catalytic interaction, BNA$^+$ binding to the same site but in the opposite orientation may be possible. Under this assumption, these kinetics results corroborate

with those from docking, as the docking score of the highest-ranked pose was the best out of the three ArM variants (Tables **3.3** and **3.4**).

Overall, these results in combination indicate the successful rational optimisation of a TbADH-rhodium based ArM based on efficiency of nicotinamide reduction. Validation and further exploration of these theories concerning the effect of genetic alterations on TbADH-based ArM component interactions are covered Section **4.2**.

3.3.4 Conclusions

The present chapter combined kinetic and computational studies on rhodium-TbADH based ArMs for the reduction of different nicotinamide cofactors, to probe the effect of catalyst positioning on substrate binding and scope. Based on the results presented in Section **3.2** it was theorised that rhodium catalyst covalent anchoring to residue location 243, near the entrance to the nicotinamide binding pocket of TbADH, inhibits the internal binding of natural nicotinamide $NAD(P)^+$ substrates and leads to flexible binding of the small BNA^+ nicotinamide mimic. Therefore, towards rational ArM optimisation, two other variants were kinetically characterised, both with the catalyst bound to residue locations deeper within the nicotinamide pocket of TbADH.
$[Cp^*Rh(5M\text{-}C37\mathbf{L1})Cl]^{2+}$ had been previously characterised for a chiral alcohol production cascade but was yet to be kinetically characterised for affinity of nicotinamide substrate binding. Docking of $NADP^+$ to this ArM suggested a possible increase in affinity compared with the location 243-modified variant, based on the highest-ranked glide XP score. Subsequent Michaelis-Menten characterisation indicated improved affinity for $NAD(P)^+$. These results support the hypothesis that relocation of the catalyst deeper within the pocket improves ArM performance.
Seeking to generate a new rational genetic ArM mutant which may achieve further improvements to substrate affinity, a new residue location for catalyst anchoring was identified. Docking studies with variant $[Cp^*Rh(7M\text{-}C110\mathbf{L1})Cl]^{2+}$ tentatively suggested a higher affinity catalytic binding site for $NADP^+$ in comparison the other variants, based on a greater overlap with the wildtype TbADH binding site. Therefore, the new variant was assembled for kinetic characterisation. Given that the presence of possible catalytically active double-labelled species could not be verified, it was considered reasonable to draw conclusions from these kinetic analyses. The Michaelis-Menten results were generally in support of the docking predictions, indicating further improvement in affinity of $NAD(P)^+$ substrates. The K_M^{BNA+} value calculated for the location 110-modified variant was also the lowest of the three ArMs, suggesting the

highest affinity. However, this conclusion is based on the assumption that the mimic can bind to this site in the reverse orientation, reducing the nicotinamide C4-Rh distance to enable interaction.

These conclusions would benefit from full structural solution of TbADH ArM variants modified at these residue locations. Meanwhile, the improved understanding of how nicotinamide cofactors bind to these ArMs may also be useful for other reduction applications. For example, where the nicotinamide serves as the cofactor rather than substrate.

4 Structural characterisation and reduction applications of iridium-TbADH artificial metalloenzymes

4.1 Introduction

The results from Chapter **3** show different binding modes for nicotinamide cofactors $NAD(P)^+$ and the mimic BNA^+ to a rhodium-TbADH based ArMs, as well as the effect of catalyst positioning in previously studied and new genetic variants. This increased understanding of ArM-substrate interactions is a step towards the objective of full structural characterisation. Indeed, solving atomic resolution structures of these ArMs with nicotinamide substrate(s) bound would enable deeper understanding of such interactions.[221] Therefore, the objective of Section **4.2** was to obtain ArM structures with $NADP^+$ bound. It was envisaged that these results would provide further insight into interactions at the ArM active site, validating and building upon the kinetics and docking results of the previous chapter. Several high-resolution crystal structures of TbADH have been solved with various substrates and cofactors bound, and point mutations introduced.[108, 220] These studies provide promise for obtaining TbADH ArM structures, as well as useful information on crystallisation conditions and space groups.

In consideration of the practicalities of achieving such structures, an issue was identified regarding covalent ArM assembly. ESI-TOF MS experiments performed on $[Cp^*Rh(5M\text{-}C37\mathbf{L1})Cl]^{2+}$ and several other variants indicate the presence of multiple species, owing in part to incomplete or possible non-specific binding of rhodium (Chapter **3**).[29, 186,213, 214] This solution heterogeneity was considered likely to decrease the success of crystal trials.[222] To address this, alternative ArM systems and applications were considered, keeping in consideration the overall project aim of rational TbADH-based ArM optimisation. Work completed by Dr S. Morra has shown that bioconjugation of iridium catalysts possessing phenanthroline to the 5M-C37 mutant yields near homogenous ArM samples according to ESI-TOF MS analysis. Therefore, it was reasoned that ArM solution heterogeneity could be improved via substitution of rhodium for iridium. Structural solution of such an ArM, with the only alteration from those variants covered in Chapter **3** being the catalyst metal, would serve as a proxy for interesting structural insight into rhodium-TbADH based ArMs.

The potential applications of such ArMs containing Cp*Ir(III)-phenanthroline complexes as transfer hydrogenation catalysts were explored in Section **4.3**. A range

of Cp*Ir piano-stool catalysts have been shown to be active for nicotinamide,[116, 131] imine[88, 89] and quinone[195] reduction as summarised in Figure **4.1a**, **b** and **c** respectively. Most interestingly, those reports on imine reduction have incorporated these catalysts into ArMs and demonstrated optimisation of control over enantioselectivity, in addition to use of the ArMs in multienzyme cascade reactions.[9]
It was envisaged that the incorporation of such catalysts into TbADH could expand the functionality of TbADH based ArMs (Figure **4.1**).

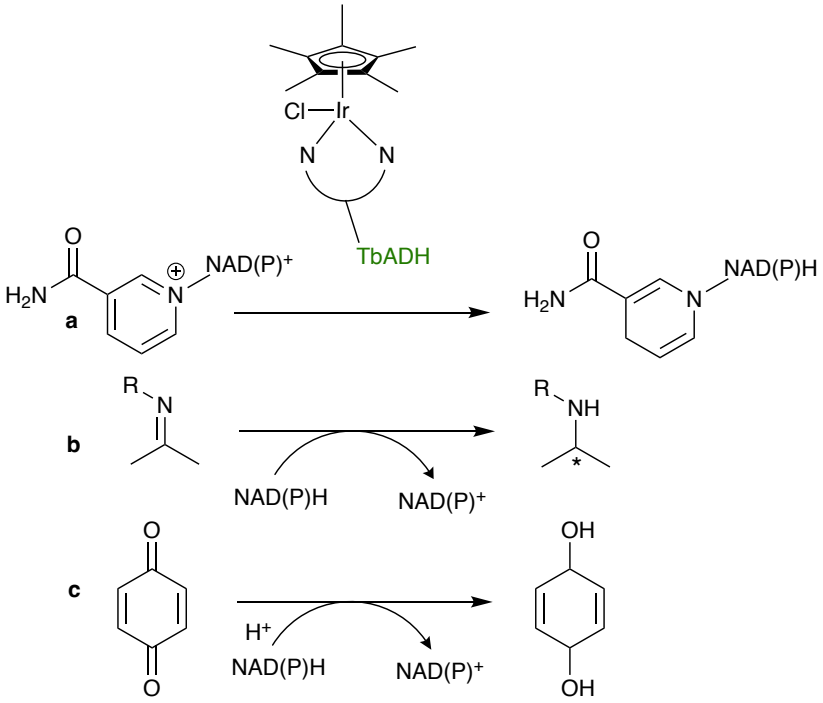

Figure 4.1: Summary of prospective iridium-TbADH ArM catalysed reduction reactions
The simplified scheme shows only one of two possible outcomes for the reduction of quinones using Cp*Ir catalysts (reaction **c**). The intricacies of this mechanism are explained in Section *4.3.3.1*. *Chiral centre.

Furthermore, the results from catalysis could then be analysed in conjunction with docking and structural insights already acquired in Chapter **3** and Section **4.2**. Such analyses may provide structure-informed explanations for differences in enantioselectivities or rates of reduction between different ArM genetic variants. The use of NAD(P)H as the hydride source and TbADH as the scaffold retains the concept of utilising a pre-existing enzyme architecture to the advantage of ArM component binding and function. In the case of the reactions in Figures **4b** and **c**, the nicotinamide serves as the ArM cofactor rather than substrate.
The rationale behind the selection of suitable Cp*Ir catalysts for these objectives is covered in the background to Sections ***4.3.1-3***.

4.2 Structural characterisation of iridium-TbADH artificial metalloenzymes

ArM variants [Cp*Ir(5M-C37**L1**)Cl]$^{2+}$ and [Cp*Ir(7M-C110**L1**)Cl]$^{2+}$ were selected for structural characterisation on the basis that the corresponding rhodium-TbADH ArM variants showed the highest affinity for NAD(P)$^{+}$ substrates (Chapter **3**). In initial work, [Cp*Ir(Br**L1**)Cl]Cl was conjugated to TbADH mutants 5M-C37 and 7M-C110 to confirm improvement of sample homogeneity in comparison to use of rhodium catalysts. Next, the structure unmodified 5M-C37 TbADH mutant was solved to confirm that the mutations from the wildtype protein required for ArM assembly did not cause any significant alterations to the overall structure. Finally, crystal trials were completed for iridium-TbADH ArM variants with and without co-crystallisation of the NADP^{+}.

*4.2.1 Assembly and analysis of [Cp*Ir(5M-C37L1)Cl]$^{2+}$ and [Cp*Ir(7M-C110L1)Cl]$^{2+}$*

4.2.1.1 Preparation of protein and catalyst ArM components

Iridium catalyst [Cp*Ir(Br**L1**)Cl]Cl was prepared by mixing ligand **L1** with Cp*Ir dimer according to the same procedure used for [Cp*Rh(Br**L1**)Cl]Cl (Figure **4.2**). The same stock of ligand **L1** was used as in Chapter **3**. Minor contaminations from triethyl amine salts and DCM were not removed but factored into stock solution calculations. Based on the presence of these impurities in catalytically active samples of [Cp*Rh(Br**L1**)Cl]Cl, they were not expected to affect subsequent experiments. The success of metalation was confirmed by ^{1}H NMR and positive ESI-MS (Appendix **6**).

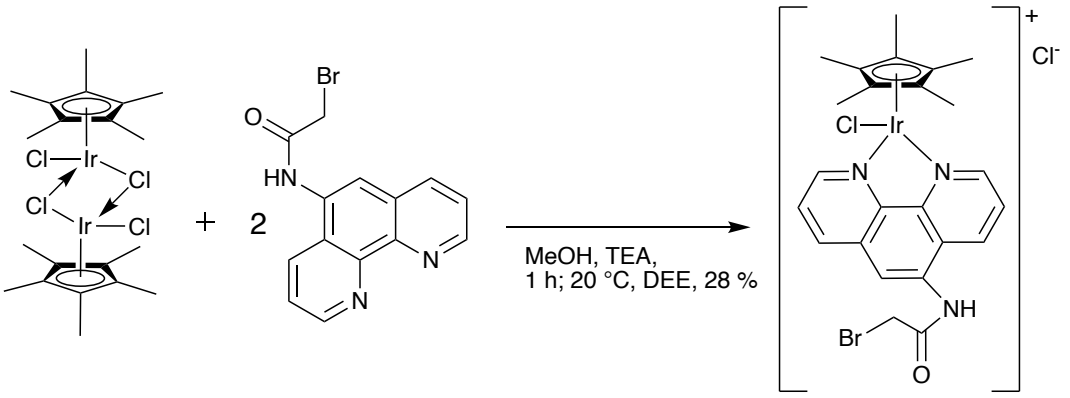

Figure 4.2: Preparation of Cp*Ir(2-bromo-N-(1,10-phenanthrolin-5-yl)acetamide)chloride

4.2.1.2 Assembly, Ellman's assay and ICP-MS analysis of ArMs

Conditions used for the bioconjugation of [Cp*Ir(Br**L1**)Cl]Cl to TbADH mutants were the same as for rhodium-based ArMs, with the exception of an increase in the molar ratio of metal catalyst to protein scaffold from 4:1 to 6:1. This change was made in attempt to improve the proportion of thiol groups successfully modified, having observed unmodified 5M-C37 TbADH in rhodium-based ArM samples (Chapter **3**). It was reasoned that with the expected decrease in non-specific catalyst-TbADH interactions owing to the substitution of rhodium for iridium, sample heterogeneity would not be significantly worsened.

Comparison between an Ellman's assay of the assembled ArMs with that of the unmodified 5M-C37 and 7M-C110 mutants indicated 61 and 79 % reduction in the available cysteine thiol groups respectively. In combination with unmodified protein availabilities of 64 and 45 % based on Bradford assay, 39 and 36 % of the total protein molecules in solution were successfully modified with iridium catalyst in these ArM samples respectively. Next, ICP-MS analysis was performed. Figure **4.3** summarises the Ellman's and ICP-MS data for all iridium-TbADH ArM variants assembled. As for the rhodium-TbADH ArMs the proportion of thiol groups modified was higher according to ICP-MS (Chapter **3**), likely owing to possible insufficient assay duration and partial accessibility of the DTNB reagent to thiol groups (Section *3.2.1.2*). Overall, samples were considered of suitable quality for further characterisation.

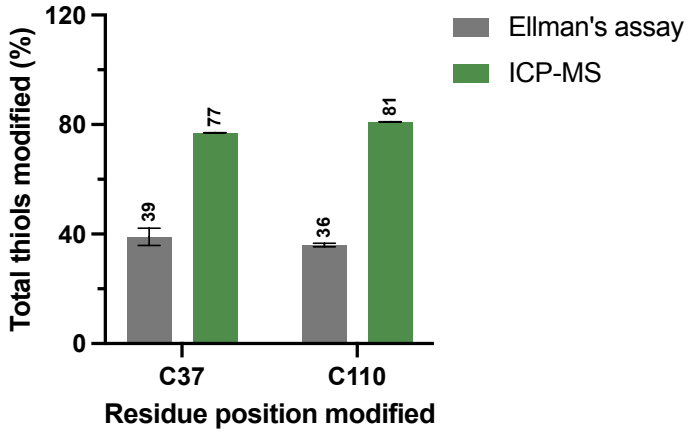

Figure 4.3: Summary of Ellman's and ICP-MS data for all iridium-based ArM variants investigated

Summary of data from Ellman's and ICP-MS analysis of TbADH samples before and after bioconjugation with [Cp*Ir(Br**L1**)Cl]Cl. The x-axis shows the single cysteine residue location in the TbADH mutant modified to produce the corresponding ArMs. The y-axis total % thiol modification values were calculated based on Bradford assay-estimated protein concentration.

4.2.1.3 ESI-TOF MS analysis of ArMs

Whole-protein denaturing ESI-TOF MS analysis was performed on the two iridium-TbADH ArMs, followed by both automatic and manual deconvolution in using tools in Bruker Compass.

In the [Cp*Ir(5M-C37**L1**)Cl]$^{2+}$ sample, the most prominent species **A** was of mass corresponding to the desirable ArM with a single covalently bound iridium catalyst, according to automatic deconvolution (Figure **4.4**). The unmodified TbADH 5M-C37 was not identified, even when the default limit on the maximum number of species to be identified was increased from 7 to 25. The secondary peaks present were of masses corresponding to the desirable ArM with a Cl atom substituted for a Br atom **B**, and lacking a Cl atom **C**, at relative intensities of 77 and 65 % respectively. Regarding the latter, hydride donation and acceptance by the metal centre should not be affected and therefore species **C** here can likely be considered catalytically active.[130] A possible location for the Br atom in Species **B** is coordinated to the iridium centre, replacing the Cl atom. Alternatively, if the Br atom remains in within bromoacetamide moiety and the Cl of the of the iridium centre is substituted for a residue such as histidine,[223] this would indicate non-specific binding of the catalyst to the unmodified 7M-110C.

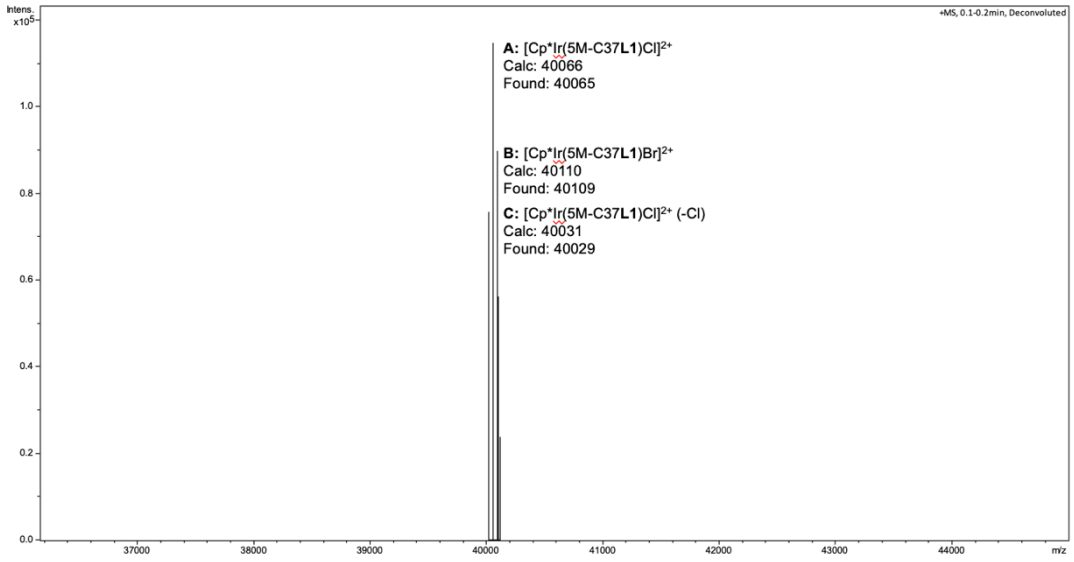

Figure 4.4: ESI-TOF MS auto-deconvoluted spectrum of [Cp*Ir(5M-C37L1)Cl]$^{2+}$

Signals were identified with mass corresponding to the desirable species **A**, in addition to **B** and **C** as described above. Bioconjugation conditions: Tris HCl buffer (100 mM, pH 7.0), 6:1 molar ratio of [Cp*Ir(Br**L1**)Cl]Cl to 5M-C37, 1 hour incubation at 30 °C with frequent sample inversion.

The existence of the desirable ArM species **A** was confirmed by manual deconvolution. Additionally, a smaller signal corresponding to the unmodified 5M-C37 **D** was identified (Figure **4.5**). These results further support the need for manual deconvolution of ArM samples, firstly to fully confirm the existence of species detected by automatic deconvolution, and secondly to detect any species missed by this algorithm, as is the case here (species **D**). Species **B** could not be reliably identified by this method in this sample.

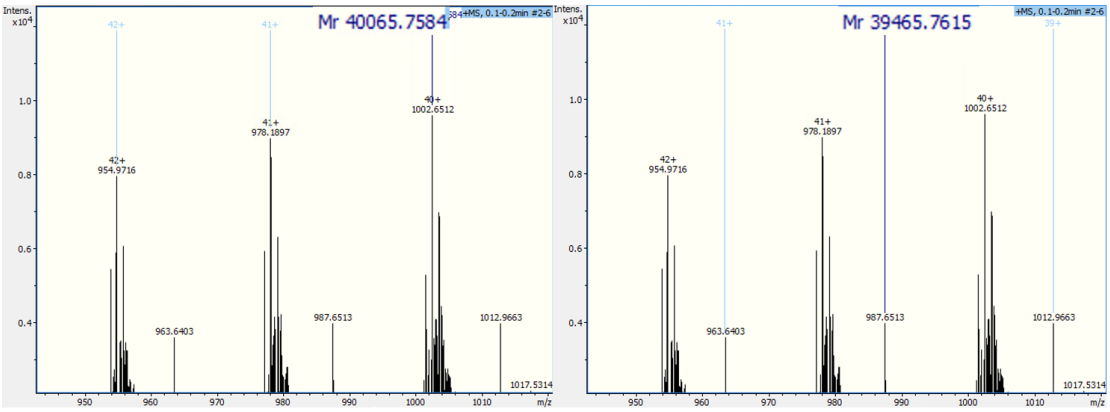

Figure 4.5: ESI-TOF MS manual-deconvoluted spectrum of [Cp*Ir(5M-C37L1)Cl]$^{2+}$
Species were identified with mass corresponding to the desirable species **A** (left) and the unmodified 5M-C37 species **D** (right). This sample was taken forward for subsequent experiments.

As for the rhodium-TbADH ArMs, the issue of instrument contamination was noted. Figure **4.6** shows a different sample of [Cp*Ir(5M-C37**L1**)Cl]$^{2+}$ (prior to contamination of the instrument), with the same species **A** and **D** identified by manual deconvolution.

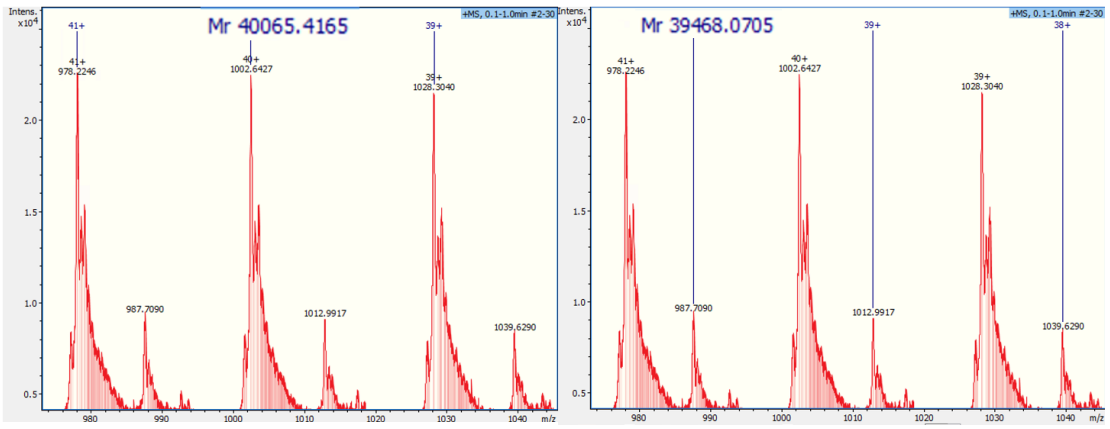

Figure 4.6: Manual-deconvoluted alternative sample of [Cp*Ir(5M-C37L1)Cl]$^{2+}$
Signals were identified with mass corresponding to the desirable species **A** (left), and the unmodified 5M-C37 species **D** (right).

Next, the ArM variant [Cp*Ir(7M-C110**L1**)Cl][2] was subject to the same analyses. The most prominent species identified by automatic deconvolution was **A** of mass corresponding to the desirable ArM. Species **B** likely corresponds to a sodium adduct of the ArM and **C** to the unmodified 7M-110C protein, at 44 and 13 % relative intensity respectively (Figure **4.7**).

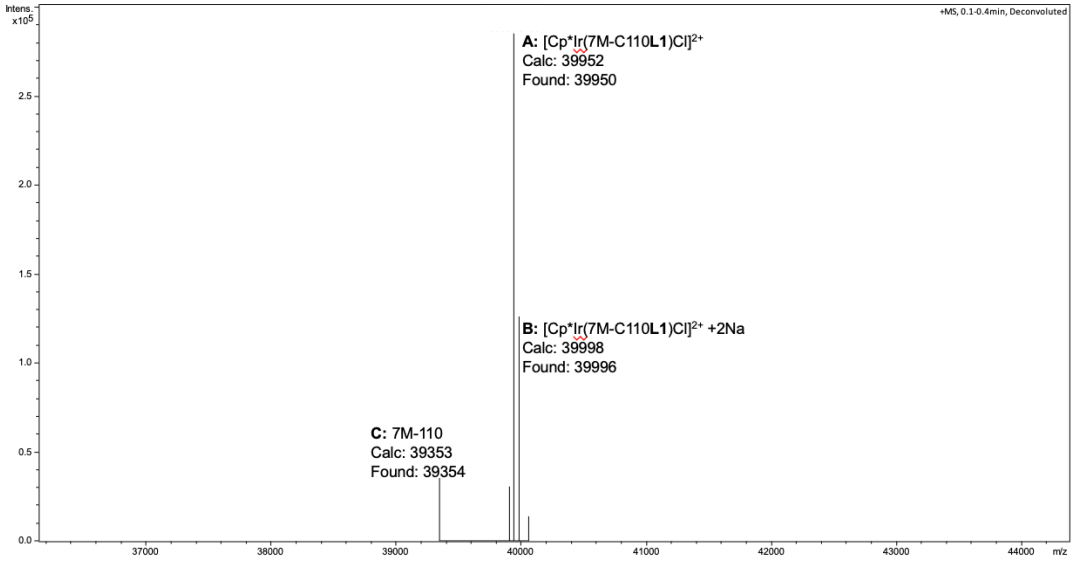

Figure 4.7: ESI-TOF MS auto-deconvoluted spectrum of [Cp*Ir(7M-C110L1)Cl]$^{2+}$
Signals were identified with mass corresponding to the desired species **A** and **B** (with two extra Na atoms), and unmodified protein **C**. Bioconjugation conditions: Tris HCl buffer (100 mM, pH 7.0), 6:1 molar ratio of [Cp*Ir(Br**L1**)Cl]Cl to 7M-C110, 1 hour incubation at 30 °C with frequent sample inversion.

Manual deconvolution of this spectrum identified species **A** and **C** (Figure **4.8**). The intensity of the unmodified species **C** was low in comparison to the desirable ArM species **A**. This can be compared to manual deconvolution of the 5M-C37 modified sample in Figure **4.5**, where the relative intensity of the unmodified species is slightly higher. Therefore, these results suggest marginally improved bioconjugation efficiency of TbADH 7M-C110 in comparison to 5M-C37.

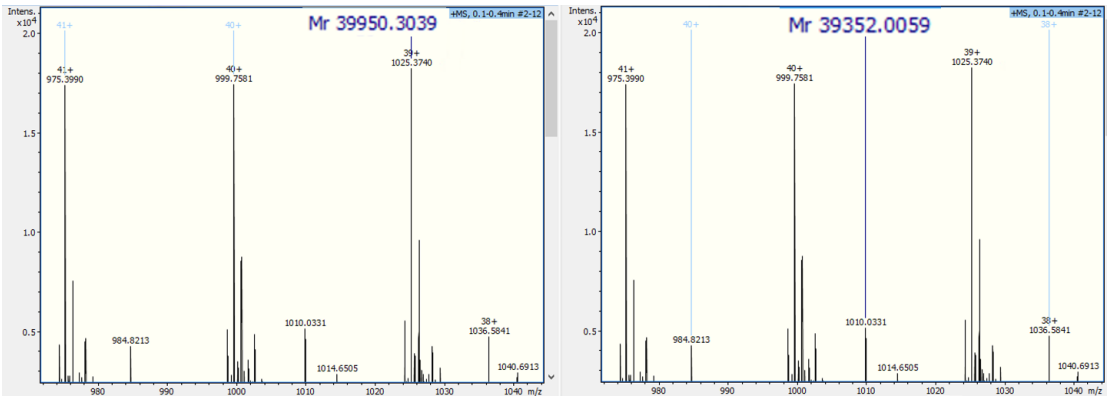

Figure 4.8: ESI-TOF MS manual-deconvoluted spectrum of [Cp*Ir(7M-C110L1)Cl]$^{2+}$
Species were identified with mass corresponding to the desirable species **A** (Mr = 39950) and the unmodified 7M-C110 species **C** (Mr = 39352).

In general, the manual deconvolution of iridium-TbADH ArM ESI-TOF MS spectra indicated a greater proportion of the desirable ArM in solution, in comparison to rhodium equivalents (Chapter **3**). For example, when comparing the [Cp*Ir(5M-C37**L1**)Cl]$^{2+}$ sample in Figure **4.6** with the equivalent rhodium-based variant in Figure **3.23**. Furthermore, the approximate percentages of successfully modified species identified by manual deconvolution broadly complied with ICP-MS results. This was true of both rhodium and iridium-based ArM samples. Therefore, this provides further support for the hypothesis of improved sample homogeneity via switching from rhodium to iridium-based ArMs. Despite this improvement, the samples obtained were not fully homogenous, and as discussed in Section *3.3.2.3* for the rhodium equivalents, the possibility of double-labelled species could not be completely ruled out. Indeed, studies on other metal complexes in the literature have shown that like rhodium, iridium can also interact with the side chains of residues such as histidine.[223-226] While manual deconvolution was considered more accurate than the automated method, the instrument contamination issue could have contributed to difficulties in identifying the presence or absence of more minor species.

Overall, these results suggest some improvement to solution homogeneity of iridium-TbADH ArMs in comparison to rhodium equivalents. This was encouraging for the prospect of solving atomic-resolution structures of these ArMs via X-ray crystallography.[222] The first step towards such structures was to confirm that an ArM constituent TbADH mutant could be successfully crystallised and would diffract to a reasonable resolution, as for wildtype TbADH[107] and other variants reported recently.[109, 112] It was reasoned that the undesirable species discussed above may be present minor enough proportions for successful crystallisation of the ArM variants to occur.

4.2.2 The structure of unmodified TbADH mutant 5M-C37

4.2.2.1 Crystallisation of unmodified 5M-C37 TbADH

For crystal trials of the unmodified 5M-C37 TbADH mutant, the purified protein was first exchanged into a suitable buffer (25 mM Tris HCl, 150 mM NaCl, pH 7.5) via size-exclusion chromatography. This buffer used recently for the crystallisation of another TbADH mutant to 2.6 Å resolution.[109] Furthermore, it is similar in composition to established purification and analyses buffers[29, 186] (Table **2.3**, Section ***2.3.4***) in which the protein is known to be stable. Crystallisation conditions for several TbADH variants have been determined. However, full screening using commercially available 96-well plates was completed in order to account for any peculiarities of the 5M-C37 mutations, as well as the presence of the N-terminal strep tag.[227] These high throughput screens (JCSG-plus Eco Screen, PACT premier, Structure Screen 1 + 2 from Molecular Dimensions) were performed with 5 and 10 mg/ml protein stock solutions using the sitting drop vapour diffusion method with a 0.8 µL drop of a 1:1 mixture of protein to well buffer next to the 75 µL well of buffer (Section ***2.8.1***). Crystallisation occurred in range of conditions after incubations at 20 °C after approximately 5 days. The most promising of those selected for diffraction with regards to appearance were cube-like crystals (Appendix **11**) formed with 0.2 M Ammonium chloride, 20 % (w/v) PEG 3350, and rod-like crystals formed with 0.1 M HEPES pH 7.0, 10 % (w/v) PEG 6000 (JCSG-plus Eco Screen wells A9 and C4 respectively). Glycerol was used as a cryoprotectant.

4.2.2.2 Structure determination of unmodified 5M-C37 TbADH

The structure of 5M-C37 TbADH was determined in the space group $P2_12_12_1$ to a resolution of 2.13 Å by molecular replacement using diffraction data collected at the Diamond Light Source synchrotron facility (Table **4.1**). The space group was found to be the same as that recently reported for another mutant of apo-TbADH, and with similar the unit cell dimensions.[109] Overall data completeness was 100 %, and overall signal to noise ratio ($I/\sigma I$) and redundancy values were 8.9 and 6.8 respectively.

Table 4.1: Crystallisation and refinement data for 5M-C37 TbADH

Data collection	
Beamline	Diamond Light Source, i03
Space group	P 21 21 21
Cell dimensions	
A, B, C	79.54, 135.25, 144.21
α, β, γ	90.00, 90.00, 90.00
Resolution	2.13 – 53.42 (2.13 – 2.17)
R_{merge}	0.166 (2.734)
$I/\sigma I$	8.9 (0.6)
Completeness (%)	100 (99.5)
Redundancy	6.8 (7.0)
Refinement	
Resolution	2.13
No. reflections	87681
R_{work} / R_{free}	18.3 / 22.6
No. atoms	
Protein	10601
Ligands (glycerol)	30
Water	330
B-factors (Å^2)	
Protein	35.82
Ligands (glycerol)	51.12
Water	47.33
R.m.s deviations	
Bond lengths (Å)	0.01
Bond angles (°)	1.64

Matthews Cell Content Analysis (CCP4)[206] confirmed the presence of four macromolecular subunits (chains) as expected. Subsequent data processing steps were performed using Phenix,[205] CCP4i2[210] and Coot.[208]

To generate a suitable model for initial phase estimation, each chain of wildtype holo-TbADH (PDB: 1YKF)[107] was modified by introducing the appropriate 5M-C37 mutations (Table **2.1**) as well as removing the native $NADP^+$ and zinc ion. The R_{work} / R_{free} values of the resulting preliminary structure following a single round of refinement were 23.7 / 27.5 %. Initial modelling was software-assisted with the use of Phenix AutoBuild under default parameters, bringing these values down to 22.5 / 25.8 %.

Subsequent rounds of manual model building in Coot (described below) and refinement in CCP4i2 Refmac5 resulted in final R_{work} / R_{free} values of 18.3 and 22.6 % respectively (Table **4.1**).

Manual model building in Coot began with improvement of protein density fit analysis, Ramachandran plot and rotamer analysis in all four polypeptide chains. As expected according to sequencing of the 5M-C37 TbADH plasmid DNA construct, 352 residues were identified in each chain (comprising the mutated protein product of the 1059 bp TBAD gene). Meanwhile, extra residues were identified at the N-termini of the chains corresponding to the thrombin cleavage site which is situated directly upstream of start codon in the plasmid construct. All six residues of the thrombin cleavage site could be modelled into the electron density at the N-terminus of chain C, while fewer could be modelled into chains A, B and D. This may be explained by higher temperature factors at the N-termini of these chains in comparison to C, owing to greater distances to the next macromolecule in the asymmetric unit. Residues of the N-terminal strep tag (further upstream from the thrombin cleavage site) could not be identified in any of the chains, also likely owing to high temperature factors.

A total of 330 waters were added to the model via a combination of the find waters feature in Coot and the add waters feature in Refmac5. Five separate regions of non-protein positive electron density were also observed. Based on size and shape, these were thought to correspond to glycerol from the cryoprotectant solution used in crystal freezing. The glycerol molecules were modelled in using the fit ligand feature in Coot, followed by a round of refinement.

Electron density corresponding to the five mutations introduced to 5M-C37 TbADH (Table **2.1**) was correct in all four subunits. It was expected that these mutations would not cause any significant structural deviations from the wildtype protein, either in terms of overall fold[107] or to the nicotinamide binding pocket. Indeed, no changes in the stability of the protein have been observed practically in preparation or analyses as a result of these mutations, either here or in previous work.[29, 186] An alignment of the crystal structure of 5M-C37 TbADH with wildtype holo-TbADH (PDB: 1YKF) supports this theory, with no major deviations observed (Figure **4.9**). Successful determination of the unmodified 5M-C37 TbADH structure to a resolution of 2.13 Å confirms scope for this process to be repeated with iridium-TbADH ArM variants.

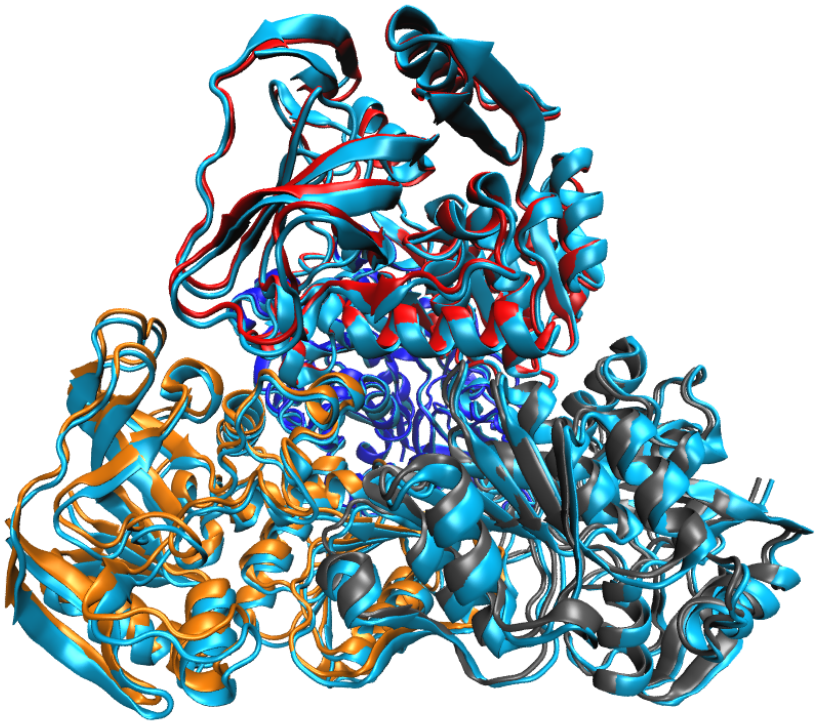

Figure 4.9: Overall structure of 5M-C37 TbADH aligned with wildtype TbADH

Final model of the mutant following all rounds of modelling and refinement coloured by chain and aligned using VMD[111] with wildtype TbADH coloured in cyan (PDB 1YKF).[107]

*4.2.3 The structure of [Cp*Ir(7M-C110L1)Cl]$^{2+}$ with NADP^{+}*

4.2.3.1 Crystallisation of iridium-TbADH ArMs

For the crystallisation of ArM variants, all samples were exchanged into the same buffer used for unmodified 5M-C37 (25 mM Tris HCl, 150 mM NaCl, pH 7.5) via size-exclusion chromatography. Protein stock solutions of 5 and 10 mg/ml were subject to screening with and without 2 mM NADP^{+}. This final cofactor concentration was selected based on reported successful co-crystallisation with wildtype TbADH.[220] The oxidised rather than reduced form of the cofactor was selected to avoid *in-crystallo* kinetic activity. It is known that NAD(P)H can readily transfer hydride to the iridium centre of such complexes.[9] Furthermore, NADP^{+} is the substrate for rhodium-TbADH ArMs on which structural insight was to be obtained. Crystallisation occurred in range of conditions after approximately 5 days of incubation at 20 °C.

As the commercial screen which yielded the most hit conditions for crystallisation of 5M-C37, JCSG-plus Eco Screen was selected for the initial round of crystal trials on [Cp*Ir(5M-C37**L1**)Cl]$^{2+}$. Crystals were obtained which diffracted, but to ~4 Å in contrast to the ~2 Å achieved with the unmodified protein. Therefore, screening around the hit conditions was completed in attempt to improve the resolution (Appendix **2**). Sitting drop vapour diffusion with a 2 µL drop of a 1:1 mixture protein to well buffer next to a 400 µL of well of buffer yielded needle-like crystals. Those containing NADP^{+} of hit condition 0.1 M MES pH 6.5, 40 % (v/v) MPD, 5 % (w/v) PEG 8000 diffracted to ~2 Å. As MPD in the condition was >30 %, no extra cryoprotectant was used.

[Cp*Ir(7M-C110**L1**)Cl]$^{2+}$ was subject to the same commercial screen with a 0.8 µL drop of a 1:1 mixture of protein to well buffer next to the 75 µL well of buffer. Cube-like crystals (Appendix **12**) containing NADP^{+} formed with 0.1 M HEPES pH 7.5, 10 % (w/v) PEG 8000, 8 % (w/v) ethylene glycol and diffracted to ~2 Å resolution. Ethylene glycol was used as a cryoprotectant.

*4.2.3.2 Structural insights into [Cp*Ir(7M-C110**L1**)Cl]$^{2+}$ complex and NADP$^+$ binding*

Molecular replacement of ArM variant [Cp*Ir(5M-C37**L1**)Cl]$^{2+}$ with and without NADP$^+$ was completed using the final refinement of 5M-C37 as the initial model with several crystal data sets. Positive electron density corresponding to the iridium complex or NADP$^+$ could not be clearly identified in any of the four subunits. It is possible that the occupancies of the complex and cofactor are low under the hit crystallisation conditions. Furthermore, the space group of the crystal data appears to be different to that of 5M-C37 and other TbADH mutants. This makes the structure more challenging to model and refine to a respectable R_{free} value following molecular replacement using one of the mutant structures. In the interest of prioritising structural insight into ArM substrate and scaffold interactions, focus was shifted to [Cp*Ir(7M-C110**L1**)Cl]$^{2+}$. This variant showed the most promising kinetics and docking results with regards to NADP$^+$ binding in Chapter **3**.

The structure of ArM variant [Cp*Ir(7M-C110**L1**)Cl]$^{2+}$ with NADP$^+$ bound was determined in the space group $P2_12_12_1$ to a resolution of 1.81 Å by molecular replacement (Table **4.2**). This was the same space group used for the unmodified 5M-C37 structure, and unit cell dimensions were almost identical. Overall data completeness was 100 %, and overall signal to noise ratio (I/σI) and redundancy were 8.5 and 13.7 respectively.

The model used for initial phase estimation was the final refinement of 5M-C37 with the appropriate 7M-C110 mutations introduced (Table **2.1**). The R_{work} / R_{free} values of the resulting preliminary structure following a single round of refinement were 27.7 / 31.3 %. Initial modelling was software-assisted with the use of Phenix AutoBuild under default parameters, bringing these values down to 24.6 / 27.6 %. Subsequent rounds of manual model building in Coot and refinement in CCP4i2 Refmac5 resulted in final R_{work} / R_{free} values of 19.8 and 23.1 % respectively (Table **4.2**). This included modelling and refinement of both the iridium complex and NADP$^+$ ligands as described below. An alignment of the final model with wildtype TbADH confirmed that as for the unmodified 5M-C37 mutant, there was no major structural deviations (Figure **4.10**). Therefore, this structure provides strong indication that the ArM functions with the TbADH scaffold fully folded as expected.

Table 4.2: Crystallisation and refinement data for [Cp*Ir(7M-C110L1)Cl]$^{2+}$

Data collection	
Beamline	Diamond Light Source, i04
Space group	P 21 21 21
Cell dimensions	
A, B, C	79.90, 136.04, 143.92
α, β, γ	90.00, 90.00, 90.00
Resolution	1.81 – 53.47 (1.81 – 1.84)
R_{merge}	0.130 (3.529)
$I/\sigma I$	8.5 (0.2)
Completeness %	100 (99.8)
Redundancy	13.7 (14)
Refinement	
Resolution	1.81
No. reflections	143071
R_{work} / R_{free}	19.8 / 23.1
No. atoms	
Protein	10496
Ligand	308
Water	329
B-factors Å^2	
Protein	31.25
Ligand	52.23
Water	42.33
R.m.s deviations	
Bond lengths Å	0.01
Bond angles °	1.48

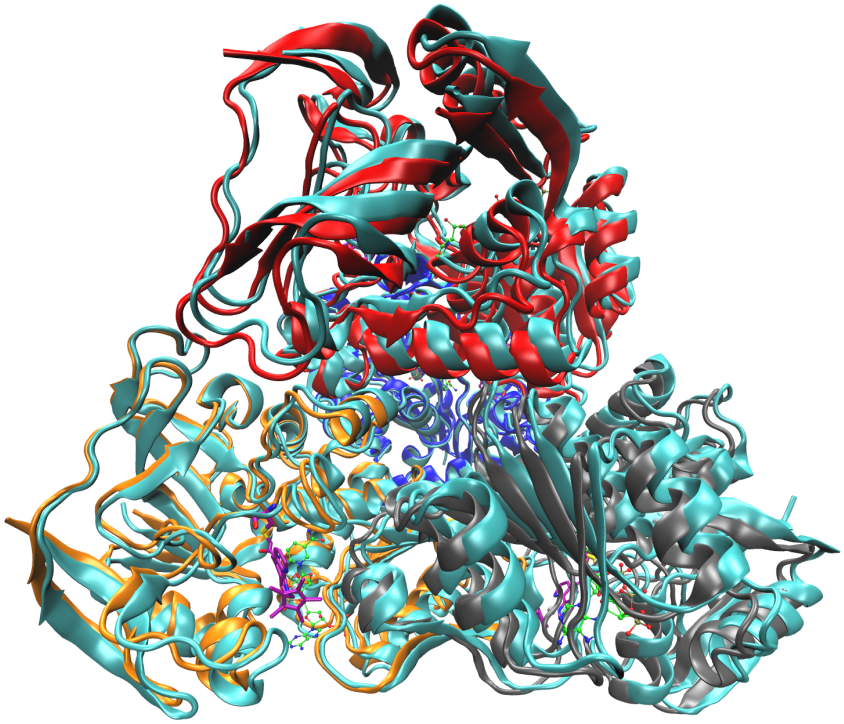

Figure 4.10: Overall structure of [Cp*Ir(7M-C110L1)Cl]$^{2+}$ with NADP^{+} bound

Final model of the ArM structure following all rounds of modelling and refinement coloured by chain and aligned using VMD[111] with wildtype TbADH coloured in cyan (PDB 1YKF).[107]

Positive difference density was identified in the Fo-Fc map which clearly corresponded to the C110-bound iridium complex in all four of the subunits. The complex ligand CIF file was generated with restraints and covalent linkage information using Phenix eLBOW. After manual fitting to the anomalous density in each subunit in Coot, Phenix ReadySet was used to prepare the ligand and protein files for refinement. Refinement and selection of appropriate atom occupancies was then completed in CCP4i2, Refmac5 and Coot respectively. To correct small areas of negative difference density following initial refinement, the occupancies of all complex atoms were set to 90 % in chains A-C, and 85 % in chain D. In conjunction with whole-protein ESI-MS TOF results, it is likely that not all of the molecules within the crystal contain the covalently bound complex. Aromatic hydrogen bonds were identified from Y267 and the backbone of L107 to the phenanthroline, which may contribute to stabilisation of the complex in this orientation (Figure **4.11a**).

The complex was found to be oriented in the same direction in all subunits of the ArM crystal structure, with some minor deviations in the position of the Cp* ring. (Figure **4.12**).

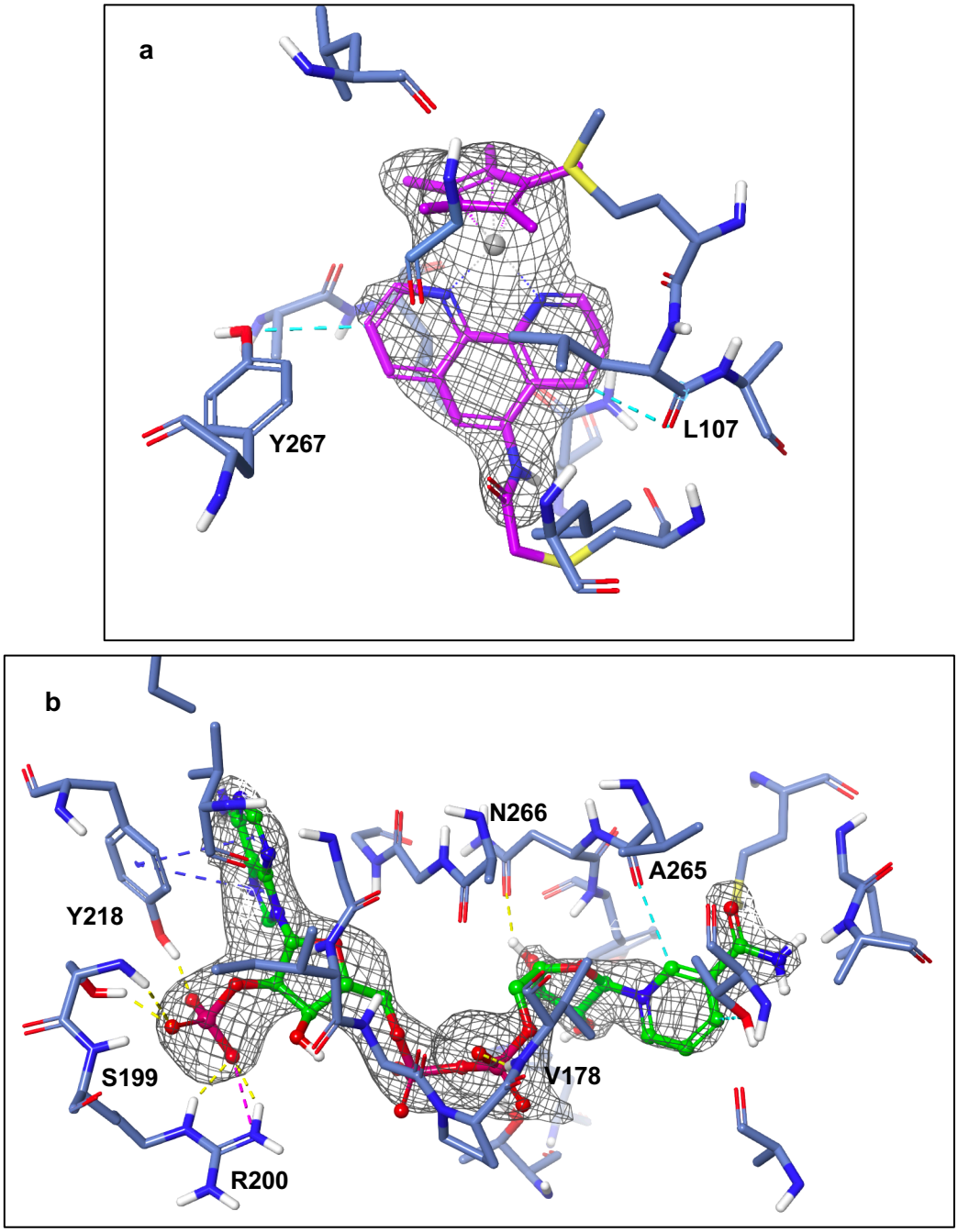

Figure 4.11: [Cp*Ir(7M-C110L1)Cl]$^{2+}$ complex and NADP^{+} *in crystallo* binding sites

Omit maps were generated for both modelled ligands **a** the complex (pink) and **b** NADP^{+} (green) by setting all atom occupancies to zero, followed by a single round of refinement. The Fo-Fc difference density is shown as grey mesh contoured at 3 and 2.5 σ for the complex and NADP^{+} respectively. Residues within a 3 Å radius of the ligands are displayed in ice blue by atom type, with those labelled which form protein-ligand interactions identified in Schrodinger Maestro (H-bonds = yellow, aromatic H-bonds = cyan, salt bridges = pink, pi-stacking = blue).

Positive difference density was also identified for $NADP^+$ in all four subunits of the ArM (Figure **4.11b**). The ligand was imported into Coot from the standard CIF dictionary followed by modelling and refinement. Numerous protein-ligand interactions were identified between the ArM TbADH scaffold and *in crystallo* $NADP^+$, including pi-stacking between the adenine and Y218, and extensive phosphate hydrogen bonding. Comparison of these interactions with those listed in Table **3.3** (Section ***3.2.3***) for the cofactor in wildtype TbADH[107] suggests similar affinities for the cofactor between the natural enzyme and ArM.

The binding site of $NADP^+$ was found to be consistent between ArM subunits (Figure **4.12**). This is with the exception of the adenine and ribose phosphate in subunit D, the former appearing to interact with R200 instead of Y218. However, the positive difference density corresponding to these moieties in this alternative conformer was poorly defined and only observed in subunit D (Appendix **3**).

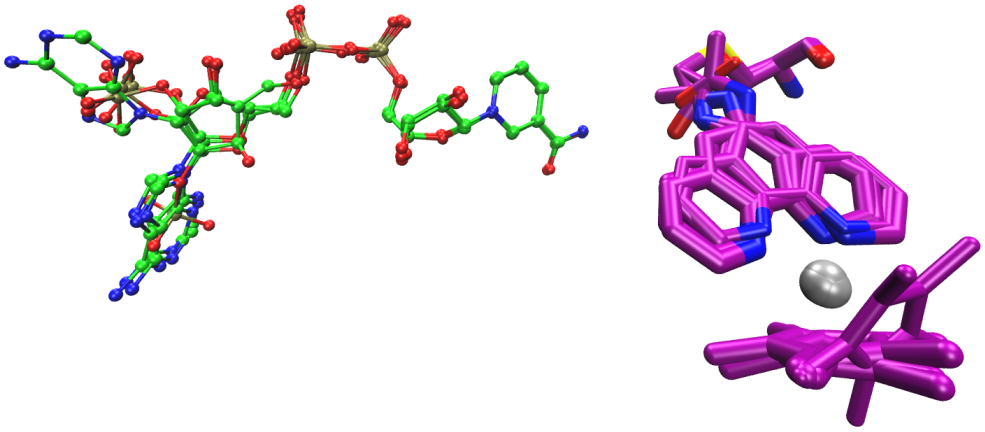

Figure 4.12: Alignment of $[Cp^*Ir(7M\text{-}C110L1)Cl]^{2+}$ subunits

The four subunits of the final model were aligned by protein backbone (omitted from view for clarity). The backbone RMSD values from subunit A were 0.23, 0.27 and 0.20 Å for subunits B, C and D respectively. The iridium complex and $NADP^+$ are coloured as in figure **4.11**.

Regarding the relative positions of the iridium complex and $NADP^+$ *in crystallo*, it is clear that the complex is oriented away from the nicotinamide and substrate binding pockets in $[Cp^*Ir(7M\text{-}C110\mathbf{L1})Cl]^{2+}$. Meanwhile, $NADP^+$ binds in almost exactly the same location and orientation as in wildtype TbADH (Figure **4.13**). It should be noted that the positive difference density corresponding to the complex in location 110-modified samples without $NADP^+$ co-crystallisation was more ambiguous. However, it was confirmed that this density was in the same orientation as in the holo-ArM structure, in all subunits of the multiple samples subjected to molecular replacement.

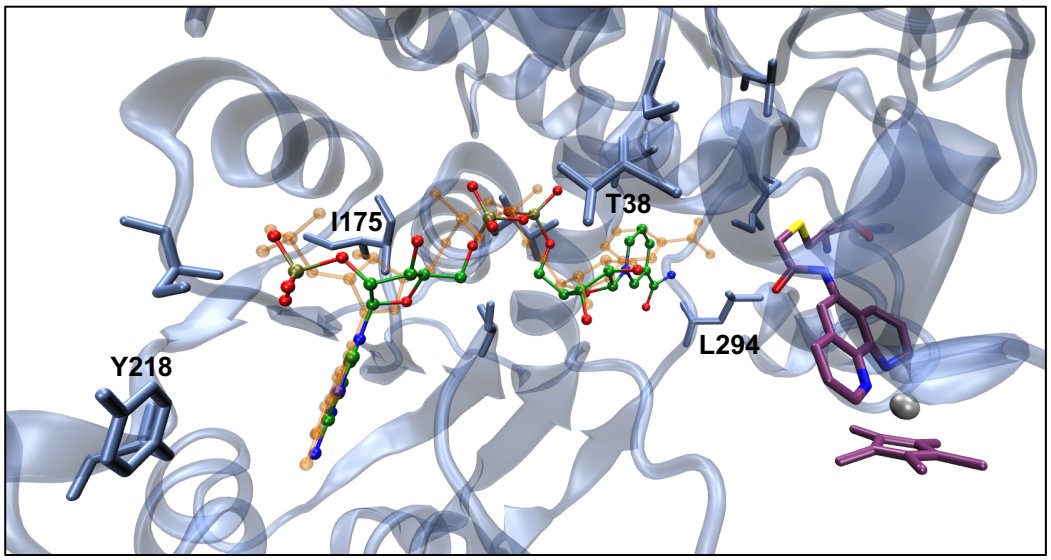

Figure 4.13: Relative positions of the complex and in NADP$^+$ in [Cp*Ir(7M-C110L1)Cl]$^{2+}$
The modelled complex and NADP$^+$ are shown by atom type in purple and green respectively. Select residues lining the natural TbADH nicotinamide and substrate binding pockets are highlighted as in Figures **3.13-17**. Overlayed in transparent orange is *in-crystallo* NADP$^+$ from wildtype TbADH (PDB: 1YKF).[107]

This orientation of the complex is very similar to that of the equivalent rhodium catalyst in the secondary (lower-ranked) covalent docking pose [Cp*Rh^{Out}(7M-C110**L1**)Cl]$^{2+}$ (Section ***3.3.1***). Figure **4.14a** shows an alignment this docking with the crystal structure. With the complex-bound C110 pointing towards the surface of the TbADH scaffold, the iridium centre is 13.24 Å away from the nicotinamide C4 *in-crystallo*. In the context of nicotinamide reduction by the rhodium-TbADH ArM counterpart, this Ir-C4 distance is clearly too great for catalytic hydride transfer to occur. In contrast, the highest-ranked covalent docking pose of the rhodium complex was oriented in the opposite direction and towards the interior of the substrate binding pocket (Figure **4.14b**). As discussed in Chapter **3**, this pose and subsequent supramolecular docking poses of NADP$^+$ provide support for the conclusions drawn from kinetics studies.

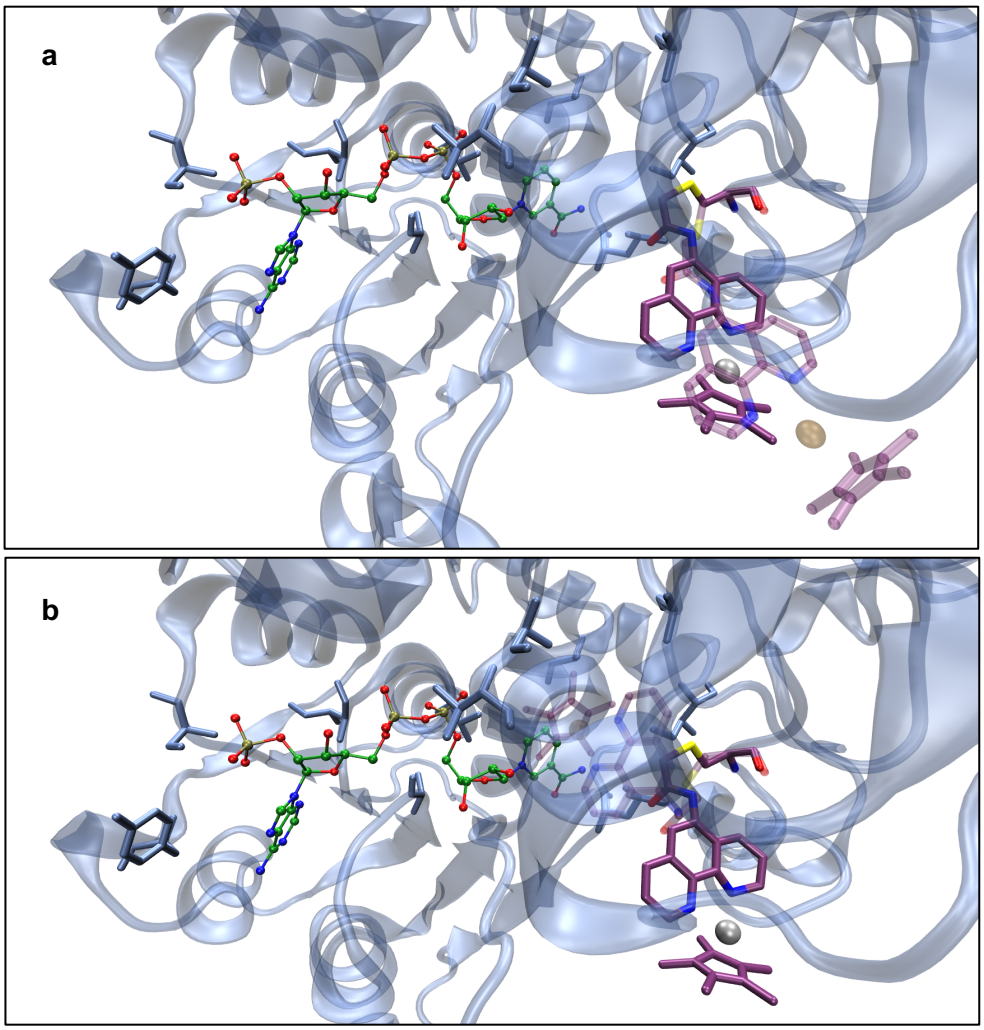

Figure 4.14: Alignment of [Cp*Ir(7M-C110L1)Cl]$^{2+}$ crystal structure with docking results
Panel **a** shows alignment of the crystal structure with the secondary [Cp*Rh^{Out}(7M-C110**L1**)Cl]$^{2+}$ covalent docking pose, and panel **b** with the highest-ranked pose (Section ***3.3.1***). In both panels, the rhodium complexes from docking are shown in transparent purple. Components of the crystal structure are displayed as in Figure **4.12**.

The possibility that reduction of NADP$^+$ occurs exclusively with the catalyst oriented as observed in the crystal structure was considered. However, this would require external interaction of the nicotinamide C4 with the metal centre on the opposite side of the subunit to the natural nicotinamide pocket entrance. In contrast to internal positioning of both the catalyst and NADP$^+$, these interactions would likely occur *a)* without binding of NADP$^+$ to a specific site, and *b)* with increased access of the substrate to the catalyst. Therefore, the values of both *a)* K_M and *b)* TOF_{max} for this residue location 110-modified ArM variant would be higher than those of the location 37-modified variant. Indeed, NADP$^+$ must bind to a relatively internal sight in the latter variant owing to the remoteness of this residue location from the surface of TbADH, and this was supported by docking. On the contrary, both K_M and TOF_{max} values were

found to be lower for the 110-modified variant (Section ***3.3.3***). In other words, the fact that estimated $NADP^+$ affinity of $[Cp^*Rh(7M\text{-}C110\mathbf{L1})Cl]^{2+}$ was the highest of the three variants tested suggests that the crystal structure may not provide the full picture of complex orientation.

Alternatively, it was reasoned that two different complex orientations via flexibility of the C110 covalent anchor may be possible in solution. The “in” conformation which was suggested by docking places the complex within the natural TbADH substrate binding pocket. On the other hand, in the “out” *in-crystallo* orientation, the phenanthroline plane is flanked by a deep cleft which leads into the natural TbADH substrate binding pocket (Figure **4.15a**). In wildtype TbADH, this cleft is lined with residues I49, L107, W110, Y267, L294, and C283, M285 from the adjacent subunit,[108] while in $[Cp^*Ir(7M\text{-}C110\mathbf{L1})Cl]^{2+}$ the tryptophan and cysteine have been mutated to C110 and A283 respectively. Interestingly, the position adopted by Y267 in the ArM is different to that in wildtype TbADH, possibly as a result of subtle deviations in secondary structure elements. This conformation was found to be consistent between subunits, and (in combination with C283A) generates marginally more space within the complex-flanking cleft (Figure **4.15b**). Assuming some flexibility of cleft-lining residues in solution, this tentatively suggests that the complex can move from the “out” to the “in” conformation. Based on the absence of electron density corresponding to the latter in any of the crystal data sets collected, it is clear that only the “out” conformation crystallised under the specific conditions analysed.

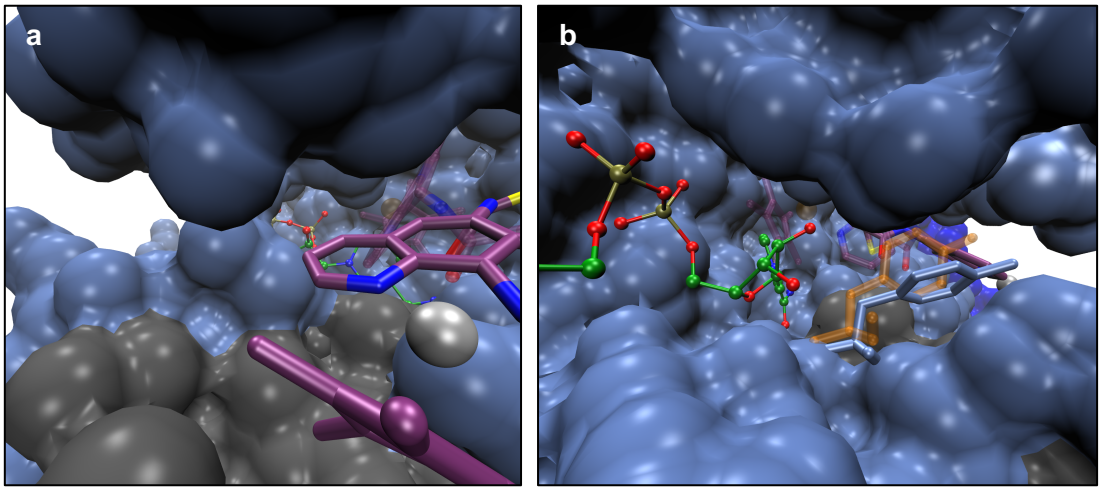

Figure 4.15: Views of the [Cp*Ir(7M-C110L1)Cl]$^{2+}$ complex-flanking cleft

Surface view of the ArM crystal structure coloured by chain and shown from two perspectives, both showing the ArM *in crystallo* complex and NADP^{+} in purple and green respectively, and the aligned [Cp*Rh(7M-C110**L1**)Cl]$^{2+}$ covalent docking "in" pose in transparent purple. Perspective **a** is along the plane of the *in crystallo* complex phenanthroline and into natural TbADH substrate binding pocket. **b** is along the nicotinamide binding pocket and into the substrate binding pocket with Y267 of the ArM coloured by chain in stick representation. Also in perspective **b** is Y267 of the aligned wildtype TbADH in transparent orange.

Overall, the crystal structure of [Cp*Ir(7M-C110**L1**)Cl]$^{2+}$ provides insight into the interactions of the scaffold, catalyst, and substrate components. The NADP^{+} binding site hints at successful utilisation of the naturally evolved pocket to the advantage of ArM catalytic efficiency. Furthermore, it is possible that the metal complex can move from the orientation observed *in crystallo* for catalytic interaction with the nicotinamide C4, as observed in docking studies.

4.2.4 Conclusions

The objective of Section **4.2** was to gain full structural understanding of TbADH-ArM catalyst, substrate, and scaffold interactions. Variants based on modification of residue locations 37 and 110 were selected based on promising kinetics and docking results from Chapter **3**. It was reasoned that the iridium equivalents to these ArMs would provide samples of suitable homogeneity for crystal trials. Therefore, [Cp*Ir(7M-C110**L1**)Cl]$^{2+}$ and [Cp*Ir(5M-C37**L1**)Cl]$^{2+}$ were assembled and characterised. Overall, both variants displayed promising results from mass spectrometric analysis. Binding of the catalyst to residue locations other than the desirable C37 or C110 was found to be unlikely. Based on these results, it was concluded that the TbADH-ArMs based on iridium would be more suitable for crystal trials than the rhodium equivalents.

As preliminary work towards the structure determination of iridium-TbADH ArMs, the unmodified C37-5M TbADH was subject to crystal trials. The protein buffer was selected based on the recently solved structure of a different mutant, and screening of a range of commercial crystallisation conditions was performed. As expected, no significant changes to the overall fold of TbADH were observed in comparison to the wildtype protein. The structure was solved to a resolution of 2.13 Å, providing promise for interesting structural insight into TbADH-ArMs.

Crystallisation, X-ray diffraction, molecular replacement and initial refinement was completed for ArM variant [Cp*Ir(5M-C37**L1**)Cl]$^{2+}$. However, positive difference density corresponding to the covalently anchored complex was ambiguous.

Focus was switched to the 110-modified variant, which had displayed the most promising kinetics and docking results in the previous chapter. Clear positive difference density was identified corresponding to the iridium complex and NADP$^+$ in all four subunits. The latter was observed in same location as in wildtype TbADH, forming similar protein-ligand interactions. Indeed, relocation of the catalyst from residue locations 243 or 37 appears to have the desired effect of enabling NADP$^+$ binding at this site. However, the orientation of the catalyst positions the metal centre 13.24 Å away from the nicotinamide C4. While this contrasts with the catalytically active orientation suggested by docking, visual inspection of the two orientations tentatively suggests that there is space available for the catalyst to move between the two conformations in solution.

4.3 Investigation of iridium-TbADH ArMs for reduction applications

Having characterised and solved the structure of [Cp*Ir(7M-C110**L1**)Cl]$^{2+}$, our focus was shifted to the potential reduction applications of iridium-TbADH ArMs. The variants were first tested for the recycling of nicotinamide cofactors as for their rhodium counterparts in Chapter **3**, followed by efforts to investigate ArM catalysis of imine and quinone reduction.

4.3.1 Iridium-TbADH ArMs for nicotinamide reduction

4.3.1.1 Background

Recently reported sulfonamide-containing Cp*Ir catalysts have displayed impressive rates of nicotinamide cofactor reduction, with reported TOF values of up to 2321 h^{-1} for NAD$^+$.[131] There have also been recent reports of Cp*-benzoic acid catalysts with displaying TOF values of up to 7825 h^{-1}.[116] Assay conditions were similar to those used to measure the TOFs of rhodium catalysts in Chapter **3** or with lower temperatures, using phosphite or formate as the hydride source.

Catalysts containing such ligands would initially appear the most obvious choice for covalent anchoring to TbADH for the purposes of nicotinamide reduction (Figure **4.1**, Section **4.1**). However, previous work by Dr M. Basle showed a lack of compatibility between this scaffold and iridium-sulfonamide piano-stool catalysts. Upon mixing, protein precipitation was observed with all TbADH mutants tested.[186] In contrast, iridium-phenanthroline catalysts display good compatibility. [Cp*Ir(Br**L1**)Cl]Cl was successfully used in the assembly of ArMs based on TbADH mutants 5M-C37 and 7M-110C (Section ***4.2.1***). As mentioned in Chapter **1**, other Cp*Ir piano-stool catalysts more similar to [Cp*Ir(Br**L1**)Cl]Cl such as those in Figure **4.16** have also been shown to catalyse NAD$^+$ reduction.[83, 124] The question of whether TbADH ArMs based on [Cp*Ir(Br**L1**)Cl]Cl could be used to catalyse nicotinamide reduction arose. It was noted that the reported TOF value for reduction of NAD$^+$ by catalyst **11**[83] (Figure **4.16**) is 23 h^{-1} which is approximately 5-fold lower than that of [Cp*Rh(Br**L1**)Cl]Cl under similar conditions (Chapter **3**). Therefore, for the purposes of regenerating nicotinamide cofactors for use in cascade reactions,[29] the usefulness of ArMs assembled using [Cp*Ir(Br**L1**)Cl]Cl would appear to be limited, assuming similar performance. However, it was reasoned that measuring the nicotinamide reduction activity of iridium-TbADH ArMs would serve as proof of principle for catalytic functionality. Differences in nicotinamide reduction rates between different ArM genetic variants [Cp*Ir(5M-C37**L1**)Cl]$^{2+}$ and [Cp*Ir(7M-C110**L1**)Cl]$^{2+}$ may provide useful information towards the

reduction of more interesting substrates. These variants were selected on the basis that the corresponding rhodium variants had displayed the highest estimated $NAD(P)^+$ affinities according to the K_M values.

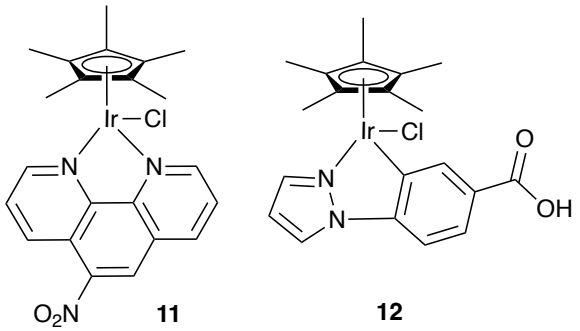

Figure 4.16: Cp*Ir catalysts for the reduction of NAD^+
Literature reported catalysts **11**[83] and **12**.[124]

4.3.1.2 Measurement of catalytic nicotinamide reduction via UV-visible spectroscopy

The first step was to confirm $NAD(P)^+$ reduction activity of the free [Cp*Ir(Br**L1**)Cl]Cl catalyst using formate as the hydride donor via measurement of absorbance at 340 nm. TOF h^{-1} values were of the same order of magnitude reported for the catalyst **12** (Figure **4.16**) under similar conditions[124], with no significant difference observed between the two natural nicotinamide cofactors (Table **4.3**). $NAD(P)^+$ reduction rates of rhodium-TbADH ArMs were approximately 20 % of free rhodium catalysts owing to reduced substrate accessibility (Chapter **3**, [29, 186, 212]). Therefore, it was assumed that this ratio would be similar for iridium catalysts and ArMs, indicating that the latter rates would be measurable in the order of TOF h^{-1}. Meanwhile, [Cp*Ir(Br**L1**)Cl]Cl BNA^+ reduction activity was approximately 10-fold lower than for $NAD(P)^+$ (Table **4.3**), comparable to the 5-fold difference observed with rhodium catalysts. Based on these values, the mimic was not taken forward for subsequent ArM assays, under the assumption that rates would be too low for quantification.

Table 4.3: Reduction of nicotinamides by [Cp*Ir(BrL1)Cl]Cl

Catalyst	Nicotinamide substrate	TOF (h^{-1})
[Cp*Ir(Br**L1**)Cl]Cl	NAD^+	61.8 ± 1.12
	$NADP^+$	60.7 ± 0.66
	BNA^+	6.1 ± 0.09

Catalyst (12.5 μM) was mixed with nicotinamide substrate (1 mM) in sodium formate (500 mM) sodium phosphate buffer (100 mM, pH 7.0), 50 °C. The reaction was monitored at 340 nm for 180 seconds. The standard errors of mean are shown (n = 3). The extinction coefficients were 6220 M^{-1} cm^{-1} and 4800 M^{-1} cm^{-1} for $NAD(P)^+$ and BNA^+ respectively at 340 nm.

In anticipation of lower iridium-TbADH ArM rates in comparison to the rhodium counterparts, final ArM concentration according to protein concentration was increased from 12.5 to 37.5 μM. The substrate concentration was doubled to 2 mM, found to be saturating for nicotinamide reduction using rhodium-TbADH ArMs (Chapter **3**). ICP-MS was used to determine the concentration of ArM in solution for the purposes of rate calculations (Table **4.4**). These results demonstrate the catalytic functionality of iridium-TbADH ArMs, indicating promise from further work to achieve more useful or novel functionality. With regards to the effect of catalyst location on nicotinamide reduction performance, the results in Table **4.4** indicates that [Cp*Ir(7M-C110**L1**)Cl]$^{2+}$ was marginally more active for $NAD(P)^+$ reduction than [Cp*Ir(5M-C37**L1**)Cl]$^{2+}$.

Table 4.4: Iridium-TbADH ArM nicotinamide reduction activity

Catalyst	Nicotinamide substrate	TOF (h^{-1})
[Cp*Ir(5M-C37**L1**)Cl]$^{2+}$	NAD^+	4.3 ± 0.21
	$NADP^+$	4.6 ± 0.5
[Cp*Ir(7M-C110**L1**)Cl]$^{2+}$	NAD^+	5.7 ± 0.28
	$NADP^+$	5.3 ± 0.01

Catalyst (37.5 μM) was mixed with nicotinamide substrate (2 mM) in sodium formate (500 mM) sodium phosphate buffer (100 mM, pH 7.0), 50 °C. The reaction was monitored at 340 nm for 900 seconds. The standard errors of mean are shown (n = 2). The extinction coefficients for $NAD(P)^+$ was 6220 M^{-1} cm^{-1} at 340 nm.

4.3.1.3 Conclusions

TOF values for the reduction of natural nicotinamide substrates with the free [Cp*Ir(Br**L1**)Cl]Cl were as expected based on literature reported values for similar catalysts. Meanwhile the calculated TOF value for BNA^+ reduction was considered too low to take forward for measurement of ArM activity. ArM variants based on TbADH mutants 5M-C37 and 7M-C110 were found to be catalytically active for the reduction of $NAD(P)^+$.

These results provide support for the catalytic functionality of iridium-TbADH ArMs, providing proof of principle for the prospect of more interesting or useful applications via modification of the catalyst. The marginally greater reduction of the residue location 110-modfied variant provides scope to further explore differences between these ArMs.

4.3.2 Iridium-TbADH ArMs for asymmetric imine reduction

4.3.2.1 Background

The genetically manipulable protein environment of ArMs has been shown to impart enantioselectivity on iridium catalysts incapable of this important feature when used free in solution. For example, a Cp*Ir(III) piano-stool catalyst was incorporated into streptavidin to generate an artificial imine reductase. It was shown that enantioselectivity in chiral amine production could be almost completely inverted by mutation of residue 112 from a neutral residue to a cationic residue.[165] Other more recent studies have achieved similarly impressive results using other protein scaffolds,[169, 170] but not yet with an alcohol dehydrogenase which possesses a naturally evolved nicotinamide binding pocket. Inspired by this work, the present section investigates the possibility of asymmetric imine reduction using iridium-TbADH ArMs.

In the selection of a suitable Cp*Ir(III) catalyst, factors such as the ability to functionalise with an electrophilic bromoacetamide handle to enable anchoring to TbADH, general compatibility with the protein and use of NAD(P)H as the hydride donor were considered. Complex **14** which is similar to [Cp*Ir(Br**L1**)Cl]Cl displayed only 4 % conversion of prochiral cyclic imine **1** under aqueous conditions and using NADH as the hydride donor (Figure **4.17**).[228] Therefore it was considered unlikely that ArMs such as [Cp*Ir(7M-C110**L1**)Cl]$^{2+}$ would be suitable for the reduction of such imines. This was confirmed in preliminary experiments using the free catalyst. The TOF value obtained for hydride donation from NADH to [Cp*Ir(Br**L1**)Cl]Cl (the step prior to transfer of the hydride to the imine substrate)[83] was 9.31 ± 0.38 h^{-1} (n = 3). Also in line with literature reported values,[228] HPLC analysis confirmed a lack of [Cp*Ir(Br**L1**)Cl]Cl imine reduction activity. It is likely that the electronic properties of the phenanthroline ring are not favourable for subsequent donation to the imine substrate.[9] Therefore, alternative variants of this catalyst were considered.

The literature was reviewed for Cp*Ir piano-stool catalysts similar to [Cp*Ir(Br**L1**)Cl]Cl but with greater imine reduction activity. As mentioned in Chapter **1**, Cp*Ir catalysts such as those in Figure **4.17** have been successfully incorporated into ArMs for the ATH of cyclic imines, using NADH as the hydride donor.[9, 87-89] Catalysts **6** and **7** were ruled out owing to the fact that they contain sulfonamide-based ligands which have shown a lack of compatibility with TbADH.[186] Reported imine conversion values indicate that electrophilic substituents on the 4 and 7 positions of phenanthroline render Cp*Ir catalysts more active for imine reduction.[9, 228] Catalyst **8** hereafter referred

to as [Cp*Ir(**L2**)Cl]Cl displayed > 80 % conversion of a prochiral cyclic imine, over 24 hours.[9] Similar catalysts have also been characterised for the purposes of bicarbonate hydrogenation,[194] providing extensive literature on their synthesis and properties. The phenanthroline ligand would appear to be amenable to functionalisation with an electrophilic handle (Br**L3**, Figure **4.18**).

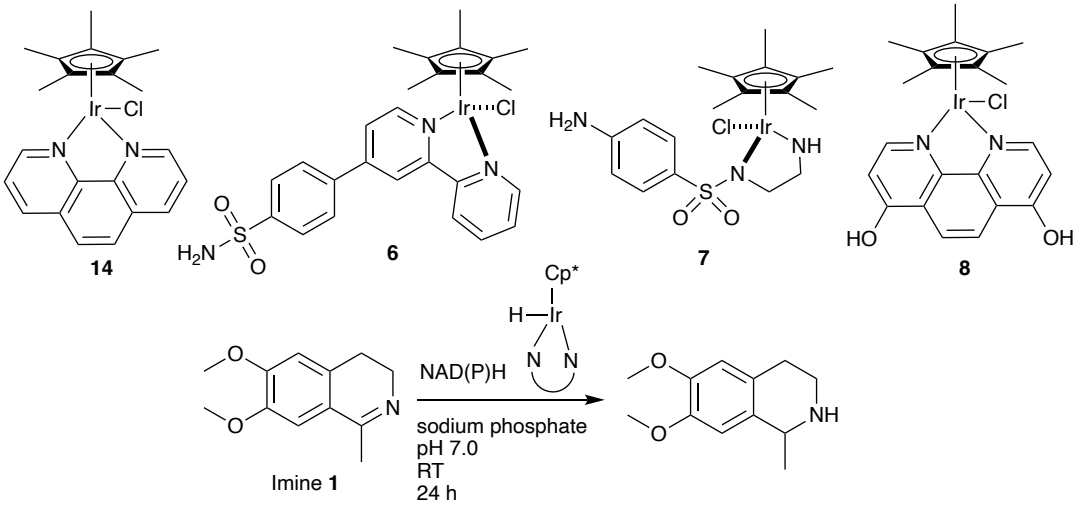

Figure 4.17: Candidate Cp*Ir catalysts for imine reduction

Candidate catalysts for the reduction of 6,7-dimethoxy-1-methyltetrahydroisoquinoline (imine **1**) using NAD(P)H as the hydride donor under exemplary conditions.[228]

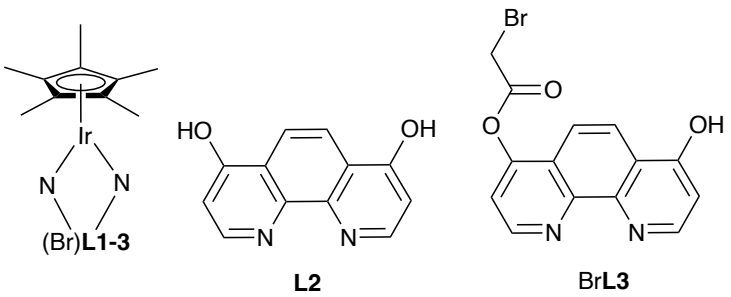

Figure 4.18: Selected Cp*Ir-phenanthroline catalysts for imine reduction

Ligand Br**L3** contains an electrophilic handle to enable bioconjugation to TbADH.

*4.3.2.2 Imine reduction using free catalyst [Cp*Ir(**L2**)Cl]Cl*

Synthesis of [Cp*Ir(**L2**)Cl]Cl was performed by adaptation of an established procedure[194] (Figure **4.19**). Chelation of the ligand **L2** nitrogen atoms occurred without the addition of triethylamine. As for [Cp*Ir(Br**L1**)Cl]Cl, the product was precipitated by addition of cold diethyl ether followed by filtration and drying. ^{1}H NMR and ESI-MS analyses confirmed the presence of the [Cp*Ir(**L2**)Cl]Cl product with sufficient purity for subsequent experiments (Appendix **7**).

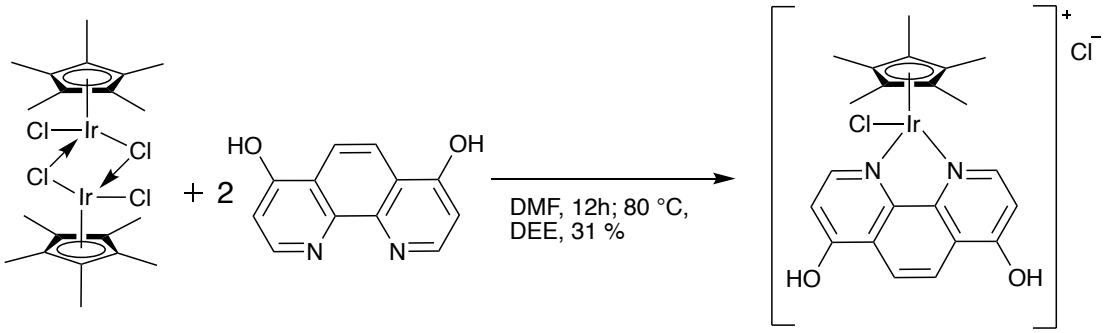

Figure 4.19: Preparation of Cp*Ir(1,10-phenanthrolin-4,7-dihydroxyl)chloride

For an initial qualitative assessment of [Cp*Ir(**L2**)Cl]Cl imine **1** reduction activity free in solution, 21-hour end-point assays were performed. Normal phase HPLC[9, 229] was used to monitor the reaction. In addition to reaction and control samples a standard of the amine **2** product was analysed to confirm column retention times (Figure **4.20**). The minor presence of imine in the latter owing to partial oxidation of the amine **2** stock was noted but not considered an issue for this initial qualitative assessment. Partial conversion of imine **1** to a racemic mixture of the amine **2** product was observed. These results were expected given the reported rate values for similar catalysts,[9, 228] and confirm the suitability of [Cp*Ir(**L2**)Cl]Cl to be taken forward towards the objective of asymmetric imine **1** reduction using iridium-TbADH ArMs.

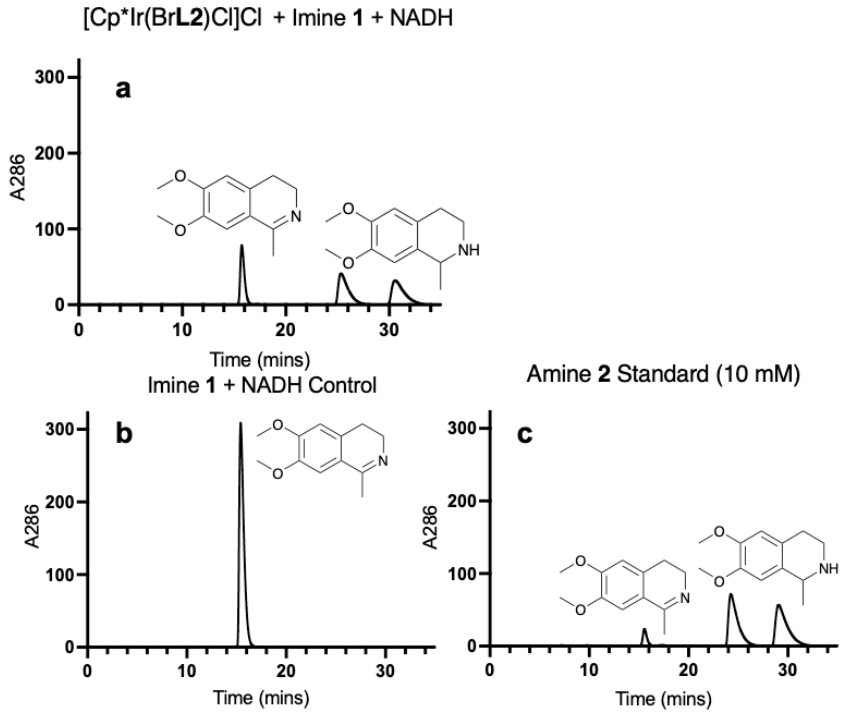

Figure 4.20: [Cp*Ir(L2)Cl]Cl catalysed reduction of imine 1 monitored by HPLC
Imine 1 (150 μM) and NADH (150 μM) in sodium phosphate buffer (100 mM, pH 7.0) were mixed **a**) with (reaction) or **b**) without (negative control) catalyst (300 μM) and incubated at room temperature for 21 hours. Panel **c**) shows a standard of the amine 2 product.

*4.3.2.3 Synthesis of [Cp*Ir(BrL3)Cl]Cl*

Having confirmed imine **1** reduction activity of [Cp*Ir(**L2**)Cl]Cl, the next step was to functionalise this catalyst with a bromoacetamide moiety (or similar) as possessed by [Cp*Ir(Br**L1**)Cl]Cl. As for rhodium-TbADH ArMs (Chapter **3**), this would enable nucleophilic substitution with the cysteine thiol group of TbADH mutant 5M-C37 or 7M-C110 to covalently assemble the corresponding ArM variants. It was reasoned that one of the hydroxyl substituents of the ligand **L2** phenanthroline ring could be esterified with bromoacetyl to yield the thiol-reactive bromoacetate group of ligand Br**L3** (Figure **4.21**), bearing an electrophilic functionality suitable for reaction with a protein thiol. This modification would retain one of the electron-rich hydroxyl substituents shown to be essential for imine reduction activity.[9]

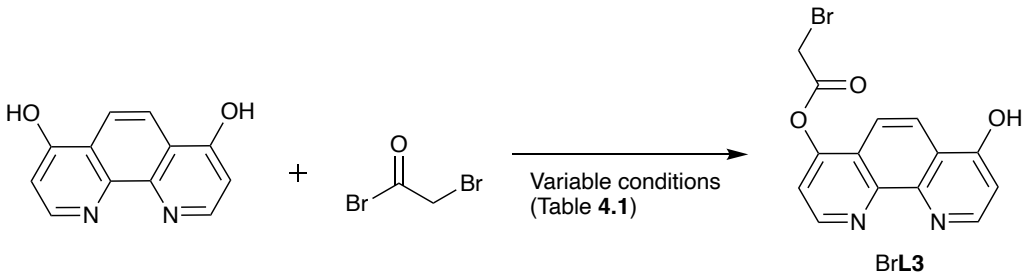

Figure 4.21: Synthesis of ligand BrL3

Unfortunately, the attempts made to synthesise Br**L3**, and variations of this ligand were unsuccessful. Thin layer chromatography, ^{1}H NMR and positive or negative ESI-MS (not shown) were used to interpret results and inform subsequent attempts, including changes to the acyl halide electrophile, base, nucleophilic activator, solvent, and temperature. Table **4.5** summarises a key selection of conditions and variations trialled, and subsequent outcomes.

Table 4.5: Example reaction conditions tested for the synthesis of BrL3

Entry	Reaction conditions	^{1}H NMR Outcome
1	1,10-phenanthroline-4,7-diol, (1 eq.), bromoacetyl bromide (1 eq.), triethylamine (3 eq.), anhydrous DMF, 20-50 °C, 3-24 h	Mixture of starting materials
2	1,10-phenanthroline-4,7-diol, (1 eq.), bromoacetyl bromide (1 eq.), NaH (1 eq.), anhydrous DMF, 20 °C, 3-24 h	Mixture of starting materials
3	1,10-phenanthroline-4,7-diol, (1 eq.), bromoacetic anhydride (1 eq.), NaH (1 eq.), anhydrous DMF, 20 °C, 3-24 h	Possible minor product formed, inseparable from starting materials

Initial synthesis attempts were based on the adaptation of methods for esterification of aliphatic hydroxyl groups.[230, 231] Reaction time, and in some cases temperature, were increased under the reasoning that the phenanthroline hydroxyl groups serve as weaker nucleophiles than those in aliphatic environments. Anhydrous dimethylformamide was selected as a solvent on the basis of successful dissolution of the dihydroxy-phenanthroline starting material, and to mitigate reaction of the bromoacetyl bromide starting material with water. Triethyl amine was added as a base to deprotonate the phenanthroline hydroxyl groups. The reactions were monitored by TLC and ESI-MS at various time points from 1 to 20 hours in attempt to achieve

esterification of one of the hydroxyl groups. TLC analysis showed only starting material, which did not migrate well despite the wide range of eluent conditions tested. From NMR analysis of the dihydroxy-phenanthroline starting material, it was expected that esterification of both hydroxyl groups would result in a single extra signal from the four bromo-proximal protons. Alternatively, the desired single esterification would result in multiple peaks owing to new proton environments (Figure **4.21**). The former case was observed. However, comparison of peak integrals suggested a mixture of starting materials. Furthermore, no product could be identified via ESI-MS analysis.

Elsewhere, successful nucleophilic substitution of phenanthroline hydroxyl groups has been reported using sodium hydride as a base.[232] Therefore, it was hypothesised that triethylamine is not a strong enough base to deprotonate phenanthroline hydroxyl groups for reaction, prompting substitution for sodium hydride. However, NMR analysis showed no change to the number of peaks in comparison to previous attempts, with integrals still indicating a mixture of starting materials. Product masses could not be identified by ESI-MS.

Based on the hypothesis that the bromoacetyl bromide starting material is not a strong enough electrophile for reaction with a phenanthroline hydroxyl group, several alternatives were considered. Bromoacetic anhydride[233] was found to be the most promising. Several new NMR peaks were identified, some of which may correspond to the desired mono-esterified product. However, these peaks could not be clearly distinguished from those corresponding to starting material, or to side products as described below. Furthermore, as in previous attempts, the NMR peak corresponding to CH_2Br did not integrate correctly, and no signals corresponding to any products could be identified by ESI-MS.
A robust assessment of whether synthesis attempts such as Table **4.5**, Entry 3 had indeed resulted in at least partial formation of desirable product, would require separation of components via column chromatography. However, movement and separation of these phenanthroline-bearing compounds on silica gel was found to be challenging, with no discernible differences observed in TLC results under the range of eluent conditions tested.

Possible side reactions which could have prevented the success of this synthesis were also considered. The UV-visible spectra of diluted NMR samples from several reaction attempts were very similar to that of the carbonyl tautomer of the phenanthroline starting material (**A**, Figure **4.22**).[234] It is known that the alcoholate form present under

basic conditions (p*K*a ~8.5) can tautomerize to **A**.[194] This may provide an explanation for the lack of clear product formation under any of the conditions trialled. It was hypothesised that the extra NMR peaks observed from the reaction conditions in Entry 3 (Table **4.1**) correspond to functionalisation of one or both of the phenanthroline nitrogens of this tautomer (**B**, Figure **4.22**), rather than the oxygens as desired.

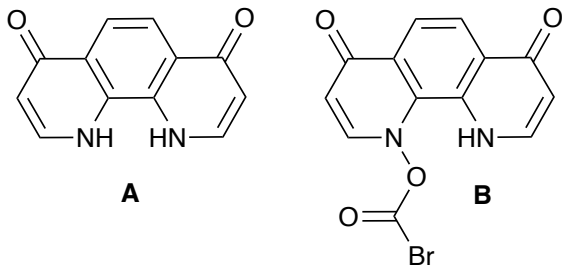

Figure 4.22: Possible side products of BrL3 synthesis attempts

4.3.2.4 Conclusions

This section reports on preliminary work towards the objective of imparting enantioselectivity on iridium catalysed imine reduction, via ArM-incorporation of the catalyst.

As shown in the literature, [Cp*Ir(Br**L1**)Cl]Cl was confirmed active for NADH oxidation but not imine reduction, while [Cp*Ir(**L2**)Cl]Cl was active for imine reduction using NADH as the hydride donor.

Unfortunately, attempts to synthesise Br**L3** to enable assembly of iridium-TbADH ArMs were unsuccessful. A range of conditions and starting materials were trialled based on literature reported methods for the syntheses of similar compounds. New proton environments were observed via NMR, potentially indicating partial formation of desirable product. Alternatively, these signals may correspond to a tautomer of the starting material. The separation of components was attempted via column chromatography. However, suitable eluent conditions could not be identified.

In the interest of obtaining catalytically active iridium-TbADH ArMs the literature was explored for alternative nicotinamide-dependent reduction activities.

4.3.3 Iridium-TbADH ArMs for quinone reduction

4.3.3.1 Background

Other reduction activities for which iridium-TbADH ArMs could be used and rationally optimised were considered. The Sadler group showed that Cp*Ir-phenanthroline catalysts such as **14** in Figure **4.17** (Section ***4.3.2***) are catalytically active for the reduction of quinones such as menadione.[195] Based on NMR and EPR analysis of the reactions, it was suggested that two menadione molecules are reduced per NADH electron donor, producing two semi-quinone radicals (Figure **4.23A**). Therefore, in contrast to nicotinamide and imine reduction which do not involve redox at the iridium (III) centre, this mechanism involves a transient iridium (II) centre. The fully reduced menadiol product (Figure **4.23B**) was not observed experimentally. These results were supported by DFT calculations which indicated that the radical mechanism was the most probable of the two pathways. In each case, the first and likely rate limiting step[235] is the donation of hydride from NADH to the iridium (III) centre.[195] Therefore, the NADH oxidation activity of [Cp*Ir(Br**L1**)Cl]Cl (confirmed in Section ***4.3.2***) suggested promise for quinone reduction activity of this catalyst, which is very similar to catalyst **14** used by the Sadler group.

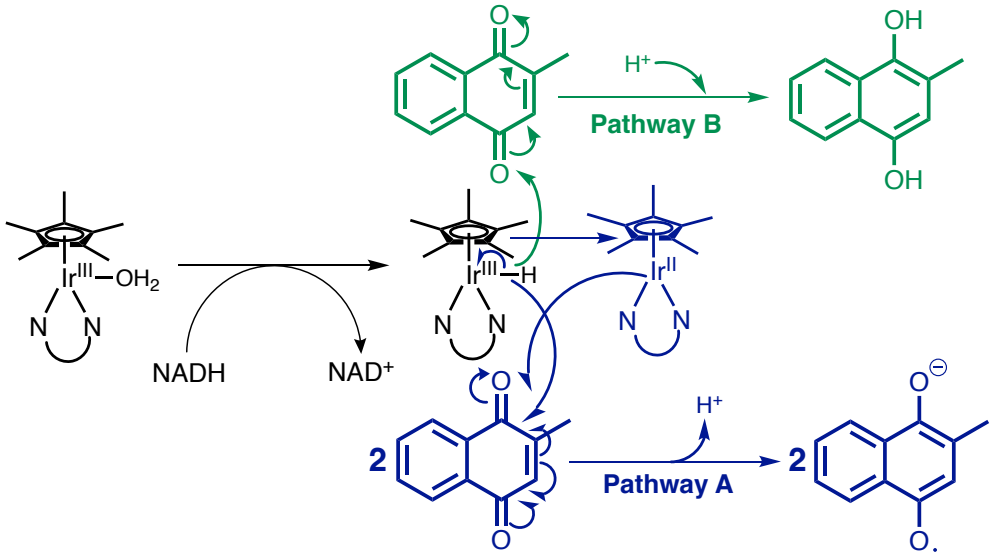

Figure 4.23: Two possible Cp*Ir catalysed quinone reduction pathways
Following hydride transfer from NADH to the iridium centre (substituting water): Pathway **A** (blue) involves two sequential single electron transfers from the Ir-hydride bond to two menadione substrate molecules with phosphate as a possible proton acceptor, yielding two semi quinone radicals; Pathway **B** (green) involves hydride transfer from the iridium centre to a single menadione, with phosphate as a possible proton donor to yield a single menadiol. In both pathways, the catalyst is regenerated by re-coordination of water. Adapted from[195]

Regarding potential applications, it has been suggested that *in vivo* reduction of menadione to semi-quinone radicals[236, 237] show promise for redox modulation in cells.[238] This implicates piano-stool iridium complexes such as [Cp*Ir(Br**L1**)Cl]Cl for potential novel cancer therapies.[195, 235] Incorporation into ArMs could provide a biocompatibility advantage. For example, by shielding the catalyst from inactivating cellular glutathione.[25] Considering other applications of iridium-TbADH ArMs, menadiol sodium phosphate is used as a procoagulant drug.[239] Assuming conversion of menadione to the fully reduced menadiol product, there is potential to incorporate ArMs into a menadiol production cascade which uses an enzymes such as formate dehydrogenase (FDH) or glucose dehydrogenase (GDH) for regeneration of the NADH hydride donor (Figure **4.16**). Similar to other ArM cascade reactions,[171, 174, 29] the advantage would be shielding of the catalyst and enzyme components from mutual inactivation. As for rhodium-TbADH ArMs (Chapter **3**), there is also potential for genetic optimisation by changing the catalyst binding site to different residue locations.

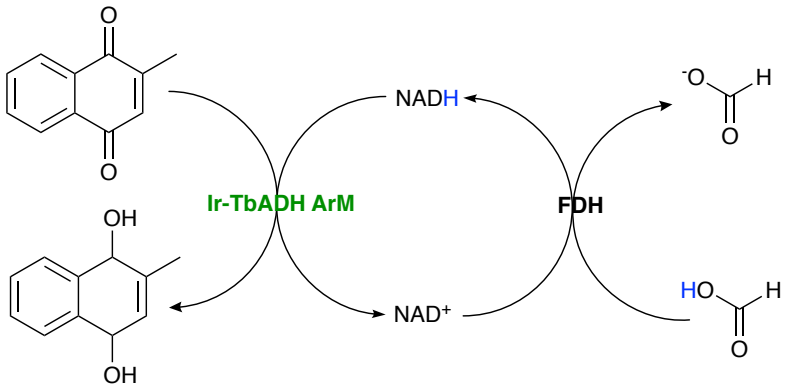

Figure 4.24: Prospective use of iridium-TbADH ArMs in a menadiol production cascade
NADH is regenerated by FDH, using formate as the hydride donor.

4.3.3.2 Measurement of catalytic quinone reduction via NMR

A method for quantification of either rate (TOF) or conversion (TON) for different variants needed to be identified. The first step was to measure the catalytic activity of the free complex [Cp*Ir(Br**L1**)Cl]Cl. Initial assays were performed under literature conditions[195] and analysed qualitatively by solvent suppressed ^{1}H NMR, along with standards of all reaction components. In accordance with the literature,[195] signals corresponding to the menadione substrate disappeared within 1 hour of mixing with [Cp*Ir(Br**L1**)Cl]Cl and the NADH electron donor under aqueous conditions at neutral pH (Figure **4.25a**). Interestingly, signals corresponding to the fully reduced menadiol product were also observed at 7.55-7.45 ppm, albeit with very low intensity.

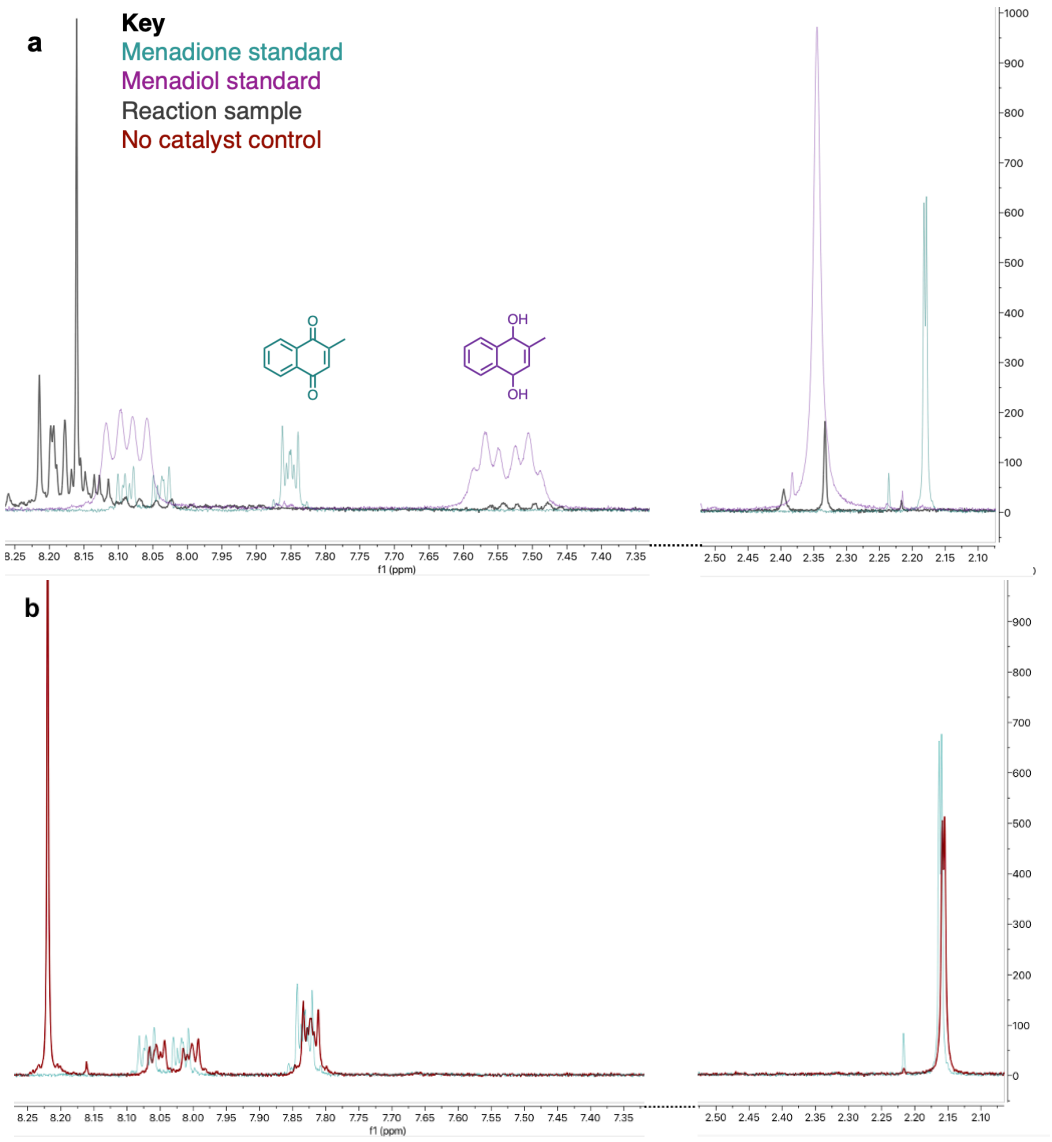

Figure 4.25: ^{1}H NMR spectra of [Cp*Ir(BrL1)Cl]Cl catalysed menadione reduction[195]

Menadione (1 mM) and NADH (2 mM) were mixed **a** with (grey) or **b** without (red) iridium complex (1 mM) and incubated at room temperature for 1 hour before analysis via NMR. The spectra have been adjusted to identical zoom-level to enable qualitative analysis of peak intensities in the control and reaction samples. These samples have been superimposed with the spectra of 20 mM standards of the menadione substrate (cyan) and menadiol product (purple). It should be noted that partial solubility of the menadione and menadiol standards were observed. This is the likely cause for the almost identical intensity of the red and cyan menadione signals in **b**, despite the greater quantity of menadione in the standard (cyan). Assays were performed in sodium phosphate buffer (100 mM, pH 7.2) with 10 % v/v methanol-*d4*.

In the no-catalyst negative control sample, depletion of menadione was considered minor within this timeframe (Figure **4.25b**), and no menadiol was observed, indicating catalytic consumption of the substrate in Figure **4.25a**. As a t = 0 timepoint spectrum was practically difficult to obtain, the no catalyst control sample was assumed to serve this purpose.

Based on these results, the possibility of using menadione consumption to quantify ArM catalytic activity was considered. However, two questions were apparent. Firstly, it would need to be confirmed that the menadione was being reduced to semi-quinone radicals (Figure **4.23A**).[195] Secondly, it was noted that in ArM assays, the concentration of catalyst would have to be much lower owing to a maximum practically achievable final ArM concentration of approximately 0.1 mM. Addressing the latter, the final concentration of [Cp*Ir(Br**L1**)Cl]Cl was lowered to 0.1 mM. However, under these conditions, signals corresponding to the menadione substrate remained even after 24 hours of incubation with the iridium complex and NADH (Figure **4.26a**).

In attempt to detect any changes in the intensity of the menadione signal, the concentration of menadione was increased to 20 mM. Subsequent NMR analysis showed both disappearance of the menadione signal, and the appearance of signals corresponding to the menadiol product, within 1 hour of mixing with NADH and the iridium complex (Figure **4.26b**).

These results suggest that the second suggested menadione reduction mechanism (**Figure 4.23B**)[195] which directly forms the menadiol may be active under these conditions. Therefore, theoretically, TOF or TON values for both free catalyst and ArM catalysed menadione reduction could be quantified via menadiol production. However, it is clear from comparison of peaks corresponding to menadiol in the reaction sample with those of the 20 mM menadiol standard that conversion is not quantitative (Figure **4.26b**). Therefore, it was reasoned that most of the menadione was still being converted to semiquinone radicals (Figure **4.23A**) which were reported to be stable for more than 20 h,[195] within the timeframe of these experiments. Under this theory, it was concluded that quantification of [Cp*Ir(Br**L1**)Cl]Cl catalysed quinone reduction would require EPR analysis.

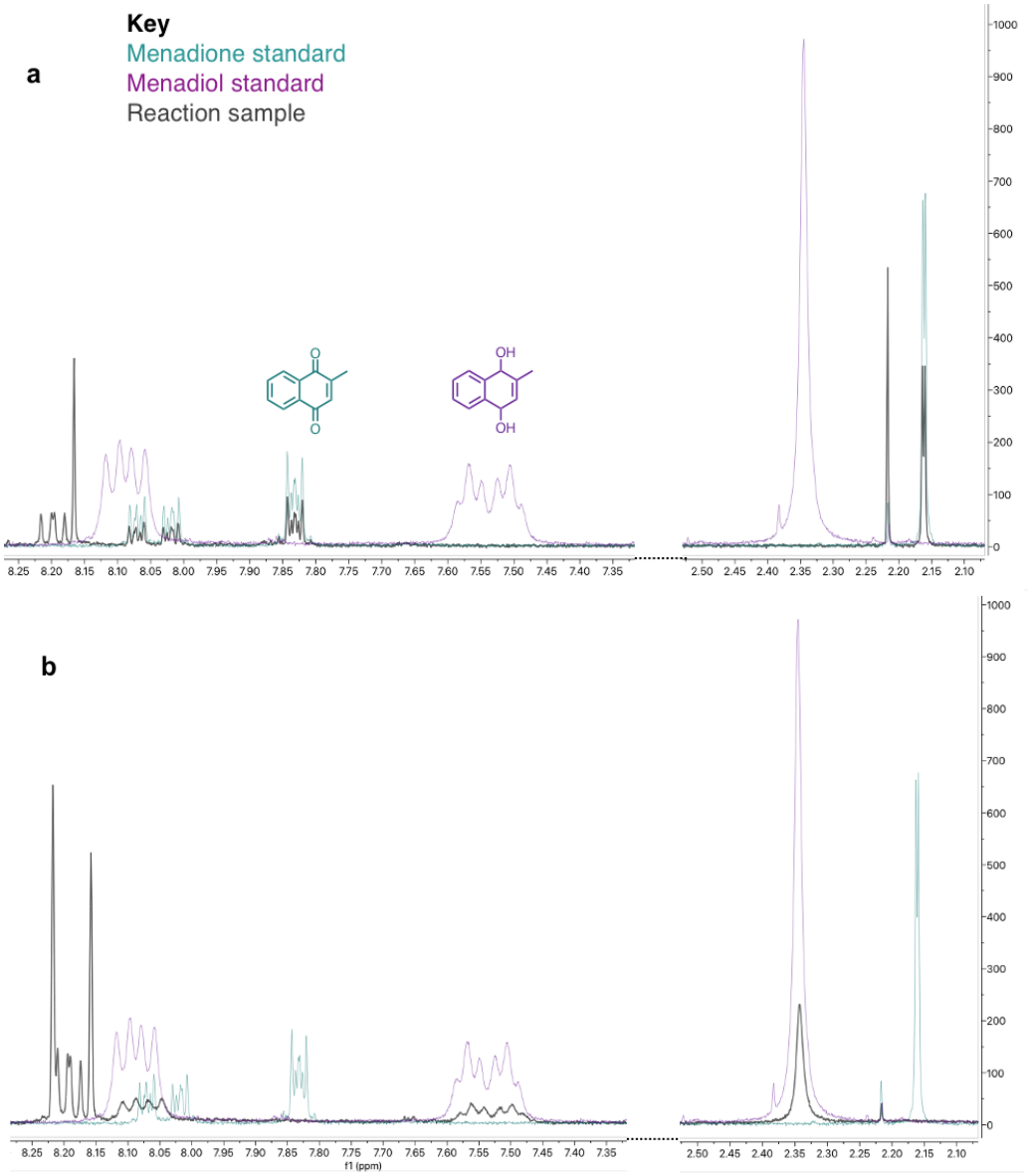

Figure 4.26: Further ^{1}H NMR spectra of [Cp*Ir(BrL1)Cl]Cl catalysed menadione reduction
Reaction samples **a** 1 mM menadione (t = 24 h) or **b** 20 mM menadione (t = 1 h) mixed with NADH (2 mM) and iridium complex (0.1 mM). Other conditions, standards, and labelling colours as for Figure **4.25**.

Prior to investigation of the reaction via EPR, the possibility that the bromoacetamide moiety of the [Cp*Ir(Br**L1**)Cl]Cl phenanthroline ring may affect the prominence of the radical mechanism (Figure **4.23A**) was considered. Therefore, the catalyst [Cp*Ir(**L4**)Cl]Cl was synthesised via the same procedure used for [Cp*Ir(Br**L1**)Cl]Cl (Figure **4.27**). ^{1}H NMR and ESI-MS indicated reasonable product purity (Appendix **8**). Measurement of menadione reduction was performed under the same conditions (Figure **4.28**). The disappearance of menadione signals and appearance of menadiol within 1 hour of mixing with iridium complex and NADH suggests that the extra phenanthroline substituent has little effect on catalytic mechanism.

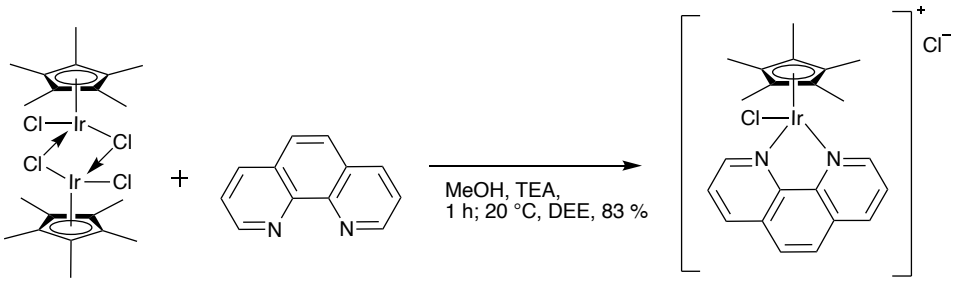

Figure 4.27 Preparation of Cp*Ir(1,10-phenanthroline)chloride ([Cp*Ir(L4)Cl]Cl)

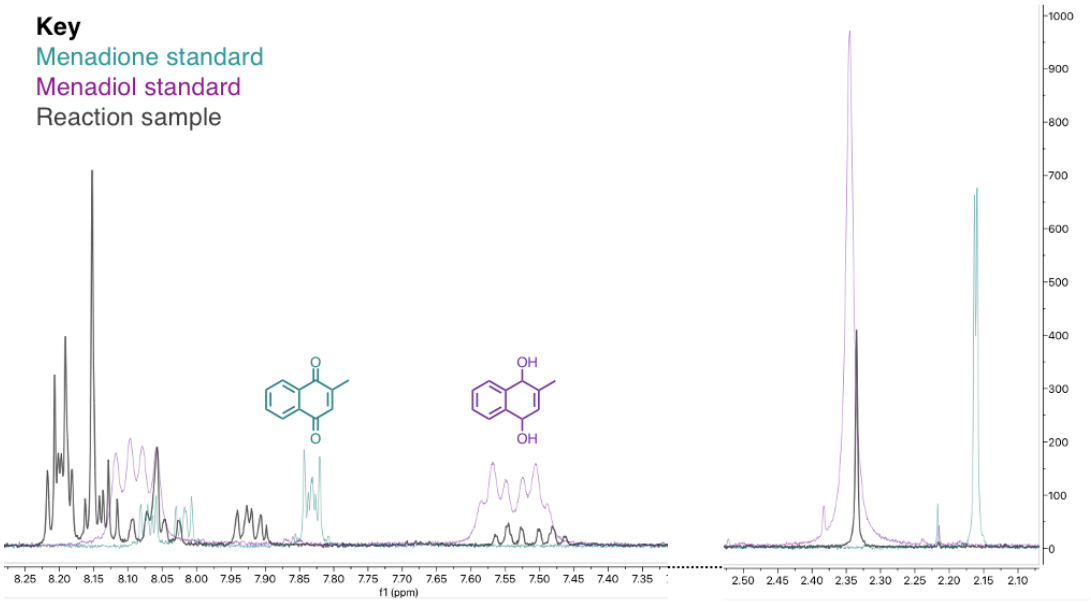

Figure 4.28: ^{1}H NMR spectra of [Cp*Ir(L4)Cl]Cl catalysed menadione reduction

Menadione (20 mM) and NADH (2 mM) were mixed with iridium complex (0.1 mM) and analysed by NMR after 1 hour. Other conditions, standards, and labelling colours as for Figure **4.25**.

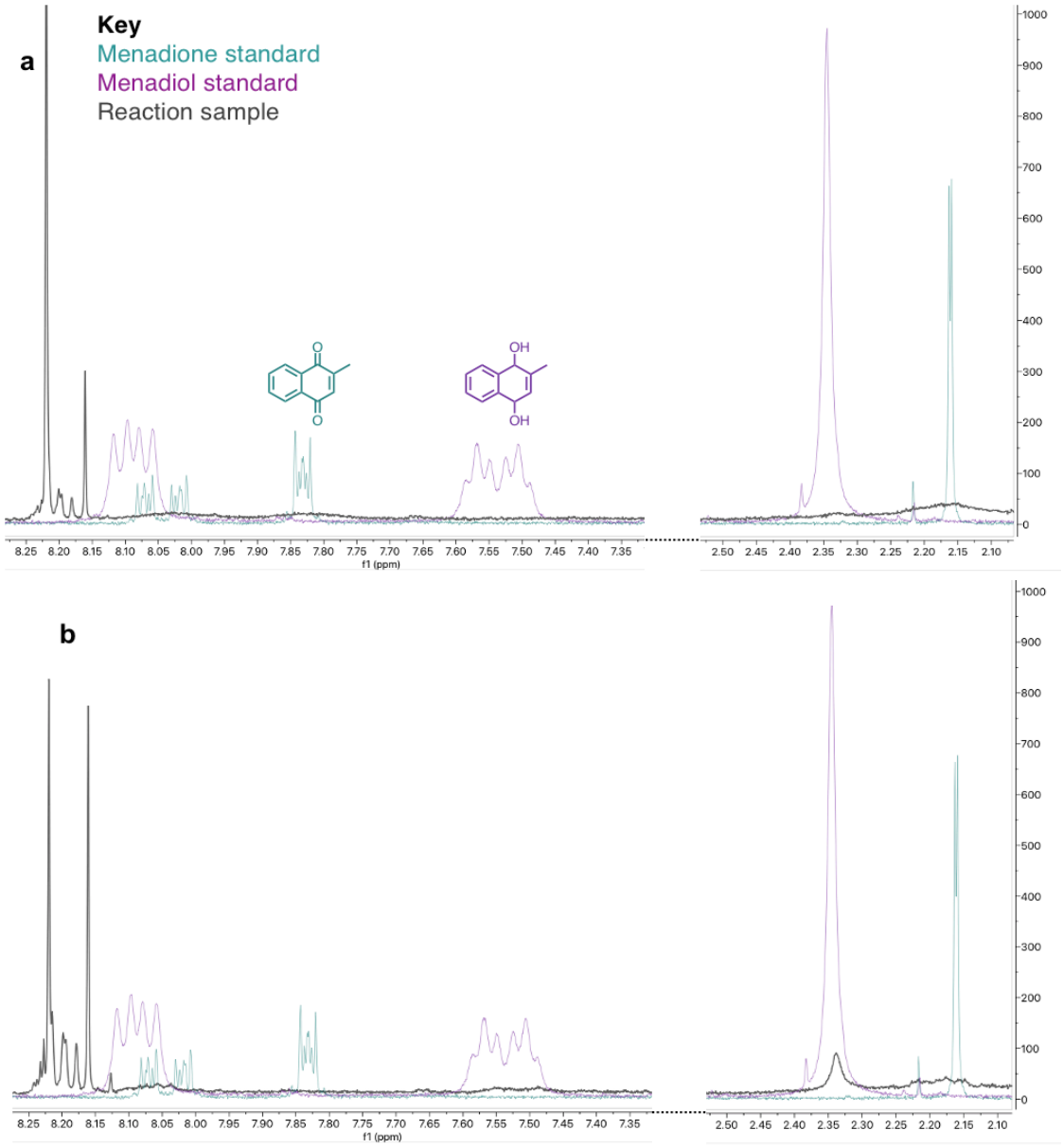

Figure 4.29: ^{1}H NMR spectra of [Cp*Ir(5M-C37L1)Cl]$^{2+}$ catalysed menadione reduction

Menadione (20 mM) and NADH (2 mM) were mixed with iridium complex (0.1 mM) and incubated at room temperature followed by NMR analysis after **a** 5 and **b** 24 hours. Other conditions, standards, and labelling colours as for Figure **4.25**.

Meanwhile, H^1 NMR monitored reactions were performed under the same conditions but with the free catalyst substituted for ArM variant [Cp*Ir(5M-C37**L1**)Cl]$^{2+}$.
Menadione disappearance but not menadiol appearance was observed after 5 hours of reaction time (Figure **4.29a**). After 24 hours, signals corresponding to menadiol were minor but detectable (Figure **4.29b**). These results in combination tentatively suggest that the ArM can catalyse menadione consumption via same mechanism as with free catalysts [Cp*Ir(Br**L1**)Cl]Cl and [Cp*Ir(**L4**)Cl]Cl. Under this theory, reduced substrate accessibility as a result of protein encapsulation of the catalyst reduces menadiol product formation. However, the possibility of detecting semiquinone radicals remains.

Overall, it appears that H^1 NMR analysis under aqueous conditions is not a suitable method for quantification of menadione reduction TOF or TON values with free iridium catalysts. These results further support the need EPR to quantify both free iridium catalyst and ArM catalysed quinone reduction.

4.3.3.3 Measurement of catalytic quinone reduction via EPR

Literature reported TON and TOF values for free Cp*Ir catalysed menadione reduction were measured via quantification of semi-quinone radicals in solution over time using EPR analysis. Signals were integrated relative to tempol solution standards. It was reasoned that the same methods could be used here to measure the catalytic activity of iridium-TbADH ArMs. EPR experiments were performed at several timepoints on both free [Cp*Ir(Br**L1**)Cl]Cl and [Cp*Ir(5M-C37**L1**)Cl]$^{2+}$ catalysed menadione reduction assays under literature conditions and procedures,[195] as well as under partially modified conditions (Table **4.6**). Unfortunately, no radicals could be detected in solution under any conditions, despite a clear signal from the 1 mM tempol standard (Appendix **9**).

Table 4.6: Conditions trialled for EPR analysis of menadione reduction

Catalyst	**Ratio** Catalyst, NADH, Menadione (mM)	**Solvent** % methanol in phosphate buffer
[Cp*Ir(Br**L1**)Cl]Cl	0.16, 0.5, 1.0†	0, 10, 100
	0.1, 0.5, 3.0	0
	0.16, 0.5, 20	0, 100
	1.6, 0.5, 20	0, 100
[Cp*Ir(**L4**)H_2O]$(PF_6)_2$	0.16, 0.5, 1.0†	0, 100
[Cp*Ir(**L4**)Cl]Cl	0.16, 0.5, 1.0†	0, 100
[Cp*Ir(5M-C37**L1**)Cl]$^{2+}$	0.16, 0.5, 20	0, 10

Reaction components were mixed in varying ratios and analysed after 1 h and 6 h via EPR with typical parameters of 2 G, 0.63 mW, 8-16 scans.[195] Assays were performed in sodium phosphate buffer (100 mM, pH 7.2) with or without 10 % v/v methanol, or 100 % methanol. †Literature-derived ratios.[195]

The possibility that the bromoacetamide substituent of **L1** affects catalytic outcomes as monitored by EPR was again considered. Therefore, catalyst [Cp*Ir(**L4**)H_2O]$(PF_6)_2$ was synthesised according to the same procedure used in the literature (Figure **4.30**). ^{1}H NMR and ESI-MS indicated reasonable product purity (Appendix **10**). This catalyst, along with [Cp*Ir(**L4**)Cl]Cl (Figure **4.27**) were subjected to EPR analysis of menadione reduction under the same analytical conditions. Again, no radical was detected under any of the reaction conditions tested (Table **4.6**).

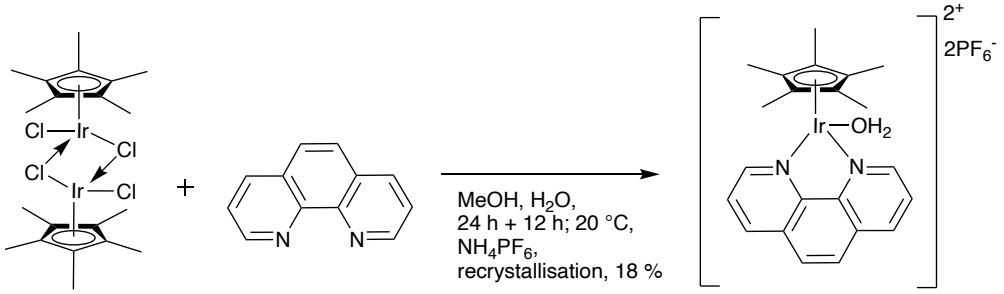

Figure 4.30: Preparation of Cp*Ir(1,10-phenanthroline)$(PF_6)_2$ ([Cp*Ir(L4)H_2O]$(PF_6)_2$

It is possible that in our hands, not enough radical is produced by the reductive action of these catalysts for detection via EPR. As the radical was only reported to be stable for around 20 h,[195] it is also possible that some or all of the menadiol detected by NMR here is formed via reductive degradation of the radicals, as was suggested more recently in the context of osmium catalysts.[238]

Given these results in combination with the lack of quantitative formation of menadiol according to NMR, the question of exactly what the rest of the menadione is converted to in Figures **25** to **29** remains unanswered. It is possible that alternative products are formed which have low aqueous solubility, making them undetectable under the aqueous conditions used for solvent suppressed NMR.

4.3.3.4 Conclusions

Work in the present subsection was directed towards the use of iridium-TbADH ArMs to catalyse the reduction of quinones such as menadione.

In initial experiments involving the free catalyst [Cp*Ir(Br**L1**)Cl]Cl, catalytic menadione consumption was qualitatively monitored via NMR analysis under aqueous conditions, reproducing literature-reported results. When substrate and catalyst concentrations were altered to reflect those suitable for ArM assays, low quantities of the fully reduced menadiol product were detected in reaction samples. Similar results were observed when using the literature reported catalyst [Cp*Ir(**L4**)Cl]Cl which lacks the bromoacetamide functionality. Meanwhile, with the [Cp*Ir(5M-C37**L1**)Cl]$^{2+}$ ArM, only negligible formation of the menadiol product was observed, likely as a result of reduced access of the iridium complex to the substrate. It was hypothesised that most of the menadione substrate in solution was being converted to semiquinone radicals, in accordance with Pathway A in Figure **4.23**.

EPR analysis was performed in attempt to detect these products. Unfortunately, no radical signals could be detected in either of the free catalyst variants (used here and in the literature), or ArM [Cp*Ir(5M-C37**L1**)Cl]$^{2+}$ catalysed reactions. It is possible that in our hands, low quantities of the semiquinone radical, along with non-aqueous soluble by-products, account for the observed disappearance of the menadione signal (in addition to the detected menadiol).

Overall, in the context of the project objectives, NMR analysis tentatively indicated low [Cp*Ir(5M-C37**L1**)Cl]$^{2+}$ ArM menadione reduction activity. However, this could not be quantified by either NMR or EPR analyses. This proof of principle for iridium-TbADH ArM functionality requires further confirmation. To achieve this, the two options which became apparent were probing further into possible quinone reduction or shifting focus

towards other reduction applications as reported in Sections ***4.3.1*** and ***4.3.2***. The latter was considered more practical and time efficient.

5 Overall discussion and conclusion

The overall aim of this project was to gain structural insight into TbADH-based ArM scaffold, catalyst, and substrate interactions, towards rational optimisation of catalytic performance. This inspired the following specific research questions, as defined by the four project objectives (Section ***1.4.2***):

1. How do the affinities of rhodium-TbADH ArMs for $NAD(P)^+$ and BNA^+ cofactors compare, and can these differences be explained by ArM-nicotinamide interactions?
2. Can changing the covalent catalyst anchoring site in rhodium-TbADH ArMs from residue location 243 to 37 or 110 increase favourable nicotinamide-ArM interactions, and therefore the efficiency of nicotinamide binding?
3. What are the binding positions and orientations of the catalyst and $NADP^+$ in high-resolution structures of iridium-TbADH ArMs, and how does this build upon the previous two research questions?
4. Is there scope for the use of iridium-TbADH ArMs based on residue locations 37 and 110 for nicotinamide and other reduction applications?

Research questions 1-3 were answered by the work presented in this thesis, as explained in the Conclusions sections of Chapter **3** and Section **4.2**. However, as discussed below, these conclusions and the subsequent broader perspectives would benefit from improved methodologies and further experiments. The alternative, supplementary or expansion methodologies discussed include: MALDI-TOF analysis of ArM samples; use of a two-substrate Michaelis-Menten equation for kinetic characterisation; stopped-flow analysis for measurement of pre-steady state kinetics; mutations to increase the space available for $NAD(P)^+$ binding within the TbADH ArM pocket; methods to further probe the structure of $NADP^+$-bound $[Cp^*Ir(7M\text{-}C110\mathbf{L1})Cl]^{2+}$, such as NMR and incorporating residue flexibility into the docking procedure.

While research question 4 was answered, exactly how these systems benefit from the protein environment of the ArM was not explored owing to difficulties in the synthesis of the required iridium catalyst, as explained in the Conclusions sections of Section **4.3**. However, work towards this objective demonstrated proof of principle for the functionality of iridium-TbADH ArMs, and provided scope for further experiments which are also discussed below.

TbADH-based ArMs were assembled by covalent conjugation of the rhodium or iridium piano-stool catalyst to the three single-cysteine mutants. Ellman's assay, ICP-MS and ESI-TOF MS were used to analyse the success of the assembly procedure. In all three TbADH mutants, the apparent availability of free thiol groups was calculated by Ellman's assay as a percentage of the expected single thiol per TbADH monomer. The values of 64 and 57 % obtained for the 5M-C37 and 7M-C243 mutants respectively broadly aligned with those obtained in previous work by the Pordea group.[29, 212] Meanwhile, the apparent availability in the new 7M-C110 mutant was 45 %. It was suggested that the lower availability in the new variant may be explained by the cysteine being deeper within the natural TbADH substrate binding pocket. Therefore, a greater Ellman's assay duration may have been required to enable more interaction between DTNB and the free thiol group. Indeed, in the case of all ArM variants, the apparent mismatch between the Ellman's and mass spectrometry results could be at least partially explained by this reasoning as discussed in Section *3.2.1.2*. In addition to increasing Ellman's assay duration, this issue may be further addressed by unfolding of the protein prior to the Ellman's assay,[240] or use of a different reagent to assess free-thiol availability.[241] An example of the latter would use of 4,4-dithiodipyridine (4-DPS) in place of DTNB. Reduction of 4-DPS via reaction with thiols produces a resonance-stabilised tautomer which absorbs at 324 nm (ε_{324} = 21000 M^{-1} cm^{-1}). The greater hydrophobicity of 4-DPS could potentially improve access to buried cysteines of interest in comparison to DTNB. However, the accompanying lower aqueous solubility at pH 7 would need to be considered and tested.[196]

Meanwhile, the mass spectrometry methods employed serve well to determine the overall success of ArM assembly, with regards to catalyst access to the reactive cysteine. The ICP-MS and ESI-TOF MS results were in broad agreement with regards to the percentage of desirable ArM species in solution across all samples. In general, the results from these analyses of iridium-TbADH ArMs suggested greater completeness of bioconjugation in comparison to the rhodium equivalents. This justified the use of these iridium samples for crystal trials, the structures of which served as a proxy for further insight into rhodium-TbADH ArM kinetics. A third method to confirm the ratio of unmodified TbADH to ArM would be tryptic digestion of samples followed by MADLI-TOF analysis of the peptide mixture.[29]

It should be noted that the possibility of catalyst binding to residues such as histidine via coordination of the metal, particularly in the case of rhodium catalysts, could not be entirely ruled out. While these species could not be reliably be identified by manual deconvolution of ESI-TOF MS spectra, automated deconvolution was not always in agreement (Section *3.3.2.3*). Therefore, subsequent conclusions drawn from ArM

kinetics studies in this thesis were made under the assumption that if such species were indeed present, their relative abundance was not sufficient to have a significant impact on the ability to compare catalytic rate values between different ArM variants. This could be further validated by both repeated ESI-TOF MS measurements on ArM samples following resolution of the instrument contamination issue referred to in Section *3.3.2.3*, in addition to MALDI-TOF analysis.

Kinetics studies on ArM variant [Cp*Rh(7M-C243**L1**)Cl]$^{2+}$ revealed differences between the binding affinities of natural and mimic nicotinamide cofactors. With support from docking, the lower affinity of BNA$^+$ was ascribed predominantly to this mimic being much smaller than NAD(P)$^+$. Fewer resulting favourable protein-ligand interactions were formed with the TbADH scaffold. In contrast, although not binding to an optimal naturally evolved site, NADP$^+$ still formed more such interactions with the ArM.

K_M^{BNA+} values for ArMs were calculated on the order of hundreds of μM. To provide a general enzyme context, K_M values reported by the Sieber group for binding of BNA$^+$ to variants of a GDH enzyme from *S. solfataricus* are on the order of thousands of μM.[136] In this study, BNAH was regenerated by the GDH to serve as the hydride donor for an enoate reductase. This of course is not an attempt to compare the overall catalytic efficiency of TbADH-based ArMs with that of enzymes such as GDH. Indeed, the latter display rates on the per second order, making them many thousands of times more efficient for the reduction of both mimic and natural nicotinamide cofactors. On the other hand, understanding the binding efficiencies of nicotinamides to ArMs is within the scope of this thesis, making such comparisons of affinity relevant. Though of course different to ADHs, GDH enzymes also possess a nicotinamide binding pocket. Therefore, from this perspective, estimated TbADH-based ArM affinities for BNA$^+$ are relatively high, providing promise for the incorporation of catalysts with higher activity on the mimic. The most impressive rates reported thus far are with iridium(III)-sulfonamide catalysts in the context of a streptavidin-based ArM designed by the Ward group.[173] However, this comparison of affinity is limited by the degree of accuracy and precision to which K_M^{BNA+} values were calculated. As discussed in Chapter **3**, this is likely owing to flexible binding of the mimic to [Cp*Rh(7M-C243**L1**)Cl]$^{2+}$ as predicted by docking. These findings could be supported and built upon by more rigorous assessment of ArM-nicotinamide affinity and kinetic behaviour. Firstly, remaining within the realms of steady state kinetics, a more complicated model of the Michaelis-Menten equation could be used. Formate (as the hydride donor for nicotinamide reduction) was maintained at saturating concentration, enabling

independent analysis of the nicotinamide substrate kinetics. While this allowed the use of the simple single-substrate model to obtain kinetic parameter values with a reasonable degree of accuracy, a two-substrate model may be more suitable for this system. Work by the Vasić-Rački group on multi-substrate systems has involved concentration series rate measurements for each substrate, followed by mathematical modelling to obtain separate K_M values.[216, 242] A similar approach could be applied here, by running a second series of experiments with varying formate concentration, such modelling could also be completed to obtain kinetics parameter values for both nicotinamide and formate.

Secondly, stopped flow analysis could be used to measure pre-steady state kinetics, as demonstrated by the Hollmann, Scrutton and Paul groups.[135] This separation of the ArM-nicotinamide binding and product formation steps of the reaction would enable calculation of dissociation constant or K_d value for the binding step. While still inversely proportional to affinity, this equilibrium constant is a more accurate measurement of K_M as it does not rely on the product formation rate constant (k_2) being negligible (Section ***2.7.7***). Obtaining such values would enable more accurate comparison with literature reported K_M^{BNA+} and K_d^{BNA+} for natural enzymes. Therefore, this would further appraise ArM efficiency and BNA^+ binding mode.

Binding of the natural $NAD(P)^+$ cofactors to TbADH-ArMs was aimed at utilising the naturally evolved nicotinamide pocket. In contrast, it is clear that affinity for the much smaller BNA^+ benefits less from this feature of the scaffold. Therefore, to increase affinity for the mimic, a different strategy could be employed. While there appear to be few examples in the literature which have focused directly on increasing ArM scaffold-substrate affinity via genetic optimisation, there are many concerned with catalyst affinity for the purposes of ArM assembly.[4, 145] Recently, the supramolecular affinity of a propyl oligopeptidase for Ru-(bipyridine)$_3^{2+}$ catalysts was increased via mutations introduced to this scaffold. For example, ArM active site aspartic acid residues were introduced to generate more electrostatic interactions with the positive catalyst. Impressive improvements in the calculated K_d values for catalyst-ArM binding were achieved by the Lewis group.[243] A similar rationale could be applied to increase the affinity of TbADH-ArMs for the BNA^+ nicotinamide substrate. Variants with negatively charged residues introduced near to the predicted ArM binding site of the mimic could be designed, followed by quantification of affinity.

The estimated affinities of rhodium-TbADH ArM variants for the natural $NAD(P)^+$ cofactors were higher for the residue location C37 and C110 variants in comparison to 243. Aside from changing the catalyst anchoring site, another way to further increase affinity of [Cp*Rh(5M-C37**L1**)Cl]$^{2+}$ for $NAD(P)^+$ might be to increase the

overall pocket space available. For example, it was reported by the Phillips group that mutation W110V was successful in reducing steric bulk within the natural TbADH substrate binding pocket. Docking and kinetics studies demonstrated that this created space for binding of both $NADP^+$ and phenylacetone. This was confirmed by catalytic activity on this bulky ketone substrate which is not accepted by wildtype TbADH owing its size.[219] Similarly, such mutations to TbADH-based ArMs may create more space to accommodate both metal complexes and nicotinamides substrates. In addition to W110, other candidate residues include those around the deep substrate cleft such as Y267 and H42. This would have the effect of increasing the width of the business-end of the nicotinamide binding pocket.

$[Cp^*Rh(7M\text{-}C110\mathbf{L1})Cl]^{2+}$ in which the catalyst is anchored deepest into the natural TbADH substrate binding pocket displayed the highest estimated affinity for $NAD(P)^+$ of the three ArM variants tested. Furthermore, docking results predicted a near-wildtype TbADH binding location of $NADP^+$, according to overlap with the wildtype co-crystallised cofactor.[107] The proximity of the nicotinamide C4 to the rhodium centre suggested catalysis could occur at this approximate binding site. From these results, the objective of increasing ArM-$NADP^+$ affinity via changing the catalyst anchoring site could be considered achieved to an extent. However, this increased affinity could not be directly explained by the crystal structure of $[Cp^*Ir(7M\text{-}C110\mathbf{L1})Cl]^{2+}$ with $NADP^+$ bound. While the cofactor was indeed observed in a near-wildtype binding location, the catalyst was observed in an “out” conformation which positioned the metal centre too far from the nicotinamide C4 for hydride transfer. Based on visual inspection of the structure overlayed with the above docking results, it was tentatively suggested that a catalytically active “in” conformation is possible in solution. This requires flexibility of the C110 anchoring residue. Further experiments would help to confirm this.

The first port of call would be to repeat crystallisation under a range of conditions both with and without co-crystallisation of $NADP^+$. Subsequent diffraction and analysis would attempt to identify the effects of conditions such as pH and buffer components on catalyst ligand orientation. Furthermore, attempts to solve the structure using cryo-EM may yield interesting results, given the nature of the sample preparation procedure. While crystallisation of the ArM with the catalyst in the “in” conformation may not be possible, the cryo-EM process involves rapid freezing of samples straight from solution, removing crystal packing constraints and potentially revealing solution-state conformations.[153] Regarding other possible experimental methods, small angle X-ray scattering (SAXS) can be used to investigate protein flexibility in the solution.[244] However, changes in ligand conformation may not be large-scale enough for detection

using this method. Alternatively, solving the structure of the ArM by NMR may reveal solution dynamics not captured by the X-ray crystal structure.[245] Regarding computational methods, the first step would be to introduce flexibility to the C110 and proximal residues in docking. To provide more robust insight into flexibility, QM calculations could be incorporated into the docking procedure to provide a QM/MM hybrid approach.[164]

Support for the theory that catalyst orientation is flexible in TbADH-based ArMs would justify the pursuit of solutions to this problem. For example, dual anchoring strategies could be investigated, in attempt to lock the catalyst in the catalytically active "in" conformation.[168] This may involve the introduction of a second cysteine-reactive electrophilic ligand to the catalyst complex, and a carefully positioned second cysteine residue within the TbADH substrate binding pocket. However, this strategy may not be possible in the already space-limited pocket. One alternative may be to introduce a negatively charged residue for electrostatic interaction with the rhodium (III) centre of the catalyst. Success in decreasing the flexibility of the catalyst my achieve increased rates of nicotinamide reduction.

Overall, the crystal structure of [Cp*Ir(7M-C110**L1**)Cl]$^{2+}$ provides support for the covalent conjugation of the Cp*Ir catalyst to the desirable residue location within TbADH. However, it also introduces further complexity in attempts to understand the functionality of this ArM, and optimise it towards improved nicotinamide affinity. Aside from a secondary (lower-ranked) covalent docking pose, the possibility of a second non-catalytically active orientation of the complex was not predicted based on kinetics and docking studies. Therefore, these results in combination highlight the challenges of rational ArM design, highlighting the need for multiple analytical methods in such efforts.

Further improvements of nicotinamide reduction performance beyond the TbADH location 110-modified ArM variant could be in the form further genetic optimisation. Albeit complicated, one design solution may be to move the catalyst anchoring location further out of the cleft (described and shown in Figure **4.15**), and towards the surface of the scaffold. For example, residue location 283. This would need to be followed by mutations to increase the steric bulk of the entrance to the cleft, forcing the catalyst into the "in" orientation (towards the nicotinamide moiety of NADP$^+$) upon binding. However, confirmation of TbADH stability following such mutations would first be required, beginning with SDS-PAGE analysis, and extending to circular dichroism[246] to confirm intact secondary structures, and X-ray crystallography.

Finally, from a biocatalysis perspective, TbADH-based ArMs designed for nicotinamide recycling cascades would of course benefit from the incorporation of

more active catalysts. Impressive nicotinamide reduction rates have been reported recently,[131, 116] although a suitable method of TbADH-anchoring would need to be devised.

The catalytic functionalities of iridium-TbADH ArMs were investigated in the final part of this thesis. The original objective was to incorporate catalysts for the reduction of cyclic imines, using the protein environment to impart enantioselectivity.[9] Quinone and nicotinamide reduction were also investigated, towards the objective of understanding how iridium catalyst anchoring location affects ArM activity. Unfortunately, the functionalisation of the catalyst ligand required for incorporation of the imine reduction catalyst into TbADH proved to be challenging. It was hypothesised tautomerisation of the phenanthroline diol starting material may be the cause for lack of successful product formation. Beyond finding a solution to this synthesis, alternative ligands to Br-**L3** (Figure **4.18**) could be investigated. For example, a Cp*Ir complex bearing a bi-oxazoline ligand in place of the phenanthroline diol was also reported to display promising imine reduction activity.[9] However, in the context of covalently assembled ArMs, a method for functionalisation to enable thiol conjugation would be needed. Alternatively, the phenanthroline diol ligand could be used unfunctionalised (catalyst **8**, [Cp*Ir(**L2**)Cl]Cl in Figure **4.17**), but with the Cl ligand substituted for a maleimide to enable thiol conjugation.[247, 248] The resulting TbADH-based ArM would benefit from possession of a naturally evolved nicotinamide binding pocket, for $NAD(P)^+$ dependent imine reduction. The ArM could be genetically optimisation towards improved enantioselectivity via either a directed evolution or rational design approach.

The NMR results from attempts to reduce menadiol with ArM variant [Cp*Ir(5M-C37**L1**)Cl]$^{2+}$ tentatively suggested very low levels of catalytic activity. However, this was not quantitative. It was hypothesised that by-products of low aqueous solubility may provide a partial explanation. Therefore, the next step would be to dry the aqueous reaction samples at one or more timepoints, followed by NMR analysis in organic solvents such as DMSO, in attempt to identify such products. Quantification would then require assignment these signals to individual protons and comparison of the integrals to an internal standard. However, in view of time and resource constraints, it was considered more efficient to shift focus towards alternative ArM reduction activities.

Despite the lack of success in obtaining a functional iridium-TbADH ArMs for imine or quinone reduction, the $NAD(P)^+$ reduction activity of these ArMs was confirmed, albeit at very low rates of between 4 and 6 turnovers per hour. [Cp*Ir(7M-C110**L1**)Cl]$^{2+}$ was found to be marginally more active than the residue location 37-modified variant, on

both of the natural cofactors. Theoretically, the greater performance of the former variant could be further confirmed by performing Michaelis-Menten analysis as for rhodium ArMs, to estimate the affinity of $NAD(P)^+$ binding. However, the low TOF h^{-1} rate values for iridium ArMs would make this practically difficult, owing to the amount of ArM sample required and the volumes of substrate needed in solution.

However, an interesting expansion of this work would be to assess the functionality of ArMs for diastereoselective nicotinamide reduction. The Ward group demonstrated the reduction of NAD^+ using deuterated sodium formate.[174] The two iridium-streptavidin ArM genetic variants tested both displayed preference for the (*S*)-enantiomer of C4-deuterated NADH. Similar methods could be applied to iridium-TbADH ArMs. Any differences observed between genetic variants may provide information about the orientation of catalyst and substrate components, useful in attempts to achieve asymmetric imine reduction using these ArMs.

In conclusion, this thesis has provided a structure and kinetics-based analysis of protein scaffold, catalyst, and substrate interactions in rhodium and iridium-TbADH ArMs. These interactions were investigated in the context of nicotinamide cofactor reduction. An improved understanding of how these three ArM components interact was achieved, particularly with regards to ArM affinity for the nicotinamide substrates. Indeed, the newly designed ArM variant, based on anchoring of the catalyst to residue location 110 displayed a higher estimated affinity for the natural nicotinamide cofactors $NAD(P)^+$ than variants based on locations 37 or 243. The results suggest an improved utilisation of the naturally evolved TbADH nicotinamide binding pocket as hypothesised. Meanwhile, ArM affinity for the nicotinamide mimic BNA^+ was found to be lower than for the natural cofactors, and was also variable between ArM variants. The results suggest that this is mainly owing to the smaller size of the mimic, and the effects of catalyst anchoring location. Further efforts will be needed to support and expand upon these outcomes. In the first instance, to further support the suggested flexibility of covalently bound catalyst orientation in the location 110-modified variant.

Finally, low levels nicotinamide reduction by iridium-TbADH ArMs modified at locations 37 and 110 were detected. This provides proof of principle for functionality in nicotinamide-dependent transfer hydrogenation reactions, such as imine reduction. Future work should be directed at building these ArMs, followed by chemo-genetic optimisation efforts.

References

1. Prier, C. K.; Arnold, F. H., Chemomimetic Biocatalysis: Exploiting the Synthetic Potential of Cofactor-Dependent Enzymes To Create New Catalysts. *Journal of the American Chemical Society* **2015,** *137* (44), 13992-14006.
2. Himiyama, T.; Okamoto, Y., Artificial Metalloenzymes: From Selective Chemical Transformations to Biochemical Applications. *Molecules* **2020,** *25* (13).
3. Lewis, J. C., Artificial Metalloenzymes and Metallopeptide Catalysts for Organic Synthesis. *ACS Catalysis* **2013,** *3* (12), 2954-2975.
4. Schwizer, F.; Okamoto, Y.; Heinisch, T.; Gu, Y. F.; Pellizzoni, M. M.; Lebrun, V.; Reuter, R.; Kohler, V.; Lewis, J. C.; Ward, T. R., Artificial Metalloenzymes: Reaction Scope and Optimization Strategies. *Chemical Reviews* **2018,** *118* (1), 142-231.
5. Davis, H. J.; Ward, T. R., Artificial Metalloenzymes: Challenges and Opportunities. *ACS Central Science* **2019,** *5* (7), 1120-1136.
6. Reetz, M. T., Directed Evolution of Artificial Metalloenzymes: A Universal Means to Tune the Selectivity of Transition Metal Catalysts? *Accounts of Chemical Research* **2019,** *52* (2), 336-344.
7. Skander, M.; Humbert, N.; Collot, J.; Gradinaru, J.; Klein, G.; Loosli, A.; Sauser, J.; Zocchi, A.; Gilardoni, F.; Ward, T. R., Artificial metalloenzymes: (Strept)avidin as host for enantioselective hydrogenation by achiral biotinylated rhodium-diphosphine complexes. *Journal of the American Chemical Society* **2004,** *126* (44), 14411-14418.
8. Hyster, T. K.; Knörr, L.; Ward, T. R.; Rovis, T., Biotinylated Rh(III) complexes in engineered streptavidin for accelerated asymmetric C-H activation. *Science* **2012,** *338* (6106), 500.
9. Okamoto, Y.; Kohler, V.; Ward, T. R., An NAD(P)H-Dependent Artificial Transfer Hydrogenase for Multienzymatic Cascades. *Journal of the American Chemical Society* **2016,** *138* (18), 5781-5784.
10. Chang, F. W.; Wang, C. Y.; Chen, Q. P.; Zhang, Y. J.; Liu, G. H., A Chemoenzymatic Cascade Combining a Hydration Catalyst with an Amine Dehydrogenase: Synthesis of Chiral Amines. *Angewandte Chemie-International Edition* **2022,** *61* (10), 5.
11. Das, S.; Incarvito, C. D.; Crabtree, R. H.; Brudvig, G. W., Molecular recognition in the selective oxygenation of saturated C-H bonds by a dimanganese catalyst. *Science* **2006,** *312* (5782), 1941.
12. Shook, R. L.; Borovik, A. S., Role of the Secondary Coordination Sphere in Metal-Mediated Dioxygen Activation. *Inorganic Chemistry* **2010,** *49* (8), 3646-3660.
13. Hartwig, J. F., Organotransition metal chemistry: from bonding to catalysis. *University Science Books*, **2010**.
14. Alonso-Cotchico, L.; Rodriguez-Guerra, J.; Lledos, A.; Marechal, J. D., Molecular Modeling for Artificial Metalloenzyme Design and Optimization. *Accounts of Chemical Research* **2020,** *53* (4), 896-905.
15. Hermanson, G. T., (Strept)avidin-Biotin Systems In Bioconjugate Techniques, 3rd Edition, *Elsevier Science*, **2013,** 465-505.
16. Wilchek, M.; Bayer, E. A., Introduction To Avidin-Biotin Technology. *Methods in Enzymology* **1990,** *184*, 5-13.
17. Reetz, M. T.; Peyralans, J. J. p.; Maichele, A.; Fu, Y.; Maywald, M., Directed evolution of hybrid enzymes: Evolving enantioselectivity of an achiral Rh-complex anchored to a protein. *Chemical Communications* **2006,** (41), 4318-4320.
18. Hyre, D. E.; Le Trong, I.; Freitag, S.; Stenkamp, R. E.; Stayton, P. S., Ser45 plays an important role in managing both the equilibrium and transition state energetics of the streptavidin-biotin system. *Protein Science* **2000,** *9* (5), 878-885.

19. Wilson, M. E.; Whitesides, G. M., Conversion Of A Protein To A Homogeneous Asymmetric Hydrogenation Catalyst By Site-Specific Modification With A Diphosphinerhodium(I) Moiety. *Journal of the American Chemical Society* **1978,** *100* (1), 306-307.
20. Letondor, C.; Pordea, A.; Humbert, N.; Ivanova, A.; Mazurek, S.; Novic, M.; Ward, T. R., Artificial transfer hydrogenases based on the biotin-(strept)avidin technology: Fine tuning the selectivity by saturation mutagenesis of the host protein. *Journal of the American Chemical Society* **2006,** *128* (25), 8320-8328.
21. Swaminathan, S.; Haribabu, J.; Balakrishnan, N.; Vasanthakumar, P.; Karvembu, R., Piano stool Ru(II)-arene complexes having three monodentate legs: A comprehensive review on their development as anticancer therapeutics over the past decade. *Coordination Chemistry Reviews* **2022,** *459*, 32.
22. Siloto, R. M. P.; Weselake, R. J., Site saturation mutagenesis: Methods and applications in protein engineering. *Biocatalysis and Agricultural Biotechnology* **2012,** *1* (3), 181-189.
23. Hassan, I. S.; Ta, A. N.; Danneman, M. W.; Semakul, N.; Burns, M.; Basch, C. H.; Dippon, V. N.; McNaughton, B. R.; Rovis, T., Asymmetric delta-Lactam Synthesis with a Monomeric Streptavidin Artificial Metalloenzyme. *Journal of the American Chemical Society* **2019,** *141* (12), 4815-4819.
24. Roelfes, G., LmrR: A Privileged Scaffold for Artificial Metalloenzymes. *Accounts of Chemical Research* **2019,** *52* (3), 545-556.
25. Eda, S.; Nasibullin, I.; Vong, K.; Kudo, N.; Yoshida, M.; Kurbangalieva, A.; Tanaka, K., Biocompatibility and therapeutic potential of glycosylated albumin artificial metalloenzymes. *Nature Catalysis* **2019,** *2* (9), 780-792.
26. Markus, J.; Raphael, R.; Tillmann, H.; Christian, T.; Juliane, K.; Sven, P.; Thomas, R. W., Directed evolution of artificial metalloenzymes for in vivo metathesis. *Nature* **2016,** *537* (7622).
27. Pierron, J.; Malan, C.; Creus, M.; Gradinaru, J.; Hafner, I.; Ivanova, A.; Sardo, A.; Ward, T. R., Artificial Metalloenzymes for Asymmetric Allylic Alkylation on the Basis of the Biotin–Avidin Technology. *Angewandte Chemie International Edition* **2008,** *47* (4), 701-705.
28. Bos, J.; Browne, W. R.; Driessen, A. J. M.; Roelfes, G., Supramolecular Assembly of Artificial Metalloenzymes Based on the Dimeric Protein LmrR as Promiscuous Scaffold. *Journal of the American Chemical Society* **2015,** *137* (31), 9796.
29. Morra, S.; Pordea, A., Biocatalyst-artificial metalloenzyme cascade based on alcohol dehydrogenase. *Chemical Science* **2018,** *9* (38), 9.
30. Fernandez-Gacio, A.; Codina, A.; Fastrez, J.; Riant, O.; Soumillion, P., Transforming carbonic anhydrase into epoxide synthase by metal exchange. *Chembiochem* **2006,** *7* (7), 1013-1016.
31. Jing, Q.; Okrasa, K.; Kazlauskas, R. J., Stereoselective Hydrogenation of Olefins Using Rhodium-Substituted Carbonic Anhydrase-A New Reductase. *Chemistry-a European Journal* **2009,** *15* (6), 1370-1376.
32. Jing, Q.; Kazlauskas, R. J., Regioselective Hydroformylation of Styrene Using Rhodium-Substituted Carbonic Anhydrase. *ChemCatChem* **2010,** *2* (8), 953-957.
33. Rebelein, J. G.; Cotelle, Y.; Garabedian, B.; Ward, T. R., Chemical Optimization of Whole-Cell Transfer Hydrogenation Using Carbonic Anhydrase as Host Protein. *ACS Catalysis* **2019,** *9* (5), 4173-4178.
34. Key, H. M.; Dydio, P.; Clark, D. S.; Hartwig, J. F., Abiological catalysis by artificial haem proteins containing noble metals in place of iron. *Nature* **2016,** *534* (7608), 534.
35. Oohora, K.; Onoda, A.; Hayashi, T., Hemoproteins Reconstituted with Artificial Metal Complexes as Biohybrid Catalysts. *Accounts of Chemical Research* **2019,** *52* (4), 945-954.

36. Rousselot-Pailley, P.; Bochot, C.; Marchi-Delapierre, C.; Jorge-Robin, A.; Martin, L.; Fontecilla-Camps, J. C.; Cavazza, C.; Ménage, S., The Protein Environment Drives Selectivity for Sulfide Oxidation by an Artificial Metalloenzyme. *ChemBioChem* **2009,** *10* (3), 545-552.
37. Takezawa, Y.; Bockmann, P.; Sugi, N.; Wang, Z. Y.; Abe, S.; Murakami, T.; Hikage, T.; Erker, G.; Watanabe, Y.; Kitagawa, S.; Ueno, T., Incorporation of organometallic Ru complexes into apo-ferritin cage. *Dalton Transactions* **2011,** *40* (10), 2190-2195.
38. Tabe, H.; Abe, S.; Hikage, T.; Kitagawa, S.; Ueno, T., Porous Protein Crystals as Catalytic Vessels for Organometallic Complexes. *Chemistry-an Asian Journal* **2014,** *9* (5), 1373-1378.
39. Pordea, A.; Creus, M.; Panek, J.; Duboc, C.; Mathis, D.; Novic, M.; Ward, T. R., Artificial metalloenzyme for enantioselective sulfoxidation based on vanadyl-loaded streptavidin. *Journal of the American Chemical Society* **2008,** *130* (25), 8085.
40. Cazares-Marinero, J. D.; Przybylski, C.; Salmain, M., Proteins as Macromolecular Ligands for Metal-Catalysed Asymmetric Transfer Hydrogenation of Ketones in Aqueous Medium. *European Journal of Inorganic Chemistry* **2018,** (12), 1383-1393.
41. Yu, Y.; Hu, C.; Xia, L.; Wang, J., Artificial Metalloenzyme Design with Unnatural Amino Acids and Non-Native Cofactors. *ACS Catalysis* **2018,** *8* (3), 1851-1863.
42. Rosati, F.; Roelfes, G., Artificial Metalloenzymes. *ChemCatChem* **2010,** *2* (8), 916-927.
43. Yang, H.; Srivastava, P.; Zhang, C.; Lewis, J. C., A General Method for Artificial Metalloenzyme Formation through Strain-Promoted Azide–Alkyne Cycloaddition. *ChemBioChem* **2014,** *15* (2), 223-227.
44. Davies, R. R.; Distefano, M. D., A semisynthetic metalloenzyme based on a protein cavity that catalyzes the enantioselective hydrolysis of ester and amide substrates. *Journal of the American Chemical Society* **1997,** *119* (48), 11643-11652.
45. Panella, L.; Broos, J.; Jin, J.; Fraaije, M. W.; Janssen, D. B.; Jeronimus-stratingh, M.; Feringa, B. L.; Minnaard, A. J.; De Vries, J. G., Merging homogeneous catalysis with biocatalysis; papain as hydrogenation catalyst. *Chemical Communications* **2005,** (45), 5656-5658.
46. Madern, N.; Queyriaux, N.; Chevalley, A.; Ghasemi, M.; Nicolotti, O.; Ciofini, I.; Mangiatordi, G. F.; Salmain, M., Piano-stool d6-rhodium(III) complexes of chelating pyridine-based ligands and their papain bioconjugates for the catalysis of transfer hydrogenation of aryl ketones in aqueous medium. *Journal of Molecular Catalysis. B, Enzymatic* **2015,** *122*, 314-322.
47. Bos, J.; Fusetti, F.; Driessen, A. J. M.; Roelfes, G., Enantioselective Artificial Metalloenzymes by Creation of a Novel Active Site at the Protein Dimer Interface. *Angewandte Chemie International Edition* **2012,** *51* (30), 7472-7475.
48. Natoli, S. N.; Hartwig, J. F., Noble-Metal Substitution in Hemoproteins: An Emerging Strategy for Abiological Catalysis. *Accounts of Chemical Research* **2019,** *52* (2), 326-335.
49. Stefane, B.; Pozgan, F., Advances in Catalyst Systems for the Asymmetric Hydrogenation and Transfer Hydrogenation of Ketones. *Catalysis Reviews-Science and Engineering* **2014,** *56* (1), 82-174.
50. Schrittwieser, J. H.; Velikogne, S.; Kroutil, W., Biocatalytic Imine Reduction and Reductive Amination of Ketones. *Advanced Synthesis & Catalysis* **2015,** *357* (8), 1655-1685.
51. France, S. P.; Howard, R. M.; Steflik, J.; Weise, N. J.; Mangas-Sanchez, J.; Montgomery, S. L.; Crook, R.; Kumar, R.; Turner, N. J., Identification of Novel Bacterial Members of the Imine Reductase Enzyme Family that Perform Reductive Amination. *ChemCatChem* **2018,** *10* (3), 510-514.

52. Vidal, L. S.; Kelly, C. L.; Mordaka, P. M.; Heap, J. T., Review of NAD(P)H-dependent oxidoreductases: Properties, engineering and application. *Biochimica Et Biophysica Acta-Proteins and Proteomics* **2018,** *1866* (2), 327-347.
53. France, S. P.; Lewis, R. D.; Martinez, C. A., The Evolving Nature of Biocatalysis in Pharmaceutical Research and Development. *Journal of the American Chemical Society Au* **2023,** *3* (3), 715-735.
54. Josa-Cullere, L.; Landenpera, A. S. K.; Ribaucourt, A.; Hofler, G. T.; Gargiulo, S.; Liu, Y. Y.; Xu, J. H.; Cassidy, J.; Paradisi, F.; Opperman, D. J.; Hollmann, F.; Paul, C. E., Synthetic Biomimetic Coenzymes and Alcohol Dehydrogenases for Asymmetric Catalysis. *Catalysts* **2019,** *9* (3), 11.
55. Knowles, W. S.; Sabacky, M. J., Catalytic Asymmetric Hydrogenation Employing A Soluble Optically Active Rhodium Complex. *Chemical Communications* **1968,** (22), 1445-&.
56. Levi, A.; Modena, G.; Scorrano, G., Asymmetric Reduction Of Carbon-Nitrogen, Carbon-Oxygen, And Carbon-Carbon Double-Bonds By Homogeneous Catalytic-Hydrogenation. *Journal of the Chemical Society-Chemical Communications* **1975,** (1), 6-7.
57. Garbe, M.; Wei, Z. H.; Tannert, B.; Spannenberg, A.; Jiao, H. J.; Bachmann, S.; Scalone, M.; Junge, K.; Beller, M., Enantioselective Hydrogenation of Ketones using Different Metal Complexes with a Chiral PNP Pincer Ligand. *Advanced Synthesis & Catalysis* **2019,** *361* (8), 1913-1920.
58. Xu, D.; Zhou, Z. M.; Dai, L.; Tang, L. W.; Zhang, J., Asymmetric hydrogenation of aromatic ketones by new recyclable ionic tagged ferrocene-ruthenium catalyst system. *Bioorganic & Medicinal Chemistry Letters* **2015,** *25* (9), 1961-1964.
59. Yao, Z. J.; Zhu, J. W.; Lin, N.; Qiao, X. C.; Deng, W., Catalytic hydrogenation of carbonyl and nitro compounds using an N,O -chelate half-sandwich ruthenium catalyst. *Dalton Transactions* **2019,** *48* (21), 7158-7166.
60. Behera, P.; Ramakrishna, D. S.; Chandrasekhar, M. M.; Kothakapu, S. R., A concise review on recent advances in catalytic asymmetric hydrogenation. *Chirality*, **2023,** *35* (8), 477-497.
61. Wang, D.; Astruc, D., The Golden Age of Transfer Hydrogenation. *Chemical Reviews* **2015,** *115* (13), 6621-6686.
62. Zassinovich, G.; Mestroni, G.; Gladiali, S., Asymmetric Hydrogen Transfer-Reactions Promoted By Homogeneous Transition-Metal Catalysts. *Chemical Reviews* **1992,** *92* (5), 1051-1069.
63. Gladiali, S.; Alberico, E., Asymmetric transfer hydrogenation: chiral ligands and applications. *Chemical Society Reviews* **2006,** *35* (3), 226-236.
64. Noyori, R.; Hashiguchi, S., Asymmetric transfer hydrogenation catalyzed by chiral ruthenium complexes. *Accounts of Chemical Research* **1997,** *30* (2), 97-102.
65. Noyori, R.; Yamakawa, M.; Hashiguchi, S., Metal-ligand bifunctional catalysis: A nonclassical mechanism for asymmetric hydrogen transfer between alcohols and carbonyl compounds. *Journal of Organic Chemistry* **2001,** *66* (24), 7931-7944.
66. Mwansa, J. M.; Stirling, M. J.; Page, M. I., Changing the kinetic order of enantiomer formation and distinguishing between iminium ion and imine as the reactive species in the asymmetric transfer hydrogenation of substituted imines using a cyclopentadienyl iridium (III) complex. *Pure and Applied Chemistry* **2020,** *92* (1), 107-121.
67. Gao, J.-X.; Ikariya, T.; Noyori, R., A Ruthenium(II) Complex with a C2-Symmetric Diphosphine/Diamine Tetradentate Ligand for Asymmetric Transfer Hydrogenation of Aromatic Ketones. *Organometallics* **1996,** *15* (4), 1087-1089.
68. Takehara, J.; Hashiguchi, S.; Fujii, A.; Inoue, S.; Ikariya, T.; Noyori, R., Amino alcohol effects on the ruthenium(II)-catalysed asymmetric transfer hydrogenation of ketones in propan-2-ol. *Chemical Communications* **1996,** (2), 233-234.

69. Uematsu, N.; Fujii, A.; Hashiguchi, S.; Ikariya, T.; Noyori, R., Asymmetric transfer hydrogenation of imines. *Journal of the American Chemical Society* **1996,** *118* (20), 4916-4917.
70. Rhyoo, H. Y.; Park, H. J.; Chung, Y. K., The first Ru(II)-catalysed asymmetric hydrogen transfer reduction of aromatic ketones in aqueous media. *Chemical Communications* **2001,** (20), 2064-2065.
71. Bubert, C.; Blacker, J.; Brown, S. M.; Crosby, J.; Fitzjohn, S.; Muxworthy, J. P.; Thorpe, T.; Williams, J. M. J., Synthesis of water-soluble aminosulfonamide ligands and their application in enantioselective transfer hydrogenation. *Tetrahedron Letters* **2001,** *42* (24), 4037-4039.
72. Ma, Y. P.; Liu, H.; Chen, L.; Cui, X.; Zhu, J.; Deng, J. E., Asymmetric transfer hydrogenation of prochiral ketones in aqueous media with new water-soluble chiral vicinal diamine as ligand. *Organic Letters* **2003,** *5* (12), 2103-2106.
73. Szollosi, G.; Kolcsar, V. J., Highly Enantioselective Transfer Hydrogenation of Prochiral Ketones Using Ru(II)-Chitosan Catalyst in Aqueous Media. *ChemCatChem* **2019,** *11* (2), 820-830.
74. Barrios-Rivera, J.; Xu, Y. J.; Clarkson, G. J.; Wills, M., Asymmetric transfer hydrogenation of heterocycle-containing acetophenone derivatives using N-functionalised (benzene) Ru(II)(TsDPEN) complexes. *Tetrahedron* **2022,** *103*, 8.
75. Wu, X. F.; Li, X. H.; Zanotti-Gerosa, A.; Pettman, A.; Liu, J. K.; Mills, A. J.; Xiao, J. L., Rh(III)- and Ir(III)-catalyzed asymmetric transfer hydrogenation of ketones in water. *Chemistry-a European Journal* **2008,** *14* (7), 2209-2222.
76. Sheeba, M. M.; Bhuvanesh, N. S. P.; Karvembu, R., Piano-stool Ru(II)-benzene complexes bearing D/L-alanine derived chiral aroylthiourea ligands for asymmetric transfer hydrogenation of ketones in water. *Journal of Chemical Sciences* **2018,** *130* (12), 8.
77. Yang, J. T.; Yao, L. J.; Wang, Z.; Zuo, Z.; Liu, S. Y.; Gao, P. X.; Han, M. Y.; Liu, Q. B.; Solan, G. A.; Sun, W. H., Manganese(I)-catalyzed asymmetric (transfer) hydrogenation of ketones: An insight into the effect of chiral PNN and NN ligands. *Journal of Catalysis* **2023,** *418*, 40-50.
78. Fujii, A.; Hashiguchi, S.; Uematsu, N.; Ikariya, T.; Noyori, R., Ruthenium(II)-catalyzed asymmetric transfer hydrogenation of ketones using a formic acid-triethylamine mixture. *Journal of the American Chemical Society* **1996,** *118* (10), 2521-2522.
79. Koike, T.; Ikariya, T., Mechanistic aspects of formation of chiral ruthenium hydride complexes from 16-electron ruthenium amide complexes and formic acid: Facile reversible decarboxylation and carboxylation. *Advanced Synthesis & Catalysis* **2004,** *346* (1), 37-41.
80. Wu, X. F.; Wang, C.; Xiao, J. L., Transfer Hydrogenation in Water. *Chemical Record* **2016,** *16* (6), 2772-2786.
81. Canivet, J.; Suss-Fink, G., Water-soluble arene ruthenium catalysts containing sulfonated diamine ligands for asymmetric transfer hydrogenation of alpha-aryl ketones and imines in aqueous solution. *Green Chemistry* **2007,** *9* (4), 391-397.
82. Martins, J. E. D.; Clarkson, G. J.; Wills, M., Ru(II) Complexes of N-Alkylated TsDPEN Ligands in Asymmetric Transfer Hydrogenation of Ketones and Imines. *Organic Letters* **2009,** *11* (4), 847-850.
83. Canivet, J.; Suss-Fink, G.; Stepnicka, P., Water-soluble phenanthroline complexes of rhodium, iridium and ruthenium for the regeneration of NADH in the enzymatic reduction of ketones. *European Journal of Inorganic Chemistry* **2007,** (30), 4736-4742.
84. Wang, L.; Zhou, Q.; Qu, C. H.; Wang, Q. W.; Cun, L. F.; Zhu, J.; Deng, J. G., Efficient asymmetric transfer hydrogenation of N-sulfonylimines on water. *Tetrahedron* **2013,** *69* (31), 6500-6506.
85. Wills, M., Imino Transfer Hydrogenation Reductions. *Topics in Current Chemistry* **2016,** *374* (2), 36.

86. Barrios-Rivera, J.; Xu, Y. J.; Wills, M.; Vyas, V. K., A diversity of recently reported methodology for asymmetric imine reduction. *Organic Chemistry Frontiers* **2020,** *7* (20), 3312-3342.
87. Monnard, F. W.; Nogueira, E. S.; Heinisch, T.; Schirmer, T.; Ward, T. R., Human carbonic anhydrase II as host protein for the creation of artificial metalloenzymes: the asymmetric transfer hydrogenation of imines. *Chemical Science* **2013,** *4* (8), 3269-3274.
88. Raines, D. J.; Clarke, J. E.; Blagova, E. V.; Dodson, E. J.; Wilson, K. S.; Duhme-Klair, A. K., Redox-switchable siderophore anchor enables reversible artificial metalloenzyme assembly. *Nature Catalysis* **2018,** *1* (9), 680-688.
89. Robles, V. M.; Dürrenberger, M.; Heinisch, T.; Lledós, A.; Schirmer, T.; Ward, T. R.; Maréchal, J.-D., Structural, kinetic, and docking studies of artificial imine reductases based on biotin-streptavidin technology: an induced lock-and-key hypothesis. *Journal of the American Chemical Society* **2014,** *136* (44), 15676.
90. Andersson, P. G.; Munslow, I. J., Modern reduction methods / edited by Pher G. Andersson and Ian J. Munslow, Wiley-VCH, **2008**.
91. Hollmann, F.; Arends, I.; Holtmann, D., Enzymatic reductions for the chemist. *Green Chemistry* **2011,** *13* (9), 2285-2314.
92. Hall, M., Enzymatic strategies for asymmetric synthesis. *RSC Chemical Biology* **2021,** *2* (4), 958-989.
93. Kratzer, R.; Woodley, J. M.; Nidetzky, B., Rules for biocatalyst and reaction engineering to implement effective, NAD(P)H-dependent, whole cell bioreductions. *Biotechnology Advances* **2015,** *33* (8), 1641-1652.
94. Garzon-Posse, F.; Becerra-Figueroa, L.; Hernandez-Arias, J.; Gamba-Sanchez, D., Whole Cells as Biocatalysts in Organic Transformations. *Molecules* **2018,** *23* (6), 37.
95. Moore, J. C.; Pollard, D. J.; Kosjek, B.; Devine, P. N., Advances in the enzymatic reduction of ketones. *Accounts of Chemical Research* **2007,** *40* (12), 1412-1419.
96. Truppo, M. D., Biocatalysis in the Pharmaceutical Industry: The Need for Speed. *ACS Medicinal Chemistry Letters* **2017,** *8* (5), 476-480.
97. Jeske, L.; Placzek, S.; Schomburg, I.; Chang, A.; Schomburg, D., BRENDA in 2019: a European ELIXIR core data resource. *Nucleic Acids Research* **2019,** *47* (D1), D542-D549.
98. Kavanagh, K.; Jornvall, H.; Persson, B.; Oppermann, U., The SDR superfamily: functional and structural diversity within a family of metabolic and regulatory enzymes. *Cell. Mol. Life Sci.* **2008,** *65* (24), 3895-3906.
99. Eklund, H.; Plapp, B. V.; Samama, J. P.; Branden, C. I., Binding Of Substrate In A Ternary Complex Of Horse Liver Alcohol-Dehydrogenase. *Journal of Biological Chemistry* **1982,** *257* (23), 4349-4358.
100. Baker, P. J.; Britton, K. L.; Fisher, M.; Esclapez, J.; Pire, C.; Bonete, M. J.; Ferrer, J.; Rice, D. W., Active site dynamics in the zinc-dependent medium chain alcohol dehydrogenase superfamily. *Proceedings of the National Academy of Sciences of the United States of America* **2009,** *106* (3), 779-784.
101. Lee, C.; Bedgar, D. L.; Davin, L. B.; Lewis, N. G., Assessment of a putative proton relay in Arabidopsis cinnamyl alcohol dehydrogenase catalysis. *Organic & Biomolecular Chemistry* **2013,** *11* (7), 1127-1134.
102. Dolega, A., Alcohol dehydrogenase and its simple inorganic models. *Coordination Chemistry Reviews* **2010,** *254* (7-8), 916-937.
103. Kleifeld, O.; Frenkel, A.; Martin, J. M. L.; Sagi, I., Active site electronic structure and dynamics during metalloenzyme catalysis. *Nature Structural Biology* **2003,** *10* (2), 98-103.
104. Lamed, R. J.; Zeikus, J. G., Novel NADP-linked alcohol--aldehyde/ketone oxidoreductase in thermophilic ethanologenic bacteria. *The Biochemical journal* **1981,** *195* (1), 183.

105. Kim, K.; Plapp, B. V., Substitution of cysteine-153 ligated to the catalytic zinc in yeast alcohol dehydrogenase with aspartic acid and analysis of mechanisms of related medium chain dehydrogenases. *Chemico-Biological Interactions* **2019,** *302*, 172-182.
106. Voet, D.; Voet, J. G., Biochemistry. 4th Edition, *John Wiley & Sons*, **2011,** 488-490.
107. Korkhin, Y.; Kalb, A. J.; Peretz, M.; Bogin, O.; Burstein, Y.; Frolow, F., NADP-dependent bacterial alcohol dehydrogenases: Crystal structure, cofactor-binding and cofactor specificity of the ADHs of Clostridium beijerinckii and Thermoanaerobacter brockii. *Journal of Molecular Biology* **1998,** *278* (5), 967-981.
108. Li, C. M.; Heatwole, J.; Soelaiman, S.; Shoham, M., Crystal structure of a thermophilic alcohol dehydrogenase substrate complex suggests determinants of substrate specificity and thermostability. *Proteins-Structure Function and Genetics* **1999,** *37* (4), 619-627.
109. Qu, G.; Bi, Y. X.; Liu, B. B.; Li, J. K.; Han, X.; Liu, W. D.; Jiang, Y. Y.; Qin, Z. M.; Sun, Z. T., Unlocking the Stereoselectivity and Substrate Acceptance of Enzymes: Proline-Induced Loop Engineering Test. *Angewandte Chemie-International Edition* **2022,** *61* (1), 8.
110. Musa, M. M.; Vieille, C.; Phillips, R. S., Secondary Alcohol Dehydrogenases from *Thermoanaerobacter pseudoethanolicus* and *Thermoanaerobacter brockii* as Robust Catalysts. *Chembiochem* **2021,** *22* (11), 1884-1893.
111. Humphrey, W.; Dalke, A.; Schulten, K., VMD: Visual molecular dynamics. *Journal of Molecular Graphics & Modelling* **1996,** *14* (1), 33-38.
112. Vidal, L. S.; Murray, J. W.; Heap, J. T., Versatile selective evolutionary pressure using synthetic defect in universal metabolism. *Nature Communications* **2021,** *12* (1), 15.
113. Mangas-Sanchez, J.; France, S. P.; Montgomery, S. L.; Aleku, G. A.; Man, H.; Sharma, M.; Ramsden, J. I.; Grogan, G.; Turner, N. J., Imine reductases (IREDs). *Current Opinion in Chemical Biology* **2017,** *37*, 19-25.
114. Wandrey, C., Biochemical reaction engineering for redox reactions. *Chemical Record* **2004,** *4* (4), 254-265.
115. Wang, X. D.; Saba, T.; Yiu, H. H. P.; Howe, R. F.; Anderson, J. A.; Shi, J. F., Cofactor NAD(P)H Regeneration Inspired by Heterogeneous Pathways. *Chem* **2017,** *2* (5), 621-654.
116. Zhao, L. J.; Yin, Z. Q.; Shi, Y. S.; Sun, W.; Sun, L. B.; Su, H. J.; Sun, X.; Zhang, W. L.; Xia, L. Y.; Qi, C. X., A highly active Cp*Ir complex with an anionic N,N-donor chelate ligand catalyzes the robust regeneration of NADH under physiological conditions. *Catalysis Science & Technology* **2021,** *11* (24), 7982-7991.
117. Uppada, V.; Bhaduri, S.; Noronha, S. B., Cofactor regeneration - an important aspect of biocatalysis. *Current Science* **2014,** *106* (7), 946-957.
118. Wykes, J. R.; Dunnill, P.; Lilly, M. D., Cofactor recycling in an enzyme reactor. A comparison Using free and immobilized dehydrogenases with free and immobilized NAD. *Biotechnology and Bioengineering* **1975,** *17* (1), 51-68.
119. Hollmann, F.; Arends, I.; Buehler, K., Biocatalytic Redox Reactions for Organic Synthesis: Nonconventional Regeneration Methods. *ChemCatChem* **2010,** *2* (7), 762-782.
120. Hollmann, F.; Witholt, B.; Schmid, A., Cp*Rh(bpy)(H2O) (2+): a versatile tool for efficient and non-enzymatic regeneration of nicotinamide and flavin coenzymes. *Journal of Molecular Catalysis B-Enzymatic* **2002,** *19*, 167-176.
121. Lo, H. C.; Fish, R. H., Biomimetic NAD(+) models for tandem cofactor regeneration, horse liver alcohol dehydrogenase recognition of 1,4-NADH derivatives, and chiral synthesis. *Angewandte Chemie-International Edition* **2002,** *41* (3), 478-481.
122. Lutz, J.; Hollmann, F.; Ho, T. V.; Schnyder, A.; Fish, R. H.; Schmid, A., Bioorganometallic chemistry: biocatalytic oxidation reactions with biomimetic

NAD(+)/NADH co-factors and Cp*Rh(bpy)H (+) for selective organic synthesis. *Journal of Organometallic Chemistry* **2004,** *689* (25), 4783-4790.
123. Zhang, L.; Vila, N.; Kohring, G. W.; Walcarius, A.; Etienne, M., Covalent Immobilization of (2,2 '-Bipyridyl) (Pentamethylcyclopentadienyl)-Rhodium Complex on a Porous Carbon Electrode for Efficient Electrocatalytic NADH Regeneration. *ACS Catalysis* **2017,** *7* (7), 4386-4394.
124. Maenaka, Y.; Suenobu, T.; Fukuzumi, S., Efficient Catalytic Interconversion between NADH and NAD(+) Accompanied by Generation and Consumption of Hydrogen with a Water-Soluble Iridium Complex at Ambient Pressure and Temperature. *Journal of the American Chemical Society* **2012,** *134* (1), 367-374.
125. Lauterbach, L.; Lenz, O.; Vincent, K. A., H2-driven cofactor regeneration with NAD(P) plus -reducing hydrogenases. *Febs Journal* **2013,** *280* (13), 3058-3068.
126. de Torres, M.; Dimroth, J.; Arends, I.; Keilitz, J.; Hollmann, F., Towards Recyclable NAD(P)H Regeneration Catalysts. *Molecules* **2012,** *17* (8), 9835-9841.
127. Paul, C. E.; Hollmann, F., A survey of synthetic nicotinamide cofactors in enzymatic processes. *Applied Microbiology and Biotechnology* **2016,** *100* (11), 4773-4778.
128. Sharma, V. K.; Hutchison, J. M.; Allgeier, A. M., Redox Biocatalysis: Quantitative Comparisons of Nicotinamide Cofactor Regeneration Methods. *Chemsuschem* **2022,** *15* (*22*), 24.
129. Westerhausen, V. D.; Herrmann, S.; Hummel, W.; Steckhan, E., Formate-Driven, Non-Enzymatic NAD(P)H Regeneration for the Alcohol Dehydrogenase Catalyzed Stereoselective Reduction of 4-Phenyl-2-butanone. *Angewandte Chemie International Edition in English* **1992,** *31* (11), 1529-1531.
130. Lo, H. C.; Buriez, O.; Kerr, J. B.; Fish, R. H., Regioselective Reduction of NAD + Models with [Cp*Rh(bpy)H] + : Structure–Activity Relationships and Mechanistic Aspects in the Formation of the 1,4-NADH Derivatives. *Angewandte Chemie International Edition* **1999,** *38* (10), 1429-1432.
131. Tensi, L.; Macchioni, A., Extremely Fast NADH-Regeneration Using Phosphonic Acid as Hydride Source and Iridium-pyridine-2-sulfonamidate Catalysts. *ACS Catalysis* **2020,** *10* (14), 7945-7949.
132. Ganesan, V.; Kim, J. J.; Shin, J.; Park, K.; Yoon, S., Efficient Nicotinamide Adenine Dinucleotide Regeneration with a Rhodium-Carbene Catalyst and Isolation of a Hydride Intermediate. *Inorganic Chemistry* **2022,** *61* (15), 5683-5690.
133. Poizat, M.; Arends, I. W. C. E.; Hollmann, F., On the nature of mutual inactivation between [Cp*Rh(bpy)(H 2O)] 2+ and enzymes – analysis and potential remedies. *Journal of Molecular Catalysis. B, Enzymatic* **2010,** *63* (3-4), 149-156.
134. Hildebrand, F.; Lutz, S., Stable Electroenzymatic Processes by Catalyst Separation. *Chemistry-a European Journal* **2009,** *15* (20), 4998-5001.
135. Knaus, T.; Paul, C. E.; Levy, C. W.; de Vries, S.; Mutti, F. G.; Hollmann, F.; Scrutton, N. S., Better than Nature: Nicotinamide Biomimetics That Outperform Natural Coenzymes. *Journal of the American Chemical Society* **2016,** *138* (3), 1033-1039.
136. Nowak, C.; Pick, A.; Lommes, P.; Sieber, V., Enzymatic Reduction of Nicotinamide Biomimetic Cofactors Using an Engineered Glucose Dehydrogenase: Providing a Regeneration System for Artificial Cofactors. *ACS Catalysis* **2017,** *7* (8), 5202-5208.
137. Fish, R. H., 1,4-NADH Biomimetic Co-Factors with Horse Liver Alcohol Dehydrogenase (HLADH), Utilizing Cp*Rh(bpy)H (OTf) for Co-factor Regeneration, Do in Fact, Produce Chiral Alcohols from Reactions with Achiral Ketones. *Catalysts* **2019,** *9* (6), 4.
138. Drenth, J.; Yang, G.; Paul, C. E.; Fraaije, M. W., A Tailor-Made Deazaflavin-Mediated Recycling System for Artificial Nicotinamide Cofactor Biomimetics. *ACS Catalysis* **2021,** *11* (18), 11561-11569.

139. Huang, R.; Chen, H.; Upp, D. M.; Lewis, J. C.; Zhang, Y., A High-Throughput Method for Directed Evolution of NAD(P)(+)-Dependent Dehydrogenases for the Reduction of Biomimetic Nicotinamide Analogues. *ACS Catalysis* **2019,** *9* (12), 11709-11719.
140. King, E.; Maxel, S.; Li, H., Engineering natural and noncanonical nicotinamide cofactor-dependent enzymes: design principles and technology development. *Current Opinion in Biotechnology* **2020,** *66*, 217-226.
141. Choi, J.-M.; Han, S.-S.; Kim, H.-S., Industrial applications of enzyme biocatalysis: Current status and future aspects. *Biotechnology Advances* **2015,** *33* (7), 1443-1454.
142. Hayashi, T.; Murata, D.; Makino, M.; Sugimoto, H.; Matsuo, T.; Sato, H.; Shiro, Y.; Hisaeda, Y., Crystal structure and peroxidase activity of myoglobin reconstituted with iron porphycene. *Inorganic Chemistry* **2006,** *45* (26), 10530-10536.
143. Cavazza, C.; Bochot, C.; Rousselot-Pailley, P.; Carpentier, P.; Cherrier, M. V.; Martin, L.; Marchi-Delapierre, C.; Fontecilla-Camps, J. C.; Menage, S., Crystallographic snapshots of the reaction of aromatic C-H with O-2 catalysed by a protein-bound iron complex. *Nature Chemistry* **2010,** *2* (12), 1069-1076.
144. Heinisch, T.; Schwizer, F.; Garabedian, B.; Csibra, E.; Jeschek, M.; Vallapurackal, J.; Pinheiro, V. B.; Marliere, P.; Panke, S.; Ward, T. R., E-coli surface display of streptavidin for directed evolution of an allylic deallylase. *Chemical Science* **2018,** *9* (24), 5383-5388.
145. Heinisch, T.; Pellizzoni, M.; Dürrenberger, M.; Tinberg, C. E.; Köhler, V.; Klehr, J.; Häussinger, D.; Baker, D.; Ward, T. R., Improving the Catalytic Performance of an Artificial Metalloenzyme by Computational Design. *Journal of the American Chemical Society* **2015,** *137* (32), 10414.
146. Van Stappen, C.; Deng, Y. L.; Liu, Y. W.; Heidari, H.; Wang, J. X.; Zhou, Y.; Ledray, A. P.; Lu, Y., Designing Artificial Metalloenzymes by Tuning of the Environment beyond the Primary Coordination Sphere. *Chemical Reviews* **2022,** *122* (14), 11974-12045.
147. Arnold, F. H., Directed Evolution: Bringing New Chemistry to Life. *Angewandte Chemie International Edition* **2018,** *57* (16), 4143-4148.
148. Michael, S. P.; David, R. L., Methods for the directed evolution of proteins. *Nature Reviews Genetics* **2015,** *16* (7), 379.
149. Steiner, K.; Schwab, H., Recent Advances In Rational Approaches For Enzyme Engineering. *Computational and Structural Biotechnology Journal* **2012,** *2* (3), e201209010.
150. Lutz, S., Beyond directed evolution-semi-rational protein engineering and design. *Current Opinion in Biotechnology* **2010,** *21* (6), 734-743.
151. Wlodawer, A.; Li, M.; Dauter, Z., High-Resolution Cryo-EM Maps and Models: A Crystallographer's Perspective. *Structure* **2017,** *25* (10), 1589-1597.e1.
152. Yip, K. M.; Fischer, N.; Paknia, E.; Chari, A.; Stark, H., Atomic-resolution protein structure determination by cryo-EM. *Nature* **2020,** *587* (7832), 157-+.
153. Wang, H. W.; Wang, J. W., How cryo-electron microscopy and X-ray crystallography complement each other. *Protein Science* **2017,** *26* (1), 32-39.
154. Cho, C.; Hong, S.; Moon, H. G.; Jang, Y.-S.; Kim, D.; Lee, S. Y.; Lovley, D. R.; Jin, Y.-S.; Yang, S., Engineering Clostridial Aldehyde/Alcohol Dehydrogenase for Selective Butanol Production. *ASM Journals* **2019,** *10* (1).
155. Leach, A. R., Molecular modelling: principles and applications, 2nd Edition, *Prentice Hall*, **2001**.
156. Liu, Y.; Kuhlman, B., RosettaDesign server for protein design. *Nucleic acids research* **2006,** *34*, 235-238.
157. Karplus, M.; Kuriyan, J., Molecular dynamics and protein function. *Proceedings of the National Academy of Sciences of the United States of America* **2005,** *102* (19), 6679.

158. Meng, X. Y.; Zhang, H. X.; Mezei, M.; Cui, M., Molecular Docking: A Powerful Approach for Structure-Based Drug Discovery. *Current Computer-Aided Drug Design* **2011,** *7* (2), 146-157.
159. Wright, W. C.; Chenge, J.; Wang, J. H.; Girvan, H. M.; Yang, L.; Chai, S. C.; Huber, A. D.; Wu, J.; Oladimeji, P. O.; Munro, A. W.; Chen, T. S., Clobetasol Propionate Is a Heme-Mediated Selective Inhibitor of Human Cytochrome P450 3A5. *Journal of Medicinal Chemistry* **2020,** *63* (3), 1415-1433.
160. Pagadala, N. S.; Syed, K.; Tuszynski, J., Software for molecular docking: a review. *Biophysical reviews* **2017,** *9* (2), 91.
161. Di Meo, T.; Kariyawasam, K.; Ghattas, W.; Valerio-Lepiniec, M.; Sciortino, G.; Marechal, J. D.; Minard, P.; Mahy, J. P.; Urvoas, A.; Ricoux, R., Functionalized Artificial Bidomain Proteins Based on an alpha-Solenoid Protein Repeat Scaffold: A New Class of Artificial Diels-Alderases. *ACS Omega* **2019,** *4* (2), 4437-4447.
162. Cassidy, J.; Bruen, L.; Rosini, E.; Molla, G.; Pollegioni, L.; Paradisi, F., Engineering substrate promiscuity in halophilic alcohol dehydrogenase (HvADH2) by in silico design. *PLOS One* **2017**.
163. Muñoz Robles, V.; Ortega-Carrasco, E.; Alonso-Cotchico, L.; Rodriguez-Guerra, J.; Lledós, A.; Maréchal, J. D., Toward the computational design of artificial metalloenzymes: From protein-ligand docking to multiscale approaches. *ACS Catalysis* **2015,** *5* (4), 2469-2480.
164. Senn, H. M.; Thiel, W., QM/MM Methods for Biomolecular Systems. *John Wiley & Sons*, **2009**.
165. Durrenberger, M.; Heinisch, T.; Wilson, Y. M.; Rossel, T.; Nogueira, E.; Knorr, L.; Mutschler, A.; Kersten, K.; Zimbron, M. J.; Pierron, J.; Schirmer, T.; Ward, T. R., Artificial Transfer Hydrogenases for the Enantioselective Reduction of Cyclic Imines. *Angewandte Chemie-International Edition* **2011,** *50* (13), 3026-3029.
166. Creus, M.; Pordea, A.; Rossel, T.; Sardo, A.; Letondor, C.; Ivanova, A.; Letrong, I.; Stenkamp, R. E.; Ward, T. R., X-ray structure and designed evolution of an artificial transfer hydrogenase. *Angewandte Chemie-International Edition* **2008,** *47* (8), 1400.
167. Stockinger, P.; Borlinghaus, N.; Sharma, M.; Aberle, B.; Grogan, G.; Pleiss, J.; Nestl, B. M., Inverting the Stereoselectivity of an NADH-Dependent Imine-Reductase Variant. *ChemCatChem* **2021,** *13* (24), 5210-5215.
168. Stein, A.; Chen, D. P.; Igareta, N. V.; Cotelle, Y.; Rebelein, J. G.; Ward, T. R., A Dual Anchoring Strategy for the Directed Evolution of Improved Artificial Transfer Hydrogenases Based on Carbonic Anhydrase. *ACS Central Science* **2021,** *7* (11), 1874-1884.
169. Booth, R. L.; Grogan, G.; Wilson, K. S.; Duhme-Klair, A. K., Artificial imine reductases: developments and future directions. *RSC Chemical Biology* **2020,** *1* (5), 369-378.
170. Igareta, N. V.; Tachibana, R.; Spiess, D. C.; Peterson, R. L.; Ward, T. R., Spiers Memorial Lecture: Shielding the active site: a streptavidin superoxide-dismutase chimera as a host protein for asymmetric transfer hydrogenation. *Faraday Discussions* **2023**.
171. Haquette, P.; Talbi, B.; Barilleau, L.; Madern, N.; Fosse, C.; Salmain, M., Chemically engineered papain as artificial formate dehydrogenase for NAD(P)H regeneration. *Organic & Biomolecular Chemistry* **2011,** *9* (16), 5720-5727.
172. Kohler, V.; Wilson, Y. M.; Durrenberger, M.; Ghislieri, D.; Churakova, E.; Quinto, T.; Knorr, L.; Haussinger, D.; Hollmann, F.; Turner, N. J.; Ward, T. R., Synthetic cascades are enabled by combining biocatalysts with artificial metalloenzymes. *Nature Chemistry* **2013,** *5* (2), 93-99.
173. Okamoto, Y.; Köhler, V.; Paul, C. E.; Hollmann, F.; Ward, T. R., Efficient in situ regeneration of NADH mimics by an artificial metalloenzyme. *ACS Catalysis* **2016,** *6* (6), 3553-3557.

174. Quinto, T.; Häussinger, D.; Köhler, V.; Ward, T. R., Artificial metalloenzymes for the diastereoselective reduction of NAD(+) to NAD(2)H. *Organic & biomolecular chemistry* **2015,** *13* (2), 357.
175. Keinan, E.; Hafeli, E. K.; Seth, K. K.; Lamed, R., Thermostable Enzymes in Organic Synthesis. 2. 1 Asymmetric Reduction of Ketones with Alcohol Dehydrogenase from Thermoanaerobium brockii. *Journal of the American Chemical Society* **1986,** *108* (1), 162-169.
176. Christoffel, F.; Igareta, N. V.; Pellizzoni, M. M.; Tiessler-Sala, L.; Lozhkin, B.; Spiess, D. C.; Lledos, A.; Marechal, J. D.; Peterson, R. L.; Ward, T. R., Design and evolution of chimeric streptavidin for protein-enabled dual gold catalysis. *Nature Catalysis* **2021,** *4* (8), 643-+.
177. Chordia, S.; Narasimhan, S.; Paioni, A. L.; Baldus, M.; Roelfes, G., In Vivo Assembly of Artificial Metalloenzymes and Application in Whole-Cell Biocatalysis. *Angewandte Chemie-International Edition* **2021,** *60* (11), 5913-5920.
178. Bersellini, M.; Roelfes, G., Multidrug resistance regulators (MDRs) as scaffolds for the design of artificial metalloenzymes. *Organic & Biomolecular Chemistry* **2017,** *15* (14), 3069-3073.
179. Di Meo, T.; Ghattas, W.; Herrero, C.; Velours, C.; Minard, P.; Mahy, J. P.; Ricoux, R.; Urvoas, A., alpha Rep A3: A Versatile Artificial Scaffold for Metalloenzyme Design. *Chemistry: a European Journal* **2017,** *23* (42), 10156-10166.
180. Harder, E.; Damm, W.; Maple, J.; Wu, C. J.; Reboul, M.; Xiang, J. Y.; Wang, L. L.; Lupyan, D.; Dahlgren, M. K.; Knight, J. L.; Kaus, J. W.; Cerutti, D. S.; Krilov, G.; Jorgensen, W. L.; Abel, R.; Friesner, R. A., OPLS3: A Force Field Providing Broad Coverage of Drug-like Small Molecules and Proteins. *Journal of Chemical Theory and Computation* **2016,** *12* (1), 281-296.
181. Guedes, I. A.; de Magalhães, C. S.; Dardenne, L. E., Receptor–ligand molecular docking. *Biophysical Reviews* **2014,** *6* (1), 75-87.
182. Friesner, R. A.; Banks, J. L.; Murphy, R. B.; Halgren, T. A.; Klicic, J. J.; Mainz, D. T.; Repasky, M. P.; Knoll, E. H.; Shelley, M.; Perry, J. K.; Shaw, D. E.; Francis, P.; Shenkin, P. S., Glide: A new approach for rapid, accurate docking and scoring. 1. Method and assessment of docking accuracy. *Journal of Medicinal Chemistry* **2004,** *47* (7), 1739-1749.
183. Anton, B. P.; Raleigh, E. A., Complete Genome Sequence of NEB 5-alpha, a Derivative of Escherichia coli K-12 DH5α. *Genome Announcements* **2016,** *4* (6), 2.
184. Jeong, H.; Kim, H. J.; Lee, S. J., Complete Genome Sequence of Escherichia coli Strain BL21. *Genome Announcements* **2015,** *3* (2), 1.
185. Tabor, S., Expression using the T7 RNA polymerase/promoter system, *Current Protocols in Molecular Biology (A Wiley Brand)* **1990**.
186. Basle, M., Development of an artificial metalloenzyme from a nicotinamide-dependent enzymatic scaffold. *University of Nottingham*, **2019**.
187. Bachman, J., Jon Lorsch., Site-Directed Mutagenesis - Methods in Enzymology. *Elsevier* **2013,** 241-248
188. Vingadassalon, A.; Bouloc, P.; Rimsky, S., Removing nucleic acids from nucleoid-associated proteins purified by affinity column. *J Biol Methods* **2016,** *3* (1).
189. Peretz, M.; Bogin, O.; TelOr, S.; Cohen, A.; Li, G. S.; Chen, J. S.; Burstein, Y., Molecular cloning, nucleotide sequencing, and expression of genes encoding alcohol dehydrogenases from the thermophile Thermoanaerobacter brockii and the mesophile Clostridium beijerinckii. *Anaerobe* **1997,** *3* (4), 259-270.
190. Schmidt, T. G. M.; Skerra, A., The Strep-tag system for one-step purification and high-affinity detection or capturing of proteins. *Nature Protocols* **2007,** *2* (6), 1528-1535.
191. Kimple, M. E.; Brill, A. L.; Pasker, R. L., Overview of affinity tags for protein purification. *Curr Protoc Protein Sci* **2013,** *73*, 9.9.1-9.9.23.

192. Nowakowski, A. B.; Wobig, W. J.; Petering, D. H., Native SDS-PAGE: high resolution electrophoretic separation of proteins with retention of native properties including bound metal ions. *Metallomics* **2014,** *6* (5), 1068-1078.
193. Anthis, N. J.; Clore, G. M., Sequence-specific determination of protein and peptide concentrations by absorbance at 205 nm. *Protein Science* **2013,** *22* (6), 851-858.
194. Himeda, Y.; Onozawa-Komatsuzaki, N.; Sugihara, H.; Arakawa, H.; Kasuga, K., Half-sandwich complexes with 4,7-dihydroxy-1,10-phenanthroline: Water-soluble, highly efficient catalysts for hydrogenation of bicarbonate attributable to the generation of an oxyanion on the catalyst ligand. *Organometallics* **2004,** *23* (7), 1480-1483.
195. Liu, Z.; Deeth, R. J.; Butler, J. S.; Habtemariam, A.; Newton, M. E.; Sadler, P. J., Reduction of Quinones by NADH Catalyzed by Organoiridium Complexes. *Angewandte Chemie-International Edition* **2013,** *52* (15), 4194-4197.
196. Winther, J. R.; Thorpe, C., Quantification of thiols and disulfides. *Biochimica Et Biophysica Acta-General Subjects* **2014,** *1840* (2), 838-846.
197. Riddles, P. W.; Blakeley, R. L.; Zerner, B., Reassessment of Ellman's reagent - Methods in Enzymology. *Elsevier* **1983,** 49-60
198. Donnelly, D. P.; Rawlins, C. M.; DeHart, C. J.; Fornelli, L.; Schachner, L. F.; Lin, Z. Q.; Lippens, J. L.; Aluri, K. C.; Sarin, R.; Chen, B. F.; Lantz, C.; Jung, W.; Johnson, K. R.; Koller, A.; Wolff, J. J.; Campuzano, I. D. G.; Auclair, J. R.; Ivanov, A. R.; Whitelegge, J. P.; Pasa-Tolic, L.; Chamot-Rooke, J.; Danis, P. O.; Smith, L. M.; Tsybin, Y. O.; Loo, J. A.; Ge, Y.; Kelleher, N. L.; Agar, J. N., Best practices and benchmarks for intact protein analysis for top-down mass spectrometry. *Nature Methods* **2019,** *16* (7), 587-594.
199. Mann, M.; Kelleher, N. L., Precision proteomics: The case for high resolution and high mass accuracy. *Proceedings of the National Academy of Sciences of the United States of America* **2008,** *105* (47), 18132-18138.
200. Tischler, D.; Gädke, E.; Eggerichs, D.; Baraibar, A. G.; Mügge, C.; Scholtissek, A.; Paul, C. E., Asymmetric Reduction of (R)-Carvone through a Thermostable and Organic-Solvent-Tolerant Ene-Reductase. *Chembiochem* **2020,** *21* (8), 1217-1225.
201. Ruppert, R.; Herrmann, S.; Steckhan, E., Very Efficient Reduction Of Nad(P)+ With Formate Catalyzed By Cationic Rhodium Complexes. *Journal of the Chemical Society-Chemical Communications* **1988,** (17), 1150-1151.
202. Veskoukis, A. S.; Margaritelis, N. V.; Kyparos, A.; Paschalis, V.; Nikolaidis, M. G., Spectrophotometric assays for measuring redox biomarkers in blood and tissues: the NADPH network. *Redox Report* **2018,** *23* (1), 47-56.
203. Biswas, S.; Patra, A.; Paul, P.; Misra, N.; Kushwaha, G. S.; Suar, M., Structural and Biochemical Studies on *Klebsiella Pneumoniae* Enoyl-ACP Reductase (FabI) Suggest Flexible Substrate Binding Site. *Protein Journal* **2024,** *43* (1), 84-95.
204. McCoy, A. J.; Grosse-Kunstleve, R. W.; Adams, P. D.; Winn, M. D.; Storoni, L. C.; Read, R. J., Phaser crystallographic software. *Journal of Applied Crystallography* **2007,** *40*, 658-674.
205. Liebschner, D.; Afonine, P. V.; Baker, M. L.; Bunkoczi, G.; Chen, V. B.; Croll, T. I.; Hintze, B.; Hung, L. W.; Jain, S.; McCoy, A. J.; Moriarty, N. W.; Oeffner, R. D.; Poon, B. K.; Prisant, M. G.; Read, R. J.; Richardson, J. S.; Richardson, D. C.; Sammito, M. D.; Sobolev, O. V.; Stockwell, D. H.; Terwilliger, T. C.; Urzhumtsev, A. G.; Videau, L. L.; Williams, C. J.; Adams, P. D., Macromolecular structure determination using X-rays, neutrons and electrons: recent developments in Phenix. *Acta Crystallographica Section D-Structural Biology* **2019,** *75*, 861-877.
206. Winn, M. D.; Ballard, C. C.; Cowtan, K. D.; Dodson, E. J.; Emsley, P.; Evans, P. R.; Keegan, R. M.; Krissinel, E. B.; Leslie, A. G. W.; McCoy, A.; McNicholas, S. J.; Murshudov, G. N.; Pannu, N. S.; Potterton, E. A.; Powell, H. R.; Read, R. J.; Vagin, A.; Wilson, K. S., Overview of the CCP4 suite and current developments. *Acta Crystallographica Section D-Structural Biology* **2011,** *67*, 235-242.

207. Terwilliger, T. C.; Grosse-Kunstleve, R. W.; Afonine, P. V.; Moriarty, N. W.; Zwart, P. H.; Hung, L. W.; Read, R. J.; Adams, P. D., Iterative model building, structure refinement and density modification with the PHENIX AutoBuild wizard. *Acta Crystallographica Section D-Biological Crystallography* **2008,** *64*, 61-69.
208. Emsley, P.; Lohkamp, B.; Scott, W. G.; Cowtan, K., Features and development of Coot. *Acta Crystallographica Section D-Biological Crystallography* **2010,** *66*, 486-501.
209. Vagin, A. A.; Steiner, R. A.; Lebedev, A. A.; Potterton, L.; McNicholas, S.; Long, F.; Murshudov, G. N., REFMAC5 dictionary: organization of prior chemical knowledge and guidelines for its use. *Acta Crystallographica Section D-Structural Biology* **2004,** *60*, 2184-2195.
210. Potterton, L.; Agirre, J.; Ballard, C.; Cowtan, K.; Dodson, E.; Evans, P. R.; Jenkins, H. T.; Keegan, R.; Krissinel, E.; Stevenson, K.; Lebedev, A.; McNicholas, S. J.; Nicholls, R. A.; Noble, M.; Pannu, N. S.; Roth, C.; Sheldrick, G.; Skubak, P.; Turkenburg, J.; Uski, V.; von Delft, F.; Waterman, D.; Wilson, K.; Winn, M.; Wojdyr, M., CCP4i2: the new graphical user interface to the CCP4 program suite. *Acta Crystallographica Section D-Structural Biology* **2018,** *74*, 68-84.
211. Moriarty, N. W.; Grosse-Kunstleve, R. W.; Adams, P. D., electronic Ligand Builder and Optimization Workbench (eLBOW): a tool for ligand coordinate and restraint generation. *Acta Crystallographica Section D-Structural Biology* **2009,** *65*, 1074-1080.
212. Basle, M.; Padley, H. A. W.; Martins, F. L.; Winkler, G. S.; Jager, C. M.; Pordea, A., Design of artificial metalloenzymes for the reduction of nicotinamide cofactors. *Journal of Inorganic Biochemistry* **2021,** *220*.
213. TryndaLemiesz, L.; Pruchnik, F. P., Studies on the interaction between human serum albumin and [Rh2(OAc)2(bpy)2(H2O)2](OAc)2. *Journal of Inorganic Biochemistry* **1997,** *66* (3), 187-192.
214. Ohata, J.; Ball, Z. T., Rhodium at the chemistry-biology interface. *Dalton Transactions* **2018,** *47* (42), 14855-14860.
215. Chadda, R.; Robertson, J. L., Measuring Membrane Protein Dimerisation Equilibrium in Lipid Bilayers by Single-Molecule Fluorescence Microscopy - Methods in Enzymology. *Elsevier* **2016,** 53-82.
216. Findrik, Z.; Vasic-Racki, D.; Lutz, S.; Daussmann, T.; Wandrey, C., Kinetic modeling of acetophenone reduction catalyzed by alcohol dehydrogenase from Thermoanaerobacter sp. *Biotechnology Letters* **2005,** *27* (15), 1087-1095.
217. Friesner, R. A.; Murphy, R. B.; Repasky, M. P.; Frye, L. L.; Greenwood, J. R.; Halgren, T. A.; Sanschagrin, P. C.; Mainz, D. T., Extra precision glide: Docking and scoring incorporating a model of hydrophobic enclosure for protein-ligand complexes. *Journal of Medicinal Chemistry* **2006,** *49* (21), 6177-6196.
218. Wells, A. F., Structural Inorganic-Chemistry, 5th Edition *Nature* **1985,** *314* (6006), 30-30.
219. Patel, J. M.; Musa, M. M.; Rodriguez, L.; Sutton, D. A.; Popik, V. V.; Phillips, R. S., Mutation of Thermoanaerobacter ethanolicus secondary alcohol dehydrogenase at Trp-110 affects stereoselectivity of aromatic ketone reduction. *Organic & Biomolecular Chemistry* **2014,** *12* (31), 5905-5910.
220. Korkhin, Y.; Frolow, F.; Bogin, O.; Peretz, M.; Kalb, A.; Burstein, Y., Crystalline alcohol dehydrogenases from the mesophilic bacterium Clostridium beijerinckii and the thermophilic bacterium Thermoanaerobium brockii: Preparation, characterization and molecular symmetry. *Acta Crystallogr. Sect. D-Biol. Crystallogr.* **1996,** *52*, 882-886.
221. Jarvis, A. G., Designer metalloenzymes for synthetic biology: Enzyme hybrids for catalysis. *Current Opinion in Chemical Biology* **2020,** *58*, 63-71.
222. Dessau, M. A.; Modis, Y., Protein Crystallization for X-ray Crystallography. *Jove-Journal of Visualized Experiments* **2011,** (47).

223. Zhou, Y. Y.; Ding, Y. M.; Huang, Y. H.; Cai, L. L.; Xu, J. W.; Ma, X., Synthesis and Structural Optimization of Iridium(III) Solvent Complex for Electrochemiluminescence Labeling of Histidine-Rich Protein and Immunoassay Applications for CRP Detection. *ACS Omega* **2020,** *5* (7), 3638-3645.
224. Wang, X. B.; Jia, J. L.; Huang, Z. Z.; Zhou, M.; Fei, H., Luminescent Peptide Labeling Based on a Histidine-Binding Iridium(III) Complex for Cell Penetration and Intracellular Targeting Studies. *Chemistry-a European Journal* **2011,** *17* (29), 8028-8032.
225. Ma, X. C.; Jia, J. L.; Cao, R.; Wang, X. B.; Fei, H., Histidine-Iridium(III) Coordination-Based Peptide Luminogenic Cyclization and Cyclo-RGD Peptides for Cancer-Cell Targeting. *Journal of the American Chemical Society* **2014,** *136* (51), 17734-17737.
226. Zhang, M. Y.; Qian, M. P.; Huang, H.; Gao, Q.; Zhang, C. X.; Qi, H. L., Carboxyl group bearing iridium(III) solvent complex as photoluminescence and electrochemiluminescence probe for the detection of histidine. *Journal of Electroanalytical Chemistry* **2022,** *920*, 6.
227. Booth, W. T.; Schlachter, C. R.; Pote, S.; Ussin, N.; Mank, N. J.; Klapper, V.; Offermann, L. R.; Tang, C. B.; Hurlburt, B. K.; Chruszcz, M., Impact of an N-terminal Polyhistidine Tag on Protein Thermal Stability. *ACS Omega* **2018,** *3* (1), 760-768.
228. Soetens, M.; Drouet, F.; Riant, O., (eta(5)-Pentamethylcyclopentadienyl)iridium Complex Catalyzed Imine Reductions Utilizing the Biomimetic 1,4-NAD(P)H Cofactor and N-Benzyl-1,4-dihydronicotinamide as the Hydride-Transfer Agent. *ChemCatChem* **2017,** *9* (6), 929-933.
229. Martins, F. L. Engineering of artificial metalloenzymes based on alcohol dehydrogenase scaffold. *University of Nottingham*, **2021**.
230. Chen, R. X.; Ogunlana, A. A.; Fang, S. W.; Long, W. H.; Sun, H. M.; Bao, X. G.; Wan, X. B., In situ generation of nitrile oxides from copper carbene and tert-butyl nitrite: synthesis of fully substituted isoxazoles. *Organic & Biomolecular Chemistry* **2018,** *16* (25), 4683-4687.
231. Ding, Y. D.; Williams, N. H.; Hunter, C. A., A Synthetic Vesicle-to-Vesicle Communication System. *Journal of the American Chemical Society* **2019,** *141* (44), 17847-17853.
232. Frisell, H.; Akermark, B., Influence Of Different 4,7-Substituted 1,10-Phenanthroline Ligands On Reactivity And Regiocontrol And Stereocontrol In Tungsten-Catalyzed Allylic Alkylations. *Organometallics* **1995,** *14* (1), 561-563.
233. Kalgutkar, A. S.; Kozak, K. R.; Crews, B. C.; Hochgesang, G. P.; Marnett, L. J., Covalent modification of cyclooxygenase-2 (COX-2) by 2-acetoxyphenyl alkyl sulfides, a new class of selective COX-2 inactivators. *Journal of Medicinal Chemistry* **1998,** *41* (24), 4800-4818.
234. Hirano, J.; Miyata, H.; Hamase, K.; Zaitsu, K., A ratiometric fluorescent chemosensor, 1,10-phenanthroline-4,7-dione, for anions in aqueous-organic media. *Tetrahedron Letters* **2007,** *48* (28), 4861-4864.
235. Betanzos-Lara, S.; Liu, Z.; Habtemariam, A.; Pizarro, A. M.; Qamar, B.; Sadler, P. J., Organometallic Ruthenium and Iridium Transfer-Hydrogenation Catalysts Using Coenzyme NADH as a Cofactor. *Angewandte Chemie-International Edition* **2012,** *51* (16), 3897-3900.
236. Li, J.; Zuo, X.; Cheng, P.; Ren, X. Y.; Sun, S. B.; Xu, J. Q.; Holmgren, A.; Lu, J., The production of reactive oxygen species enhanced with the reduction of menadione by active thioredoxin reductase. *Metallomics* **2019,** *11* (9), 1490-1497.
237. Ren, X. Y.; Santhosh, S. M.; Coppo, L.; Ogata, F. T.; Lu, J.; Holmgren, A., The combination of ascorbate and menadione causes cancer cell death by oxidative stress and replicative stress. *Free Radical Biology and Medicine* **2019,** *134*, 350-358.

238. Bolitho, E. M.; Worby, N. G.; Coverdale, J. P. C.; Wolny, J. A.; Schunemann, V.; Sadler, P. J., Quinone Reduction by Organo-Osmium Half-Sandwich Transfer Hydrogenation Catalysts. *Organometallics* **2021,** *40* (17), 3012-3023.
239. Green, B.; Cairns, S.; Harvey, R.; Pettit, M., Phytomenadione or menadiol in the management of an elevated international normalized ratio (prothrombin time). *Alimentary Pharmacology & Therapeutics* **2000,** *14* (12), 1685-1689.
240. Branigan, E.; Pliotas, C.; Hagelueken, G.; Naismith, J. H., Quantification of free cysteines in membrane and soluble proteins using a fluorescent dye and thermal unfolding. *Nature Protocols* **2013,** *8* (11), 2090-2097.
241. Riener, C. K.; Kada, G.; Gruber, H. J., Quick measurement of protein sulfhydryls with Ellman's reagent and with 4,4'-dithiodipyridine. *Analytical and Bioanalytical Chemistry* **2002,** *373* (4-5), 266-276.
242. Sudar, M.; Vasic-Racki, D.; Müller, M.; Walter, A.; Blazevic, Z. F., Mathematical model of the MenD-catalyzed 1,4-addition (Stetter reaction) of α-ketoglutaric acid to acrylonitrile. *Journal of Biotechnology* **2018,** *268*, 71-80.
243. Zubi, Y. S.; Liu, B. Q.; Gu, Y. F.; Sahoo, D.; Lewis, J. C., Controlling the optical and catalytic properties of artificial metalloenzyme photocatalysts using chemogenetic engineering. *Chemical Science* **2022,** *13* (5), 1459-1468.
244. Byer, A. S.; Pei, X. K.; Patterson, M. G.; Ando, N., Small-angle X-ray scattering studies of enzymes. *Current Opinion in Chemical Biology* **2023,** *72*, 9.
245. Puthenveetil, R.; Vinogradova, O., Solution NMR: A powerful tool for structural and functional studies of membrane proteins in reconstituted environments. *Journal of Biological Chemistry* **2019,** *294* (44), 15914-15931.
246. Greenfield, N. J., Using circular dichroism spectra to estimate protein secondary structure. *Nature Protocols* **2006,** *1* (6), 2876-2890.
247. Juszczak, M.; Das, S.; Kosinska, A.; Rybarczyk-Pirek, A. J.; Wzgarda-Raj, K.; Tokarz, P.; Vasudevan, S.; Chworos, A.; Wozniak, K.; Rudolf, B., Piano-stool ruthenium(II) complexes with maleimide and phosphine or phosphite ligands: synthesis and activity against normal and cancer cells. *Dalton Transactions* **2023,** *52* (13), 4237-4250.
248. Reetz, M. T.; Rentzsch, M.; Pletsch, A.; Taglieber, A.; Hollmann, F.; Mondiere, R. J. G.; Dickmann, N.; Hocker, B.; Cerrone, S.; Haeger, M. C.; Sterner, R., A robust protein host for anchoring chelating ligands and organocatalysts. *Chembiochem* **2008,** *9* (4), 552-564.

Appendices

Appendix 1 – Kinetic parameter and adjusted R^2 values from Michaelis-Menten characterisation rhodium-TbADH ArM nicotinamide reduction

	*[Cp*Rh(7M-C243**L1**)Cl]$^{2+}$	[Cp*Rh(5M-C37**L1**)Cl]$^{2+}$	[Cp*Rh(7M-C110**L1**)Cl]$^{2+}$
K_M^{NADP+} (μM)	52 ± 2.9	36 ± 0.9	32 ± 2.3
Adjusted R^2	*0.99*	*0.97*	*0.99*
*TOF_{max}^{NADP+} (h^{-1})	78 ± 0.7	57 ± 0.8	49 ± 0.4
K_M^{NAD+} (μM)	44 ± 1.6	41 ± 4.8	30 ± 2.3
Adjusted R^2	*0.99*	*0.99*	*0.99*
*TOF_{max}^{NAD+} (h^{-1})	77 ± 0.5	59 ± 1.7	50 ± 0.7
K_M^{BNA+} (μM)	690 ± 69	382 ± 14	263 ± 8
Adjusted R^2	*0.95*	*0.95*	*0.89*
*TOF_{max}^{BNA+} (h^{-1})	68 ± 0.8	33 ± 0.1	27 ± 0.2

*It should be noted that an optimised ICP-MS digestion procedure was used to calculate the solution concentration of ArM variants modified at residue locations 37 and 110, while the TOF_{max} values for the location 243-modified variant may be less accurate.

Appendix 2 – Crystallisation conditions tested for ArM variant [Cp*Ir(5M-C37**L1**)Cl]$^{2+}$

0.1 M MES pH 6.5 **40 % v/v MPD** **5 % w/v PEG 8000**	0.1 M MES pH 6.5 40 % v/v MPD 3 % w/v PEG 8000	0.1 M MES pH 6.5 40 % v/v MPD 7 % w/v PEG 8000	0.08 M MES pH 6.5 40 % v/v MPD 5 % w/v PEG 8000	0.08 M MES pH 6.5 40 % v/v MPD 3 % w/v PEG 8000	0.08 M MES pH 6.5 40 % v/v MPD 7 % w/v PEG 8000
0.1 M HEPES pH7.5 **10 % w/v PEG 8000** **8 % v/v Ethylene glycol**	0.1 M HEPES pH7.5 8 % w/v PEG 8000 8 % v/v Ethylene glycol	0.1 M HEPES pH7.5 12 % w/v PEG 8000 8 % v/v Ethylene glycol	0.08 M HEPES pH7.5 10 % w/v PEG 8000 8 % v/v Ethylene glycol	0.08 M HEPES pH7.5 8 % w/v PEG 8000 8 % v/v Ethylene glycol	0.08 M HEPES pH7.5 12 % w/v PEG 8000 8 % v/v Ethylene glycol

Screening around crystallisation conditions for ArM variant [Cp*Ir(5M-C37**L1**)Cl]$^{2+}$ based on JCSG-plus ECO Screen conditions B4 (blue) and B5 (black), with the original conditions shown in bold.

Appendix 3 – Omit map for [Cp*Ir(7M-C110**L1**)Cl]$^{2+}$ NADP^{+} *in crystallo* binding site in subunit D

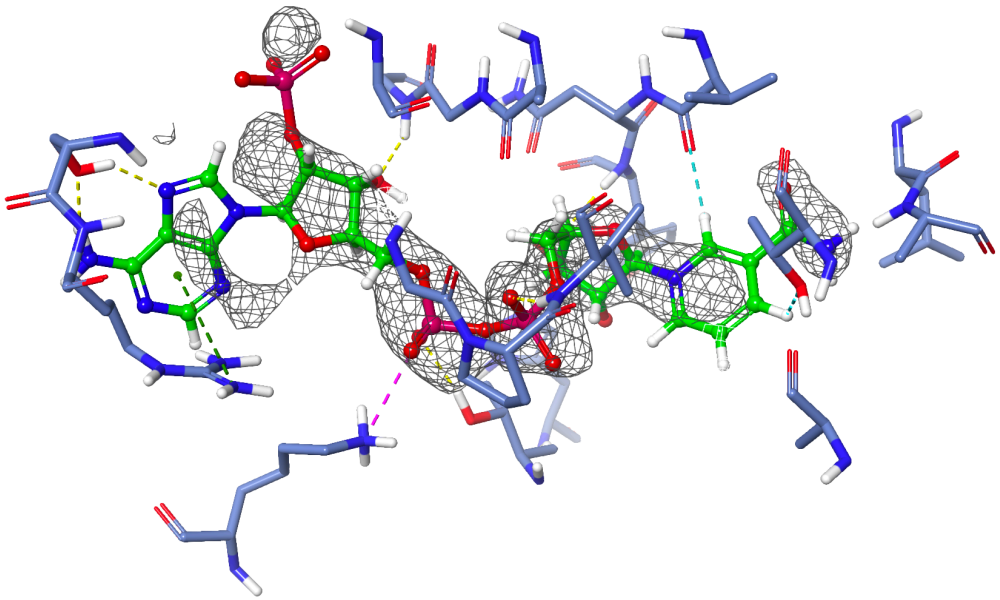

Alternative *in-crystallo* conformation of the NADP^{+} adenine and ribose phosphate moieties in [Cp*Ir(7M-C110**L1**)Cl]$^{2+}$ subunit D with poorly defined positive difference density (omit map shown in grey mesh, contoured to 2.5 σ). Residues within a 3 Å radius of the ligand are displayed in ice blue by atom type. Schrodinger Maestro identified interactions are shown (H-bonds = yellow, aromatic H-bonds = cyan, salt bridges = pink, pi-cation = dark green).

Appendix 4 – ^{1}H NMR and ESI-MS^{+} spectra of *2-bromo-N-(1,10-phenanthrolin-5-yl)acetamide* (**L1**)

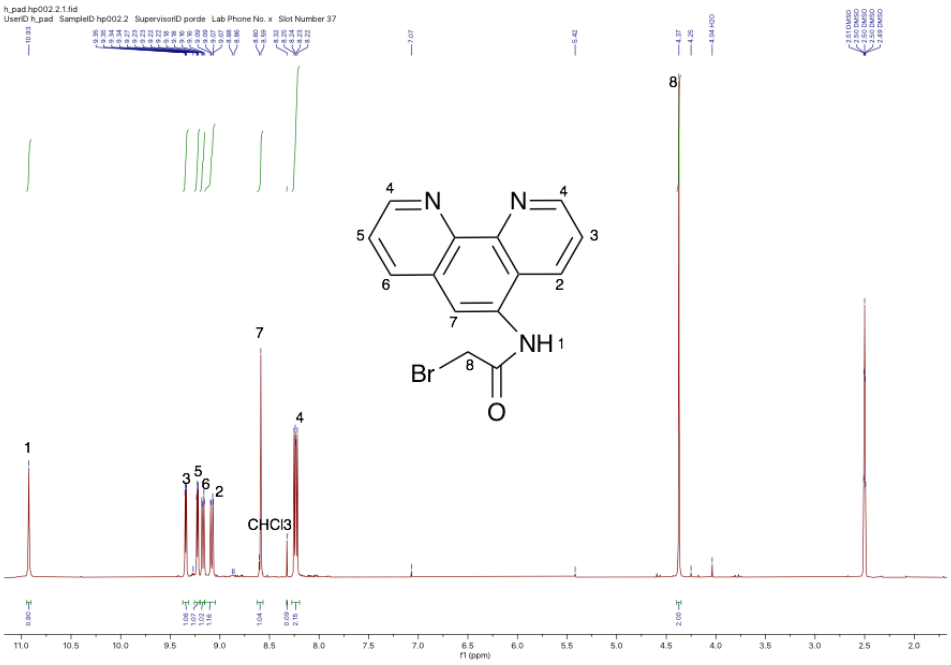

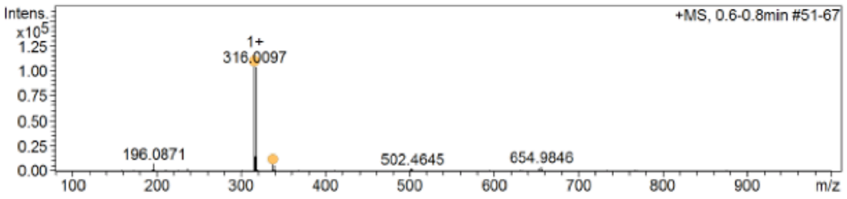

#	m/z	I %
1	195.0798	1.3
2	196.0871	7.5
3	197.0883	1.2
4	236.0801	2.3
5	316.0097	100.0
6	317.0124	14.0
7	318.0086	99.5
8	319.0105	14.4
9	320.0108	1.3
10	337.9903	6.3
11	339.9880	5.3
12	368.1795	1.1
13	501.4681	2.1
14	501.9701	1.3
15	502.4645	2.5
16	594.8396	1.1
17	652.9934	2.3
18	654.9846	4.0
19	655.9907	1.5
20	656.9900	1.8

Appendix 5 – ^{1}H NMR and ESI-MS^{+} spectra of complex [Cp*Rh(Br**L1**)Cl]Cl

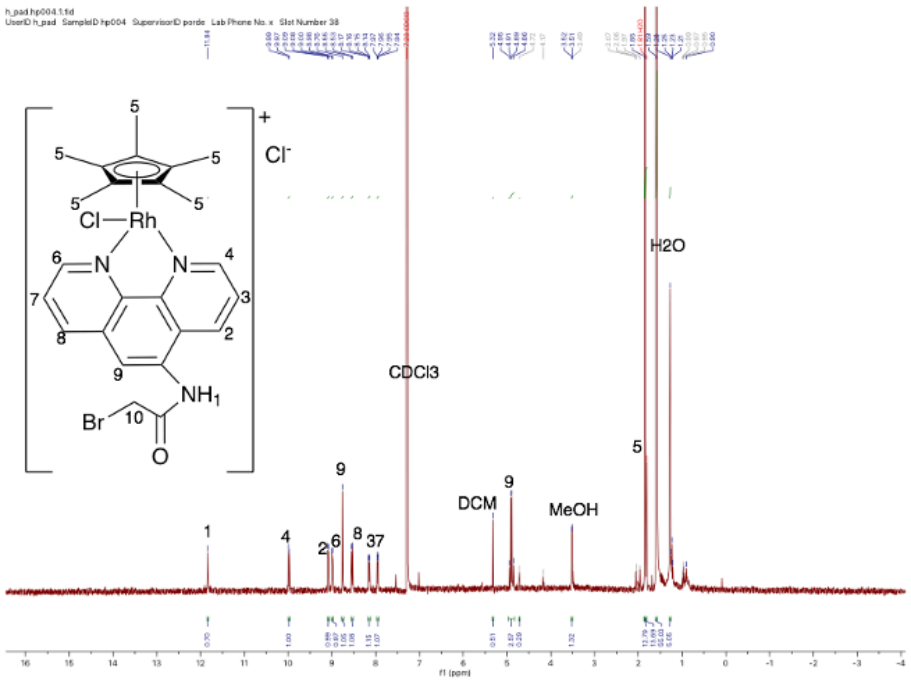

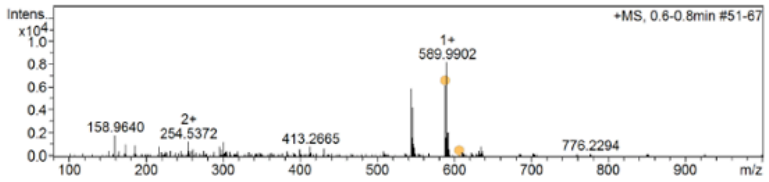

#	m/z	I %
1	158.9640	21.9
2	173.0779	11.7
3	185.1133	10.8
4	217.1042	9.5
5	254.5372	15.2
6	294.9379	9.4
7	301.1402	14.7
8	413.2665	9.7
9	430.9117	7.2
10	544.0421	71.8
11	545.0472	19.7
12	546.0396	52.0
13	547.0427	12.8
14	548.0379	8.9
15	587.9921	75.3
16	588.9939	19.7
17	589.9902	100.0
18	590.9921	24.8
19	591.9875	25.2
20	633.9413	9.7

Appendix 6 – ^{1}H NMR and ESI-MS^{+} spectra of complex [Cp*Ir(Br**L1**)Cl]C

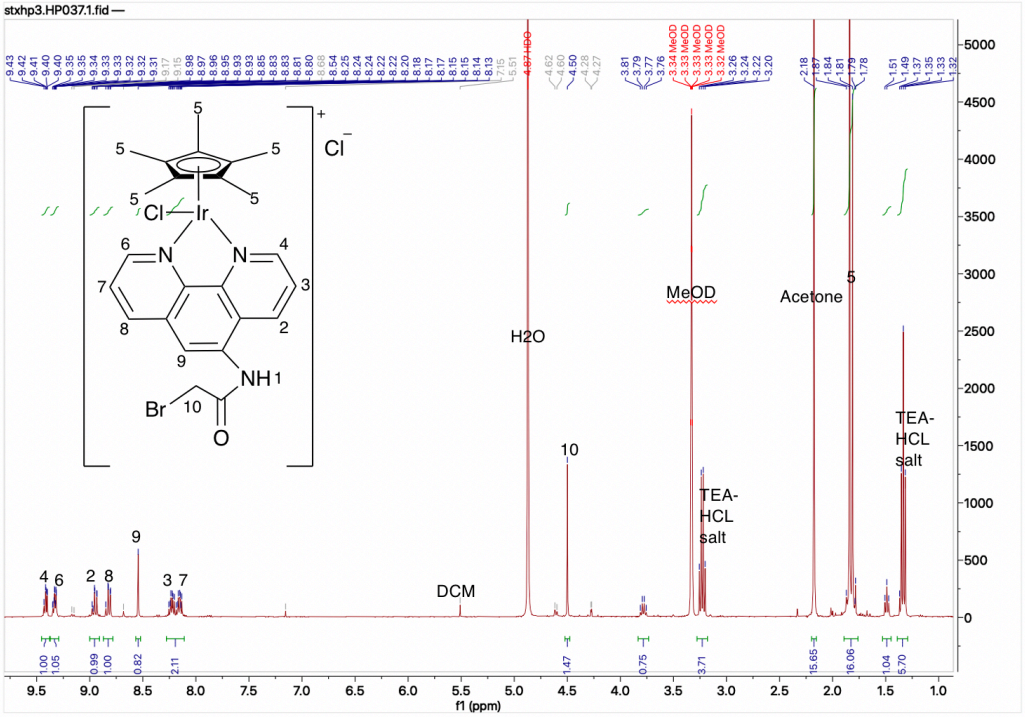

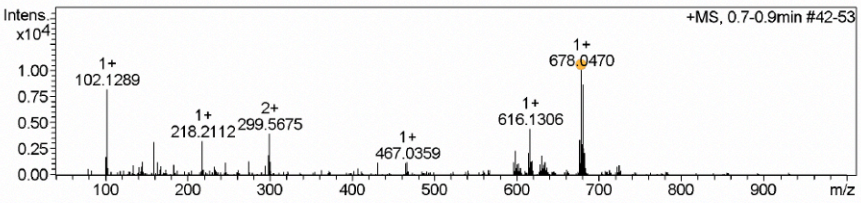

#	m/z	I %
1	101.0040	17.3
2	102.1289	81.7
3	145.1332	12.3
4	158.9635	31.6
5	218.2112	32.8
6	274.2748	12.7
7	298.5683	19.1
8	299.5675	39.5
9	300.5681	12.3
10	598.1228	23.6
11	614.1281	21.0
12	616.1306	44.0
13	618.1285	13.4
14	630.1507	18.9
15	676.0467	33.4
16	678.0470	100.0
17	679.0473	29.2
18	680.0448	86.1
19	681.0500	25.7
20	682.0418	21.2

Appendix 7 – ^{1}H NMR and ESI-MS^{+} spectra of complex [Cp*Ir(Br**L2**)Cl]Cl

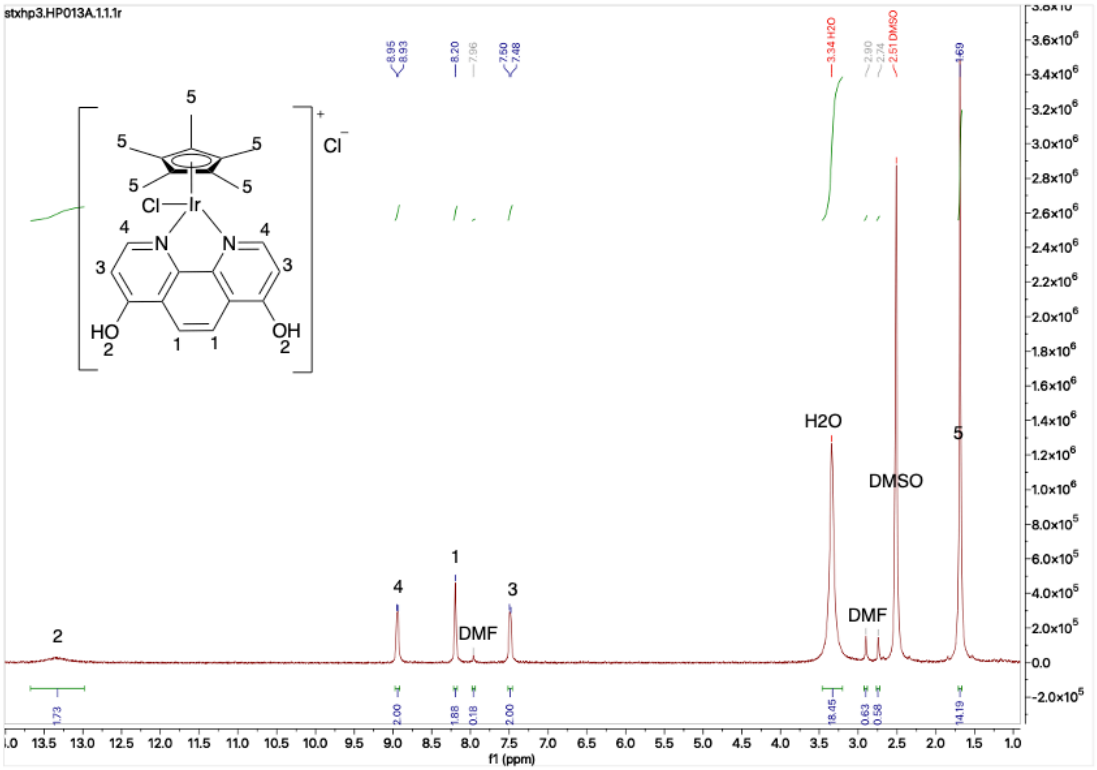

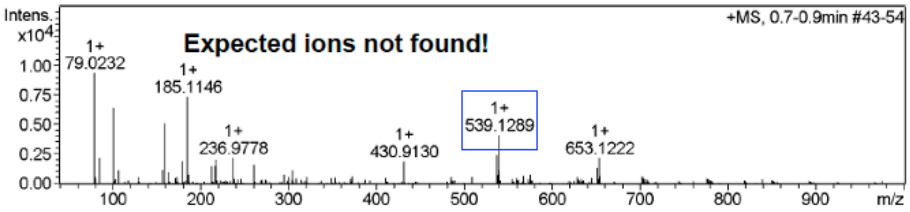

#	m/z	I %
1	79.0232	100.0
2	85.0603	23.4
3	101.0047	68.6
4	107.0421	11.7
5	157.0509	12.5
6	158.9636	54.6
7	179.0172	20.4
8	185.1146	78.2
9	213.1455	16.0
10	217.1035	16.4
11	218.2117	22.1
12	236.9778	23.5
13	261.1291	17.3
14	305.1569	11.9
15	430.9130	20.1
16	537.1279	26.2
17	539.1289	43.8
18	540.1313	12.2
19	651.1175	14.5
20	653.1222	23.3

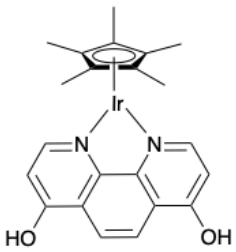

Mr = 539

Appendix 8 – ^{1}H NMR and ESI-MS^{+} spectra of complex [Cp*Ir(Br**L4**)Cl]Cl

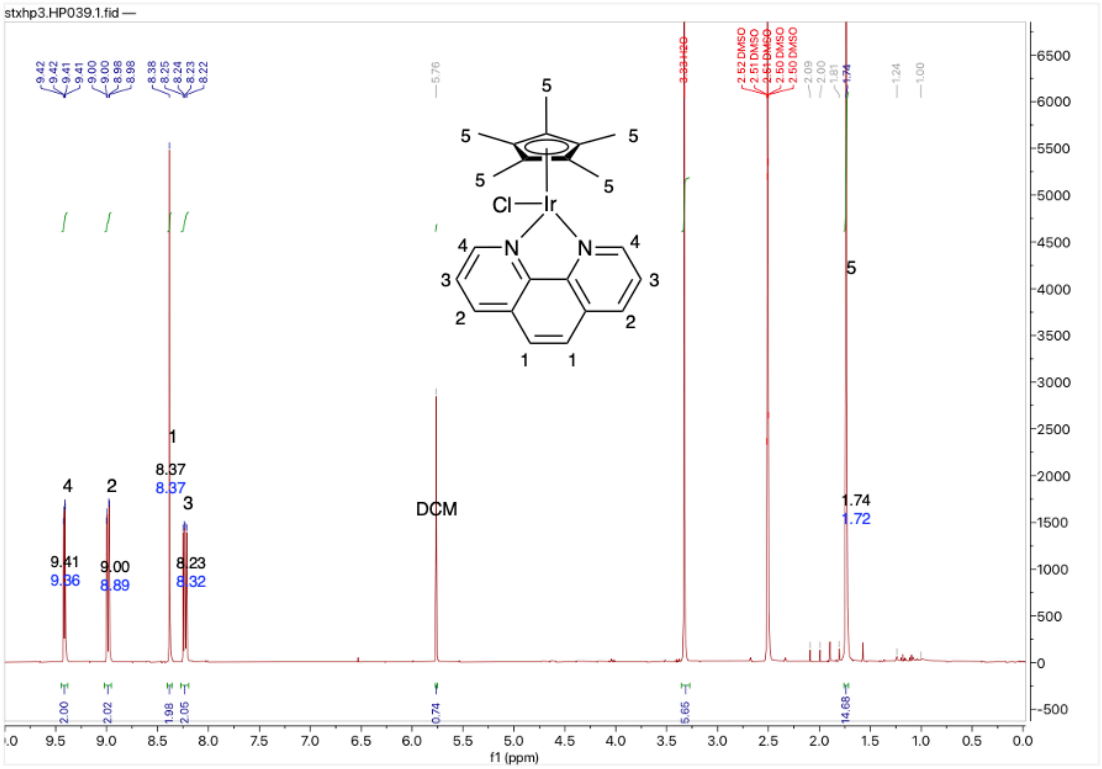

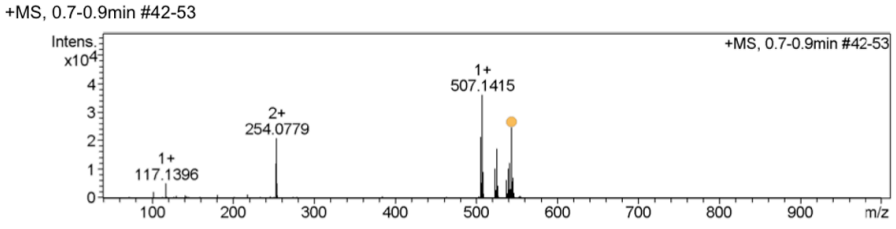

#	m/z	I %
1	117.1396	14.3
2	253.0759	33.9
3	253.5772	8.8
4	254.0779	57.8
5	254.5790	14.4
6	505.1382	59.2
7	506.1392	14.9
8	507.1415	100.0
9	508.1434	25.4
10	523.1485	28.5
11	525.1510	47.8
12	526.1536	12.1
13	537.1645	17.6
14	539.1664	28.9
15	540.1709	8.3
16	541.1157	34.2
17	542.1176	8.5
18	543.1165	68.5
19	544.1203	16.4
20	545.1150	20.1

The ^{1}H NMR chemical shift values identified here and by the Sadler group[195] are highlighted in black and blue respectively.

Appendix 9 – EPR spectra of 4-hydroxy-TEMPO standard and attempted [Cp*Ir(Br**L1**)Cl]Cl catalysed menadione reduction

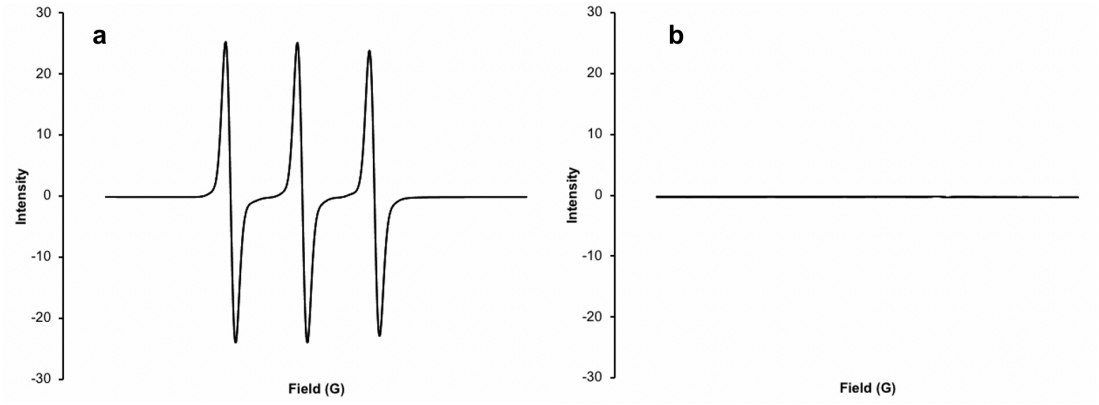

Example reaction and standard spectra from EPR analysis of menadione reduction. EPR spectra of **a** 1 mM 4-hydroxy-TEMPO standard, **b** [Cp*Ir(Br**L1**)Cl]Cl catalysed menadione reduction under literature conditions (Table **4.6**) after 6 h incubation.[195]

Appendix 10 – ^{1}H NMR and ESI-MS^{+} spectra of complex ([Cp*Ir(**L4**)H$_2$O](PF$_6$)$_2$

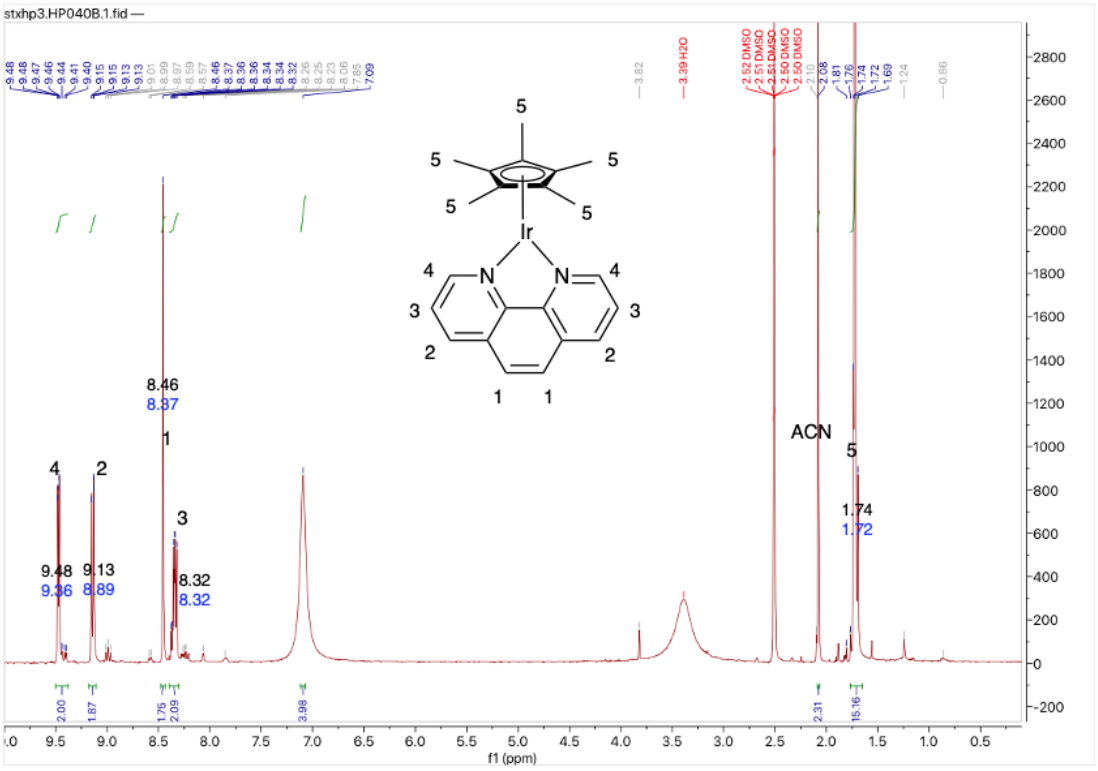

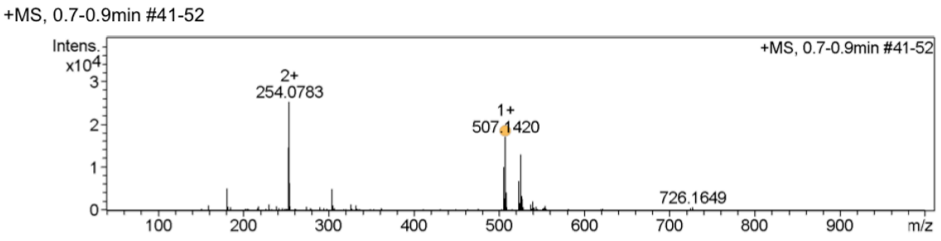

#	m/z	I %
1	181.0775	20.4
2	230.2492	5.3
3	253.0768	57.9
4	253.5779	15.0
5	254.0783	100.0
6	254.5796	25.5
7	304.3009	20.1
8	305.3033	4.7
9	326.3805	5.3
10	505.1391	39.9
11	506.1419	10.8
12	507.1420	67.8
13	508.1439	16.9
14	523.1504	27.3
15	524.1521	6.9
16	525.1516	51.4
17	526.1521	13.2
18	527.1478	10.6
19	537.1672	5.3
20	539.1668	8.4

The ^{1}H NMR chemical shift values identified here and by the Sadler group[195] are highlighted in black and blue respectively.

Appendix 11 – Example of 5M-C37 TbADH mutant crystals

The cube-like crystals were formed after approximately 5 days of sitting drop vapour diffusion incubation at 20 °C in 0.2 M Ammonium chloride, 20 % (w/v) PEG 3350.

Appendix 12 – Example of [Cp*Ir(7M-C110**L1**)Cl]$^{2+}$ ArM crystals

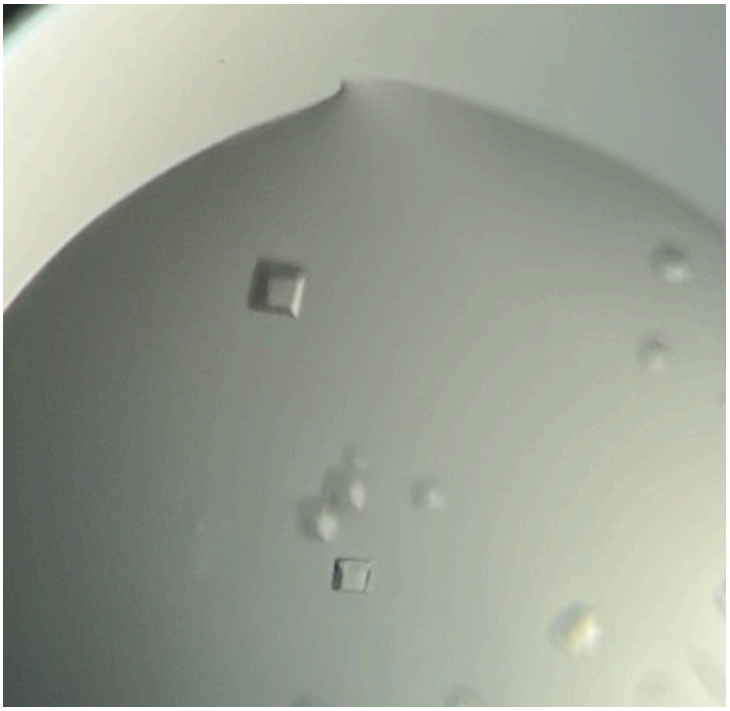

The cube-like crystals were formed after approximately 5 days of sitting drop vapour diffusion incubation at 20 °C in 0.1 M HEPES pH 7.5, 10 % (w/v) PEG 8000, 8 % (w/v) ethylene glycol.